UNIVERSITÀ DI SIENA 1240

UAM
Universidad Autónoma de Madrid

Ph.D. Thesis

Cosmic-ray transport in the Milky Way and related phenomenology

Author
Ottavio Fornieri

Tutor
Prof. Pier Simone Marrocchesi

Advisor
Dr. Daniele Gaggero
Tutor
Prof. Carlos Muñoz

A thesis submitted in fulfillment of the requirements for the degree of Doctor of Philosophy

at the

University of Siena — Autonomous University of Madrid

Academic year 2020/2021

UNIVERSITÀ DI SIENA 1240

Department of Physical Sciences, Earth and Environment

Ph.D. course in Experimental Physics

Cycle XXXIII

Coordinator: Prof. Riccardo Paoletti

Cosmic-ray transport in the Milky Way and related phenomenology

Disciplinary Scientific Sector: FIS/02

Candidate
Ottavio Fornieri, *matr.:* 076681

Supervisor
Dr. Daniele Gaggero
Universidad Autonoma de Madrid

Tutor
Prof. Pier Simone Marrocchesi
Università di Siena

Academic year 2020/2021

Universidad Autónoma
de Madrid

Department of Theoretical Physics

Ph.D. course in Theoretical Physics

Coordinator: Prof. Claudia Beatriz Glasman Kuguel

Cosmic-ray transport in the Milky Way and related phenomenology

Candidate
Ottavio Fornieri, *NIA:* 410343

Supervisor
Dr. Daniele Gaggero
Universidad Autonoma de Madrid

Tutor
Prof. Carlos Muñoz
Universidad Autonoma de Madrid

Academic year 2020/2021

Reviewer

Prof. Fiorenza Donato
Department of Physics, University of Torino
Torino, Italy

Reviewer

Dr. Andrew Taylor
Deutches Elektronen-Synchrotron, DESY
Zeuthen, Germany

Abstract

In this thesis, we aim at studying some of the open questions regarding the origin of the *Cosmic Rays* (CRs), as well as their transport properties.

The exceptional quality of the experimentally measured cosmic-ray observables, especially at the recently-achieved energies in the range $\sim \mathcal{O}(100\,\mathrm{GeV} - 1\,\mathrm{TeV})$, started to question the standard picture, based on a *Supernova Remnant-* (SNR)-only origin of the CRs and a diffusive propagation inspired by the *Quasi-Linear Theory* (QLT) of pitch-angle interaction against alfvénic turbulence.

First, we reproduce the most relevant cosmic-ray observables to tune the propagation setup, numerically solving the transport equation with the `DRAGON` code. On top of this, to account for the rising of the e^+ above $\sim 10\,\mathrm{GeV}$, we fit a primary population of positrons originating in *Pulsar Wind Nebulae*, in a model-independent setup that considers the uncertainties in the pulsar injections mechanism. Since the all-lepton spectrum is still not reproduced above $\sim 50\,\mathrm{GeV}$ — and in particular the $\sim$ TeV break — we consider the contribution from a nearby source of e^-, and conclude that an old ($t_{\mathrm{age}} \sim 10^5\,\mathrm{yr}$) SNR, located between $\sim 600\,\mathrm{pc}$ and $\sim 1\,\mathrm{kpc}$, is probably missing from the Catalogues.

Within the hypothesis of such old remnant in its radiative phase contributing to the $e^+ + e^-$, we search for its signature in the proton flux as well. To do this, we consider a phenomenological propagation setup that reproduces the hadronic spectral hardening at $\sim 200\,\mathrm{GeV}$ as a diffusive feature ($D(E) \propto E^{\delta(E)}$), and adopt it consistently for the large-scale background and for the nearby source. Within this framework, we account for the all-lepton spectrum, the proton spectrum and the cosmic-ray dipole anisotropy with the same old ($t_{\mathrm{age}} = 2 \cdot 10^5\,\mathrm{yr}$), nearby ($d = 300\,\mathrm{pc}$) remnant. We highlight that the progressively hardening diffusion coefficient is a crucial ingredient, since, in a single-power-law diffusion scenario, the dipole anisotropy data would be overshot by, at least, one order of magnitude.

Finally, we explore the phenomenological implications of a change of paradigm in the standard cosmic-ray diffusion — based on wave-particle interaction with Alfvén fluctuations — considering a non-linear extension of the QLT that enhances the efficiency of CR-scattering with the other *Magneto-Hydro-Dynamic* (MHD) modes. Indeed, assuming the anisotropy of the alfvénic cascade, its scattering rate at all energies below $\sim 100\,\mathrm{TeV}$ is not able to confine charged cosmic rays, and the *fast magnetosonic* modes alone shape the diffusion coefficient that particles experience in the Galaxy. Within such picture, we implement the resulting $D(E)$ in `DRAGON2`, where two independent zones differently affect the evolution of the MHD cascade: the Halo ($L_{\mathrm{Halo}} \sim 5 - 6\,\mathrm{kpc}$) and the *Warm Ionized Medium* ($L_{\mathrm{WIM}} \sim 1\,\mathrm{kpc}$). We find that, with a reasonable choice of selected quantities, representing the physics of the environments, we can reproduce the hadronic fluxes, as well as the boron-over-carbon ratio, from $\sim 200\,\mathrm{GeV}$ above. We assign to the rising of the *streaming instabilities* the cosmic-ray transport below this energy.

Riassunto

In questa tesi, ci proponiamo di studiare alcune delle domande ancora aperte riguardo l'origine dei *Raggi Cosmici* (RC) e riguardo le loro proprietà di trasporto.

L'eccezionale qualità delle osservabili sperimentali relative ai RC, specialmente nell'intervallo di energia intorno a $\sim \mathcal{O}(100\,\mathrm{GeV} - 1\,\mathrm{TeV})$, raggiunto recentemente, ha fatto sì che si mettesse in discussione lo scenario standard, basato sulla loro origine solo da *Resti di Supernova* (SNR) e su una fisica della diffusione ispirata dalla *Quasi-Linear Theory* (QLT) dello scattering contro turbolenza alfvénica.

Prima di tutto, riproduciamo le osservabili più importanti per regolare il setup di propagazione, risolvendo numericamente l'equazione del trasporto con il codice `DRAGON`. Con questo sfondo, per tenere in considerazione l'innalzamento dei e^+ a partire da $\sim 10\,\mathrm{GeV}$, fittiamo una popolazione di positroni primari provenienti da *Pulsar Wind Nebulae*, in un setup che non dipende dalla scelta di uno specifico modello, per considerare le incertezze tuttora presenti nei meccanismi di iniezione da pulsar. Siccome lo spettro dei $e^+ + e^-$ non è riprodotto sopra i $\sim 50\,\mathrm{GeV}$ — e in particolare nemmeno il break al $\sim \mathrm{TeV}$ — studiamo il contributo proveniente da una sorgente di e^- vicina, concludendo che un vecchio ($t_{\mathrm{age}} \sim 10^5\,\mathrm{yr}$) SNR, situato tra $\sim 600\,\mathrm{pc}$ e $\sim 1\,\mathrm{kpc}$, probabilmente manca dai Cataloghi.

Sotto l'ipotesi che questo vecchio remnant in fase radiativa contribuisca ai $e^+ + e^-$, cerchiamo una sua impronta nel flusso di protoni. Per farlo, consideriamo un setup di propagazione fenomenologico che riproduca l'hardening spettrale a $\sim 200\,\mathrm{GeV}$ come una caratteristica diffusiva ($D(E) \propto E^{\delta(E)}$), e lo adottiamo consistentemente sia per il background di larga scala, sia per la sorgente vicina. Dentro questo scenario, riproduciamo lo spettro dei leptoni totali, il flusso dei protoni e l'anisotropia di dipolo con lo stesso vecchio ($t_{\mathrm{age}} = 2 \cdot 10^5\,\mathrm{yr}$) remnant vicino ($d = 300\,\mathrm{pc}$). Sottolineiamo che il coefficiente di diffusione che si appiattisce progressivamente è un ingrediente cruciale, perchè, in uno scenario con singola legge di potenza, i dati sull'anisotropia vengono oltrepassati di almeno un ordine di grandezza.

Infine, esploriamo le implicazioni fenomenologiche di un cambio di paradigma rispetto alla diffusione standard — basata sull'interazione onda-particella con fluttuazioni di Alfvén — considerando una estensione non lineare della QLT che aumenti l'efficienza di scattering con altri modi *Magneto-Idro-Dinamici* (MHD). Infatti, assumendo un'anisotropia della cascata alfvénica, il suo rate di scattering a tutte le energie sotto i $\sim 100\,\mathrm{TeV}$ non è in grado di confinare raggi cosmici carichi, e sono i modi *magnetosonici veloci* a formare il coefficiente di diffusione che le particelle sentono nella Galassia. All'interno di questo scenario, implementiamo i $D(E)$ risultanti in `DRAGON2`, in cui due zone indipendenti della Galassia influiscono in modo diverso sulla evoluzione della cascata MHD: l'Alone $L_{\mathrm{Halo}} \sim 5 - 6\,\mathrm{kpc}$ e il *Mezzo Ionizzato Caldo* ($L_{\mathrm{WIM}} \sim 1\,\mathrm{kpc}$). Troviamo che, con una scelta ragionevole di alcune grandezze selezionate, che rappresentino la fisica di questi ambienti, riproduciamo i flussi adronici e il rapporto boro-su-carbonio, da $\sim 200\,\mathrm{GeV}$ in su. Assegniamo all'emergere delle *instabilità di flusso* il trasporto dei raggi cosmici al di sotto di tale energia.

Resumen

En esta tesis, nos proponemos estudiar algunas de las preguntas aún abiertas sobre el origen de los *Rayos Cósmicos* (CR) y sobre sus propiedades de transporte.

La excepcional calidad de las observables experimentales relacionadas con los CRs, especialmente en el rango de energía $\sim \mathcal{O}(100\,\mathrm{GeV} - 1\,\mathrm{TeV})$, alcanzado recientemente, hizo que se cuestionara el escenario estándar, basado en su origen desde *Remanentes de Supernova* (SNR) y en la física de la difusión inspirada por la *Quasi-Linear Theory* (QLT) del scattering contra la turbulencia alfvénica.

En primer lugar, reproducimos los observables más importantes para ajustar la configuración de la propagación, resolviendo la ecuación de transporte numéricamente con el código `DRAGON`. Para tener en cuenta el aumento de e^+ a partir de $\sim 10\,\mathrm{GeV}$, ajustamos una población de positrones primarios de *Pulsar Wind Nebulae*, en una configuración que no depende de un modelo específico, para considerar las incertidumbres aún presentes en los mecanismos de inyección de púlsar. Como el espectro de $e^+ + e^-$ no se reproduce con esta configuración por encima de $\sim 50\,\mathrm{GeV}$ — y, en particular, ni siquiera el cambio de pendiente a $\sim \mathrm{TeV}$ — estudiamos la contribución de una fuente cercana de e^-, concluyendo que un antiguo ($t_{\mathrm{age}} \sim 10^5\,\mathrm{yr}$) SNR, ubicado entre $\sim 600\,\mathrm{pc}$ y $\sim 1\,\mathrm{kpc}$, no se encuentra en los catálogos.

En la hipótesis de que este SNR contribuye al flujo de $e^+ + e^-$, buscamos su huella en los protones. Para hacer esto, consideramos una configuración de la propagación fenomenológica que reproduce el cambio espectral a $\sim 200\,\mathrm{GeV}$ como una característica de la difusión, ($D(E) \propto E^{\delta(E)}$), y lo adoptamos tanto para el fondo, a gran escala, como para la fuente cercana. Dentro de este escenario, reproducimos el espectro total de leptones, el flujo de protones y la anisotropía dipolar con el mismo ($t_{\mathrm{age}} = 2 \cdot 10^5\,\mathrm{yr}$) SNR, a una distancia de $d = 300\,\mathrm{pc}$. Enfatizamos que el $D(E)$ que se aplana gradualmente conforme al cambio de energía es un ingrediente crucial porque, en un escenario de ley de potencia única, los datos de anisotropía se exceden en, al menos, un orden de magnitud.

Finalmente, exploramos las implicaciones fenomenológicas de un cambio de paradigma con respecto a la difusión estándar — basado en la interacción onda-partícula con fluctuaciones de Alfvén — considerando una extensión no lineal del QLT que aumenta la eficiencia de dispersión con otros modos de *Magneto-Hydro-Dynamics* (MHD). De hecho, asumiendo una anisotropía de la cascada alfvénica, su tasa de dispersión para todas las energías por debajo de $\sim 100\,\mathrm{TeV}$ no es capaz de confinar los CRs, y son los modos *magnetosónico rápido* los que forman el coeficiente de difusión que las partículas sienten en la Galaxia. En este escenario, implementamos el $D(E)$ que resulta en `DRAGON2`, en el que dos zonas independientes de la Galaxia afectan la evolución de la cascada MHD de manera diferente: el Halo $L_{\mathrm{Halo}} \sim 5 - 6\,\mathrm{kpc}$ y el *medio ionizado caliente* ($L_{\mathrm{WIM}} \sim 1\,\mathrm{kpc}$). Encontramos que, con una elección razonable de algunas cantidades seleccionadas, que representan la física de estos entornos, reproducimos los flujos hadrónicos y la relación de B/C, desde $\sim 200\,\mathrm{GeV}$ en adelante. La aparición de *inestabilidades de flujo* puede explicar de forma natural el transporte de CRs por debajo de esta energía.

Contents

Listing of figures 2

Listing of tables 3

0 **Introduction** 5
- 0.1 Introduction & Motivations . . . 5
- 0.2 Outline of the Thesis . . . 8
- 0.3 Research Contributions . . . 9

I Cosmic-ray physics 11

1 **Theoretical foundations of cosmic-ray acceleration and transport** 13
- 1.1 Overview of the experimental status . . . 14
- 1.2 Cosmic-ray acceleration at the sources . . . 18
  - 1.2.1 Second-order Fermi acceleration . . . 18
  - 1.2.2 First-order Fermi acceleration . . . 21
- 1.3 Cosmic-ray diffusion through the Galaxy . . . 28
  - 1.3.1 The equations of the ideal MHD . . . 31
  - 1.3.2 The *Fokker-Planck* coefficients within the QLT . . . 34
  - 1.3.3 The transport equation in physical space: the physics of parallel diffusion $D_{\parallel}$ 48
  - 1.3.4 Limitations of the QLT . . . 54
- 1.4 Summary of the chapter . . . 57

2 **Implementation in the DRAGON code and multi-messenger implications** 59
- 2.1 DRAGON: a general overview . . . 60
- 2.2 Astrophysics in DRAGON . . . 64
  - 2.2.1 Parametrization of the interstellar environment . . . 64
  - 2.2.2 Cosmic-ray non-adiabatic energy losses . . . 68
- 2.3 Multi-messenger implications of CR transport in the Galaxy . . . 78
- 2.4 Summary of the chapter . . . 84

II Impact of local sources on the hadronic and leptonic spectra 85

3 **Features in the lepton spectra set the ground for a hidden nearby source** 87
- 3.1 Motivations . . . 88
- 3.2 Characterization of the large-scale CR transport scenario . . . 89
  - 3.2.1 Setting source and transport parameters against CR nuclei data . . . 90
  - 3.2.2 Primary electrons and secondary positrons . . . 93
- 3.3 The positron excess . . . 94
  - 3.3.1 Basic aspects of injection pulsar wind nebulae and relevant caveats . . . 94
  - 3.3.2 Diffusive propagation of leptons in the Galaxy: study of the analytical solution . . . 97
  - 3.3.3 Contribution from old and young pulsars to the positron flux . . . 100
  - 3.3.4 Characterization of the high-energy flux . . . 102
- 3.4 Local electron accelerators explain the high-energy electron data . . . 106
  - 3.4.1 Contribution from the known objects . . . 106

3.4.2 Characterization of a source reproducing the ~ 1 TeV break . . . 109
3.5 Summary of the chapter . . . 113
Appendix 3.A1 Estimation of the release time from PWNe . . . 114
Appendix 3.A2 Posterior distribution functions for the fit to the positron flux . . . 116
Appendix 3.A3 Notes on the pulsars from ATNF Catalogue . . . 117

4 A varying-slope diffusion coefficient connects the lepton and proton spectra 121
4.1 Motivations . . . 122
4.2 Our transport setup . . . 123
4.3 A consistent picture for the electron, proton and anisotropy data . . . 126
4.3.1 All-lepton spectrum . . . 127
4.3.2 Proton spectrum . . . 129
4.3.3 CR dipole anisotropy . . . 131
4.4 Discussion . . . 133
4.5 Summary of the chapter . . . 136
Appendix 4.A1 Energy-dependent release time from Supernova remnant shocks . . . 137
Appendix 4.A2 On the expected number of nearby hidden remnants . . . 139

III Impact of the microphysics of the MHD modes on CR transport 141

5 The role of fast magnetosonic modes in cosmic-ray diffusion 143
5.1 Motivations . . . 144
5.2 Scattering rate and diffusion coefficient in MHD turbulence . . . 146
5.3 Diffusion coefficients in Galactic disk and halo and ISM properties . . . 151
5.4 Phenomenological implications of the theory . . . 156
5.5 Discussion . . . 160
5.6 Summary of the chapter . . . 163
Appendix 5.A1 Pitch-angle coefficient for MHD turbulence . . . 164
5.A1.1 $D_{\mu\mu}$ from Alfvén modes . . . 166
5.A1.2 $D_{\mu\mu}$ from fast modes . . . 171
5.A1.3 $D_{\mu\mu}$ from slow modes . . . 174

Conclusions i

References iii

Listing of figures

1.1 All-particle cosmic-ray spectrum. 14
1.2 Photon spectral energy distributions characteristic of leptonic and hadronic emission and Supernova Remnant examples. 16
1.3 HAWC observation of the TeV-*halos* around two nearby pulsars. 18
1.4 Relative motion of two reference frames. 19
1.5 Physical sketch of the situation in presence of an infinitesimal shock. 22
1.6 Physical sketch of the diffusive shock acceleration process. 24
1.7 The displacement and propagation directions of the MHD modes are sketched. . . . 34
1.8 Helical motion of a charged particle in a uniform and perturbed magnetic field . . . 44
1.9 Perpendicular diffusion of a charged particle caused by $\delta\boldsymbol{B}$. 55

2.1 2D approximation of our Galaxy. 61
2.2 Realistic Galactic magnetic field and consequent D_{rr} and D_{zz} profiles. 62
2.3 Spectrum of the photons coming from neutral-pion decay. 75
2.4 Loss-timescales for leptons and hadrons around the solar system and at the Galactic center. 77
2.5 Photon emissivities due to IC, π^0 decay and bremsstrahlung, for $E_\gamma = 1.5\,\mathrm{GeV}$. . . . 80
2.6 Photon emissivities due to IC, π^0 decay and bremsstrahlung, for $E_\gamma = 100\,\mathrm{GeV}$. . . . 81
2.7 Photon emissivities due to IC, π^0 decay and bremsstrahlung, for $E_\gamma = 1\,\mathrm{TeV}$. 82
2.8 *Fermi*-LAT γ-ray sky integrated over energies above $E_\gamma = 1\,\mathrm{GeV}$, after 5 years of data taking. 83

3.1 Cosmic-ray propagation setup from our DRAGON reference model. 92
3.2 Solution of the single-source transport equation, in age and distance. 100
3.3 Fit to the AMS-02 positron flux. 104
3.4 Fit of the H.E.S.S. + AMS-02 $e^+ + e^-$ flux: case with known sources only. 108
3.5 Fit of the H.E.S.S. + AMS-02 $e^+ + e^-$ flux: case with the additional hidden source. . 111
3.6 Intersection between the time-evolution of a type-Ia SN shock radius and the distance travelled by a pulsar with given initial kick. 115
3.7 Posterior distribution functions for the fits to the positron flux. 116
3.8 ATNF Catalogue pulsars with $d < 1\,\mathrm{kpc}$ and $t_\mathrm{age} < 2 \cdot 10^8\,\mathrm{yr}$. 119
3.9 Propagated e^+ from ATNF Catalogue pulsars with $d < 1\,\mathrm{kpc}$ and $t_\mathrm{age} < 2 \cdot 10^8\,\mathrm{yr}$. . . 119

4.1 Progressively hardening diffusion coefficient $D(E) \sim E^{\delta(E)}$. 124
4.2 B/C ratio for the reference transport setup with the varying $D(E)$. 125

4.3 All-lepton spectrum with the nearby-source injected particles propagated in $D(E) \sim E^{\delta(E)}$ . . . 128
4.4 Proton flux, where the nearby-source injected particles are transported in $D(E) \sim E^{\delta(E)}$ . . . 130
4.5 Cosmic-ray dipole anisotropy resulting from the large-scale background plus the nearby source. . . . 133

5.1 Diffusion coefficients resulting from the MHD modes, in the Halo and in the extended disk. . . . 152
5.2 Effect of the damping mechanisms in the Halo and in the extended disk. . . . 153
5.3 Ineffectiveness of alfvénic confinement. . . . 154
5.4 B/C ratio as a function of $M_{\rm A}$. . . . 158
5.5 B/C ratio as a function of $M_{\rm A}$, for different values of the disk size. . . . 159
5.6 Fluxes of H, B, C for selected values of our parameters. . . . 160

Listing of tables

2.1 Overview of the interaction processes involving emission of γ's and ν's. 78

3.1 Injection parameters of our reference transport model. 91
3.2 Pulsar parameters resulting from the fit to the e^+ flux: case with an injection break. . 103
3.3 Pulsar parameters resulting from the fit to the e^+ flux: case with an injection cutoff. 103
3.4 Nominal ages and distances of the five closest observed SNRs. 107
3.5 Parameters resulting from the fit to the $e^+ + e^-$ flux. 108
3.6 Parameters resulting from the fit to the $e^+ + e^-$ flux: case with the hidden source. . . 110

0 Introduction

0.1 Introduction & Motivations

More than a century after the discovery of *Cosmic Rays* (CRs), our understanding of the ensemble of processes governing their physics is still not satisfactory, due to our incomplete knowledge of both their acceleration mechanisms and their transport properties across the Milky Way.

At first order, there is a general consensus on the overall picture: CRs are accelerated at *Supernova Remnants* (SNRs) via *Diffusive Shock Acceleration* (DSA) and then propagate through the Galaxy according to the so-called *transport equation*, derived within the approximate framework of the so-called *Quasi-Linear Theory* (QLT) of pitch-angle scattering against *Magneto-Hydro-Dynamic* (MHD) fluctuations — such wave-particle interaction implies that particles *diffuse*. This equation effectively captures the relevant physical processes occurring to charged particles in the Galaxy (Ginzburg and Syrovatskii, 1964a). To support this picture, a series of numerical/semi-analytical codes solving the transport equation (*e.g.* `DRAGON`, `GALPROP` or `USINE`) are able to reproduce most of the observable data with a limited number of free parameters.

However, the exceptional quality of the observations, achieved in the last decade, highlighted a set of anomalies that seriously challenge the standard scenario, and questions regarding the origin of each CR-observable and their propagation properties still remain open. Among the most relevant features, we consider the following: (i) an excess of positrons with respect to the standard secondary-only production (Adriani et al., 2009), (ii) a spectral break in the all-lepton spectrum at $\sim 1\,\mathrm{TeV}$ (Adriani et al., 2011b), (iii) a hardening in the spectra of primary and secondary hadronic species around $\sim 250\,\mathrm{GV}$ (Adriani et al., 2011a).

(i) Solving the transport equation for secondary e^+ — generated by the spallation of protons and helium nuclei against targets of the *Interstellar Medium* (ISM) — and for primary e^-, the quantity

known as the *positron fraction* is expected to scale as $e^+/\left(e^+ + e^-\right) \approx e^+/e^- \sim E^{-\Gamma^p_{\rm inj}-\delta}/E^{-\Gamma^{e^-}_{\rm inj}}$, where $\delta > 0$ is the slope of the diffusion coefficient parametrized as $D(E) \propto E^\delta$. Assuming typical injection slopes $\Gamma^p_{\rm inj} = 2.4$ and $\Gamma^{e^-}_{\rm inj} = 2.4 - 2.7$, and $\delta \simeq 0.3 - 0.5$, then we would expect the *positron fraction* to decline with energy. This is in contrast with the findings of the PAMELA Collaboration (Adriani et al., 2009), later confirmed with higher accuracy by AMS (Aguilar et al., 2013), that observed a rising in the positron fraction around $E \sim 10\,{\rm GeV}$. Furthermore, the measurements of the absolute positron- and electron-fluxes by AMS-02 (Aguilar et al., 2019a,b) suggested that such excess is originated by a rising population of primary positrons, rather than from a declining flux of electrons. A plausible origin is the injection of $e^\pm$ pairs by pulsars, strongly supported by the recent observation of extended ($\sim 20\,{\rm pc}$) γ-ray halos around two nearby pulsars (Abeysekara et al., 2017), compatible with the *Inverse Compton* scattering of $\sim 100\,{\rm TeV}$ leptons against the *Cosmic Microwave Background* photons. However, pulsar injection mechanisms are not well understood yet, and phenomenological fits to the positron flux are required to bracket their uncertainties within a model-independent picture (Fornieri et al., 2020b).

(ii) The convoluted spectra from the large-scale, smooth distribution of SNRs plus the positron discrete sources are not able to reproduce a large portion of the high-energy (above $E \sim 50\,{\rm GeV}$) $e^+ + e^-$ spectrum — consistently with Boudaud et al. (2017) — including the $\sim 1\,{\rm TeV}$ break reported by several ground- and space-based detectors (see Fornieri et al. (2020b) and references therein). The contribution to both e^+ and e^- from the class of sources that inject positrons is guaranteed by assuming that they are generated in electromagnetic showers as $e^\pm$ pairs, and ignoring the unlikely hypothesis of sources of anti-matter only. Therefore, we can conclude that a source of e^- only — likely a Supernova Remnant — could be missing from the Catalogues. Invoking the incompleteness of the Catalogues, however, would still require running large Monte Carlo simulations to quantify up to what extent it is possible to observe the stochastic nature of the source-distribution at such high energy, considering the lepton horizon at the $\sim$ TeV scale to be $d_{\rm leptons} \lesssim 1\,{\rm kpc}$. Interesting works towards this direction have been carried out in Evoli et al. (2020a); Mertsch (2018), but their results are still dependent on the injection models and on the geometry of the source distribution. The latter, especially, is an important point, since a not-accurate implementation of the local ($\sim 1\,{\rm kpc}$) Galactic structure is able to discriminate the outcomes.

(iii) Studying this spectral anomaly has potential implications on the microphysics of cosmic-ray diffusion. As a matter of fact, the AMS-02 Collaboration reports a spectral hardening for secondary species that is twice as large as that for primaries (Aguilar et al., 2018b). Solving the transport equation in a diffusive regime, we obtain the distribution function at the disk level to be $f_0(E) \sim N(E)/D(E)$, where $N(E)$ is the particle injection-spectrum. For primary species, $N(E) \sim E^{-\Gamma_{\rm inj}}$, from which we get $f_0^{\rm pri} \sim E^{-\Gamma_{\rm inj}-\delta}$, while, for secondaries, the injection spectrum is the propagated spectrum of the primaries, resulting in $f_0^{\rm sec} \sim E^{-\Gamma_{\rm inj}-\delta}/D(E) = E^{-\Gamma_{\rm inj}-2\delta}$. Therefore, the above measurement is likely

interpreted as the footprint of a diffusive origin of the spectral hardening. An interesting interpretation of this feature is provided in Tomassetti (2012), where the authors show that it arises naturally by considering two different diffusion-scalings with rigidity in the Halo and in the Disk of our Galaxy, and that this picture is equivalent to consider a diffusion coefficient that progressively hardens as rigidity increases, namely $D(E) \propto E^{\delta(E)}$.

Several solutions have been proposed for each one of the previous issues, separately. An attempt to reconcile all of the observational anomalies and obtain a unified picture is made in Fornieri et al. (2020c), where the hypothesis of a nearby SNR is considered for the $e^+ + e^-$ spectrum. We know from the theory that Supernova Remnants inject both electrons and protons, therefore we expect a signature in the measured p flux as well. Under the hypothesis of a diffusive origin for the spectral break, the phenomenological model proposed in Tomassetti (2012) is adopted for the CR propagation of the large-scale source-distribution and for the propagation of e^- and p from the nearby remnant. The outcome of this work is that the spectral hardening in the hadronic species results from the superposition of a diffusion feature *and* an additional source. This is supported by (a) the complex structure observed in the proton spectrum by DAMPE (An et al., 2019) — in addition to the well-established hardening, they measure a softening at $\sim 13\,\mathrm{TeV}$, interpreted as an intrinsic source-cutoff — and (b) by the different rigidity at which the spectral hardening occurs, in some of the observed species (Niu, 2020), that is compatible with a superposition of effects. The latter point, however, derives from a different fitting of the nuclear species with respect to AMS-02 fits and thus requires further analysis to be confirmed. Interestingly, such solution can also explain the CR dipole-anisotropy amplitude associated to the nearby source, that would overshoot the data in a single-power-law diffusion scenario.

Nonetheless, a physical motivation for the different diffusive behaviours in the two Galactic regions is still missing. In Blasi et al. (2012), the break is assigned to the transition between a regime where diffusion is caused by CR scattering against self-generated alfvénic turbulence (*streaming instabilities*) and a regime where the alfvénic turbulence is externally injected from a larger spatial scale (*e.g.* $L_{\mathrm{inj}} \sim \mathcal{O}(10 - 100)$ pc for SN explosions). This idea is based on a picture where wave-particle interaction is dominated by the Alfvén modes via gyroresonant interaction, ignoring however the other MHD modes (*magnetosonic fast* and *slow*). While this is partially motivated by the fact that magnetosonic modes undergo severe damping processes such as *Landau damping* or *Transit-Time Damping* (TTD) (Ginzburg et al., 1962), on the other hand a series of papers (Yan and Lazarian, 2002a, 2004, 2008) show the inefficiency of CR scattering against Alfvén and slow modes as compared to that with fast modes.

This tension arises when including an anisotropic treatment of the turbulence: as Alfvén modes cascade, their turbulent spectrum keep the condition of *critical balance* $k_\parallel \sim k_\perp^{2/3}$ between the wavevector's components parallel and perpendicular with respect to the local field (Goldreich and Sridhar,

1995). Therefore, as the cascade evolves towards large wave vectors, most of the turbulent power is transferred to the $k_\perp$, whereas the component involved in the wave-particle scattering is $k_\parallel$ — due to the form of the resonance function $\delta(k_\parallel v_\parallel \pm \Omega)$, being Ω the gyrofrequency of the CR. This implies that very little scattering efficiency is left in the Alfvén modes. As it can be easily understood, at small wave vectors, the anisotropy of the cascade is not developed yet, and scattering efficiency is in principle restored. Since $k_\parallel \sim \ell_\parallel^{-1}$, then small $k_\parallel$'s resonate with particles with large $\Omega/v_\parallel$, hence with high energy. This is quantified in Fornieri et al. (2020a), where it is shown that the anisotropy of the Alfvén cascade causes the inefficiency of such modes in confining cosmic rays, at least up to an energy $E_{\rm CR} \sim 100\,{\rm TeV}$. In the same work, therefore, a change of paradigm is proposed, according to which cosmic-ray confinement is caused by particle interaction with fast magnetosonic modes from high energies ($E_{\rm CR} \sim 100\,{\rm TeV}$), down to $\sim 200\,{\rm GeV}$, where emerging self-generated modes start to dominate the diffusion process, as first predicted by Farmer and Goldreich (2004). Within such picture, the high-energy ($E_{\rm CR} > 200\,{\rm GeV}$) hadronic spectra, as well as the boron-over-carbon ratio, are reproduced with a reasonable choice of the physical parameters connected to the Galactic environments.

0.2 Outline of the Thesis

The thesis is organized in three main parts.

Part I. *Cosmic-ray physics.*

In Chapter 1, we give an overview of the key experimental results that lead to the overall picture regarding the origin and transport of cosmic rays. Then, we describe the *diffusive shock acceleration* mechanism, as the main responsible for accelerating and injecting CRs in the ISM. Finally, we study the *quasi-linear theory* derivation of the *transport equation*, reviewing the main hypotheses it relies on, discussing the nature of the turbulent waves that are the scattering centers for charged cosmic rays.

In Chapter 2, we describe the general structure of the numerical code that will be used to solve the transport equation for the large-scale CR background throughout the thesis, the `DRAGON` code, introducing the physical ingredients (*e.g.* gas distribution, magnetic field, non-adiabatic energy-losses) implemented in it. Then, we discuss the multi-messenger implications of the charged-particle energy-losses on other detection channels, namely γ-rays and neutrinos.

Part II. *Impact of local sources on the hadronic and leptonic spectra.*

In Chapter 3, we reproduce the most relevant cosmic-ray hadronic observables, in order to fix the free parameters of the code, and set up the propagation model. We then use this model as a background to fit the positron flux from pulsars in a model-independent picture, and to study the the idea of a hidden source of electrons.

In Chapter 4, we build upon the hypothesis of a nearby source of electrons and explore potential connections with the feature recently observed by DAMPE in the proton spectrum, with a progressively hardening diffusion-coefficient setup that is able to reproduce the hadronic spectral hardening at $\sim 200\,\mathrm{GeV}$. Within such framework, we study the distance and age of a plausible nearby source, that reproduces as well the cosmic-ray dipole anisotropy.

Part III. *Impact of the microphysics of the MHD modes on CR transport.*

In Chapter 5, we implement a non-linear extension of the QLT that enhances the efficiency of wave-particle interaction with *fast magnetosonic* modes, studying up to what extent an anisotropic alfvénic cascade is inefficient in confining cosmic rays. With this paradigm, we implement the diffusion coefficients in `DRAGON2` in a two-zone model where the Halo and the *Warm Ionized Medium* involve different damping mechanisms for the turbulent spectra. Finally, we explore the parameter space of selected physical quantities, which represent the two environments, to reproduce the hadronic CR-observables and the B/C ratio.

0.3 Research Contributions

The work presented in Part II and Part III of the thesis is original and reflects the following research contributions.

- O. Fornieri, D. Gaggero, D. Grasso. *Features in cosmic-ray lepton data unveil the properties of nearby cosmic accelerators*. Journal of Cosmology and Astroparticle Physics - 02 (2020) 009, https://iopscience.iop.org/article/10.1088/1475-7516/2020/02/009.

- O. Fornieri, D. Gaggero, D. Guberman, L. Brahimi, A. Marcowith. *Changes in cosmic-ray transport properties connect the high-energy features in the electron and proton data*. Joint submission Phys. Rev. D/Phys. Rev. Lett., https://arxiv.org/abs/2007.15321.

- O. Fornieri, D. Gaggero, S.S. Cerri, P. Luque, S. Gabici. *The theory of cosmic-ray scattering on pre-existing MHD modes meets data*. Monthly Notices of the Royal Astronomical Society - 502, 5821 – 5838 (2021), https://doi.org/10.1093/mnras/stab355.

In particular, the first paper is based on Chapter 3, the second one on Chapter 4 and the third one on Chapter 5.

Part I
Cosmic-ray physics

1

Theoretical foundations of cosmic-ray acceleration and transport

In this chapter, we present an introductory overview on the physics of Galactic cosmic rays (CRs), namely the charged particles that are likely originated within the Milky Way. Experimental evidence, collected in the past hundred years, tells us that charged particles do not follow ballistic trajectories in the *Interstellar Medium* (ISM), but rather they *diffuse*, due to the presence of turbulent magnetic-field fluctuations. Besides, as large-scale regular magnetic fields are embedded in our Galaxy, they deviate the CR direction of motion, to the point that is made impossible to identify their sources. Same evidence — along with a strong theoretical support — points towards catastrophic events (*e.g.* Supernova Remnants) or peculiar geometrical structures (*e.g.* pulsars' magnetosphere) for accelerating charged particles and injecting them into the ISM. However, a coherent interpretation of the CR observed spectra still represents a major challenge that the astroparticle community has to face, as it is hampered by our incomplete knowledge about both the acceleration mechanisms at the sources and the transport properties across the Galaxy. The present chapter is thus structured as follows. First, we will give an overview of the experimental measurements directly and indirectly related to cosmic rays, carried out at both space-born and ground-based detectors. Then, we will discuss in detail the physics behind the origin of cosmic rays, in particular their acceleration mechanisms at the sources. Finally, we will examine the CR transport across the Galaxy, by introducing a derivation of the *Fokker-Planck* equation and discussing its generalizations, with particular attention to the typical assumptions that a phenomenological interpretation of the observations should always take into account.

1.1 Overview of the experimental status

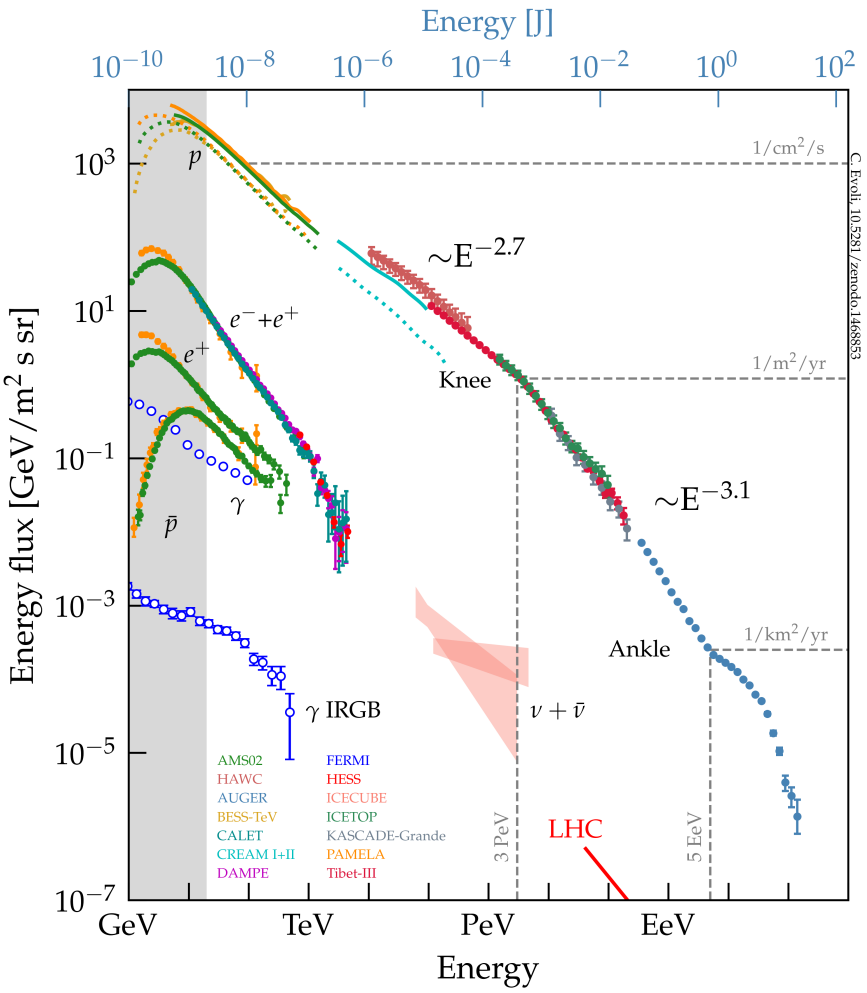

Figure 1.1: The figure reports the *all-particle spectrum* of cosmic rays, *i.e.* the rescaled differential flux $E^2 \cdot \frac{dN}{dE}$. About $\sim$ 99% of the flux is composed by protons and helium nuclei, with small contributions from heavier nuclei, while leptons $(e^+ + e^-)$ are about $\sim$ 1%. The differential-spectrum slope is clearly indicated before and above the *knee*. Figure from Evoli (2018).

The expression *Cosmic Rays* (CR) was first used about a hundred years ago by Robert Millikan (Millikan and Cameron, 1928), who thought that objects that were capable to ionize the crossed medium had to be high-energy γ radiation. But the research on CRs dates back to 1912, when Victor Hess described his remarkable findings, analyzing data collected during two balloon flights with experimental purposes (Hess, 1912). In particular, he measured an increasing ionization at higher altitudes. Today, we know that Hess was measuring the showers connected to the impact of the cosmic rays with the atmospheric gas and that such ionizing radiation is not electromagnetic radiation, but rather charged particles.

In Figure 1.1 we report the *all-particle spectrum*, namely the differential flux — per energy bin, rescaled by E^2 — of all the particles observed on Earth that are coming from outside of the atmosphere. As we see from the figure, CRs are manly protons and helium nuclei — together they constitute $\sim 99\%$ of the total flux — and the remaining part is composed by heavier nuclei and leptons, that are about $\sim 10^2$ times less abundant than protons.

At a first look, the proton spectrum is essentially featureless up to the so-called *knee* ($E_{\rm knee} \simeq 3\,{\rm PeV}$), showing the following differential flux:

$$\left.\frac{dN}{dE}\right|_{E \lesssim 3\,{\rm PeV}} \propto E^{-2.7}.$$

Above the *knee* it exhibits a softening $\left(\left.\frac{dN}{dE}\right|_{3\,{\rm PeV} \lesssim E \lesssim 5\,{\rm EeV}} \propto E^{-3.1}\right)$, likely corresponding to the highest accelerated energy of the CR's main sources. Then, at $\sim 5\,{\rm EeV}$, a hardening is probably a signature of the entrance of a new population of extra-Galactic origin. Finally, at $\sim 10^{20}\,{\rm eV}$ the spectrum shows an abrupt cutoff, that corresponds to the excitation energy of a hadronic resonance (the Δ^+) in the scattering process of a CR proton off the photons of the ubiquitous *cosmic microwave background* (CMB) radiation. This phenomenon was already explained in the 60's and known as *GZK cutoff*, named after Greisen, Zatsepin and Kuz'min, who first discovered it (Greisen, 1966; Zatsepin and Kuz'min, 1966).

The identification of the origin of the cosmic-ray particles is complicated by the presence of large-scale magnetic fields embedded in our Galaxy, as charges moving inside them follow intricate trajectories and make impossible to point directly to the sources. This is, conversely, possible for weakly interacting particles, namely photons and neutrinos, that therefore potentially represent the *smoking guns* of the astrophysical events originating cosmic rays.

In fact, as it will be explained in detail in Section 2.2.2, the interaction of both hadronic and leptonic CRs generates photons, via several channels. In particular:

(i) leptons massively loose energy due to their light mass and consequently emit electromagnetic radiation in characteristic energy bands. This is sketched in Figure 1.2a, where we observe the leptonic *spectral energy distribution* (SED), characterized by the typical two peaks at energies clearly separated. The peak in the *Radio* band (lower energy) comes from *synchrotron* losses, while that in the γ-ray band (higher energy) comes from *Inverse Compton* scattering off different components of the ISRF. *Bremsstrahlung* emission is absent from the picture, overlapping the γ-ray IC emission.

(ii) Protons, on the other hand, scatter off the *Interstellar-Medium* (ISM) gas and the *Interstellar-Radiation-Field* (ISRF) photons creating, among others, neutral pions, which eventually decay as $\pi^0 \to \gamma\gamma$, showing the typical *pion bump* at an energy corresponding, in $\log_{10}$-scale, to half

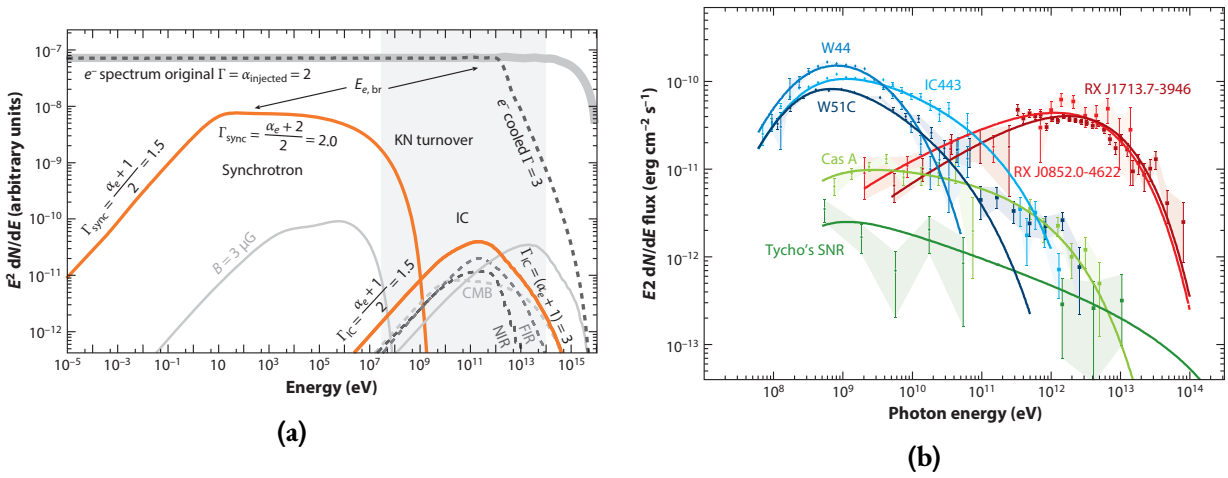

Figure 1.2: The figure shows the characteristic *spectral energy distribution* (SED) of the leptonic and hadronic emission from SNRs. **(a)** A characteristic double-peaked (*synchrotron* and IC) leptonic SED, from a reference electron injection slope $\Gamma^{e^-}_{\rm inj} = 2$. The principal scenario (orange solid line) reproduces the inner $100\,{\rm pc}$ of the Milky Way, with $B = 100\,\mu{\rm G}$. The IC peak is drawn as resulting from different contributions to the ISRF, in dashed grey lines. Same peaks are shown for a much lower magnetic field $B = 3\,\mu{\rm G}$ (light grey solid line). **(b)** Real case-studies of seven SNRs' hadronic emission. The different color-scheme refers to the object age: green corresponds to the youngest sources ($t_{\rm age} < 10^3\,{\rm yr}$), red to $t_{\rm age} \sim 2 \cdot 10^3\,{\rm yr}$, blue to $t_{\rm age} \sim 2 \cdot 10^4\,{\rm yr}$. Both figures are taken from Funk (2015).

of the rest mass of the pion, $m_{\pi^0}/2 \simeq 70\,{\rm MeV}$. Note that, in the usual rescaled units multiplied by E^2, this bump appears shifted in energy, at $\sim 200\,{\rm MeV}$. The resulting SED is shown in Figure 1.2b for seven *Supernova Remnants* (SNR), classified in terms of their ages with the color code described in the caption. All of the sources but two (red solid lines) are consistent with a hadronic emission model. Those two represents however particular cases that still require dedicated studies (see *e.g.* Section 5.1.1 from Funk (2015)).

With regard to the choice of the model, we mention that, although, in the GeV – TeV range, *Bremsstrahlung*, IC and π^0-decay overlap, observations of the surrounding medium typically disentangle the problem, by means of energetics considerations (see *e.g.* Ackermann et al. (2013)). In conclusion, the unambiguous interpretation of the photon SEDs of leptonic and hadronic origin leads to identify Supernova Remnants as the most promising sources of cosmic rays (see *e.g.* Aharonian (2013)), even though many details on this picture are still under debate (see *e.g.* Gabici et al. (2016) and references therein). Such hypothesis is further supported by the theoretical studies of the CR-acceleration mechanisms at SN shocks, as it will be discussed in Section 1.2.

Another important piece of information comes from the observation of the large-scale photon emission of hadronic origin, derived by Galactic surveys, *e.g.* as done by the *Fermi* Collaboration*.

*https://fermi.gsfc.nasa.gov/

As we will see in Section 2.3, the γ-ray emission observed in the Galactic plane closely matches the morphology of the interstellar gas, indicating a longer residence time of the cosmic rays around those regions, as compared to a hypothetical ballistic motion. As a consequence, it follows that charged cosmic rays do not follow ballistic trajectories, but rather they *diffuse*. Supporting this picture, the two following classes of evidence have to be considered.

- The observation of the small-scale anisotropy amplitude in the cosmic-ray flux: the high degree of directional isotropy, whose dipole amplitude is up to $\sim 10^{-3}$ (see Ahlers and Mertsch (2017) and references therein), can be derived within a theory of cosmic-ray scattering against randomly distributed turbulent waves. This point will be discussed in more detail in Section 1.3.3.
- The measurement of the abundance and lifetime of unstable elements: based on these observations, the average residence time of cosmic-ray particles in the Milky Way is estimated in $\tau_{\rm esc} \simeq 1.5 \cdot 10^7\,{\rm yr}$ for particles of energy $\sim$ GeV (Yanasak et al., 2001). On the other hand, for a Galactic-halo size of approximately $L_{\rm Halo} \sim 5 - 10\,{\rm kpc}$, if CRs were streaming freely, their escape time would be as small as $\tau_{\rm esc}^{\rm free} \sim L_{\rm Halo}/v_{\rm CR} \simeq 1.5 \cdot 10^4\,{\rm yr}$, for a typical CR velocity $v_{\rm CR} \approx c$, being c the speed of light. This anomalously short residence time is not enough to account for the observed B/C ratio, as well as for other secondary-over-primary ratios.

As a final key-point, we want to mention the recent observation of a γ-ray halo around two nearby pulsars — Geminga and Monogem — by the HAWC Collaboration (Abeysekara et al., 2017). The measurement, shown in Figure 1.3a, reports an extended region ($\sim 20 - 25\,{\rm pc}$) around each pulsar, where photons in the $\sim$ TeV range are present. Such an extension is much larger than the pulsars' magnetospheres.

This shell-structure, later confirmed in a lower energy range ($E_\gamma > 8\,{\rm GeV}$) by the *Fermi* Collaboration (Di Mauro et al., 2019), is commonly referred to as TeV-*halo* and it is observed in the region between the *Pulsar Wind Nebula* and the surrounding SNR-shell, as sketched in Figure 1.3b. Its energy seems compatible with IC-scattering against the photons from the CMB of confined lepton populations of energy $E_{e^\pm} \sim 100\,{\rm TeV}$ — in the HAWC range — and $350\,{\rm GeV} \lesssim E_{e^\pm} \lesssim 1.5\,{\rm TeV}$ — in the Fermi band. As a consequence, this measurement potentially represents the first evidence of pulsars as accelerating sites for lepton pairs.

In this section, we have reported a key observational evidence that leads us to conclude that (i) cosmic rays follow a diffusive motion, (ii) they come mainly from Supernova Remnants, and (iii) tha there is increasing indication of a lepton population of primary $e^\pm$ pairs originating around pulsars. From this point ahead, we will work under these hypotheses and introduce the physics of cosmic-ray acceleration and transport in the Galaxy.

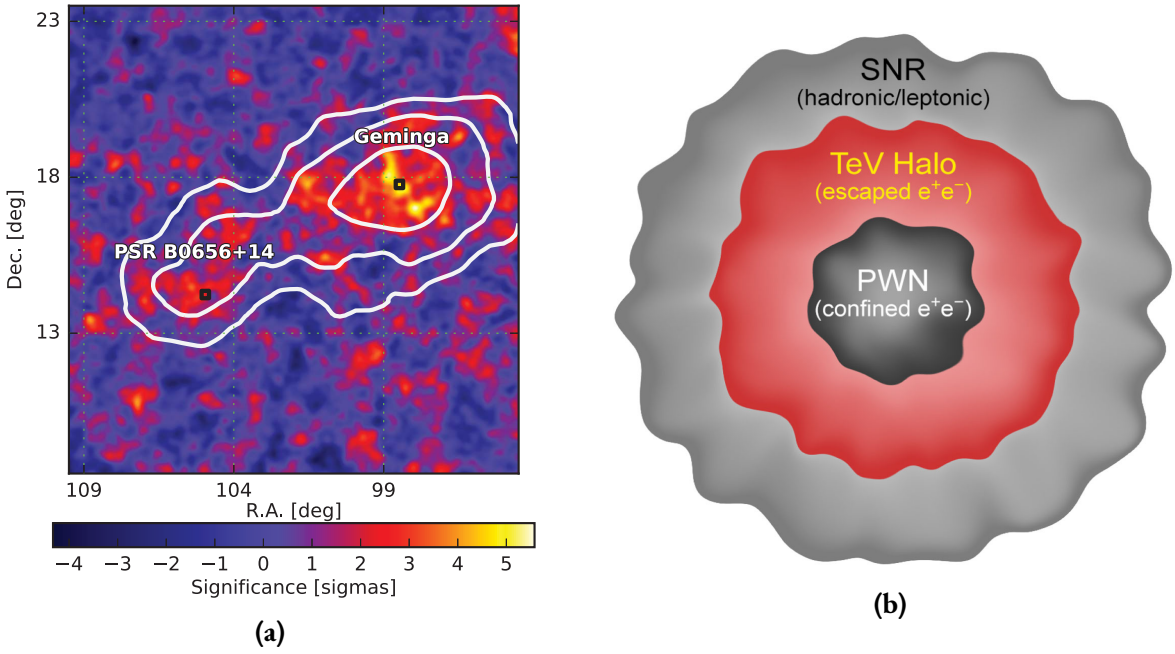

(a) **(b)**

Figure 1.3: The new structures known as TeV-*halos* are shown. **(a)** The figure reports the observation of γ-ray extended halos in the $\sim$ TeV range around two nearby ($d \sim 250\,\mathrm{pc}$) pulsars, Geminga and Monogem. Figure from Abeysekara et al. (2017). **(b)** This is a sketch of the halo structure within the whole pulsar region. Figure from Sudoh et al. (2019).

1.2 Cosmic-ray acceleration at the sources

The first step in discussing the physics of cosmic rays is the study of the acceleration stage. When many collisions occur among particles in a system, an equilibrium is reached and the system is *thermalized*, which implies that particles follow a *Maxwell-Boltzmann* distribution for their velocities. In the presence of perturbations or catastrophic events though, these equilibrium conditions are disturbed and particles gain velocity, *i.e.* they get accelerated and injected in the surrounding *interstellar medium*. As we know from basic physics courses, charged particles can be accelerated by applying an electric field: however, as will see in more detail in Section 1.3.2, typical ISM conditions do not allow the presence of large-scale electric field ($\langle \boldsymbol{E} \rangle = 0$), unless specific topological structure are involved. Another possibility is based on *stochastic* processes — namely for which $\langle \boldsymbol{E}^2 \rangle \neq 0$ — that allow the particles to gain energy after a certain number of cycles. They represent $\sim 99\%$ of the accelerating mechanisms in nature and are the focus of the present section.

1.2.1 Second-order Fermi acceleration

This process is based on the relative motion of a charged particle with respect to a moving *magnetized* plasma cloud (Fermi, 1949, 1954). In the moving-cloud reference frame, a particle with energy and

momentum $(E', |p'_z|)$ scatters off the cloud elastically, reversing the direction of its momentum, $|p'_z| \to -|p'_z|$. However, if we observe this event in the Earth frame, we will measure a net gain (or net loss) in the particle momentum corresponding to their relative speed (either positive or negative in direction).

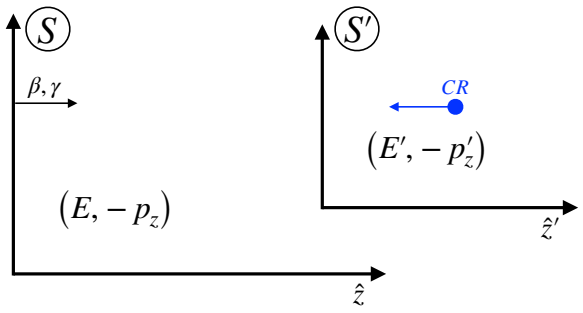

Figure 1.4: The figure shows the relative motion of two reference frames. S is the Earth frame and is moving along the positive $\hat{z}$-axis of S', the cloud frame, with Lorentz factors (β, γ). The CR-particle, shown in blue, is moving in the opposite direction with energy and momentum $(E', -p'_z)$, as measured in the cloud, or $(E, -p_z)$, as measured from the Earth.

As we see from Figure 1.4, in the case where the particle and the cloud move towards each other, the energy and momentum of the particle, in the cloud reference frame, are written, with respect to the same quantities measured on Earth, according to the Lorentz transformations (Barone, 2004):

$$\begin{cases} E' = \gamma \left(E - \beta c(-p_z) \right) = \gamma E + \beta c \gamma p \mu \\ p'_z = \gamma \left(p_z + \dfrac{\beta}{c} E \right) = \gamma p \mu + \gamma \dfrac{\beta}{c} E, \end{cases}$$

where $\mu \equiv \cos\theta$ is the component projected on the $\hat{z} \parallel \hat{z}'$ axis, $\beta = v/c$ and $\gamma = 1/\sqrt{1-\beta^2}$ are the Lorentz factors, and the particle energy and momentum are $(E, -p_z)$, as observed in S.

After the impact, the particle reverses its momentum, so that in the Earth frame its energy becomes:

$$E_{\text{after}} = \gamma \left(E' + \beta c p'_z \right),$$

as it is now moving along the positive $\hat{z}$ axis.

The net energy variation in a single impact — in this case a gain — can be found taking into account the two previous expressions:

$$\frac{\Delta E}{E} = \frac{E_{\text{after}} - E}{E} = \frac{\gamma^2 E + 2\gamma^2 \beta c p \mu + \gamma^2 \beta^2 E}{E} - 1 = \gamma^2 + 2\gamma^2 \beta c \mu \frac{p}{E} + \gamma^2 \beta^2 - 1 \tag{1.1}$$

Since, as we will see in Section 1.3.2, the collective motion of a magnetized plasma-cloud is of the

order of $v_{\rm cloud} \simeq v_A \sim 1 - 100\,{\rm km\cdot s^{-1}}$, then $\gamma \simeq 1$. This implies that we can Taylor-expand $\gamma^2 = (1-\beta^2)^{-1} \simeq 1+\beta^2$, so that Equation (1.1) becomes:

$$\left\langle \frac{\Delta E}{E} \right\rangle \approx 2\frac{v_{\rm cloud} v_{\rm CR}}{c^2}\mu + 2\beta^2, \tag{1.2}$$

which is valid up to order $\mathcal{O}(v_{\rm cloud}^2/c^2)$.

Over time, the particle encounters many clouds that are randomly oriented, therefore, to average over the angles, we integrate over $\mu \in [-1,+1]$ the quantity in Equation (1.2) times the probability to have the impact at that angle. Such probability is proportional to relative velocity of the cloud with respect to the particle velocity and therefore, according to the relativistic velocity composition (Barone, 2004), depends on μ:

$$P(\mu) \propto v_{\rm rel} \quad \Rightarrow \quad P(\mu) = A\,\frac{v_{\rm cloud}\mu + v_{\rm CR}}{1+\frac{v_{\rm CR}v_{\rm cloud}}{c^2}\mu} = A\,\frac{\beta\mu c + v_{\rm CR}}{1+\frac{v_{\rm CR}}{c}\beta\mu}. \tag{1.3}$$

At first order in $\beta = v_{\rm cloud}/c$ — as mentioned, this probability will be multiplied by a quantity that brings its own powers of β to the equation — and considering $v_{\rm CR} \approx c$, we have $P(\mu) \simeq A(v_{\rm CR} + v_{\rm cloud}\mu) \approx Ac(1+\beta\mu)$, from which, normalizing the probability to 1, we get:

$$\int_{-1}^{+1} d\mu\, P(\mu) \stackrel{!}{=} 1 \quad \Rightarrow \quad A = \frac{1}{2c}.$$

As a final step, we average the net gain in Equation (1.2) and obtain:

$$\int_{-1}^{+1} d\mu\, P(\mu) \left\langle \frac{\Delta E}{E} \right\rangle \approx \int_{-1}^{+1} d\mu\, (1+\beta\mu)\left(\beta^2 + \beta\frac{v_{\rm CR}}{c}\mu\right) \underset{v_{\rm CR}\approx c}{\approx} \frac{8}{3}\beta^2. \tag{1.4}$$

The net gain just obtained from the calculation is physically motivated by the higher probability to have *head-on* collisions, with respect to all the other pitch-angles, since $P(\mu)$ depends on the relative speed. However, this process gives only a second-order contribution to the energy gain of cosmic rays, hence might be not the dominant one.

To support the last statement, we can search for an order-of-magnitude estimate of the acceleration time scale, considering a simplified model where particles travel at the speed of light in a non-magnetized plasma and are accelerated by elastically bouncing off moving clouds, whose typical distance is $L_{\rm cloud} \sim 1\,{\rm pc}$, not spending time inside each cloud. The acceleration time is defined in terms of the acceleration *rate*, dE/dt, as follows:

$$\tau_{\rm acc,Fermi2}(E) = \int_{E_{\rm min}}^{E} \left(\frac{1}{dE/dt}\right) dE \simeq \left(\frac{E}{dE/dt}\right), \tag{1.5}$$

where the approximation is possible if we consider a small energy bin in the interval $[E, E + dE]$.

Within such picture, the acceleration rate can be estimated as $dE/dt \simeq \Delta E / \langle t_{\rm coll} \rangle$, where $\langle t_{\rm coll} \rangle \sim L_{\rm cloud}/c$ is the average time between one collision and the next one. Therefore, based on the net energy gain calculated in (1.4), we have:

$$\tau_{\rm acc,Fermi2} \simeq \frac{E}{\Delta E / \langle t_{\rm coll} \rangle} \simeq \frac{3 \langle t_{\rm coll} \rangle}{8 \beta_{\rm cloud}^2} \simeq \frac{3 L_{\rm cloud}}{8 c \beta_{\rm cloud}^2}, \tag{1.6}$$

where $\beta_{\rm cloud} \sim 10^{-4}$ is the Lorentz factor of the moving clouds, typical for standard ISM conditions.

If we now assume an exponentially growing rate for the energy gain, we can compute the time scale needed for a particle to double its energy:

$$E(t) = E_0 \cdot e^{t/\tau_{\rm acc,Fermi2}} \quad \underset{E(t)=2E_0}{\Longrightarrow} \quad t = \frac{3}{8} \cdot \frac{L_{\rm cloud}}{c \beta_{\rm cloud}^2} \cdot \log 2 \approx 10^8 \, {\rm yr}, \tag{1.7}$$

which is in large tension with the estimation of the residence time of CRs in our Galaxy, $\tau_{\rm esc} \simeq 1.5 \cdot 10^7$ yr, discussed in Section 1.1.

1.2.2 First-order Fermi acceleration

We have seen that the acceleration process described above leads to an anomalously long acceleration time for cosmic-ray particles. Nonetheless, we notice that if only *head-on* collisions ($\theta = \pi$) were occurring, second-order Fermi acceleration would lead to a way larger energy enhancement. In fact, from Equation (1.2), we easily see that, imposing $\mu = -1$, the net energy gain would be proportional to β rather than β^2, providing an orders-or-magnitude more efficient acceleration mechanism. Indeed, second-order Fermi mechanism became the seed of the modern understanding of the acceleration processes, as soon as it was discovered that it could be promoted to a first-order mechanism around shocks (Axford et al., 1977; Bell, 1978; Blandford and Ostriker, 1978; Krymskii, 1977).

Physically speaking, a shock forms when something propagates faster than the information of its propagation. In the dense media that characterize our astrophysical environments, this information is carried by the molecules, that communicate the passage of the shock front by hitting with each other, *i.e.* via pressure waves propagating at the sound speed c_s. As a consequence, the two regions separated by such shock front have relevant thermodynamical quantities — density ρ, pressure P and temperature T — that have different values. In other words, a *discontinuity* is formed at the shock front.

A sketch of the physical situation is reported in Figure 1.5, where we watch the scene in the reference frame of the shock front. In this reference, we identity the two regions separated by the discontinuity as *upstream*, the pre-shock region moving towards the shock frame with velocity u_U, and *downstream*, the post-shock region, streaming away from the discontinuity with velocity u_D. We eas-

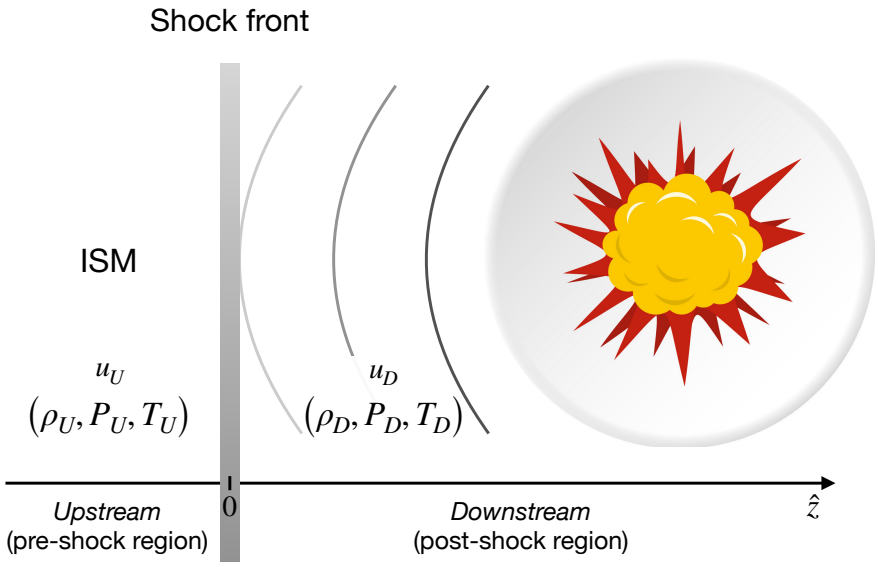

Figure 1.5: In the reference frame of the infinitesimal shock front, two regions are identified with different thermodynamical quantities: the *upstream* pre-shock region, that is moving towards the shock front with velocity u_U, and the *downstream* region, which is already shocked and flow away from the shock at velocity u_D.

ily convince that, in the region that has already been shocked, pressure waves, that are slower than the shock, "pile up" and compress the shocked medium. As a consequence, *downstream* the medium is denser than *upstream*:

$$\rho_D > \rho_U \quad \Rightarrow \quad \frac{\rho_D}{\rho_U} > 1.$$

Since the mass flux has to be conserved at the (infintesimal) shock front, then we have:

$$\frac{d}{dz}(\rho u) = 0 \quad \Rightarrow \quad \rho_D u_D = \rho_U u_U \quad \Rightarrow \quad \frac{\rho_D}{\rho_U} = \frac{u_U}{u_D},$$

where $u_{D,U}$ identify the collective velocities in the two regions.

Hence, we see that, even though the pressure in the *downstream* region is enhanced, the collective velocity of its particles is lower than before the passage of the shock. This implies that the pressure enhancement must contribute to the thermal agitation of the single particles of the cloud, namely the temperature of the *downstream* region increases. To summarize, we have the following conditions:

$$\begin{aligned} &\rho_D > \rho_U \\ &u_D < u_U \\ &P_D > P_U \\ &T_D > T_U, \end{aligned} \tag{1.8}$$

according to which we identify the *upstream* region with fast and cold undisturbed gas, and the *downstream* region, where the shocked gas is slow and warm.

The quantitative treatment, corresponding to the relations (1.8) between the physical quantities at the two sides of the shock, must take into account the strength of the shock and the environment where it originates. The calculations can be carried out imposing the conservation of the flux (in dimensional units $\frac{[\text{quantity}]}{T \cdot L^2}$) of mass, momentum and energy at the approximately-infinitesimal shock front (Longair, 2011):

$$\frac{d}{dz}(\rho u) = 0 \qquad \frac{d}{dz}\left(\rho u^2 + P\right) = 0 \qquad \frac{d}{dz}\left(\frac{1}{2}\rho u^3 + \frac{\gamma}{\gamma - 1} u P\right) = 0,$$

where in the last equation we considered the energy flux through a surface $\Sigma \perp \boldsymbol{u}$ as $\Phi_{\text{energy}} = \rho u \left(\frac{1}{2}u^2 + h\right)$, being $h = \frac{\gamma_a}{\gamma_a - 1}\frac{P}{\rho}$ the enthalpy per unit mass in a perfect gas, with γ_a coefficient of adiabatic expansion, that, for an ideal gas, assumes the value $\gamma_a = 5/3$. We notice that the infinitesimal-shock approximation works as long as we are dealing with non-thermal particles, whose Larmor radius is much larger than that of the thermal ones.

The *jump conditions*, known as *Rankine-Hugoniot* equations (Hugoniot, 1885; Rankine, 1870), then become:

$$\begin{cases} \rho_U u_U = \rho_D u_D \\ \rho_U u_U^2 + P_U = \rho_D u_D^2 + P_D \\ \frac{1}{2}\rho_U u_U^2 + \frac{\gamma_a}{\gamma_a - 1} P_U = \frac{1}{2}\rho_D u_D^2 + \frac{\gamma_a}{\gamma_a - 1} P_D. \end{cases} \tag{1.9}$$

The system above admits a non-trivial solution, *i.e.* such that $u_U \neq u_D$, $P_U \neq P_D$, $\rho_U \neq \rho_D$, only in the case $M_U > 1$, where $M_U \equiv \dfrac{u_U}{c_{s,U}}$ is the Mach number in the *upstream* region, namely the ratio between the collective velocity of the cloud and the sound velocity in this environment, $c_{s,U} = \gamma_a \dfrac{P_U}{\rho_U}$. This is physically expected, as it is the formal definition of what described at the beginning of this section: "*a shock forms when something propagates faster than the information of its propagation*". The corresponding solution reads:

$$\begin{aligned} \mathcal{R} &\equiv \frac{\rho_D}{\rho_U} = \frac{u_U}{u_D} = \frac{(\gamma_a + 1) M_U^2}{(\gamma_a - 1) M_U^2 + 2} \\ \frac{P_D}{P_U} &= \frac{2\gamma_a M_U^2}{\gamma_a + 1} - \frac{\gamma_a - 1}{\gamma_a + 1} \\ \frac{T_D}{T_U} &= \frac{\left[2\gamma_a M_U^2 - \gamma_a(\gamma_a - 1)\right]\left[(\gamma_a - 1) M_U^2 + 2\right]}{(\gamma_a + 1)^2 M_U^2}, \end{aligned} \tag{1.10}$$

where $\mathcal{R}$ is commonly known as *compression factor*. We notice that, for strong shocks — namely such

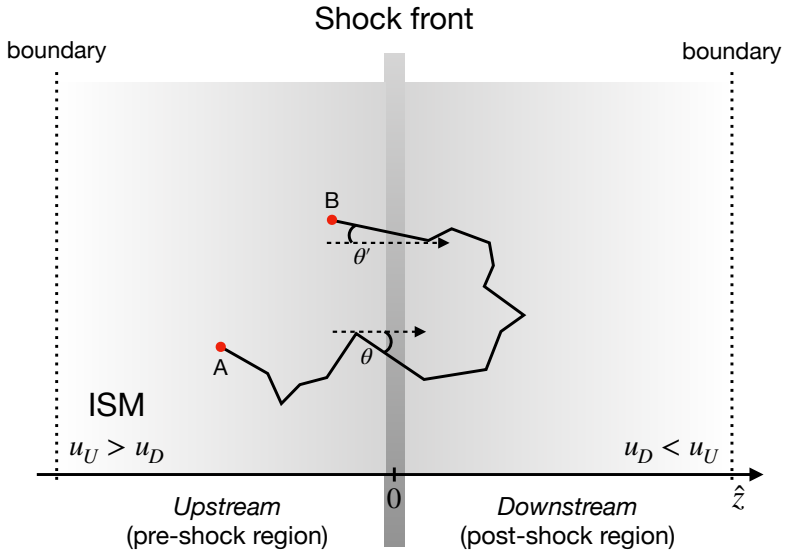

Figure 1.6: The diffusive path of a particle trapped in the acceleration process is sketched, in the reference frame of the shock front. The particle traverses the shock from *upstream* to *downstream* with pitch-angle θ and returns to the *upstream* region, with a pitch-angle θ', with a net velocity gain.

that $M_U \gg 1$, which is the case for typical ISM conditions, where $v_{\rm shock} \sim 10^3\,{\rm km}\cdot{\rm s}^{-1}$ (Blasi, 2013) — we have $\mathcal{R} \to \frac{(5/3+1)}{(5/3-1)} = 4$ in an ideal-gas environment.

The acceleration process will be here formalized taking into account the discontinuities implied by the solution above. However, we can give a physical introduction for it. In the reference frame of the shock front, flowing away from the explosion, particles of the undisturbed gas *upstream* travel towards our direction at velocity u_U, eventually crossing the shock front. On the other side of the front, *downstream* of the shock, the impact a cloud that has collective velocity $u_D < u_U$. This is equivalent as impacting a wall at rest with velocity $|u_U - u_D| > 0$ and being scattering in the other direction with the same velocity, in the wall's reference frame. However, in the frame of an observer on Earth, the particle gained the above relative velocity, and now moves at speed $u_U + |u_U - u_D| > u_U$. Now the same event will repeat, as the particle is traveling faster than the collective velocity of the *upstream* region. This bouncing process repeats many times, until the energy reaches a value allowing the accelerated particle to escape from the shock and be injected in the ISM as a cosmic ray.

In the realistic case, of course we do not often see the *head-on* collisions that would imply the velocity variations just mentioned, but rather the picture sketched in Figure 1.6. As we can see from the figure, once a particle traverses the shock front, it keeps diffusing because of the scattering centers in the plasma clouds — we will see in detail in the next section that these scattering centers are magnetic turbulence-waves — and the velocity gain depends on the pitch-angle, with respect to the normal to the shock-front surface, that the particle has every time it crosses the shock — in the picture $\theta \equiv \theta_{U\to D}$ and $\theta' \equiv \theta_{D\to U}$. Particles can escape from the shock for mainly two reasons, connected to the particle

mean free path, $\lambda_{\rm m.f.p.}$, and Larmor radius, r_L:

1. when $\lambda_{\rm m.f.p.}$ is large enough to prevent the particle from returning to the shock, namely the particle has reached a region where the scattering centers are less dense,
2. when r_L is such that the time scale needed for a particle to return to the shock is longer that the dissipation time of the shock itself.

The *problem of the escape* is highly non-linear in the particle-wave interaction and requires sophisticated simulations to be treated. We remind to Berezhko and Krymskii (1988); Drury (1983) for classical reviews on the topic, and to Marcowith et al. (2016) for a more recent one and with a wider perspective.

The mathematical treatment of the acceleration mechanism is somewhat similar to what described for the second-order Fermi process. We assume a particle with energy and momentum (E, p) crosses the shock from *upstream* to the *downstream* region. In the *downstream* reference frame, we see the *upstream* cloud moving at $\beta = u_U - u_D$. Therefore, the particle energy is transformed as follows (Barone, 2004):

$$E_D = \gamma \left(E + \beta c p_z\right) \simeq \gamma E \left(1 + \beta \mu\right),$$

where $\mu \equiv \cos\theta \in [0, 1]$ and we approximated $pc \approx E$, as we are in the ultra-relativistic case.

We assume now the particle is able to return to the *upstream* region, where the Lorentz-transformed energy reads:

$$E_U = \gamma \left(E_D - \beta c p_{D,z}\right) \simeq \gamma E_D \left(1 - \beta \mu'\right),$$

where now $\mu' \equiv \cos\theta' \in [-1, 0]$.

Hence, the particle energy-gain in one *U-D-U* cycle is:

$$\frac{\Delta E}{E} = \frac{E_U - E}{E} = \gamma^2 \left(1 + \beta\mu\right)\left(1 - \beta\mu'\right) - 1 \equiv f(\mu, \mu').$$

To average over the two pitch-angles (μ, μ'), we have to define the probability to have a flux in the μ (or μ') direction, as a ratio over the total flux $\Phi^{\rm tot}_{U\to D} = \int \frac{N}{4\pi} d\Omega\, v_{\rm CR}\mu$ (or, alternatively, $\Phi^{\rm tot}_{D\to U} = \int \frac{N}{4\pi} d\Omega \left(-v_{\rm CR}\mu'\right)$) in the same direction, assuming that diffusion in the two regions tends to isotropize the particle distribution and denoting with N the total number of particles. Therefore, we can write:

$$P(\mu) \propto \frac{N v_{\rm CR}\mu}{\Phi^{\rm tot}_{U\to D}} \quad \Rightarrow \quad P(\mu) = A\, \frac{N v_{\rm CR}\mu}{\frac{N v_{\rm CR}}{4\pi}\int_0^{2\pi} d\phi \int_0^1 d\mu\, \mu} = 4A\mu,$$

as μ is non-zero in $[0, 1]$ only. Equivalently, $P(\mu') = -4A'\mu'$, since $\mu' \in [-1, 0]$.

We compute the coefficients A, A' by normalizing the probabilities $\int_{-1}^{+1} d\mu\, P(\mu') \stackrel{!}{=} 1$, with the same equation for μ', and we easily get $A = A' = \frac{1}{2}$. Therefore, averaging the energy gain for a single cycle,

we obtain:

$$\left\langle \frac{\Delta E}{E} \right\rangle_{\mu,\,\mu'} = \int_0^1 d\mu\,(2\mu) \int_{-1}^0 (-2\mu') \left[\gamma^2\,(1+\beta\mu)\,(1-\beta\mu') - 1\right] \simeq \frac{4}{3}\beta, \tag{1.11}$$

in the approximation where $\gamma \to 1$ neglecting $\mathcal{O}(\beta^2)$.

Hence, we notice from Equation (1.11) that the energy gain is now of first order in β. Besides, β is here the shock speed, which we have seen to be of the order $\sim 10^3\,\mathrm{km}\cdot\mathrm{s}^{-1}$, namely at least one order of magnitude larger than the velocity of the moving clouds involved in the second-order mechanism.

As a last step, we want to compute the spectrum of the injected particles, since, as understood from above, not all the accelerated particles are able to cross the shocks repeatedly to be trapped in the acceleration process. A rigorous derivation would allow to consider the relativistic as well as non-relativistic case for the accelerated particles, but this is beyond the illustrative purpose of this chapter. Rather, we present the simpler relativistic case for the injected particles and remind to Blasi (2013) for the full calculation.

To find the injection spectrum, we compute the probability $P_{D\to U}$ for a particle to cross the shock from *downstream* to *upstream*, dividing the flux of outgoing particles (*i.e.* from D to U) by the flux of ingoing particle (*i.e.* from U to D). These fluxes are written as follows:

$$\Phi_{U\to D} = \int_{-u_D/c}^1 d\mu\, n\,(u_D + \mu c) \qquad \Phi_{D\to U} = \int_{-1}^{-u_D/c} d\mu'\, n\,(u_D + \mu' c)\,, \tag{1.12}$$

where n is the number density of the particles and we computed the relative velocity — a relativistic particle ($v_{\mathrm{CR}} \approx c$) with pitch-angle μ moves *downstream* towards the shock front, that is moving oppositely at velocity u_D — at zero-*th* order in $\mathcal{O}(u_D/c)$.

Carrying out the integrals in Equation (1.12), we get $\Phi_{U\to D} = \frac{c}{2}\left(1+\frac{u_D}{c}\right)^2$ and $\Phi_{D\to U} = -\frac{c}{2}\left(1-\frac{u_D}{c}\right)^2$, so that the probability we are looking for is the following:

$$P_{D\to U} \equiv \frac{|\Phi_{D\to U}|}{\Phi_{U\to D}} = \frac{\left(1-\frac{u_D}{c}\right)^2}{\left(1+\frac{u_D}{c}\right)^2} \simeq \left(1-2\frac{u_D}{c}\right)\left(1-2\frac{u_D}{c}\right) \approx 1 - 4\frac{u_D}{c} \tag{1.13}$$

neglecting terms from order $\mathcal{O}\left(u_D^2/c^2\right)$.

On the other hand, every particle in the undisturbed-gas region *upstream* is run over by the shock initially, so that we can write $P_{D\to U} = 1$.

With the results in Equations (1.11) and (1.13), we can now write the number of particles N_k that

survived the first k cycles $(U-D-U)$ and their energy as follows:

$$\begin{cases} E_1 = E_0\left(1+\frac{4}{3}\frac{u_U-u_D}{c}\right) \\ N_1 = N_0\left(1-\frac{4u_D}{c}\right) \end{cases} \quad \Rightarrow \quad \begin{cases} E_k = E_0\left(1+\frac{4}{3}\frac{u_U-u_D}{c}\right)^k \\ N_k = N_0\left(1-\frac{4u_D}{c}\right)^k \end{cases} \tag{1.14}$$

where (E_0, N_0) are the initial energy and number, respectively.

By solving both equations of the system with respect to k, we are left with:

$$\log\left(\frac{N_k}{N_0}\right) = \log\left[\left(\frac{E_k}{E_0}\right)^{\frac{\log\left(1-4u_D/c\right)}{\log\left(1+4(u_U-u_D)/(3c)\right)}}\right] \tag{1.15}$$

where the exponent can be Taylor-expanded at first order as follows:

$$\frac{\log\left(1-\frac{4u_D}{c}\right)}{\log\left(1+\frac{4}{3}\frac{u_U-u_D}{c}\right)} \simeq \frac{-\frac{4u_D}{c}}{\frac{4}{3}\frac{u_U-u_D}{c}} = -3\frac{u_D}{u_U-u_D} = -\frac{3}{\mathcal{R}-1},$$

where the last step comes from the definition of the *compression factor* in Equation (1.10).

From the procedure above, we note that N_k is the *integral spectrum*, namely the number of particles that have at least an energy E_k. To obtain the differential spectrum that — *i.e.* the number of particles per energy bin, to compare it with the experimental observations — we differentiate the equation above, to obtain:

$$\frac{dN(E)}{dE} \propto \left(\frac{E}{E_0}\right)^{-\left(\frac{3}{\mathcal{R}-1}+1\right)} \tag{1.16}$$

from which we derive $\Gamma_{\rm inj} \equiv \frac{3}{\mathcal{R}-1}+1 = 2$, for the case of strong shock $(M_U \gg 1)$, which implies $\mathcal{R}=4$.

We see that the cosmic-ray injection spectra required to account for the observed phenomenology are significantly steeper than what predicted in Equation (1.16), since they are as large as $\propto E^{-2.4}$ — we will see that this is the injection spectrum we use in our DRAGON runs for the large-scale component described in Part II. Again, we remark that what presented above is a physics introduction in the test-particle regime, namely it neglects every feedback effect that particles have on the shock (Caprioli, 2012).

We can qualitatively estimate the time scale required to accelerate particles up to a given energy E as $\tau_{\rm acc} \simeq \frac{\tau_{\rm cycle}}{\Delta E/E}$, where $\tau_{\rm cycle}$ is the time needed to complete a *U-D-U* cycle. Considering a cylindrical flux tube — with base-area Σ — around the shock front and equating the number of particles crossing the shock from U to D with the particles inside the volume of the cylinder corresponding to one diffusion length $L_U(E) = D_U(E)/u_U$, being $D_U(E)$ the diffusion coefficient, we obtain the diffusion time scale

in the *upstream* region as:

$$\left(\frac{N v_{\rm CR}}{4\pi}\int_0^{2\pi} d\phi \int_0^1 d\mu\, \mu\right)\cdot \frac{1}{V}\left(\Sigma\tau_{{\rm diff},U}\right) \stackrel{!}{=} n\Sigma\frac{D_U(E)}{u_U} \quad \Rightarrow \quad \tau_{{\rm diff},U} \approx \frac{4D_U}{c u_U}$$

being $N = nV$ the total number of particles for a number density n in a volume V and, as usual, $v_{\rm CR} \approx c$.

Similarly, we obtain that, in the *downstream* region, particles spend on average the time $\tau_{{\rm diff},D} \approx \frac{4D_D}{cu_D}$. Therefore, $\tau_{\rm cycle} = \tau_{{\rm diff},U} + \tau_{{\rm diff},D}$ and, using Equation (1.11), we get:

$$\tau_{\rm acc}(E) \simeq \frac{3}{u_U - u_D}\left(\frac{D_U(E)}{u_U} + \frac{D_D(E)}{u_D}\right), \tag{1.17}$$

which is qualitatively similar to the full calculation first reported in Drury (1983); Lagage and Cesarsky (1983).

The problem described in this section is known as *diffusive shock acceleration* (DSA). Even though, as mentioned above, the non-linear treatment of the mechanism is here missing, DSA is the basis for the modern cosmic-ray acceleration studies. Its enormous success supports today the common agreement of the astroparticle community on the Supernova origin of cosmic rays (see for instance Bykov et al. (2018); Gabici (2011)). For this reason, we will rely on this for the phenomenological study presented in Part II, as far as the Supernova shocks are concerned.

On the other hand, as mentioned at the beginning of this section, there are specific astrophysical environments where a large-scale electric field is admitted, and direct particle acceleration can occur. One of them is the *pulsar magnetosphere*, namely the region surrounding the rotating star where the magnetic field originates from the pulsar itself. In this region, the peculiar configuration of the magnetic-field lines allows a recombination with the magnetized wind — a propagating wave emitted from the rotating object at the rotation frequency. This alternating component is thought to accelerate particles, thus powering the surrounding shell of the star that is called *Pulsar Wind Nebula* (PWN). The particle spectrum resulting from such mechanism is steeper than that derived for DSA, with a typical injection slope $\Gamma_{\rm inj}^{\rm mag\,rec} \in [1, 2]$. For detailed reviews on the topic, we remind to Kirk et al. (2009); Lyubarsky and Kirk (2001).

1.3 Cosmic-ray diffusion through the Galaxy

Now that we have introduced the principal acceleration mechanisms, we can deal with the independent physical problems connected with the propagation of the injected particles from the sources to the Earth. The transport properties of cosmic rays can be studied by means of a stochastic method commonly known as the *Fokker-Planck* equation (Chandrasekhar, 1943; Vietri, 2008).

To derive it, we consider the CR distribution function f, defined as the number of particles per unit volume dV in the cell of momentum $d\boldsymbol{p}$ — namely a *phase-space* density — with the following units:

$$[f(\boldsymbol{x},\boldsymbol{p},t)] = \frac{\#}{[L]^3\cdot[\boldsymbol{p}]} \tag{1.18}$$

and look for its change — in the same momentum cell — when the particles move from the position $\boldsymbol{x}$ to the position $\boldsymbol{x}+\Delta\boldsymbol{x} = \boldsymbol{x}+\boldsymbol{v}\Delta t$, where $\boldsymbol{v}$ is the cosmic-ray velocity. In other words, we want to evaluate the expression $f(\boldsymbol{x}+\boldsymbol{v}\Delta t,\boldsymbol{p},t+\Delta t)$.

Let $\Psi(\boldsymbol{p},\Delta\boldsymbol{p})$ be the probability density of a particle of momentum $\boldsymbol{p}$ to change it as $\boldsymbol{p}\to\boldsymbol{p}+\Delta\boldsymbol{p}$, such that the integral over all the possible changes $\Sigma(\Delta\boldsymbol{p})$ is normalized to 1:

$$\int_{\Sigma(\Delta\boldsymbol{p})} d(\Delta\boldsymbol{p})\,\Psi(\boldsymbol{p},\Delta\boldsymbol{p}) = 1.$$

The distribution function we are looking for is then written:

$$f(\boldsymbol{x}+\boldsymbol{v}\Delta t,\boldsymbol{p},t+\Delta t) = \int d(\Delta\boldsymbol{p})\, f(\boldsymbol{x},\boldsymbol{p}-\Delta\boldsymbol{p},t)\,\Psi(\boldsymbol{p}-\Delta\boldsymbol{p},\boldsymbol{p}), \tag{1.19}$$

where we notice that the change in the distribution function only depends on the previous step, which makes this process a *Markov process*. For sake of simplicity we dropped the explicit integral space $\Sigma(\Delta\boldsymbol{p})$.

If the changes $\Delta\boldsymbol{p}$ are small during the time Δt compared to the particle's momentum, then we can Taylor-expand Equation (1.19) — we expand the left-hand side up to $\mathcal{O}(\Delta t)$ and the right-hand side up to $\mathcal{O}(\Delta\boldsymbol{p}^2)$:

$$\begin{aligned}
f(\boldsymbol{x}+\boldsymbol{v}\Delta t,\boldsymbol{p},t+\Delta t) &\simeq f(\boldsymbol{x},\boldsymbol{p},t) + \frac{\partial f}{\partial t}\Delta t + \left(\boldsymbol{v}\cdot\frac{\partial}{\partial\boldsymbol{x}}\right)\Delta t\\
f(\boldsymbol{x},\boldsymbol{p}-\Delta\boldsymbol{p},t) &\simeq f(\boldsymbol{x},\boldsymbol{p},t) - \frac{\partial f}{\partial\boldsymbol{p}}\cdot\Delta\boldsymbol{p} + \frac{1}{2}\frac{\partial^2 f}{\partial\boldsymbol{p}^2}(\Delta\boldsymbol{p})^2\\
\Psi(\boldsymbol{p}-\Delta\boldsymbol{p},\Delta\boldsymbol{p}) &\simeq \Psi(\boldsymbol{p},\Delta\boldsymbol{p}) - \frac{\partial\Psi}{\partial\boldsymbol{p}}\cdot\Delta\boldsymbol{p} + \frac{1}{2}\frac{\partial^2\Psi}{\partial\boldsymbol{p}^2}(\Delta\boldsymbol{p})^2.
\end{aligned}$$

If we insert the above expressions in (1.19), we obtain:

$$\begin{aligned}
f + \left(\frac{\partial}{\partial t} + \boldsymbol{v}\cdot\frac{\partial}{\partial\boldsymbol{x}}\right) f\Delta t &\simeq \int d(\Delta\boldsymbol{p})\left[f - \frac{\partial f}{\partial\boldsymbol{p}}\cdot\Delta\boldsymbol{p} + \frac{1}{2}\frac{\partial^2 f}{\partial\boldsymbol{p}^2}(\Delta\boldsymbol{p})^2\right]\cdot\left[\Psi - \frac{\partial\Psi}{\partial\boldsymbol{p}}\cdot\Delta\boldsymbol{p} + \frac{1}{2}\frac{\partial^2\Psi}{\partial\boldsymbol{p}^2}(\Delta\boldsymbol{p})^2\right]\\
&\simeq \int d(\Delta\boldsymbol{p})\left\{f\Psi - \left(f\frac{\partial\Psi}{\partial\boldsymbol{p}} + \Psi\frac{\partial f}{\partial\boldsymbol{p}}\right)\cdot\Delta\boldsymbol{p} + \frac{1}{2}\left[f\frac{\partial^2\Psi}{\partial\boldsymbol{p}^2} + 2\frac{\partial f}{\partial\boldsymbol{p}}\frac{\partial\Psi}{\partial\boldsymbol{p}} + \Psi\frac{\partial^2 f}{\partial\boldsymbol{p}^2}\right](\Delta\boldsymbol{p})^2\right\},
\end{aligned}$$

where we neglected the terms from order $\mathcal{O}(\Delta \boldsymbol{p})^3$ on.

Considering $\int d(\Delta \boldsymbol{p})\, f(\boldsymbol{x}, \boldsymbol{p}, t)\Psi(\boldsymbol{p}, \Delta \boldsymbol{p}) = f(\boldsymbol{x}, \boldsymbol{p}, t) \int d(\Delta \boldsymbol{p})\, \Psi(\boldsymbol{p}, \Delta \boldsymbol{p}) = f$, we can rearrange the right-hand side and obtain:

$$\left(\frac{\partial}{\partial t} + \boldsymbol{v} \cdot \frac{\partial}{\partial \boldsymbol{x}}\right) f \Delta t = -\frac{\partial}{\partial \boldsymbol{p}} \int d(\Delta \boldsymbol{p})\, f\Psi\, \Delta \boldsymbol{p} + \frac{1}{2} \frac{\partial^2}{\partial \boldsymbol{p}^2} \int d(\Delta \boldsymbol{p})\, f\Psi\, (\Delta \boldsymbol{p})^2. \tag{1.20}$$

Furthermore, we can define the *Fokker-Planck* coefficients as follows:

$$\begin{aligned} \left\langle \frac{\Delta \boldsymbol{p}}{\Delta t} \right\rangle &\equiv A_{\boldsymbol{p}} := \frac{1}{\Delta t} \int d(\Delta \boldsymbol{p}) \Delta \boldsymbol{p}\, \Psi \\ \left\langle \frac{\Delta \boldsymbol{p} \Delta \boldsymbol{p}}{\Delta t} \right\rangle &\equiv D_{\boldsymbol{pp}} := \frac{1}{2\Delta t} \int d(\Delta \boldsymbol{p}) (\Delta \boldsymbol{p})^2\, \Psi \end{aligned} \tag{1.21}$$

and rewrite Equation (1.20):

$$\frac{\partial f}{\partial t} + \boldsymbol{v} \cdot \frac{\partial f}{\partial \boldsymbol{x}} = -\frac{\partial}{\partial \boldsymbol{p}} \left[f \left\langle \frac{\Delta \boldsymbol{p}}{\Delta t} \right\rangle \right] + \frac{\partial^2}{\partial \boldsymbol{p}^2} \left[f \left\langle \frac{\Delta \boldsymbol{p} \Delta \boldsymbol{p}}{\Delta t} \right\rangle \right]. \tag{1.22}$$

In order to rewrite both the coefficients in terms of the second-order one only, we assume that the probability density of a particle with momentum $\boldsymbol{p}$ to loose a quantity $\Delta \boldsymbol{p}$ is the same as the probability density of a particle with momentum $\boldsymbol{p} - \Delta \boldsymbol{p}$ to gain $\Delta \boldsymbol{p}$, a property known as *detailed balance*. This leads to:

$$\Psi(\boldsymbol{p}, -\Delta \boldsymbol{p}) \overset{\text{det.bal.}}{=} \Psi(\boldsymbol{p} - \Delta \boldsymbol{p}, \Delta \boldsymbol{p}) \simeq \Psi(\boldsymbol{p}, \Delta \boldsymbol{p}) - \frac{\partial \Psi}{\partial \boldsymbol{p}} \cdot \Delta \boldsymbol{p} + \frac{1}{2} \frac{\partial^2 \Psi}{\partial \boldsymbol{p}^2} (\Delta \boldsymbol{p})^2 \tag{1.23}$$

which can be divided by Δt and integrated, to give:

$$\begin{aligned} \frac{1}{\Delta t} &= \frac{1}{\Delta t} - \frac{\partial}{\partial \boldsymbol{p}} \left\langle \frac{\Delta \boldsymbol{p}}{\Delta t} \right\rangle + \frac{\partial^2}{\partial \boldsymbol{p}^2} \left\langle \frac{\Delta \boldsymbol{p} \Delta \boldsymbol{p}}{\Delta t} \right\rangle \\ \Rightarrow \quad & \frac{\partial}{\partial \boldsymbol{p}} \left[\left\langle \frac{\Delta \boldsymbol{p}}{\Delta t} \right\rangle - \frac{\partial}{\partial \boldsymbol{p}} \left\langle \frac{\Delta \boldsymbol{p} \Delta \boldsymbol{p}}{\Delta t} \right\rangle \right] = 0 \end{aligned}$$

This shows that the quantity inside the square brackets does not depend on $\boldsymbol{p}$. Also, for $\boldsymbol{p} \to 0$ both the *Fokker-Planck* coefficients tend to be 0, so that:

$$\left\langle \frac{\Delta \boldsymbol{p}}{\Delta t} \right\rangle = \frac{\partial}{\partial \boldsymbol{p}} \left\langle \frac{\Delta \boldsymbol{p} \Delta \boldsymbol{p}}{\Delta t} \right\rangle. \tag{1.24}$$

If we now plug this expression in Equation (1.22), we get:

$$\frac{\partial f}{\partial t} + \boldsymbol{v} \cdot \frac{\partial f}{\partial \boldsymbol{x}} = -\frac{\partial}{\partial \boldsymbol{p}} \left[f \frac{\partial D_{\boldsymbol{pp}}}{\partial \boldsymbol{p}} \right] + \frac{\partial^2}{\partial \boldsymbol{p}^2} \left(f D_{\boldsymbol{pp}} \right)$$

$$= \left\{ \cancel{-\frac{\partial}{\partial \boldsymbol{p}} \left(f \frac{\partial D_{\boldsymbol{pp}}}{\partial \boldsymbol{p}} \right)} + \frac{\partial}{\partial \boldsymbol{p}} \left(\frac{\partial f}{\partial \boldsymbol{p}} D_{\boldsymbol{pp}} \right) \cancel{+ \frac{\partial}{\partial \boldsymbol{p}} \left(f \frac{\partial D_{\boldsymbol{pp}}}{\partial \boldsymbol{p}} \right)} \right\}$$

from which we finally get:

$$\frac{\partial f}{\partial t} + \boldsymbol{v} \cdot \frac{\partial f}{\partial \boldsymbol{x}} = \frac{\partial}{\partial \boldsymbol{p}} \left(\frac{\partial f}{\partial \boldsymbol{p}} D_{\boldsymbol{pp}} \right). \tag{1.25}$$

This equation tells us that the variation of the distribution function depends on the squared momentum change of the cosmic rays, $\Delta \boldsymbol{p} \Delta \boldsymbol{p}$. This has been done, however, without specifying what physical processes caused such variation, which makes it impossible to derive an expression of practical use for the *Fokker-Planck* coefficients. Moreover, in order to have information on the CR propagation, we will need to derive a corresponding equation in the physical space.

1.3.1 The equations of the ideal MHD

The ISM magnetized plasmas in equilibrium can be easily perturbed, and small-amplitude oscillating fluctuations can be excited. In order to characterize the propagation properties of such fluctuations, we need to solve a closed set of equations, that can be derived coupling the Maxwell's equations — for the electric- and magnetic-field part — to the equations describing the dynamics of fluids. The resulting field of research is called *magneto-hydro-dynamics* (MHD).

Since the *interstellar medium* is a highly-ionized gas (*i.e.* a plasma), then no electric field can be felt by charges at distances larger than the *Debye length**, which corresponds to state that the ISM has nearly-infinite *conductivity* (or, equivalently, no *resistivity*). This condition is commonly referred to as *ideal magneto-hydro-dynamics*.

*The Debye length λ_D is the reference distance that appears in the solution of the Poisson's equation for the scalar potential generated by an isolated positive charge in an ionized medium. If $n_i \approx n_0 \exp\left(-\frac{e\phi}{k_B T}\right)$, $n_e \approx n_0 \exp\left(\frac{e\phi}{k_B T}\right)$ are respectively the densities of ions and electrons, k_B is the Boltzmann constant and T the temperature of the gas, then $-\nabla^2 \phi = 4\pi e \left[(n_i - n_e) + \delta(\boldsymbol{r}) \right]$, then the spherically symmetric scalar potential results $\phi(r) \propto \frac{1}{r} \exp\left(-\frac{\sqrt{2}\, r}{\lambda_D}\right)$, where as expected $\lambda_D = \sqrt{\frac{k_B T}{4\pi n_0 e^2}}$ depends on the environment conditions. The units are as follows: $[n_0] = \mathrm{L}^{-3}$, $[k_B T] = \mathrm{E}$, $[e^2/r] = \mathrm{E}$.

The corresponding set of equations can be written as follows (Boyd and Sanderson, 2003):

$$\begin{cases} \dfrac{\partial \rho}{\partial t} + \rho \boldsymbol{\nabla} \cdot \boldsymbol{u} = 0 \\ \rho \dfrac{\partial \boldsymbol{u}}{\partial t} + \rho \left(\boldsymbol{u} \cdot \boldsymbol{\nabla} \right) \boldsymbol{u} + \boldsymbol{\nabla} P - \dfrac{(\boldsymbol{\nabla} \wedge \boldsymbol{B}) \wedge \boldsymbol{B}}{\mu_0} = 0 \\ -\dfrac{\partial \boldsymbol{B}}{\partial t} + \boldsymbol{\nabla} \wedge (\boldsymbol{u} \wedge \boldsymbol{B}) = 0 \\ \left(\dfrac{\partial}{\partial t} + \boldsymbol{u} \cdot \boldsymbol{\nabla} \right) P \rho^{-\gamma_a} = 0, \end{cases} \tag{1.26}$$

where $[\rho] = M \cdot L^{-3}$ is the mass density of the medium, $\boldsymbol{u}$ the velocity of the plasma particles, P the gas pressure, μ_0 the magnetic permeability, γ_a the adiabatic coefficient, and $\boldsymbol{B}$ is the local total magnetic field.

We want to solve the above system for the physical quantities that are assumed to receive a *small perturbation*. Note that this condition is essential to find a propagating function, since the original equations are non-linear. Under this assumption, we can now linearize the equations, considering the plasma to be homogeneous and stationary at 0-*th* order, which further implies an overall pressure equilibrium and no magnetic stress:

$$\boldsymbol{u}_0 = 0, \qquad \boldsymbol{\nabla} \left(P_0 + \frac{B_0^2}{2\mu_0} \right) = 0, \qquad \left(\boldsymbol{B}_0 \cdot \boldsymbol{\nabla} \right) \boldsymbol{B}_0 = 0.$$

The perturbed quantities then become:

$$\begin{aligned} \boldsymbol{u} &= \delta \boldsymbol{u} & \boldsymbol{B} &= \boldsymbol{B}_0 + \delta \boldsymbol{B} \\ \rho &= \rho_0 + \delta \rho & P &= P_0 + \delta P \end{aligned} \tag{1.27}$$

and, plugged into the System (1.26) give a system of linear equations that can be solved searching for wave-like solutions of the type $\delta \boldsymbol{u}(\boldsymbol{r}, t) = \sum_{\boldsymbol{k},\omega} \delta \boldsymbol{u}(\boldsymbol{k}, \omega) e^{i(\boldsymbol{k} \cdot \boldsymbol{r} - \omega t)}$, *i.e.* Fourier-transforming the physical quantities:

$$\begin{cases} \dfrac{\partial \delta \rho}{\partial t} + \rho_0 \boldsymbol{\nabla} \cdot \delta \boldsymbol{u} = 0 \\ \rho_0 \dfrac{\partial \delta \boldsymbol{u}}{\partial t} + \boldsymbol{\nabla} \delta P - \dfrac{(\boldsymbol{\nabla} \wedge \delta \boldsymbol{B}) \wedge \boldsymbol{B}_0}{\mu_0} = 0 \\ -\dfrac{\partial \delta \boldsymbol{B}}{\partial t} + \boldsymbol{\nabla} \wedge (\delta \boldsymbol{u} \wedge \boldsymbol{B}_0) = 0 \\ \dfrac{\partial}{\partial t} \left(\dfrac{\delta P}{P_0} - \dfrac{\gamma_a \delta \rho}{\rho_0} \right) = 0 \end{cases} \quad \overset{\mathcal{F}}{\Longrightarrow} \quad \begin{cases} -\omega \delta \rho + \rho_0 \boldsymbol{k} \cdot \delta \boldsymbol{u} = 0 \\ -\omega \rho_0 \delta \boldsymbol{u} + \boldsymbol{k} \delta P - \dfrac{(\boldsymbol{k} \wedge \delta \boldsymbol{B}) \wedge \boldsymbol{B}_0}{\mu_0} = 0 \\ \omega \delta \boldsymbol{B} + \boldsymbol{k} \wedge (\delta \boldsymbol{u} \wedge \boldsymbol{B}_0) = 0 \\ -\omega \left(\dfrac{\delta P}{P_0} - \dfrac{\gamma_a \delta \rho}{\rho_0} \right) = 0, \end{cases} \tag{1.28}$$

where we remark that $(\boldsymbol{k}, \omega)$ are, respectively, the wave vector and frequency of the perturbation.

Solving the equations 1-3-4 with respect to $\delta\rho,\ \delta P,\ \delta\boldsymbol{B}$, respectively, and plugging the solutions into the second equation gives:

$$\left[\omega^2 - \frac{(\boldsymbol{k}\cdot\boldsymbol{B}_0)^2}{\mu_0\rho_0}\right]\delta\boldsymbol{u} = \left\{\left[\frac{\gamma_a P_0}{\rho_0} + \frac{\boldsymbol{B}_0^2}{\mu_0\rho_0}\right]\boldsymbol{k} - \frac{\boldsymbol{k}\cdot\boldsymbol{B}_0}{\mu_0\rho_0}\boldsymbol{B}_0\right\}(\boldsymbol{k}\cdot\delta\boldsymbol{u}) - \frac{(\boldsymbol{k}\cdot\boldsymbol{B}_0)\,(\delta\boldsymbol{u}\cdot\boldsymbol{B}_0)}{\mu_0\rho_0}\boldsymbol{k}. \tag{1.29}$$

Looking at the three terms, we notice that we do not loose any solution — namely we are able to excite all the available normal modes — of the above equation if we take the perturbation wave vector to have components on the axis parallel to $\boldsymbol{B}_0$ and on, at least, one of the perpendicular axes. Hence, considering Cartesian coordinates $(\hat{\boldsymbol{x}}, \hat{\boldsymbol{y}}, \hat{\boldsymbol{z}})$ and placing the regular field along $\hat{\boldsymbol{z}}$, we choose $\boldsymbol{B}_0 = B_0\hat{\boldsymbol{z}}$ and $\boldsymbol{k} = k_\perp\hat{\boldsymbol{x}} + k_\parallel\hat{\boldsymbol{z}}$. Thus, Equation (1.29) becomes the following matrix equation:

$$\begin{pmatrix} \omega^2 - k^2v_A^2 - k_\perp^2c_s^2 & 0 & -k_\perp k_\parallel c_s^2 \\ 0 & \omega^2 - k_\parallel^2 v_A^2 & 0 \\ -k_\perp k_\parallel c_s^2 & 0 & \omega^2 - k_\parallel^2 c_s^2 \end{pmatrix}\begin{pmatrix}\delta u_x \\ \delta u_y \\ \delta u_z\end{pmatrix} = 0, \tag{1.30}$$

where c_s is the sound speed and v_A is called Alfvén velocity, and they are defined as follows:

$$c_s^2 = \frac{\delta P}{\delta\rho} = \gamma_a\frac{P_0}{\rho_0}, \qquad v_A = \frac{B_0^2}{\sqrt{\mu_0\rho_0}}.$$

The eigenvalues of the matrix (1.30) can be found nullifying its determinant:

$$\left(\omega^2 - k_\parallel^2 v_A^2\right)\left[\omega^4 - k^2\left(v_A^2 + c_s^2\right)\omega^2 + k^2k_\parallel^2v_A^2c_s^2\right] = 0$$

$$\Rightarrow \qquad \begin{cases} \omega_A^2 = k_\parallel^2 v_A^2 & (0, \delta u_y, 0) \\ \omega_+^2 = k^2\,\dfrac{1}{2}\left(v_A^2 + c_s^2 + \sqrt{\left(v_A^2 + c_s^2\right)^2 - 4v_A^2c_s^2\dfrac{k_\parallel^2}{k^2}}\right) & (\delta u_x, 0, \delta u_z) \\ \omega_-^2 = k^2\,\dfrac{1}{2}\left(v_A^2 + c_s^2 - \sqrt{\left(v_A^2 + c_s^2\right)^2 - 4v_A^2c_s^2\dfrac{k_\parallel^2}{k^2}}\right) & (\delta u_x, 0, \delta u_z) \end{cases} \tag{1.31}$$

They represent three different relations between the wave vector and the frequency of the perturbation, *i.e.* they allow to find the three phase velocities of the propagating (and counter-propagating) normal modes. The corresponding eigenvectors are therefore the direction of the plasma displacement, *i.e.* the direction of oscillation. In particular:

- the first solution propagates parallel to $\boldsymbol{B}_0$ (it contains only $k_\parallel$) at the Alfvén speed v_A and its wave

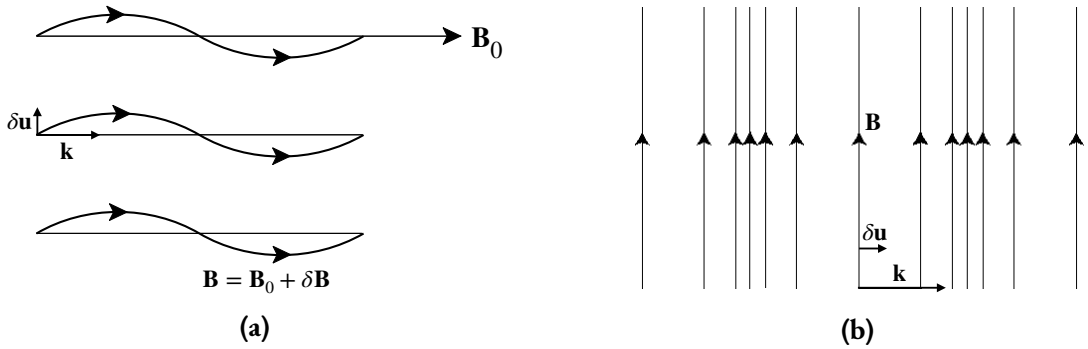

Figure 1.7: The direction of the displacement $\delta\boldsymbol{u}$ and of the propagation $\boldsymbol{k}$ of the magnetosonic modes are shown, for the case $\boldsymbol{k} \perp \boldsymbol{B}_0$, where the slow modes does not propagate. The total field $\boldsymbol{B} = \boldsymbol{B}_0 + \delta\boldsymbol{B}$ is also indicated. **(a)** The *shear Alfvén* mode propagates along the magnetic field as a transverse wave. **(b)** The *fast* mode propagates orthogonal to the regular, as well as total, magnetic field, while the plasma displacement is such that the field lines are squeezed.

vector is characterized by $\boldsymbol{k} \cdot \delta\boldsymbol{u} = 0$ and $\delta\boldsymbol{u} \cdot \boldsymbol{B}_0 = 0$, which means that it oscillates transversely with respect to the direction of propagation and also with respect to the magnetic-field axis. This mode is referred to as *shear Alfvén wave* and it is a *transverse wave* where no pressure nor density change are involved — it is an *incompressible* mode;

- the other two solutions have $\boldsymbol{k} \cdot \delta\boldsymbol{u} \neq 0$ and $\delta\boldsymbol{u} \cdot \boldsymbol{B} \neq 0$, namely the plasma displacement, in general, has non-zero components along the propagation direction and the magnetic-field axis. These modes are called *fast* and *slow magnetosonic modes* and they are *longitudinal waves* that can squeeze the field lines — they are *compressible* modes.

A visual sketch of these considerations is given in Figure 1.7, where the case $\boldsymbol{k} \perp \boldsymbol{B}_0$ is considered, for which slow modes cannot propagate $\omega_- = 0$.

As mentioned before, all the three modes can in principle act as scattering centers for the cosmic-ray particles. Throughout the thesis, we will see that the choice of whether or not they all have to be considered has important physical implications.

1.3.2 The *Fokker-Planck* coefficients within the QLT

In this paragraph, we present in detail the calculation of the *Fokker-Planck* coefficients contributing to the CR propagation equation. First, a rigorous derivation of this equation is reviewed, with particular attention to the necessary physical assumptions. Then, an alternative approach to calculate the pitch-angle *Fokker-Planck* coefficient $D_{\mu\mu}$ is discussed, that starts from an intuitive physical picture. In the latter part, we focus our attention on the effect of particle scattering off Alfvén waves exclusively — namely the modes propagating in the direction longitudinal to the background magnetic field $\boldsymbol{B}_0 = B_0\hat{\boldsymbol{z}}$, oscillating transversely. This choice is motivated by two reasons: (i) as it will be clear later, in

the case of purely alfvénic turbulence, the *Quasi-Linear Theory* (QLT) that we here present is exact, (ii) magnetosonic modes are severely damped during their propagating motion, while Alfvén modes are nearly free of damping (Ginzburg et al., 1962; Kulsrud and Pearce, 1969). Regarding (i), during the treatment we will discuss the implications of our assumptions — in particular about the geometry of the turbulence involved — on the physics of CR transport. For what concerns (ii), in Chapter 5 we will see that this picture is actually not entirely true, and can lead to significant modifications in the expression of the diffusion coefficient.

We start by evaluating the change in momentum of a particle in the reference frame of the Alfvén wave, where no force is exerted in the direction of the particle motion, and thus no exchange of energy occurs between the particle and the wave. Writing $\Delta p = m\gamma\,\Delta v_{\parallel} = m\gamma\,\Delta(v\mu)$, where $\gamma = \frac{1}{\sqrt{1-v^2/c^2}}$ is the Lorentz factor and $\mu \equiv \cos\theta$ is the cosine of the angle between the particle and $\boldsymbol{B}_0$, in the wave reference we have $\Delta p = m\gamma\, v\Delta\mu$. Besides, we are considering waves propagating in an ordered magnetic field oriented along $\hat{\boldsymbol{z}}$, which implies that at first approximation we can neglect the spatial derivatives of the distribution function with respect to the orthogonal variables $\hat{\boldsymbol{x}}$ and $\hat{\boldsymbol{y}}$. Within this 1D picture, the corresponding *Fokker-Planck* equation becomes:

$$\frac{\partial f}{\partial t} + v\mu\frac{\partial f}{\partial z} = \frac{\partial}{\partial \mu}\left(D_{\mu\mu}\frac{\partial f}{\partial \mu}\right), \tag{1.32}$$

where $D_{\mu\mu}$ is called *pitch-angle diffusion coefficient* — the reason why we invoke a diffusive behaviour will be clear in a moment.

From the equation above, we can derive that — for large times Δt and in the reference frame of the turbulent wave — $f \neq f(\mu)$. In other words, the CR distribution function does not depend on the arrival direction of the waves, which means that scattering must cause simple *diffusion* in pitch-angle. This can be seen by applying the Liouville's theorem* (Jokipii, 1966a; Lemaitre and Vallarta, 1933; Swann, 1933).

Fokker-Planck coefficients from the Vlasov equation. In order to derive an expression for $D_{\mu\mu}$, it is convenient to recall that the *Fokker-Planck* equation (1.32) can be formally obtained from the relativistic *Vlasov* equations (Vlasov, 1968):

$$\frac{\partial f}{\partial t} + \boldsymbol{v}\cdot\frac{\partial f}{\partial \boldsymbol{x}} + \dot{\boldsymbol{p}}\cdot\frac{\partial f}{\partial \boldsymbol{p}} = S(\boldsymbol{x},\boldsymbol{p},t), \tag{1.33}$$

where $S(\boldsymbol{x},\boldsymbol{p},t)$ denotes sources and sinks of particles and $\dot{\boldsymbol{p}}$ is given by the equations of motion (EOMs) specific for the system. Equation (1.33) is written in the six-dimensional phase space (x, y, z, p_x, p_y, p_z).

From Equation (1.33), the transport equation is then derived in the so-called *diffusion approxima-*

*From Jokipii (1966a): "If scattering did not tend toward isotropy, a spatially uniform, isotropic distribution [of magnetic fluctuations $\delta\boldsymbol{B}$] would relax toward anisotropy, in violation of Liouville's theorem."

tion. This procedure is originally due to Hall and Sturrock (1967); Kennel and Engelmann (1966); Kulsrud and Pearce (1969); Lerche (1968); Voelk (1975) and it is extensively revised in Schlickeiser (2002). We present the derivation following the path described in the last reference, in order to understand the physical assumptions connected to the use of (1.32).

To write the equations of motion, we consider a charged particle moving inside total magnetic and electric fields $(\boldsymbol{B}_{\rm tot},\ \boldsymbol{E}_{\rm tot})$. For what concerns the magnetic field, this results from the background regular field $\boldsymbol{B}_0 = B_0\hat{\boldsymbol{z}}$ plus a small perturbation (Jokipii, 1966a). On the other hand, we have seen in the previous section that no large-scale electric field is to be considered within our ideal MHD conditions. Thus we can write:

$$\begin{aligned} &\boldsymbol{B}_{\rm tot} = \boldsymbol{B}_0 + \delta\boldsymbol{B} \\ &\boldsymbol{E}_{\rm tot} = \delta\boldsymbol{E} \end{aligned} \qquad \text{such that} \qquad \begin{aligned} &|\delta\boldsymbol{B}| \ll |\boldsymbol{B}_0| \\ &\langle\boldsymbol{B}_{\rm tot}\rangle \approx \langle\boldsymbol{B}_0\rangle \\ &\langle\boldsymbol{E}_{\rm tot}\rangle \approx 0, \end{aligned} \tag{1.34}$$

where the $\langle\rangle$ operator denotes the *ensemble* average over all the possible realizations of the system that have the same macroscopic boundary conditions. For what follows, it is useful to rearrange the components of the vector perturbations $\delta\boldsymbol{B} = (\delta B_x, \delta B_y, \delta B_z)$ and $\delta\boldsymbol{E} = (\delta E_x, \delta E_y, \delta E_z)$ as

$$\begin{aligned} &\delta B_{R,L} \equiv \frac{1}{\sqrt{2}}\left(\delta B_x \pm i\delta B_y\right) && \delta E_{R,L} \equiv \frac{1}{\sqrt{2}}\left(\delta E_x \pm i\delta E_y\right) \\ &\delta B_{\parallel} = \delta B_z && \delta E_{\parallel} = \delta E_z, \end{aligned}$$

where $R,\ L$ denote the right-handed and left-handed polarizations of the fields, which simply indicates that the direction of oscillation of the field is counter-clockwise or clockwise in the $\widehat{xy}$-plane, respectively.

A charge moving at velocity $\boldsymbol{v}$ feels the Lorentz force:

$$\dot{\boldsymbol{p}} = q\left[\boldsymbol{E}_{\rm tot} + \frac{\boldsymbol{v}\wedge\boldsymbol{B}_{\rm tot}}{c}\right],$$

so that, if there was no perturbing field, then the resulting motion would be a helical motion composed by circles on the $\widehat{xy}$-plane and a uniform drift along $\hat{\boldsymbol{z}}$ (Jackson, 1975), as sketched in Figure 1.8a (we will see later a derivation of this result). Therefore, based on this helicoidal structure, it is very instructive to adopt the coordinates of the so-called *guiding center*:

$$(X, Y, Z) = (x, y, z) + \frac{\boldsymbol{v}\wedge\hat{\boldsymbol{z}}}{\Omega}$$

that are composed by the usual cartesian coordinates plus the position of the particle in the circle of radius defined by the angular frequency of rotation. This radius is called *Larmor radius* $r_L = v_\perp/\Omega$ and the angular frequency is known as *gyrofrequency* or, equivalently, *Larmor frequency* $\Omega = \frac{qB}{m\gamma c}$.

Similarly, spherical coordinates are useful, and can be found with the following transformations:

$$\begin{cases} p_x = p\sqrt{1-\mu^2}\cos\phi \\ p_y = p\sqrt{1-\mu^2}\sin\phi \\ p_z = p\mu \end{cases}$$

with polar and azimuthal angle (θ, ϕ), respectively, and $\sin\theta = \sqrt{1-\cos^2\theta} \equiv \sqrt{1-\mu^2}$.

Therefore, we can apply the following change of coordinates:

$$\begin{gathered} (x, y, z, p_x, p_y, p_z) \quad \longrightarrow \quad (X, Y, Z, p, \mu, \phi) \\ \begin{cases} X = x + \dfrac{p/(m\gamma)\sqrt{1-\mu^2}\sin\phi}{\Omega} \\ Y = y - \dfrac{p/(m\gamma)\sqrt{1-\mu^2}\cos\phi}{\Omega} \\ Z = z \end{cases} \qquad \begin{cases} p = \sqrt{p_x^2 + p_y^2 + p_z^2} \\ \mu = \dfrac{p_z}{p} \\ \phi = \arctan\left(\dfrac{p_y}{p_x}\right). \end{cases} \end{gathered} \tag{1.35}$$

In the new system of coordinates, the *Vlasov* equation becomes:

$$\frac{\partial f}{\partial t} + \boldsymbol{v}\cdot\frac{\partial f}{\partial \boldsymbol{X}} - \Omega\frac{\partial f}{\partial \phi} + \frac{1}{p^2}\frac{\partial}{\partial x_\sigma}\left(p^2 g_{x_\sigma} f\right) = S(\boldsymbol{X}, p, \mu, \phi, t), \tag{1.36}$$

where the Einstein summation convention is used, $x_\sigma = (X, Y, Z, p, \mu, \phi)$ and the functions $g_{x_\sigma} \equiv \dot{x}_\sigma$,

that contain all the physical information, are written as follows:

$$\dot{X} = -p/(m\gamma)\sqrt{1-\mu^2}\cos\phi\frac{\delta B_\parallel}{B_0} + \frac{ic}{\sqrt{2}B_0}\left[\delta E_R - \delta E_L - \frac{i\mu p/(m\gamma)}{c}\left(\delta B_L + \delta B_R\right)\right] \tag{1.37a}$$

$$\dot{Y} = -p/(m\gamma)\sqrt{1-\mu^2}\sin\phi\frac{\delta B_\parallel}{B_0} - \frac{c}{\sqrt{2}B_0}\left[\delta E_R + \delta E_L + \frac{i\mu p/(m\gamma)}{c}\left(\delta B_L - \delta B_R\right)\right] \tag{1.37b}$$

$$\dot{Z} = 0 \tag{1.37c}$$

$$\dot{p} = \frac{\Omega m\gamma c}{B_0}\left[\mu\delta E_\parallel + \sqrt{\frac{1-\mu^2}{2}}\left(\delta E_L e^{-i\phi} + \delta E_R e^{i\phi}\right)\right] \tag{1.37d}$$

$$\begin{aligned}\dot{\mu} = \frac{\Omega\sqrt{1-\mu^2}}{B_0}\Bigg\{\frac{c}{p/(m\gamma)}\sqrt{1-\mu^2}\delta E_\parallel + \frac{i}{\sqrt{2}}\Bigg[e^{i\phi}\left(\delta B_R + i\mu\frac{c}{p/(m\gamma)}\delta E_R\right)\\ -e^{-i\phi}\left(\delta B_L - i\mu\frac{c}{p/(m\gamma)}\delta E_L\right)\Bigg]\Bigg\}\end{aligned} \tag{1.37e}$$

$$\dot{\phi} = -\Omega\frac{\delta B_\parallel}{B_0} + \frac{\Omega}{\sqrt{2(1-\mu^2)}B_0}\left[e^{i\phi}\left(\mu\delta B_R + \frac{ic}{p/(m\gamma)}\delta E_R\right) + e^{-i\phi}\left(\mu\delta B_L - \frac{ic}{p/(m\gamma)}\delta E_L\right)\right]. \tag{1.37f}$$

It can be easily understood that solutions of the *Vlasov* equations with $g_{x_\sigma} = 0$ do not receive any contribution from the turbulent fields and describe the usual helicoidal motion, so that are called *unperturbed orbits*.

Note that, since magnetic irregularities are likely a consequence of turbulence, *i.e.* randomly varying in phase and amplitude, the statistical treatment obtained *ensemble*-averaging the fields is necessary. As a consequence, also the phase-space distribution function gets affected in a random way. Thus, we can decompose it as follows:

$$\begin{aligned}f(\boldsymbol{x},\boldsymbol{p},t) &= F(\boldsymbol{x},\boldsymbol{p},t) + \delta f(\boldsymbol{x},\boldsymbol{p},t)\\ \langle f(\boldsymbol{x},\boldsymbol{p},t)\rangle &\approx F(\boldsymbol{x},\boldsymbol{p},t),\end{aligned} \tag{1.38}$$

so that an expectation value for f must be found in terms of the statistical properties of the functions g_{x_σ}. The macroscopic condition for each member of the *ensemble* is here that they all have the same value at a time $t = t_0$, before the perturbations start modifying them. Then, the *ensemble*-averaged *Vlasov* equation reads:

$$\frac{\partial F}{\partial t} + \boldsymbol{v}\cdot\frac{\partial F}{\partial \boldsymbol{X}} - \Omega\frac{\partial F}{\partial\phi} = S(\boldsymbol{X},p,\mu,\phi,t) - \frac{1}{p^2}\frac{\partial}{\partial x_\sigma}\left(\left\langle p^2 g_{x_\sigma}\delta f\right\rangle\right). \tag{1.39}$$

The equation above contains the fluctuations and we now need an equation for them. To obtain

it, according to (1.38), we subtract (1.39) from (1.36):

$$\frac{\partial \delta f}{\partial t} + \boldsymbol{v} \cdot \frac{\partial \delta f}{\partial \boldsymbol{X}} - \Omega \frac{\partial \delta f}{\partial \phi} = -\frac{1}{p^2}\frac{\partial}{\partial x_\sigma}\left(p^2 g_{x_\sigma} f\right) + \frac{1}{p^2}\frac{\partial}{\partial x_\sigma}\left(\langle p^2 g_{x_\sigma} \delta f \rangle\right) \tag{1.40}$$

where rearrangements can be done on the right-hand side:

$$\begin{aligned}
&-\frac{1}{p^2}\frac{\partial}{\partial x_\sigma}\left(p^2 g_{x_\sigma} f\right) + \frac{1}{p^2}\frac{\partial}{\partial x_\sigma}\left(\langle p^2 g_{x_\sigma} \delta f \rangle\right) \\
&= \frac{1}{p^2}\left\langle p^2 g_{x_\sigma} \frac{\partial \delta f}{\partial x_\sigma} \right\rangle + \frac{1}{p^2}\left\langle \delta f \frac{\partial (p^2 g_{x_\sigma})}{\partial x_\sigma} \right\rangle - \frac{1}{p^2} p^2 g_{x_\sigma} \frac{\partial f}{\partial x_\sigma} - \frac{1}{p^2} f \frac{\partial (p^2 g_{x_\sigma})}{\partial x_\sigma} \\
&= \left\langle g_{x_\sigma} \frac{\partial \delta f}{\partial x_\sigma} \right\rangle + \frac{1}{p^2}\left\langle \delta f \frac{\partial (p^2 g_{x_\sigma})}{\partial x_\sigma} \right\rangle - g_{x_\sigma} \frac{\partial f}{\partial x_\sigma} - f \frac{1}{p^2} \frac{\partial (p^2 g_{x_\sigma})}{\partial x_\sigma} \\
&= \left\langle g_{x_\sigma} \frac{\partial \delta f}{\partial x_\sigma} \right\rangle + \frac{1}{p^2}\left\langle \delta f \frac{\partial (p^2 g_{x_\sigma})}{\partial x_\sigma} \right\rangle - g_{x_\sigma} \left(\frac{\partial F}{\partial x_\sigma} + \frac{\partial \delta f}{\partial x_\sigma} \right) - f \frac{1}{p^2} \frac{\partial (p^2 g_{x_\sigma})}{\partial x_\sigma}
\end{aligned}$$

Since we are only considering the Lorentz force acting on the CR's distribution function, we assume it to be divergence free, so that in spherical coordinates we have $\frac{1}{p^2}\frac{\partial}{\partial x_\sigma}(p^2 g_{x_\sigma}) = 0$, $\frac{1}{p^2}\left\langle \frac{\partial}{\partial x_\sigma}(p^2 g_{x_\sigma}) \right\rangle = 0$ (Hall and Sturrock, 1967). Hence, Equation (1.40) becomes:

$$\frac{\partial \delta f}{\partial t} + \boldsymbol{v} \cdot \frac{\partial \delta f}{\partial \boldsymbol{X}} - \Omega \frac{\partial \delta f}{\partial \phi} = -g_{x_\sigma} \frac{\partial F}{\partial x_\sigma} - g_{x_\sigma} \frac{\partial \delta f}{\partial x_\sigma} + \left\langle g_{x_\sigma} \frac{\partial \delta f}{\partial x_\sigma} \right\rangle . \tag{1.41}$$

Now the assumption of small fluctuations is used: in particular, we assume that the time scale T when we are evaluating the resulting phase-space distribution function F is much smaller that the time required for F to vary significantly — of the quantity $\delta f \not\approx 0$ — due to those fluctuations:

$$T \ll t_F \approx F \Big/ \left| g_{x_\sigma} \frac{\partial F}{\partial x_\sigma} \right| ,$$

thanks to which we can write Equation (1.41) as follows:

$$\frac{\partial \delta f}{\partial t} + \boldsymbol{v} \cdot \frac{\partial \delta f}{\partial \boldsymbol{X}} - \Omega \frac{\partial \delta f}{\partial \phi} \simeq -g_{x_\sigma} \frac{\partial F}{\partial x_\sigma} . \tag{1.42}$$

The equation above can be solved along its *characteristics*, namely we derive one *ordinary differential equation* (ODE) for each variable of the *partial differential equation* (PDE), assumed to be a function of a certain s. In practice, Equation (1.42) is formally written as:

$$\begin{aligned}
&\frac{d}{ds}\left\{ \delta f \left(t(s), X(s), Y(s), Z(s), p(s), \mu(s), \phi(s), \right) \right\} = G\left(\delta f, t(s), X(s), Y(s), Z(s), p(s), \mu(s), \phi(s) \right) \\
&\Rightarrow \quad \frac{\partial \delta f}{\partial t}\frac{dt}{ds} + \frac{\partial \delta f}{\partial X}\frac{dX}{ds} + \frac{\partial \delta f}{\partial Y}\frac{dY}{ds} + \frac{\partial \delta f}{\partial Z}\frac{dZ}{ds} + \frac{\partial \delta f}{\partial p}\frac{dp}{ds} + \frac{\partial \delta f}{\partial \mu}\frac{d\mu}{ds} + \frac{\partial \delta f}{\partial \phi}\frac{d\phi}{ds} = G
\end{aligned}$$

and becomes the following system of equations:

$$\frac{d(\delta f)}{ds} = -g_{x_\sigma}\frac{\partial F}{\partial x_\sigma} \qquad \text{such that} \qquad \begin{cases} \dfrac{dt}{ds} = 1 \\ \dfrac{dX}{ds} = p/(m\gamma)\sqrt{1-\mu^2}\cos\phi(s) \\ \dfrac{dY}{ds} = p/(m\gamma)\sqrt{1-\mu^2}\sin\phi(s) \\ \dfrac{dY}{ds} = p/(m\gamma)\mu \\ \dfrac{dp}{ds} = 0 \\ \dfrac{d\mu}{ds} = 0 \\ \dfrac{d\phi}{ds} = -\Omega. \end{cases} \tag{1.43}$$

Their solutions are easily found as:

$$\delta f(t) = \delta f(t_0) - \int_{t_0}^{t} ds \left[g_{x_\sigma}(x_\nu, s)\frac{\partial F}{\partial x_\sigma}\right]' \tag{1.44}$$

$$\begin{aligned} \bar{X} &= X_0 - \frac{p/(m\gamma)\sqrt{1-\mu^2}\sin\bar{\phi}}{\Omega} & \bar{p} &= p_0 \\ \bar{Y} &= Y_0 + \frac{p/(m\gamma)\sqrt{1-\mu^2}\cos\bar{\phi}}{\Omega} & \bar{\mu} &= \mu_0 \\ \bar{Z} &= Z_0 + p/(m\gamma)\mu(s-t) & \bar{\phi} &= \phi_0 - \Omega(s-t) \end{aligned}$$

where $(X_0, Y_0, Z_0, p_0, \mu_0, \phi_0)$ are the initial conditions and the prime indicates that the quantities are evaluated along the characteristic curves. Note that the latter identify the unperturbed particle orbits.

Now, with straightforward steps, we can plug the solution above in the second-term of the right-hand side of the Equation (1.39) for F. This term becomes:

$$\begin{aligned} -\frac{1}{p^2}\frac{\partial}{\partial x_\sigma}\left(\left\langle p^2 g_{x_\sigma}\delta f(t)\right\rangle\right) &= +\frac{1}{p^2}\frac{\partial}{\partial x_\sigma}\left(\left\langle p^2 g_{x_\sigma}\int_{t_0}^{t} ds\left[g_{x_\sigma}(x_\nu,s)\frac{\partial F}{\partial x_\sigma}\right]'\right\rangle\right) \\ &\simeq \frac{1}{p^2}\frac{\partial}{\partial x_\sigma}\left(p^2\left[\int_0^t ds\,\left\langle g_{x_\sigma}\, g_{x_\nu}(x_\nu,s)\right\rangle\right]'\frac{\partial F(x_\nu,t)}{\partial x_\nu}\right), \end{aligned}$$

where the following assumptions have been made:

- at the initial time t_0, the variation of the phase-space density $\delta f(t_0)$ is uncorrelated to the turbulent fields, $\langle \delta f(t_0)\, g_{x_\sigma}\rangle = 0$,

- we are evaluating our solution at a time T larger that the time interval $[t-t_c, t]$ when the turbulent fields are correlated — $\langle g_{x_\sigma}\, g_{x_\nu}\rangle$ — so that the lower bound of the integral is $t - t_c \to 0$,
- during the correlation interval the distribution function only changes negligibly with respect to its value not along the unperturbed orbits.

With these considerations, we finally get to:

$$\frac{\partial F}{\partial t} + \boldsymbol{v}\cdot\frac{\partial F}{\partial \boldsymbol{X}} - \Omega\frac{\partial F}{\partial \phi} = S(\boldsymbol{X}, p, \mu, \phi, t) + \frac{1}{p^2}\frac{\partial}{\partial x_\sigma}\left(p^2 D_{x_\sigma x_\nu}\frac{\partial F}{\partial x_\nu}\right), \tag{1.45}$$

where $D_{x_\sigma x_\nu}$ are referred to as the *Fokker-Planck* coefficients and take the following form:

$$D_{x_\sigma x_\nu}(\boldsymbol{x}, t) = \int_0^t ds\, \langle \bar{g}_{x_\sigma}(t)\, \bar{g}_{x_\nu}(s)\rangle \approx \int_0^t ds\, \langle g_{x_\sigma}(t)\, g_{x_\nu}(s)\rangle. \tag{1.46}$$

The *Fokker-Planck* coefficients above are calculated using the set of equations (1.37) assuming that their values is approximately equal to the ones computed along the unperturbed orbits. This, the condition $\left[\frac{\partial F}{\partial x_\sigma}\right]' \approx \frac{\partial F}{\partial x_\sigma}$ and the assumption of small fluctuations all contribute to give the whole apparatus the name of *Quasi-Linear Theory* (QLT). The *ensemble* averages $\langle g_{x_\sigma}\, g_{x_\nu}\rangle$, due to the expressions of the functions g_{x_σ} in Equation (1.37), are basically a set of two-point *correlation tensors* for the turbulent electric and magnetic fields*. The field fluctuations $\delta\boldsymbol{A}(\boldsymbol{r})$ are *homogeneous random functions* of position, in the sense that for their probability distributions holds $\mathcal{E}\left[\delta\boldsymbol{A}(\boldsymbol{x}_i)\right] \equiv \langle\delta\boldsymbol{A}(\alpha\boldsymbol{x}_i)\rangle = \langle\delta\boldsymbol{A}(\boldsymbol{x}_i)\rangle$, where $\alpha \in \mathbb{R}$ and we denoted the expectation value with $\mathcal{E}$ (Yaglom and Silverman, 2004). In other words, the expectation values above — and, consequently, the two-point correlation tensors — are invariant under translation along any axis. Since from a point $\boldsymbol{x}_1$ we can reach a point $\boldsymbol{x}_2$ by applying a scalar ($\boldsymbol{x}_2 = \alpha\boldsymbol{x}_1$), then the statistical *ensemble* average $\langle\delta\boldsymbol{A}(\boldsymbol{x}_1)\,\delta\boldsymbol{A}(\boldsymbol{x}_2)\rangle$ reduces to a simple average over space (Jokipii, 1966a).

In order to evaluate which $D_{x_\sigma x_\nu}$'s give Equation (1.45) the largest contributions, looking at the g_{x_σ} functions in Equation (1.37), several considerations can be done:

- g_p contains only $\delta\boldsymbol{E}$, hence, as no external electric field can be felt, these fluctuations are induced by the moving magnetic field, according to the Faraday's induction law $\delta\boldsymbol{E} \approx -\frac{1}{c}\left(\boldsymbol{v}_A \wedge \delta\boldsymbol{B}\right)$. Since we are assuming $v_A \ll c$ then we can neglect electric fluctuations up to order $\mathcal{O}(v_A/c)$, so that $D_{px_\sigma} = D_{x_\sigma p} \approx 0$. As a further consequence, at order $\mathcal{O}(v_A/c)$ there is no exchange of energy between the particle and the wave.
- The correlation tensors scale as†: $D_{\mu\mu} \simeq D_{\phi\phi} \simeq D_{\mu\phi} \sim \Omega^2\left(\frac{\delta B}{B_0}\right)^2[T]$, $D_{XX} \simeq D_{YY} \simeq D_{XY} \sim$

*It can be shown that the correlation tensor of order m, $\langle\delta\boldsymbol{A}(\boldsymbol{x}_1)\,\delta\boldsymbol{A}(\boldsymbol{x}_2)\ldots\delta\boldsymbol{A}(\boldsymbol{x}_m)\rangle$, constitutes a complete specification of a turbulent random field (Yaglom, 1962). Besides, the two-point correlation tensors correspond to the Gaussian part of the turbulent fields (Mertsch, 2020).

†Note that in each $D_{x_\sigma x_\nu}$ there is an extra dimensional factor $[T]$, that cannot be seen trivially from (1.37): it

$r_L^2\Omega^2\left(\frac{\delta \boldsymbol{B}}{\boldsymbol{B}_0}\right)^2[T]$, $D_{\mu X(Y)} \simeq D_{\phi X(Y)} \sim r_L\Omega^2\left(\frac{\delta \boldsymbol{B}}{\boldsymbol{B}_0}\right)^2[T]$. From dimensional analysis, we find that their time scales scale as follows: $T_{\mu\mu} \simeq T_{\phi\phi} \simeq T_{\mu\phi} \sim D_{\mu\mu}^{-1}$, $T_{XX} \simeq T_{YY} \simeq T_{XY} \sim L_\perp \cdot D_{XX}^{-1} \sim \left(\frac{L_\perp}{r_L}\right)^2 D_{\mu\mu}^{-1}$, $T_{\mu X(Y)} \simeq T_{\phi X(Y)} \sim L_\perp \cdot D_{\mu X}^{-1} \sim \frac{L_\perp}{r_L} D_{\mu\mu}^{-1}$, where $L_\perp$ is a typical length scale for the variation of the distribution function F in the orthogonal direction with respect to $\boldsymbol{B}_0$. We reasonably assume that a non-negligible perpendicular shift of the guiding center occurs on time scales much longer than a single Larmor radius of the charge. Therefore, only $D_{\mu\mu}$, $D_{\mu\phi}$, $D_{\phi\phi}$ survive at order $(O)(L_\perp/r_L)$, which tells us that pitch-angle and azimuthal scattering are the fastest processes in these conditions.

- Finally, we will average the equations over the azimuthal angle ϕ. In other words, our equation will give us the isotropic part of the distribution function, so that we can assume now $\frac{\partial F}{\partial \phi} \approx 0$ in Equation (1.45).

Within the assumptions and time scales discussed above, the *Vlasov* equation reduces to:

$$\frac{\partial F}{\partial t} + v\mu\frac{\partial F}{\partial Z} = S(\boldsymbol{X}, p, \mu, \phi, t) + \frac{\partial}{\partial \mu}\left(D_{\mu\mu}\frac{\partial F}{\partial \mu}\right), \tag{1.47}$$

which is the analogous of Equation (1.32), where we will set $S(\boldsymbol{X}, p, \mu, \phi, t) = 0$ and $Z \equiv z$, with:

$$D_{\mu\mu}(\boldsymbol{x}, t) = \int_0^t ds\, \langle \dot{\mu}(t)\, \dot{\mu}(s)\rangle. \tag{1.48}$$

In conclusion, we have found that the *Fokker-Planck* equation (1.32) is valid within QLT (Jokipii, 1966a; Kulsrud and Pearce, 1969). Furthermore, we will see in Section 1.3.3 that the condition $v_A \ll v_{CR} \approx c$ is in particular referred to as *diffusion approximation*.

A practical expression for $D_{\mu\mu}$ under our conditions is found in Kulsrud and Pearce (1969); Voelk (1975):

$$D_{\mu\mu} = \Omega^2(1-\mu^2)\int d\boldsymbol{k} \sum_{n=-\infty}^{+\infty} \delta(k_\parallel v_\parallel - \omega + n\Omega)\left[\frac{n^2 J_n^2(w)}{w^2} I^A(\boldsymbol{k}) + \frac{k_\parallel^2}{k^2} J_n'^2(w) I^M(\boldsymbol{k})\right], \tag{1.49}$$

where $J_n(w), J_n'(w)$ are the Bessel functions* of order n and its derivative, respectively, $w \equiv \frac{k_\perp v\sqrt{1-\mu^2}}{\Omega}$, and $I^{A,M}$ are the Alfvén and magnetosonic (fast and slow) modes of the magnetic turbulent spectra, normalized to the energy density of the background field, such that:

$$\frac{\langle \delta \boldsymbol{B}^2(\boldsymbol{x})\rangle}{\boldsymbol{B}_0^2} = \int d\boldsymbol{k}\left(I^A(\boldsymbol{k}) + I^F(\boldsymbol{k}) + I^S(\boldsymbol{k})\right).$$

comes from the complete calculation of the two-point correlation functions, as will be explicitly seen later in the section. The exact expressions for the $D_{x_\sigma x_\nu}$'s can be found in Schlickeiser (2002) (their Chapter 12).

*The Bessel function are introduced due to the Fourier decomposition of the turbulent field $\delta\boldsymbol{B} = \int_{-\infty}^{+\infty} d\boldsymbol{k}\, \boldsymbol{B}(\boldsymbol{k}, t) e^{i\boldsymbol{k}\cdot\boldsymbol{x}(t)}$ and the identity $e^{iw\sin\phi} = \sum_{-\infty}^{+\infty} J_n(w) e^{in\phi}$ (Tademaru, 1969).

$D_{\mu\mu}$ from pure alfvénic perturbation. An alternative approach for finding $D_{\mu\mu}$, which is probably more pedagogical and instructive, makes use of the result found in Equation (1.48) and allows to directly compute the *Fokker-Planck* coefficient from approximate solutions of the particle orbits, based on the physics of the system and the previous knowledge of the turbulent spectra, especially its geometry. This is originally to be found in Jokipii (1966a), with small later editing (Hasselmann and Wibberenz, 1970; Jokipii, 1968), while our treatment is based on Blasi (2013).

To do this, we first consider the equations of motion of a cosmic-ray particle traveling inside an ordered magnetic field directed along the $\hat{\boldsymbol{z}}$ axis, $\boldsymbol{B}_0 = B_0\hat{\boldsymbol{z}}$. With no large-scale electric field $\boldsymbol{E}_0$, we can write the EOMs as follows:

$$\frac{d\boldsymbol{p}}{dt} = \frac{q}{c}(\boldsymbol{v} \wedge \boldsymbol{B}_0). \tag{1.50}$$

The Lorentz force acts in the direction perpendicular to the particle motion, so that the modulus of the velocity is preserved, thus if we split the motion in its components we get:

$$m\gamma\frac{d\boldsymbol{v}}{dt} = \frac{q}{c}(\boldsymbol{v} \wedge \boldsymbol{B}_0) \quad \Rightarrow \quad \begin{cases} m\gamma\dfrac{dv_x}{dt} = \dfrac{q}{c}v_y B_0 \\ m\gamma\dfrac{dv_y}{dt} = -\dfrac{q}{c}v_x B_0 \\ m\gamma\dfrac{dv_z}{dt} = 0. \end{cases} \tag{1.51}$$

We can combine the first two equations and find a second-order differential equation:

$$m\gamma\frac{d}{dt}\left(m\gamma\frac{dv_x}{dt}\frac{c}{qB_0}\right) = -\frac{q}{c}v_x B_0 \quad \Rightarrow \quad \frac{d^2v_x}{dt^2} = -\Omega^2 v_x,$$

where we find again the Larmor frequency $\Omega \equiv \frac{qB_0}{m\gamma c}$.

The above equation can be easily solved as a harmonic motion along the $\hat{\boldsymbol{x}}$ axis, as $v_x = v_{0,x}\cos(\Omega t)$. With this solution, we can univocally solve the system (1.51) as follows:

$$\begin{cases} v_x = v_{0,\perp}\cos(\Omega t) \\ v_y = -v_{0,\perp}\sin(\Omega t) \\ v_z = v_{0,\parallel} \end{cases} = \begin{cases} v_x = v_0(1-\mu^2)^{\frac{1}{2}}\cos(\Omega t) \\ v_y = -v_0(1-\mu^2)^{\frac{1}{2}}\sin(\Omega t) \\ v_z = v_0\mu \end{cases} \tag{1.52}$$

where $v_{0,\perp}$ is the initial velocity of the particle in the $\widehat{xy}$-plane, so that $v_{0,\perp} = v_0\sin\theta = v_0\sqrt{1-\cos^2\theta}$. The solution above is of course well known and, as anticipated before, corresponds to a helicoidal structure with circular motion on the $\hat{xy}$-plane and a uniform drift along $\hat{\boldsymbol{z}}$. Clearly the pitch-angle μ does not change in time. A visual representation of this solution is shown in Figure 1.8a.

Now we add a perturbation $\delta\boldsymbol{B}$ — with general components $\delta\boldsymbol{B} \equiv (\delta B_x, \delta B_y, \delta B_z)$ — such that $|\delta\boldsymbol{B}| \ll |\boldsymbol{B}_0|$ and write the EOMs in the reference frame of the perturbation, that is moving with respect

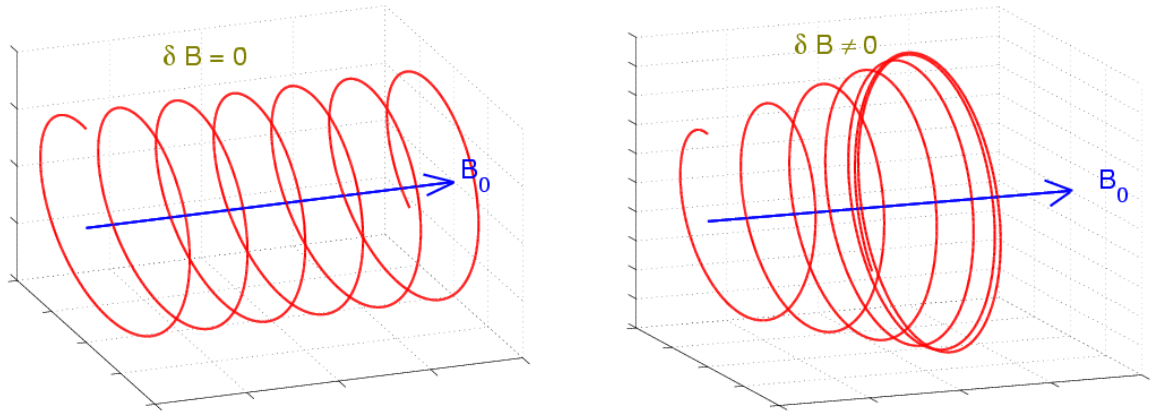

Figure 1.8: **(a)** Charged particle in a uniform magnetic field: the particle has an initial velocity component on the $\hat{\boldsymbol{z}}$ axis, $v_{z,0} = \boldsymbol{v}\cos\theta \equiv \boldsymbol{v}\mu \neq 0$ and the resulting motion is helicoidal. **(b)** The perturbation $\delta\boldsymbol{B}$ in the plane perpendicular to $\boldsymbol{B}_0$ changes the CR pitch-angle μ and thus the size of the circles, while the guiding center holds.

to the Earth at the Alfvén speed v_A. As mentioned at the beginning, we consider a pure alfvénic wave, so its wavevector $\boldsymbol{k}$ propagates along the background magnetic field $\boldsymbol{B}_0 = B_0\hat{\boldsymbol{z}}$ and the wave oscillates as $\delta\boldsymbol{B} \perp \boldsymbol{k}$. Hence in general:

$$\begin{aligned}
\delta\boldsymbol{B} = (\delta B_x, \delta B_y, 0) &= \left(|\delta B_x| \cdot e^{i(kz-\omega t+\phi_x)}, |\delta B_y| \cdot e^{i\left(kz-\omega t+\phi_y\right)}, 0\right) \\
&= \left(|\delta B_x| \cdot e^{i(kz-\omega t+\phi_x)}, |\delta B_y| \cdot e^{i\left(kz-\omega t+\phi_x+\frac{\pi}{2}-\phi_x-\frac{\pi}{2}+\phi_y\right)}, 0\right) \\
&= \left(|\delta B_x| \cdot e^{i(kz-\omega t+\phi_x)}, i|\delta B_y| \cdot e^{i(kz-\omega t+\phi_x)} \cdot e^{i\left(\Delta\phi-\frac{\pi}{2}\right)}, 0\right)
\end{aligned}$$

where ω is the angular frequency of the wave, ruled by the dispersion relation $\omega = v_A|\boldsymbol{k}|$, and we denoted with $\Delta\phi = \phi_y - \phi_x$ the phase difference between the two components, that is in general not null.

The absolute phase ϕ_x is not relevant, while the physics is actually encoded in the difference $\Delta\phi$. Besides, in order to simplify the algebra in the next steps, we chose to consider the phase difference with respect to a $\frac{\pi}{2}$-difference between ϕ_y and ϕ_x — we call this $\Delta\phi' \equiv \Delta\phi - \frac{\pi}{2}$. Notice that this argument works just as well if we rotate clockwise, *i.e.* if we consider a phase difference with respect to a $-\frac{\pi}{2}$-difference. Hence, the perturbation becomes:

$$\delta\boldsymbol{B} = \left(|\delta B_x| \cdot e^{i(kz-\omega t)}, \pm i|\delta B_y| \cdot e^{i\left(kz-\omega t+\Delta\phi'\right)}, 0\right)$$

If we assume the wave components to have the same amplitude ($|\delta B_x| = |\delta B_y| \equiv |\delta B|$) — this is a reasonable assumption in a locally homogeneous environment — the wave is said to be in *elliptical* polarization.

As a final requirement for our analysis, recall that we are implicitly considering the real part of the fields, so that:

$$\mathrm{Re}[\delta\boldsymbol{B}] = \left(|\delta B_x|\cos\left(kz-\omega t\right), \pm|\delta B_y|\sin\left(kz-\omega t+\Delta\phi'\right), 0\right). \tag{1.53}$$

With these considerations, the EOMs become:

$$m\gamma\frac{d\boldsymbol{v}}{dt} = \frac{q}{c}\boldsymbol{v}\wedge(\boldsymbol{B}_0+\mathrm{Re}[\delta\boldsymbol{B}]) \quad \Rightarrow$$

$$\Rightarrow \quad \begin{cases} m\gamma\dfrac{dv_x}{dt} = \dfrac{q}{c}(v_yB_0 - v_z\mathrm{Re}[\delta B_y]) \\ m\gamma\dfrac{dv_y}{dt} = -\dfrac{q}{c}(v_xB_0 - v_z\mathrm{Re}[\delta B_x]) \\ m\gamma\dfrac{dv_z}{dt} = \dfrac{q}{c}(v_x\mathrm{Re}[\delta B_y] - v_y\mathrm{Re}[\delta B_x]) \end{cases} \quad \simeq \quad \begin{cases} m\gamma\dfrac{dv_x}{dt} = \dfrac{q}{c}v_yB_0 \\ m\gamma\dfrac{dv_y}{dt} = -\dfrac{q}{c}v_xB_0 \\ m\gamma\dfrac{dv_z}{dt} = \dfrac{q}{c}(v_x\mathrm{Re}[\delta B_y] - v_y\mathrm{Re}[\delta B_x]). \end{cases} \tag{1.54}$$

As it is evident, we neglected the perturbation field in the x and y components since we are in QLT ($\delta\boldsymbol{B} \ll \boldsymbol{B}_0$), so the circular orbits in the plane perpendicular to the background field are approximately unaltered. On the other hand, in general $\dot{v}_z \neq 0$ due to the perturbation, that therefore acts as to change the pitch-angle μ of the particle — not the momentum value though, as we are still in the wave reference, so the only force acting on the particle is the Lorentz force. This picture is represented in Figure 1.8b, where the helical CR motion is perturbed as to change — exclusively — the size of the concentric circles. Intuitively, we can already see that a large number of pitch-angle changes can eventually reverse the parallel velocity of the particle, but cannot shift the guiding center of the orbits.

To study the entity of the change, we are going to focus on the last equation of the system above. In virtue of Equation (1.53) and of the particle velocity components (1.52), we find:

$$\begin{aligned} \frac{dv_z}{dt} &= \frac{q}{m\gamma c}\left[v_0(1-\mu^2)^{\frac{1}{2}}\cos(\Omega t)|\delta B|\cos(kz-\omega t) \pm v_0(1-\mu^2)^{\frac{1}{2}}\sin(\Omega t)|\delta B|\sin(kz-\omega t+\Delta\phi')\right] \\ &= \frac{qv_0|\delta B|}{m\gamma c}(1-\mu^2)^{\frac{1}{2}}\left[\cos(kz-\omega t)\cos(\Omega t) \pm \sin(kz-\omega t+\Delta\phi')\sin(\Omega t)\right] \\ &= \frac{qv_0|\delta B|}{m\gamma c}(1-\mu^2)^{\frac{1}{2}}\left\{\cos(kz-\omega t)\cos(\Omega t) \pm \left[\sin(kz-\omega t)+\sin(kz-\omega t+\Delta\phi')-\sin(kz-\omega t)\right]\sin(\Omega t)\right\}. \end{aligned}$$

Due to the last step, we can use the trigonometric relation $\cos\alpha\cos\beta \pm \sin\alpha\sin\beta = \cos(\alpha\pm\beta)$ and we are left with the difference $\left[\sin(kz-\omega t+\Delta\phi')-\sin(kz-\omega t)\right]\sin(\Omega t)$. Now, since the initial phase of the wave components is randomly distributed, we want to average over it, and the difference above does not contribute, as we are integrating in a whole period: $\frac{1}{2\pi}\int_0^{2\pi} d(\Delta\phi')\sin(kz-\omega t+\Delta\phi')-\sin(kz-\omega t) = 0$.

Thus, applying the trigonometric formula above and having averaged over a period $[0, 2\pi]$, we get:

$$\begin{aligned} \cancel{v_0}\frac{d\mu}{dt} &= \frac{q\cancel{v_0}|\delta B|}{m\gamma c}(1-\mu^2)^{\frac{1}{2}}\cos(kz-\omega t\pm\Omega t) \\ &\approx \frac{q|\delta B|}{m\gamma c}(1-\mu^2)^{\frac{1}{2}}\cos(kz\pm\Omega t), \end{aligned} \tag{1.55}$$

where we used that, after a distance $z = v_0\mu t$ walked by a CR, $\frac{kz}{\omega t} = \frac{kv_0\mu t}{kv_A t} = \mu\frac{v_0}{v_A} \gg 1$.

Since the above equation implies a periodic variation, if we integrate over a long time interval, we average to zero, which is physically expected, as the particle orbits are concentric circles. On the other hand, in order to have a measure of how much a CR has been hit by a wave, we consider the square of the pitch-angle variation:

$$\langle\Delta\mu\Delta\mu\rangle = \left(\frac{q\delta B}{m\gamma c}\right)^2(1-\mu^2)\int_0^{\Delta t}dt_1\int_0^{\Delta t}dt_2\,\cos(kz\pm\Omega t_1)\cos(kz\pm\Omega t_2), \tag{1.56}$$

where we defined $\langle\Delta\mu\rangle \equiv \int_0^{\Delta t}dt\,\left(\frac{d\mu}{dt}\right)$.

The integrand functions are even, so we can extend the interval of the dt_2 integral as $[0,\Delta t] \to [-\Delta t,\Delta t]$ and add a factor $\frac{1}{2}$. Besides, as we are considering sufficiently large times to evaluate the effect of the scattering ($\Delta t \gg t_2, t_1$), the same interval can be approximated as $[-\infty,+\infty]$. These arrangements simplify the calculations, since we can now write the cosine function as $\cos(kv_0\mu\pm\Omega)t = \mathrm{Re}\left\{\exp\left[i\left(kv_0\mu\pm\Omega\right)t\right]\right\}$ and solve the integral on t_2, as to obtain a *delta* function:

$$\langle\Delta\mu\Delta\mu\rangle = \left(\frac{q\delta B}{m\gamma c}\right)^2\frac{1-\mu^2}{2}\int_0^{\Delta t}dt_1\,\mathrm{Re}\left\{e^{i(kv_0\mu\pm\Omega)t_1}\right\}2\pi\delta(kv_0\mu\pm\Omega).$$

Now the second integral, because of the presence of the *delta* function, gives just a factor $\int_0^{\Delta t}dt_1 = \Delta t$, and we find:

$$\left\langle\frac{\Delta\mu\Delta\mu}{\Delta t}\right\rangle = \left(\frac{qB_0}{m\gamma c}\right)^2\left(\frac{\delta B(z)}{B_0}\right)^2(1-\mu^2)\,\pi\delta(kv_\parallel\pm\Omega), \tag{1.57}$$

where we can explicitly notice that the perturbation δB is here a function of position and we easily recognize the Larmor frequency $\frac{qB_0}{m\gamma c} \equiv \Omega$. Since in general we have a packet of turbulent waves, it is useful to consider an energy distribution per wave number $W(k)dk$, as the energy density contained in the range of wavenumbers $[k, k+dk]$, normalized to the energy density of the background field $\frac{B_0^2}{8\pi}$:

$$\left(\frac{\delta B(k)}{B_0}\right)^2 \stackrel{\mathrm{def}}{=} W(k)dk.$$

With this precaution, Equation (1.57) gets modified as follows:

$$D_{\mu\mu} \equiv \left\langle \frac{\Delta\mu\Delta\mu}{\Delta t} \right\rangle = \Omega^2(1-\mu^2)\pi \int dk\, W(k)\delta(kv_\parallel \pm \Omega). \tag{1.58}$$

If we divide the argument of the *delta* function by $v_\parallel$ and use the property $\int dx\, \delta(cx) = \frac{1}{|c|}\int dx\, \delta(x)$, we get to the following expression for $D_{\mu\mu}$:

$$D_{\mu\mu} = \Omega(1-\mu^2)\pi k_{\rm res} \int dk\, W(k)\delta(k \pm k_{\rm res}), \tag{1.59}$$

where we defined a quantity similar to the inverse Larmor radius as $\Omega/v_\parallel = \tilde{r}_L^{-1} \equiv k_{\rm res}$.

The above equations clearly show that, under the assumptions made so far, a wave-particle interaction is only possible when the inverse Larmor radius of the particle matches ($\equiv$ is resonant) — with the wavenumber of the turbulent wave: this kind of process is in fact called *gyroresonant scattering*. Note that Equation (1.58) can be obtained by the general expression of the $D_{\mu\mu}$ in (1.49) for the case where only Alfvén modes are present ($I^M = 0$), and particles have small Larmor radius ($w \equiv \frac{k_\perp v\sqrt{1-\mu^2}}{\Omega} \ll 1$, so that $J_1(w) \simeq w/2$) and do not interact with the waves *via* the $n = 0$ mode (*Landau* resonance).

We can notice that the pitch-angle diffusion coefficient just defined is expressed in units $[D_{\mu\mu}] = T^{-1}$, so we can interpret it as the rate of pitch-angle variation. This implies that we can compute the time between one such variation and the next one as:

$$\Delta t \sim \frac{1}{D_{\mu\mu}} \sim \frac{1}{\Omega k_{\rm res} W(k_{\rm res})}.$$

From kinetic theory of gases*, we know that the parallel diffusion coefficient can be written as $D_\parallel = \frac{v_\parallel \lambda_{\rm m.f.p.}}{3}$, where $v_\parallel$ is the CR velocity along $\boldsymbol{B}_0$ (*not* the drift velocity) and $\lambda_{\rm m.f.p.}$ is its mean free path. Therefore, $\lambda_{\rm m.f.p.} = v_\parallel \Delta t$, where Δt is the time interval computed above. Hence:

$$D_\parallel = \frac{1}{3}v_\parallel^2 \Delta t \sim \frac{c^2}{\Omega k_{\rm res} W(k_{\rm res})} = \frac{c\, r_L}{k_{\rm res} W(k_{\rm res})}. \tag{1.60}$$

With this arrangement, we can express $D_\parallel$ as a function of the CR energy E. Indeed, $r_L \propto E$, $k_{\rm res} = r_L^{-1} \propto E^{-1}$ and, as defined above, $W(k)$ is the energy distribution per wavenumber, namely an energy spectrum, that goes as $W(k) \sim k^{-\alpha} \sim E^{+\alpha}$. Therefore:

$$D_\parallel \propto E^{2-\alpha} \quad \Rightarrow \quad D_\parallel = D_0 \cdot \left(\frac{E}{E_0}\right)^\delta, \tag{1.61}$$

where we introduced D_0 as the normalization of the diffusion coefficient at the reference energy E_0

*In particular, this can be seen re-deriving the Fick's law $J_z = -D_{zz}\frac{\partial n_a}{\partial z}$ in terms of the kinetic motion of particles of type a in a background gas (see for instance Feynman et al. (2011)).

and we defined $2 - \alpha \equiv \delta$.

The phenomenological expression above represents the scaling with energy — or, equivalently, rigidity $\rho \equiv \frac{pc}{Ze}$, where Z and e are respectively the atomic number and the charge of the CR — of $D_{\parallel}$. It is of large use in the literature and is evidently connected to the spectrum of the turbulence that caused the parallel diffusion, although with some *caveats*. In particular, (i) $W(k) \sim k^{-\alpha}$, so the turbulent power is transferred isotropically to larger wave numbers, so to both directions $k_{\parallel}$ and $k_{\perp}$, (ii) besides, a typical use does not distinguish between D and $D_{\parallel}$. For what concerns the former, given the mutual orthogonal relation between the Alfvén and magnetosonic modes, their polarizations span the whole plane perpendicular to the perturbation wave number $\boldsymbol{k}$, if their spectra had the same statistics and equal intensities (Voelk, 1975). On the latter, it has been argued that the presence of magnetic fluctuations of very large scale ($L_{\delta B} \sim \mathcal{O}(100\,\mathrm{pc})$) tends to isotropize the CR diffusion in the Galaxy (Strong et al., 2007), so that the tensorial nature of the spatial diffusion coefficient D_{ij} can be approximately neglected.

In conclusion, Equation (1.61) can be used to *empirically* model the Galactic cosmic-ray diffusion. This is typically implemented in the numerical codes that compute the particle spectra propagated on Earth by solving the transport equation, such as `GALPROP`*, `DRAGON`†, `USINE`‡ or `PICARD` (Kissmann, 2014), while a seminal attempt to separate the parallel and perpendicular diffusion in a realistic Galactic magnetic-field structure has recently opened the way (Cerri et al., 2017a). Nonetheless, it is worth to recall that the expression above has been found assuming the smallness of magnetic fluctuations, and even though QLT has been proven to be a very good approximation to the exact solution for CR transport equation in a number of situations (Jokipii and Lerche, 1973), we will see in Section 1.3.4 that the use of Equations (1.58)-(1.59) involves intrinsic inaccuracies that must be revised.

1.3.3 The transport equation in physical space: the physics of parallel diffusion $D_{\parallel}$

We have seen in Section 1.3.2 that Equation (1.32) implies the isotropic behaviour of CR scattering against magnetic turbulence. This can be approached in a more physical way as in Kulsrud and Pearce (1969); Skilling (1971), where a solution for the transport equation is found by expanding the distribution function in powers of the scattering rate ν, such that $f_r = \mathcal{O}(\nu^{-r})$. With this procedure, it is explicitly shown that the isotropy statement is as stronger as larger the scattering rate is.

So the zeroth-order picture is that the waves act to make cosmic rays isotropic in the wave frame. To physically understand the next term of the expansion, we easily convince ourselves that any anisotropy

*`https://galprop.stanford.edu/`
†`https://github.com/cosmicrays/DRAGON`
‡`https://dmaurin.gitlab.io/USINE/`

would be caused by a net force exerted on the particle along its direction of motion ($\mu \approx 1$). We can then write:

$$f \to M + f_1 \mu, \tag{1.62}$$

where $M \equiv f_0$ is the isotropic average, such that $\frac{1}{2}\int_{-1}^{+1} d\mu\, f = \frac{1}{2}\int_{-1}^{+1} d\mu\, f_0 + \frac{1}{2}\int_{-1}^{+1} d\mu\, f_1 \mu \approx f_0 + 0$, as we are integrating an odd function in a symmetric interval.

Such force would be given by the induced electric field $\delta\boldsymbol{E}$ generated by the moving magnetic turbulence $\delta\boldsymbol{B}$, and its amount — estimated according to the Faraday's law mentioned above — is $|\delta\boldsymbol{E}| \sim v_A/c\,|\delta\boldsymbol{B}|$. In order for a particle to feel such $\delta\boldsymbol{E}$, it should move as slow as the wave, at the Alfvén speed v_A. This implies that we can expect a level of anisotropy of the order $\sim v_A/v_{\rm CR} \approx v_A/c$ (Blasi, 2018). For typical parameters of the ISM, $v_A \sim 10 - 100\,\mathrm{km/s}$, and this corresponds to an anisotropy amplitude of the order $\sim 10^{-3} - 10^{-4}$, which is confirmed by experimental observations (see Ahlers and Mertsch (2017) and reference therein).

In order to obtain the transport equation in the physical space, we first have to average over the pitch-angle distribution. So we start by applying the isotropic operator $\frac{1}{2}\int_{-1}^{+1} d\mu$ to Equation (1.32) and then proceed as described in Schlickeiser (1989); Shalchi (2006, 2009). This and alternative derivations are originally due to Earl (1973, 1974); Jokipii (1966a); Kulsrud and Pearce (1969).

The different terms of Equation (1.32) become:

$$\frac{1}{2}\int_{-1}^{+1} d\mu\, \frac{\partial f(z,t,\mu)}{\partial t} = \frac{1}{2}\frac{\partial}{\partial t}\int_{-1}^{+1} d\mu\, f(z,t,\mu) = \frac{\partial M(z,t)}{\partial t},$$

$$\frac{1}{2}\int_{-1}^{+1} d\mu\, v\mu\, \frac{\partial f(z,t,\mu)}{\partial z} = \frac{1}{2}v\frac{\partial}{\partial z}\int_{-1}^{+1} d\mu\, \mu f(z,t,\mu) = \frac{\partial}{\partial z}\left[\frac{1}{2}v\int_{-1}^{+1} d\mu\, \mu f(z,t,\mu)\right] \equiv \frac{\partial J(z,t)}{\partial z},$$

$$\frac{1}{2}\int_{-1}^{+1} d\mu\, \frac{\partial}{\partial \mu}\left(D_{\mu\mu}\frac{\partial f(z,t,\mu)}{\partial \mu}\right) = \frac{1}{2}\int_{-1}^{+1} d\left(D_{\mu\mu}\frac{\partial f(z,t,\mu)}{\partial \mu}\right) = D_{\mu\mu}\frac{\partial f}{\partial \mu}\bigg|_{-1}^{+1} = 0,$$

where we defined $J(z,t) \equiv \frac{1}{2}v\int_{-1}^{+1} d\mu\, \mu f(z,t,\mu)$ as a *current density* and used that $D_{\mu\mu} = 0$ for $\mu = \pm 1$ since $D_{\mu\mu} \propto (1-\mu^2)$, as seen in the previous section.

With these rearrangement we can write the *Fokker-Planck* equation as follows:

$$\begin{cases} \dfrac{\partial M(z,t)}{\partial t} + \dfrac{\partial J(z,t)}{\partial z} = 0 \\ J(z,t) = \dfrac{1}{2}v\displaystyle\int_{-1}^{+1} d\mu\, \mu f(z,t,\mu) \end{cases} \tag{1.63}$$

that, due to the definition of the current density $J(z,t)$, is a continuity equation for the isotropic part of the CR distribution function.

Still, there is a term with $f(z,t,\mu)$ that needs to be replaced. Besides, we cannot directly use Equa-

tion (1.63), as for large enough times ($t \to \infty$) it simply shows that there is no current for an isotropic CR distribution, which is trivial.

To extract an informative equation, we rewrite $J(z,t)$:

$$\begin{aligned} J(z,t) &= \frac{1}{2} v \int_{-1}^{+1} d\mu\, \mu f(z,t,\mu) \overset{\text{identity}}{=} -\frac{1}{2} \cdot \frac{1}{2} v \int_{-1}^{+1} d\mu\, \frac{\partial (1-\mu^2)}{\partial \mu} f(z,t,\mu) \\ &= -\frac{v}{4} \left\{ (1-\mu^2) f(z,t,\mu) \big|_{-1}^{+1} - \int_{-1}^{+1} d\mu\, (1-\mu^2) \frac{\partial f(z,t,\mu)}{\partial \mu} \right\} \\ &= +\frac{v}{4} \int_{-1}^{+1} d\mu (1-\mu^2) \frac{\partial f(z,t,\mu)}{\partial \mu}. \end{aligned} \tag{1.64}$$

We want to obtain the same expression from the *Fokker-Planck* equation (1.32). This will allow us to eliminate the complete distribution function $f(z,t,\mu)$. By applying the operator $\int_{-1}^{\mu} d\mu'$, the three terms become:

$$\int_{-1}^{\mu} d\mu' \, \frac{\partial f(z,t,\mu')}{\partial t} = \frac{\partial}{\partial t} \int_{-1}^{\mu} d\mu' f(z,t,\mu'),$$

$$\int_{-1}^{\mu} d\mu' \, v\mu' \frac{\partial f(z,t,\mu')}{\partial z} = v \frac{\partial}{\partial z} \int_{-1}^{\mu} d\mu' \, \mu' f(z,t,\mu'),$$

$$\int_{-1}^{\mu} d\mu' \, \frac{\partial}{\partial \mu'} \left(D_{\mu\mu} \frac{\partial (z,t,\mu')}{\partial \mu'} \right) = D_{\mu\mu} \frac{\partial f(z,t,\mu)}{\partial \mu} - \cancel{D_{\mu\mu} \frac{\partial f(z,t,\mu')}{\partial \mu'} \Big|_{-1}}.$$

To obtain the same $J(z,t)$ we multiply the three terms by $\frac{1-\mu^2}{D_{\mu\mu}}$:

$$\frac{1-\mu^2}{D_{\mu\mu}} \cdot \frac{\partial}{\partial t} \int_{-1}^{\mu} d\mu' \, f(z,t,\mu') + \frac{1-\mu^2}{D_{\mu\mu}} \cdot \frac{\partial}{\partial z} \int_{-1}^{\mu} d\mu' \, v\mu' f(z,t,\mu') = \frac{1-\mu^2}{\cancel{D_{\mu\mu}}} \cdot \cancel{D_{\mu\mu}} \frac{\partial f(z,t,\mu)}{\partial \mu}.$$

Finally, we average over the pitch-angle space:

$$\begin{aligned} \int_{-1}^{+1} d\mu \, \frac{1-\mu^2}{D_{\mu\mu}} \cdot \frac{\partial}{\partial t} \int_{-1}^{\mu} d\mu' \, f(z,t,\mu') + v \int_{-1}^{+1} d\mu \, \frac{1-\mu^2}{D_{\mu\mu}} \cdot \frac{\partial}{\partial z} \int_{-1}^{\mu} d\mu' \, \mu' f(z,t,\mu') \\ = \int_{-1}^{+1} d\mu \, (1-\mu^2) \cdot \frac{\partial f(z,t,\mu)}{\partial \mu} \equiv J(z,t) \cdot \frac{4}{v}, \end{aligned}$$

where the last step holds because of Equation (1.64).

We now want to extract the isotropic part of the distribution function — we have seen that it is the largest — namely we consider $t \to \infty$:

$$\frac{v}{4} \int_{-1}^{+1} d\mu \, \frac{1-\mu^2}{D_{\mu\mu}} \cdot \frac{\partial M(z,t)}{\partial t} \int_{-1}^{\mu} d\mu' + \frac{v^2}{4} \int_{-1}^{+1} d\mu \, \frac{1-\mu^2}{D_{\mu\mu}} \cdot \frac{\partial M(z,t)}{\partial z} \int_{-1}^{\mu} d\mu' \, \mu' = J(z,t)$$

and, by solving the two internal integrals on $d\mu'$, we get:

$$\frac{v}{4}\cdot\frac{\partial M(z,t)}{\partial t}\int_{-1}^{+1}d\mu\,\frac{(1-\mu^2)(1+\mu)}{D_{\mu\mu}}-\frac{v^2}{8}\cdot\frac{\partial M(z,t)}{\partial z}\int_{-1}^{+1}d\mu\,\frac{(1-\mu^2)^2}{D_{\mu\mu}}=J(z,t). \tag{1.65}$$

So we found an equation that relates the temporal and spacial dependencies of the CR isotropic distribution, which is then a form of *transport equation*. Therefore, we can define:

$$\begin{cases} D_{zt}\equiv\dfrac{v}{4}\displaystyle\int_{-1}^{+1}d\mu\,\frac{(1-\mu^2)(1+\mu)}{D_{\mu\mu}} \\ D_{zz}\equiv\dfrac{v^2}{8}\displaystyle\int_{-1}^{+1}d\mu\,\frac{(1-\mu^2)^2}{D_{\mu\mu}} \end{cases} \tag{1.66}$$

and write the above equation as follows:

$$J(z,t)=D_{zt}\frac{\partial M(z,t)}{\partial t}-D_{zz}\frac{\partial M(z,t)}{\partial z}. \tag{1.67}$$

From the continuity equation (1.63), we have that:

$$\frac{\partial M(z,t)}{\partial t}+\frac{\partial J(z,t)}{\partial z}=0\quad\Rightarrow\quad\frac{\partial M(z,t)}{\partial t}=-\frac{\partial J(z,t)}{\partial z}$$

and, by plugging in Equation (1.67):

$$\frac{\partial M(z,t)}{\partial t}=-\frac{\partial}{\partial z}\left(D_{zt}\frac{\partial M(z,t)}{\partial t}-D_{zz}\frac{\partial M(z,t)}{\partial z}\right).$$

The spatial variation of a function can be evaluated in terms of its temporal variation as $\frac{\partial}{\partial t}\sim v\frac{\partial}{\partial z}$, so that the factor v compensates for the difference in the factors $v/4$ and $v^2/8$ before the two coefficients D_{zt} and D_{zz}. Besides, looking at the integrand functions $(1-\mu^2)^2$ and $(1-\mu^2)\cdot(1+\mu)$, it easily shows that D_{zt} and D_{zz} are of the same order.

On the other hand, we can evaluate the two differential operators on the right-hand side. Due to the continuity equation, $\frac{\partial M(z,t)}{\partial t}=-\frac{\partial J(z,t)}{\partial z}$, and we are evaluating the variations $\frac{\partial M(z,t)}{\partial z}\sim\mathcal{O}(M/L_0)$ and $\frac{\partial J(z,t)}{\partial z}\sim\mathcal{O}(J/L_0)$ on a spatial scale where the isotropic part can appreciable change, *i.e.* $L_0\gg\lambda_{\text{m.f.p.}}$, where $\lambda_{\text{m.f.p.}}=v\tau$, $\tau\equiv T_{\mu\mu}\sim D_{\mu\mu}^{-1}$ being the time between one wave-particle scattering and the following one. This implies that in one L_0 length many scatterings have occurred, and the anisotropy generating the current density $J(z,t)$ had the time to rearrange to a near-equilibrium condition. For this reason, $D_{zt}\partial_t M\ll D_{zz}\partial_z M$, and we can approximate the transport equation as follows:

$$\frac{\partial M(z,t)}{\partial t}\simeq\frac{\partial}{\partial z}\left(D_{zz}\frac{\partial M(z,t)}{\partial z}\right). \tag{1.68}$$

Obviously, this rearrangement holds when the scattering between the cosmic rays and the waves is very frequent, implying a diffusive behaviour. This is why Equation (1.68) is referred to as a transport equation in *diffusion approximation* (Kirk et al., 1988).

We have seen that Equation (1.68) describes the CR transport in the reference frame of the turbulent waves. As a general rule of thumb, we can picture the ISM as filled with moving magnetized-plasma clouds, and inside those clouds there is a random distribution of turbulent waves, such as the Alfvén waves. In the reference frame of the waves — we call it $\mathcal{S}$ —, cosmic rays are traveling at a speed $v \approx c$, while the waves are propagating at a speed $\sim \pm v_A$ inside the plasma cloud moving at $\boldsymbol{u}$. Typically, we have seen that $v_A \sim 10 - 100\,\mathrm{km/s} \ll |\boldsymbol{u}|$ and, in turn $|\boldsymbol{u}| \ll v$, whereas in general $|\boldsymbol{u}| \not\ll v\mu$. As a final point then, we have to transform the quantities in Equation (1.32) from $\mathcal{S}$ to the reference frame of the Earth, that is moving with respect to the waves at a velocity $|\boldsymbol{u}| \pm v_A \approx |\boldsymbol{u}|$ — we call it $\mathcal{S}'$. Since $|\boldsymbol{u}| \ll v$, we will use the general Lorentz transformation in the Newtonian limit, accurate *modulo* $\mathcal{O}(u/c)^2$ (Webb and Gleeson, 1979). In formulas, when passing from $\mathcal{S}$ to $\mathcal{S}'$ we have:

$$f(\boldsymbol{r}, t, \mu) \to f'(\boldsymbol{r'}, \boldsymbol{p'}, t', \mu)$$

such that (Barone, 2004):

$$\begin{cases} x' = x \\ y' = y \\ z' = \gamma(z - ut) \\ t' = \gamma\left(t - \dfrac{u}{c^2} z\right) \end{cases} \qquad \begin{cases} p'_x = p_x \\ p'_y = p_y \\ p'_z = \gamma\left(p_z - \dfrac{u}{c^2} E\right) \\ E' = \gamma(E - u p_z) \end{cases}$$

where $\beta = u/c$, $\gamma = \frac{1}{\sqrt{1-(u/c)^2}} \approx 1$ and the only component of the momentum that gets transformed is the one along $\hat{\boldsymbol{z}}$, because we are assuming $\boldsymbol{u} \parallel \boldsymbol{B}_0$, since the plasma is magnetized.

The terms of the *Fokker-Planck* equation get transformed as follows:

$$\frac{\partial f'}{\partial t} = \frac{\partial f'}{\partial t'} \cdot \frac{\partial t'}{\partial t} = \frac{\partial f'}{\partial t'}\left(\gamma \frac{\partial f}{\partial t} - \frac{u}{c^2}\frac{\partial z}{\partial t}\right) \approx \frac{\partial f'}{\partial t'}\left[1 + \mathcal{O}\left(\frac{u}{c}\right)^2\right],$$

$v\mu \to (u + v\mu)$,

$$\frac{\partial f'}{\partial z} = \frac{\partial f'}{\partial z'} \cdot \frac{\partial z'}{\partial z} + \frac{\partial f'}{\partial p'_z} \cdot \frac{\partial p'_z}{\partial z} \approx \frac{\partial f'}{\partial z'} + \frac{\partial f'}{\partial p'_z} \cdot \frac{\partial p'_z}{\partial z},$$

where we are assuming $\frac{\partial p'_z}{\partial z} \neq 0$ since, in moving from the Galactic plane ($z = 0$) to the outer regions ($|z| > 0$), plasma clouds accelerate and expand. A consequence of this phenomenon is that the en-

ergy per particle inside the clouds decreases. Cosmic rays embedded in moving plasma are said to be *advecting* and the consequent energy losses are called *adiabatic losses* (Parker, 1965).

The *Fokker-Planck* equation then becomes:

$$\frac{\partial f'}{\partial t'} + (v\mu + u)\frac{\partial f'}{\partial z'} + (v\mu + u)\frac{\partial f'}{\partial p'_z}\frac{\partial p'_z}{\partial z} = \frac{\partial}{\partial \mu}\left(D_{\mu\mu}\frac{\partial f'}{\partial \mu}\right).$$

Looking at the Lorentz transformations, we have that $\frac{\partial p'_z}{\partial z} \approx -\frac{E}{c^2}\frac{\partial u}{\partial z}$, hence, up to order $\mathcal{O}(u/c)^2$, we have:

$$\frac{\partial f'}{\partial t'} + (v\mu + u)\frac{\partial f'}{\partial z'} - \frac{Ev}{c^2}\mu\frac{\partial f'}{\partial p'_z}\frac{\partial u}{\partial z} = \frac{\partial}{\partial \mu}\left(D_{\mu\mu}\frac{\partial f'}{\partial \mu}\right).$$

We have to evaluate the derivative $\frac{\partial f'}{\partial p'_z} \equiv \frac{\partial f'}{\partial p'_\parallel}$, where the direction $\parallel$ refers to the background field $\boldsymbol{B}_0$. In particular:

$$p'_\parallel = p'\mu, \quad \rightarrow \quad dp'_\parallel = \mu dp' + p' d\mu$$

so that:

$$\frac{\partial f'}{\partial p'_\parallel} = \frac{\partial f'}{\partial p'}\cdot\frac{\partial p'}{\partial p'_\parallel} + \frac{\partial f'}{\partial \mu}\cdot\frac{\partial \mu}{\partial p'_\parallel}.$$

To write $\frac{\partial p'}{\partial p'_\parallel}$ and $\frac{\partial \mu}{\partial p'_\parallel}$, we separate p' in its parallel and perpendicular component:

$$dp' = \mu dp'_\parallel + (1-\mu^2)^{\frac{1}{2}} dp'_\perp$$

and plug in this expression in the differential $dp'_\parallel$ above:

$$dp'_\parallel = \mu\left(\mu dp'_\parallel + (1-\mu^2)^{\frac{1}{2}} dp'_\perp\right) + p' d\mu \quad \Rightarrow \quad dp'_\parallel = \mu^2 dp'_\parallel + \mu(1-\mu^2)^{\frac{1}{2}} dp'_\perp + p' d\mu$$

$$\Rightarrow \quad d\mu = \frac{1-\mu^2}{p'} dp'_\parallel - \frac{\mu(1-\mu^2)^{\frac{1}{2}}}{p'} dp'_\perp.$$

From the above expressions we thus get:

$$\frac{\partial \mu}{\partial p'_\parallel} = \frac{1-\mu^2}{p'}, \qquad \frac{\partial p'}{\partial p'_\parallel} = \mu$$

$$\Rightarrow \quad \frac{\partial f'}{\partial p'_\parallel} = \frac{\partial f'}{\partial p'}\mu + \frac{\partial f'}{\partial \mu}\frac{1-\mu^2}{p'} \overset{f' \not\approx f'(\mu)}{\approx} \frac{\partial f'}{\partial p'}\mu.$$

So finally, the *Fokker-Planck* equation gets transformed as follows:

$$\frac{\partial f'}{\partial t'} + (v\mu + u)\frac{\partial f'}{\partial z'} - \mu^2\frac{\partial f'}{\partial p'}p'\frac{\partial u}{\partial z} = \frac{\partial}{\partial \mu}\left(D_{\mu\mu}\frac{\partial f'}{\partial \mu}\right), \tag{1.69}$$

where the factor p' in the adiabatic term comes from $Ev/c^2 \approx E/c = p$ and $p' \approx p$, as the two quantities

in that specific term would differ only at order $\mathcal{O}\left(u/c\right)^2$.

From the above equation, we want to obtain a transport equation in space, as we did with Equation (1.68). Applying exactly the same procedure as before we find that we only have to add the result coming from averaging the adiabatic term over the pitch-angle space — we can also notice that the first two terms are simply the total derivative of the distribution function:

$$\frac{1}{2}\int_{-1}^{+1} d\mu\, \mu^2 \frac{\partial f'}{\partial p'} p' \frac{\partial u}{\partial z} \approx \frac{1}{2}\frac{\partial u}{\partial z} p' \frac{\partial M}{\partial p'} \int_{-1}^{+1} d\mu\, \mu^2 = \frac{1}{3}\frac{\partial u}{\partial z} p' \frac{\partial M}{\partial p'}.$$

Therefore, within the same diffusion approximation discussed above, the transport equation takes the following definitive form:

$$\frac{\partial M}{\partial t} + u\frac{\partial M}{\partial z} - \frac{1}{3}\frac{\partial u}{\partial z} p \frac{\partial M}{\partial p} \simeq \frac{\partial}{\partial z}\left(D_{zz}\frac{\partial M}{\partial z}\right), \tag{1.70}$$

where we dropped the apices for clarity.

The above equation describes the propagation of charged — recall that pitch-angle scattering is an electromagnetic process — cosmic rays in an ordered background magnetic field — it is 1D — due to advection and diffusion, and affected by adiabatic losses originated by the moving clouds.

In conclusion, we have seen that once we know $D_{\mu\mu}$, that is directly related to the microphysics of the CR scattering against the turbulent waves, we also know the diffusion of particles in space. In particular, we explicitly showed that pitch-angle diffusion in phase-space implies a *parallel* diffusion in the real space. In words, cumulative changes in the particle pitch-angle μ — hence in the particle velocity-component parallel to $\boldsymbol{B}_0$ — can ultimately result in the particle reversing its direction, leading to spatial diffusion. On the other hand, due to the computed $D_{\mu\mu}$, very small changes affect the transverse direction of the gyration centers, resulting in a very small spatial transverse motion (Jokipii, 1966a; Voelk, 1975).

1.3.4 Limitations of the QLT

The derivation's steps we went through in the previous sections highlighted that the pitch-angle scattering coefficient $D_{\mu\mu}$ in Equations (1.58)-(1.59) and the parallel diffusion coefficient $D_{\parallel}$ in Equation (1.61) rely on the assumption of small magnetic fluctuations ($\delta\boldsymbol{B} \ll \boldsymbol{B}_0$) and transversely oscillating turbulent waves — the transverse direction taken with respect to the particle velocity $v_{\parallel}$. As a consequence and more general perspective, we therefore expect *quasi-linear theory* to give a good description of CR transport *only* in the case of what is referred to as purely *slab* turbulence. This conclusion is supported by a number of inconsistencies that are well known when treating cosmic ray transport with QLT (Mertsch, 2020; Shalchi, 2005):

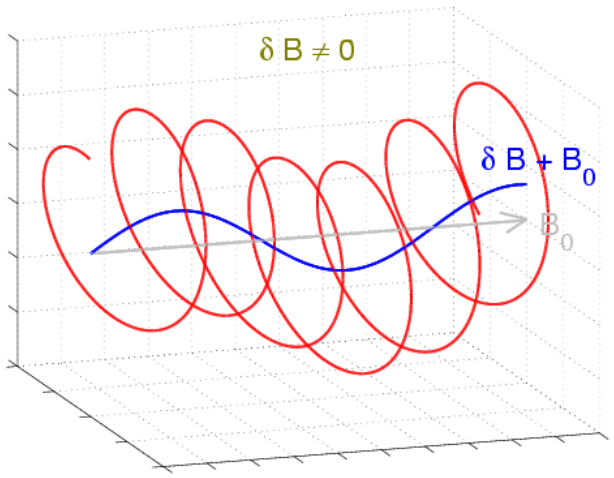

Figure 1.9: Diffusion of a charged particle due to a perturbation field $\delta\boldsymbol{B}$, without neglecting the perpendicular terms in the diffusion equation. The guiding center displacement is evident.

1. The 90° problem: due to the resonant condition in Equation (1.59), we see that particles with pitch-angle close to $\mu \approx 0$ ($k_{\rm res} = \Omega/(v\mu) \to \infty$) can only interact with extremely large wavenumbers. Given the scaling of turbulent power spectra ($W(k) \sim k^{-\alpha}$), high k's typically contain very little energy, which would imply an inefficient scattering around that direction. This is of course in large tension with the observed highly isotropic propagation of CRs in the Galaxy.

2. The problem of perpendicular diffusion $D_\perp$: pitch-angle scattering through QLT only describes parallel diffusion, while it has been shown in Jokipii and Parker (1969a,b) that, for $|\delta\boldsymbol{B}| \sim |\boldsymbol{B}_0|$, the random walk of the magnetic field lines could be the main responsible for particle transport, and it would act in the direction perpendicular to the background field $\boldsymbol{B}_0$. Specifically, neglecting D_{xx} and D_{yy}, we are ignoring the motion sketched in Figure 1.9.

3. The geometry problem: QLT predictions on particle diffusion are in tension with the simulations when *non-slab* turbulence geometry is considered. It seems likely that this and the previous issue are strongly related.

One of the significant implications of the assumptions mentioned above is that, up to zeroth-order in $\mathcal{O}(v_A/c)$, the distribution function resulting from the *Fokker-Planck* equation is isotropic, $f \approx M + f_1\mu$. Ignoring higher-order corrections implies that we are turning off any possibility of energy exchange between the particle and the wave. In particular, at order $\mathcal{O}(v_A/c)$, we are neglecting the effect of the momentum *Fokker-Planck* coefficient D_{pp}, as seen in Section 1.3.3, which is responsible for the process known as *reacceleration*, that it will be discussed in Section 2.2.1. Further, at order $\mathcal{O}(v_A/c)^2$, the second-order Fermi acceleration would occur, as discussed in Section 1.2.1. Besides, at the same order, in Kulsrud and Pearce (1969); Lerche (1967); Wentzel (1968) the wave-particle energy

exchange is calculated, according to the following rate:

$$\Gamma_{\boldsymbol{k}} = 2\pi^2 q^2 \left(\frac{v_A}{c}\right)^2 \sum_{n=-\infty}^{+\infty} \int d^3\boldsymbol{p}\, v_\perp^2\, \delta(\omega_{\boldsymbol{k}} - k_\parallel v_\parallel - n\Omega) \left\{ \begin{array}{c} J_n'^2(w) \\ \dfrac{n^2 J_n^2(w)}{w^2} \end{array} \right\} \left[\frac{\partial F}{\partial E} + \frac{k_\parallel}{\omega_{\boldsymbol{k}} p} \frac{\partial F}{\partial \mu}\right], \tag{1.71}$$

where the first and second rows in the curly braces refer to the magnetosonic and Alfvén modes, respectively, and again $w \equiv \frac{k_\perp v \sqrt{1-\mu^2}}{\Omega}$.

The first term in the square brackets is the slope of the distribution function with the particle-energy, and it is negative for typical CR spectra $F \sim E^{-\gamma}$. On the other hand, the second term depends on the CR anisotropy, which is small but is highly enhanced by the factor $\frac{k_\parallel}{\omega_{\boldsymbol{k}} p}$, that, after a few rearrangements of the integrand, is seen to be of the order $kv/\omega \sim c/v_A$. This implies that the quantity $\Gamma_{\boldsymbol{k}}$ can be a *growth* or a *damping* rate, depending on the sign of $\frac{\partial F}{\partial \mu}$. Intuitively speaking, traveling CRs can interact with waves moving along the same direction, exchanging energy with them. In the opposite direction, we have the same behaviour, as both CRs and waves are roughly isotropically distributed. However, from a statistical point of view, particles have less energy than waves, leading to an overall small damping for the waves*. This is the so-called *linear Landau damping* (Landau, 1946). If an anisotropy is present in the CR distribution, there is no longer compensation, creating an instability for the propagating wave. This phenomenon is commonly referred to as *streaming instability* of the waves.

From the above considerations, corrections due to CR feedback mechanisms on the waves should be taken into account. In Shalchi et al. (2004), a non-linear extension of the CR transport is derived, called *weakly non-linear theory*. This approach is able to solve the issues 2-3, without however affecting the pitch-angle dependence of diffusion. Therefore, this argument is complementary to the study of the 90° problem. In Felice and Kulsrud (2001), the authors show how this can be solved by considering the action of a mirroring force between the particle and the scattering wave. An empirical approach is discussed in Voelk (1975); Völk (1973), where a function describing the particle-wave resonance is proposed, based on this mirroring force exerted specifically by magnetosonic modes. An extension of this idea is contained in a series of paper (Yan and Lazarian, 2002a, 2004, 2008) where parallel and perpendicular diffusions are treated in a specific turbulent geometry supported by simulations, and where scattering at 90° does not even need any particular treatment. Even though this could be ascribed as a non-systematic derivation, the recent identification of such plasma modes in Galactic turbulence (Zhang et al., 2020a) certainly represents an important step for the validation of the theory.

*This is a consequence of the *Maxwell-Boltzmann* distribution of the velocities of the plasma-particles of an ideal MHD plasma and the resonant nature of the CR-wave interaction. In fact, while the plasma-particle's velocities peak around a certain value, CR spectra decrease with energy, so that there are less higher-energy resonant CRs than lower-energy ones, with reference to the resonant energy. Hence, on a statistical basis, plasma waves give CRs more energy than what they gain from them.

In Chapter 5 we will adopt this interpretation and describe how CR propagation can change. In particular we will see that, under these conditions, the cosmic-ray spatial diffusion coefficient may not be a single power-law.

1.4 Summary of the chapter

In this chapter, we have introduced the experimental and theoretical setup that will be exploited throughout the thesis. We have shown the key experimental observations that make us conclude that cosmic rays diffuse in the *interstellar medium*, and we pointed towards Supernova Remnants as the main responsible for CR origin. Then, we described the most accredited acceleration mechanism, namely the *diffusive shock acceleration* at shock events, where discontinuities in the medium — caused by the propagating shock-front — are responsible for the bouncing process that enhances the energy of the particles that are trapped in the shock. For what concerns the transport of the cosmic rays across the Galaxy we have seen that, due to the random nature of the magnetic irregularities, a statistical treatment of the distribution function is required, which led to the famous *Fokker-Planck* equation (1.25) — this is an equation in momentum space. In order to have a practical expression for the *Fokker-Planck* coefficients, we specified the nature of the interaction of CRs with the turbulent waves, by means of the particle's equations of motion, and the nature of the scattering centers. For the latter, in particular, we solved the MHD equations and found three different propagation modes — *Alfvén* mode, *fast* and *slow magnetosonic* mode. Within this picture, we derived Equation (1.32) — an equation in pitch-angle space and in the reference frame of the wave — in the framework of the so-called *quasi-linear theory*. This equation implies the isotropic behaviour of the distribution function in the pitch-angle μ, thus the diffusive nature of cosmic-ray propagation. In order to discuss all the assumptions on which this equation relies, we derived the same *Fokker-Planck* equation in a more rigorous way, which let us find an explicit expression for the largest *Fokker-Planck* coefficient, $D_{\mu\mu}$. Then, we found a transport-equation in physical space and in the Earth reference frame, deriving an expression for the parallel diffusion coefficient $D_{\parallel}$. Finally, re-examining all the assumptions made during the previous treatments, we argued the limitations of the presented QLT in terms of particle-wave energy exchange.

2

Implementation in the DRAGON code and multi-messenger implications

In this chapter, we aim at giving an exhaustive presentation of the series of processes occurring to cosmic-ray particles propagating through our Galaxy. In fact, while Chapter 1 was entirely dedicated to the study of the transport equation for hadrons in a *diffusive regime*, we remark that this is only valid above an energy of about $E \geq 1\,\mathrm{GeV}$. At lower energies, for instance, CRs get trapped in interstellar winds and get advected by them, as a dominant transport process. Besides, the transport equation derived before does not take into account the hadronic interactions of CRs with particles of the interstellar gas. In dense media, in fact, CR nuclei scatter off particles of the clouds and break apart to give smaller nuclei (a process known as *spallation*), or can give rise to hadronic showers. On the other hand, for what concerns leptons, their massive energy losses further reduce the range of applicability of the pure *diffusive regime* and loss terms must be added to the equation at all energies. All of these phenomena have to be taken into account — as they shape the CR spectra observed on Earth — significantly complicating the propagation equation for CR particles. Here we present the DRAGON numerical solver for the transport equation and discuss the astrophysical ingredients implemented in it, with particular reference to the configuration that will be used throughout this thesis. Finally, we give an overview of the implications that CR propagation has on detectable secondary γ-rays and ν's.

2.1 DRAGON: A GENERAL OVERVIEW

It was pointed out in Section 1.1 how the remarkable progress achieved in the last decade of cosmic-ray measurements has revealed a series of observational anomalies. As introduced above, a number of effects contribute to the shaping of the measured CR spectra, in their hadronic as well as leptonic components. In this context, therefore, it would be necessary to introduce in the transport equation the distribution of the gas that CRs are traveling in. As a consequence, searching for an *analytical* solution of the transport equation would require a set of oversimplifying assumptions, not allowing to reproduce the observations with the necessary accuracy. Therefore, the use of sophisticated numerical codes is clearly of paramount importance to study the propagated spectra. In what follows, we refer to the DRAGON technical papers Evoli et al. (2008); Evoli et al. (2017a); Evoli et al. (2018b); Maccione et al. (2011) to introduce the main features of the code.

The usual starting point is the phenomenological equation that extends the spatial transport equation derived in Chapter 1 — Equation (1.70) — to capture CR diffusion in space and momentum, energy losses, advection, re-acceleration, nuclear spallation and decay (Berezinsky et al., 1990; Ginzburg and Syrovatskii, 1964b):

$$\begin{aligned} \boldsymbol{\nabla} \cdot (D\, \boldsymbol{\nabla} N_i - \boldsymbol{u}_w N_i) + \frac{\partial}{\partial p}\left[p^2 D_{pp}\, \frac{\partial}{\partial p}\left(\frac{N_i}{p^2}\right)\right] - \frac{\partial}{\partial p}\left[\dot{p} N_i - \frac{p}{3}\,(\boldsymbol{\nabla}\cdot\boldsymbol{u}_w)\, N_i\right] = \\ S + \sum_{j>i}\left(c\beta n_{\rm gas}\,\sigma_{j\to i} + \frac{1}{\gamma\tau_{j\to i}}\right) N_j - \left(c\beta n_{\rm gas}\,\sigma_i + \frac{1}{\gamma\tau_i}\right) N_i, \end{aligned} \tag{2.1}$$

where $N_i(\boldsymbol{r}, p)$ is the particle spectrum density of the i species in units $[N_i] = [L]^{-3}\cdot[p]^{-1}$ — this quantity is connected to the phase-space density introduced in Chapter 1 by $N_i(p)dp = 4\pi p^2 f_i(\boldsymbol{p})dp$ —, D_{pp} is the momentum diffusion coefficient, $D \equiv D_{ij}$ is the spatial diffusion tensor, $\boldsymbol{u}_w(\boldsymbol{r})$ is the wind velocity, responsible for CR advection, and $S(\boldsymbol{r}, p)$ a term describing the distribution of the CR sources. Still unknown quantities are:

- a term proportional to $\dot{p}$, that accounts for momentum losses,
- two terms describing spallation of a CR nucleus with the interstellar gas of density $n_{\rm gas}$, creating a lighter nucleus: one contributing to the species i with probability proportional to the cross-section $\sigma_{j\to i}$ of the single process $j \to i$ summed over the possible j ($+\sum_{j>i} c\beta n_{\rm gas}\,\sigma_{j\to i}\,N_j$); the other one, reducing the particle density N_i, proportional to the cross-section σ_i of the *inclusive* process $i \to$ {everything else} ($-c\beta n_{\rm gas}\,\sigma_i\,N_i$). For the nuclear cross-section tables, here we implement the GALPROP setup, as described in Evoli et al. (2018b), while for the production of secondary leptons in pp interaction, we use the implementation from Kamae et al. (2006). Alter-

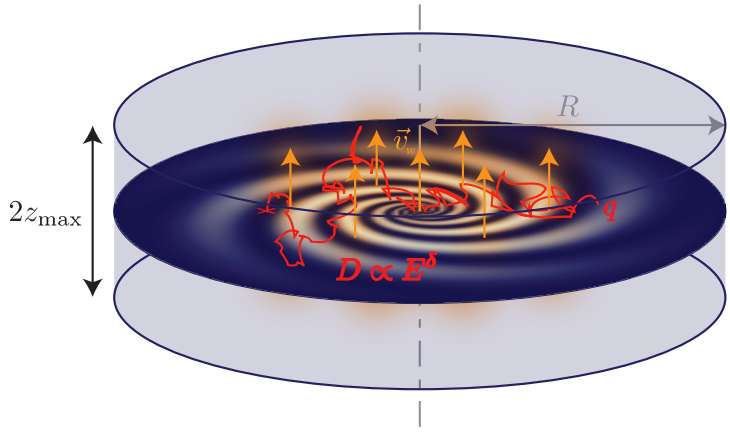

Figure 2.1: A 2D configuration of a Galaxy with cylindrical symmetry, with a thin dense disk surrounded by a much larger fainted halo of vertical size $2z_{\rm max}$. The advection velocity is indicated as directed away from the disk and a typical CR diffusion path is pictured.

native compilations are also possible, although we verified that lead to negligible changes.

- Two terms accounting for: the nuclear decay of a nucleus $j > i$ on a time scale $\tau_{j\to i}$, increasing the N_i; the destruction of the nucleus of the species i on a time scale τ_i.

These processes will be discussed in Section 2.2, as well as all the necessary modelizations of the astrophysical ingredients. The equation above is evaluated at steady state $\partial_t N_i = 0$.

Galactic structure. Equation (2.1) can be solved in DRAGON in a $(2+1)$-dimensional (2D) or $(3+1)$-dimensional (3D) configuration, where the extra dimension regards for the particle energy. The 2D case pictures a Galaxy with azimuthal ($\equiv$ cylindrical) symmetry, where the cylinder axis is perpendicular to the thin-disk region, while in the 3D configuration the spiral arms are resolved. The results on the diffuse component of the cosmic-rays presented in Part II and Part III of the present thesis are carried out on Galactic scales, for which it is reasonable to reduce to azimuthal symmetry, according to which, in the system of cylindrical coordinates (r, ϕ, z), we set $\partial_\phi N_i = 0$. This is sketched in Figure 2.1: the dense disk has typical half-size $z_{\rm d} \sim 0.1\,{\rm kpc}$ and the fainted halo $z_{\rm H} \sim 4\,{\rm kpc}$, while their radius is typically as large as $R_{\rm d,H} \sim 20\,{\rm kpc}$. Details on their modeling will be discussed in Section 2.2.

Overall magnetic-field structure. For what concerns the large-scale magnetic-field structure, it basically reflects the Galactic geometry, with concentric circles piled up (but exponentially decreasing at larger latitudes) along the cylinder axis and a vertical component (Cerri et al., 2017a; Jansson and Farrar, 2012). This is pictured in Figure 2.2a, where the vertical magnetic field lines dense up towards the Galactic bulge ($X, Y < 2.9\,{\rm kpc}$) and thin out in the outer regions ($X, Y \geq 5\,{\rm kpc}$). As a consequence, it is in general appropriate to consider a vertical component for $\boldsymbol{B}$ that vanishes going further away from

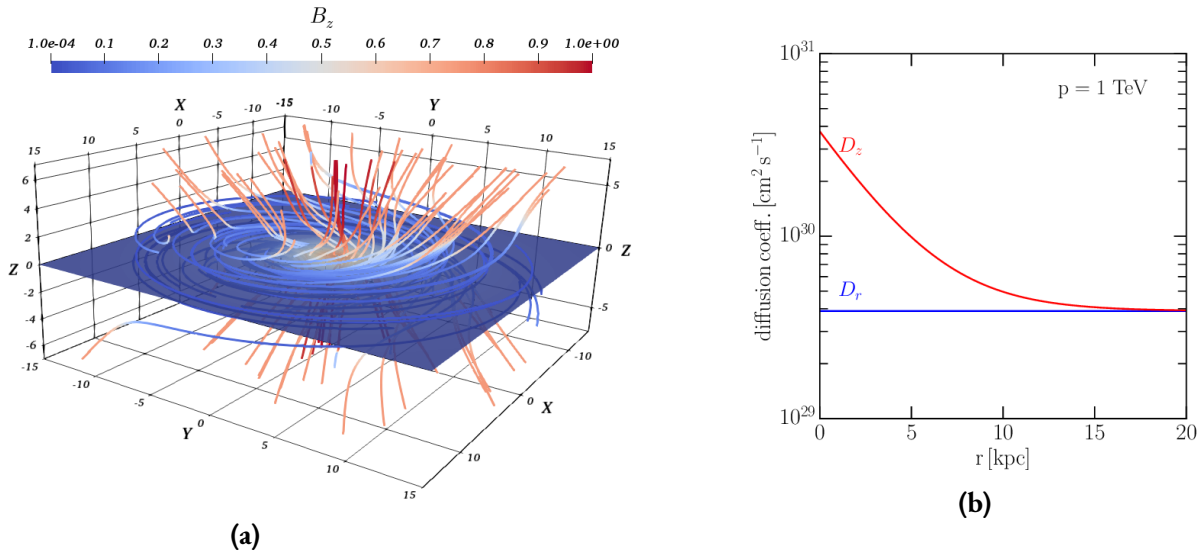

(a) **(b)**

Figure 2.2: **(a)** A realistic configuration of the Galactic magnetic field is pictured, with the magnetic field lines directed along the azimuthal component, and a vertical component significantly contributing around the Galactic center. Figure from Cerri et al. (2017a). **(b)** Typical perpendicular diffusion coefficients reflecting a Galactic magnetic disk with a denser vertical component at low longitudes, for a CR momentum $p = 1\,\mathrm{TeV}$. Figure from Evoli et al. (2017a).

the Galactic center, *e.g.* exponentially:

$$\begin{aligned} D_{rr} &= D_\perp(r,p) \\ D_{zz} &= D_\perp(r,p) + D_\parallel(r,p) = D_\perp(r,p) + e^{-r} D_\parallel(p). \end{aligned} \tag{2.2}$$

This is shown in Figure 2.2b, where the phenomenological parametrization is taken from De Marco et al. (2007). Due to our location inside the Milky Way ($R_\odot = 8.3\,\mathrm{kpc}$), for the problems studied in this work we are going to assume an azimuthal-only magnetic field ($\boldsymbol{B} = B\hat{\phi}$) such that in Equation (2.1) $D_{rr} = D_{zz} \equiv D_\perp$ and $D_\parallel$ plays no role, as it would appear only connected to $\partial_\phi N_i = 0$. Coupled to the assumed 2D configuration, this corresponds to the following substitution in Equation (2.1):

$$\boldsymbol{\nabla} \cdot D\boldsymbol{\nabla} N_i \;\rightarrow\; D_{rr}(r,z,p)\frac{\partial^2 N_i}{\partial r^2} + D_{zz}(r,z,p)\frac{\partial^2 N_i}{\partial z^2} + \chi(r,z,p)\frac{\partial N_i}{\partial r} + \psi(r,z,p)\frac{\partial N_i}{\partial z}$$

$$\chi(r,z,p) = \frac{D_{rr}(r,z,p)}{r} + \frac{\partial D_{rr}(r,z,p)}{\partial r}$$

$$\psi(r,z,p) = \frac{\partial D_{zz}(r,z,p)}{\partial z}$$

$$D_{rr} = D_{zz} \equiv D_\perp.$$

Incidentally, this approximation is likely at the origin of the so-called *gradient problem*, namely

the well known discrepancy (for $E_\gamma \geq 100\,\mathrm{MeV}$) between the theoretical CR-flux profile obtained by assuming SNRs to be the sources of Galactic CRs and that inferred from the EGRET (Hunter et al., 1997) and *Fermi*-LAT (Abdo et al., 2010; Ackermann et al., 2011) γ-ray diffuse observations. In fact, neglecting the parallel component $e^{-r}D_\parallel(p)$ of the diffusion coefficient in Equation (2.2) causes a longer residence time (*i.e.* less-efficient diffusion) — with respect to the exact spatial $D(p)$ parametrization — of the particles around the Galactic center, resulting in a larger production of photons. Requesting the normalization of the CR source term at our position in the Galaxy eventually leads to a sharper longitudinal profile. We would expect to find a solution in a framework of anisotropic diffusion.

As anticipated in Chapter 1, it is a common practice to assume an isotropization mechanism for the transport, due to large-scale fluctuations of the magnetic field, which allows us to consider $D_\perp \approx D_\parallel \equiv D(r,z,p)$ and adopt the phenomenological parametrization in Equation (1.61), inspired by the results of the *quasi-linear theory*, with the free parameters typically fitted over the data (Strong et al., 2007):

$$D(r,z,p) = D_0 \left(\frac{p}{p_0}\right)^\delta g(r,z), \tag{2.3}$$

where the spatial dependence is assigned to the function g. The results presented in Part II are based on a homogeneous diffusion, thus with $g(r,z)=1$, while Part III considers a two-zone model where CR diffusion in the halo and in the disk is caused by different mechanisms. In this case, the parametrization above does not hold any longer, as $D(r,z,p)$ will not be separable in momentum and space.

Discretization procedure. Equation (2.1) is linear in the unknown function, therefore can be split in a set of linear operators to be evaluated separately. The general solution for each species will be therefore the sum of the particular solutions of the set of equations. This method is referred to as *Local One Dimensional operator splitting*. The basic idea is to consider the equation in its time-dependent version:

$$\frac{\partial N_i}{\partial t} = \sum_l \mathcal{L}_l(N_i) + S, \tag{2.4}$$

where we denoted with $\mathcal{L}_l$ the l-th linear operator, then to give an *ansatz* for the initial condition and finally to evolve iteratively until an equilibrium situation is reached, which corresponds to the stationary condition of the original Equation (2.1). With this approach, each linear operator can be independently discretized.

In Equation (2.4), for each node of the space-energy grid we have $\frac{\partial N_i}{\partial t} \to \frac{N_i^{n+1}-N_i^n}{\Delta t}$, where $(n,\, n+1)$ are nodes of the time grid, therefore we have to choose whether the differential operators on the right-hand side have to evaluated at the time-node n or $n+1$. A third option is to consider the mean value of the two. The DRAGON code is based on this discretization scheme, which is known as *Cranck-Nicholson*

method (Press et al., 2002).

2.2 Astrophysics in DRAGON

This section is dedicated to the astrophysical modeling of the code configuration used in the present work. For all the alternative choices, the reader can refer to the technical papers cited above.

2.2.1 Parametrization of the interstellar environment

Gas distribution. As mentioned in the previous section, modelization of the interstellar gas is of paramount importance for its interaction with cosmic-ray particles, which gives rise to energy losses, caused by particle-scattering, and to secondary-particle production. Interstellar gas is mostly composed by hydrogen and helium, in proportions $[He]/[H] \simeq 0.11$ (Grevesse et al., 1996). Hydrogen, in turn, is present in form of atomic (HI), ionized (HII) and molecular (H_2) gas, HI and H_2 being the most abundant.

The HI is distributed as in Strong and Moskalenko (1998):

$$n_{HI}(r,z) = n_{HI}(r) \cdot \exp\left[-\frac{\log 2}{(z/z_0(r))^2}\right], \tag{2.5}$$

where $n_{HI}(r)$ is taken from Gordon and Burton (1976) and the parameter z_0 from Cox et al. (1986):

$$z_0(r) = \begin{cases} 0.25\,\mathrm{kpc} & r \leq 10\,\mathrm{kpc} \\ 0.083\,e^{0.11r}\,\mathrm{kpc} & r > 10\,\mathrm{kpc}. \end{cases}$$

The ionized hydrogen (HII) is composed by two terms (Cordes et al., 1991):

$$n_{HII}(r,z) = 0.025\,\exp\left[-\frac{|z|}{1\,\mathrm{kpc}} - \left(\frac{r}{20\,\mathrm{kpc}}\right)^2\right] + 0.2\,\exp\left[-\frac{|z|}{0.15\,\mathrm{kpc}} - \left(\frac{r}{2\,\mathrm{kpc}} - 2\right)^2\right]\mathrm{cm}^{-3}, \tag{2.6}$$

where the first term represents the *warm ionized medium* (WIM) and the second term is a distribution peaked around $r = 4\,\mathrm{kpc}$. This modelization is specifically derived for a distribution of free electrons in a cylindrically symmetric Galaxy, as we are assuming here.

Molecular hydrogen is not directly observable due to its long-lifetime decay ($\tau_{\mathrm{decay}} \sim 100\,\mathrm{yr}$) and hardly-excited transitions (at temperature $T \sim 100\,\mathrm{K}$), but it is traced by means of the observation of other molecules that are in a mixture with it. In particular, the most abundant one is the $^{12}C^{16}O$ — hereinafter simply referred to as CO — for which the $2.6\,\mathrm{mm}$ emission line is observed, corresponding

to the $J = 1 \to 0$ angular-momentum transition. The relevant factor to estimate the H_2 is therefore the CO-to-H_2 conversion factor at each point of the Galaxy, commonly called X_{CO}:

$$n_{H_2}(r) = X_{CO}(r) \cdot W(^{12}C^{16}O, J = 1 \to 0), \tag{2.7}$$

where $[n_{H_2}] = \mathrm{cm}^{-2}$ is the *column density*, $[W(CO)] = \mathrm{K} \cdot \mathrm{km\,s}^{-1}$ is the *integrated line intensity* and X_{CO} is in general a function of the longitudinal (radial) coordinate. Here we use for the Milky Way disk the value $X_{CO} = 1.9 \cdot 10^{20}\,\mathrm{cm}^{-2}/(\mathrm{K} \cdot \mathrm{km\,s}^{-1})$, consistent with the value inferred in Bolatto et al. (2013), and a uniform longitudinal profile (Strong and Mattox, 1996). The H_2 distribution is then taken as follows (Bronfman et al., 1988):

$$n_{H_2}(r, z) = n_{H_2}(r) \cdot \exp\left[-\frac{\log 2}{(z/70\,\mathrm{pc})^2}\right], \tag{2.8}$$

where n_{H_2} results from Equation (2.7).

Magnetic field model. The knowledge of the magnetic field structure in the code significantly affects the energy losses that leptons undergo during their wandering in the Galaxy. Measurements of the Galactic magnetic field are mainly based on the observation of the *rotation measures** of the polarized light and on leptonic synchrotron emission, the latter especially to infer its vertical extent. Typically, the total field is parametrized separating a regular and a turbulent (*random*) component, that are treated independently (see *e.g.* for a review on the topic Beck et al. (1996).)

The regular component is in turn separated into the field in the disk and in the halo. In the disk, the magnetic field is parametrized in cylindrical coordinates as follows (Sun et al., 2008):

$$\begin{cases} B_r^{\mathrm{d}} = D_1(r, \phi, z),\ D_2(r, \phi, z)\ \sin p \\ B_\phi^{\mathrm{d}} = -D_1(r, \phi, z),\ D_2(r, \phi, z)\ \cos p \\ B_z^{\mathrm{d}} = 0, \end{cases} \tag{2.9}$$

where $p = \arctan\left(\frac{B_r^{\mathrm{d}}}{B_\phi^{\mathrm{d}}}\right)$ is called *pitch-angle* and $(D_1,\ D_2)$ regulate $\boldsymbol{B}$ spatial variations, including possible reversal and asymmetries. Their parametrization and values are given as in Pshirkov et al. (2011), in particular $B_0^{\mathrm{d}} = 2\,\mu\mathrm{G}$.

In the halo, the magnetic field structure is a double-torus in one half of the Galaxy and the reversed

*When a source at distance d emits linearly-polarized light, at wavelength λ, this can be decomposed into two opposite-polarized circular waves, that gain a phase difference when passing through the magnetized plasma, $\Delta\phi_{\mathrm{obs}} \propto \lambda^2$ (*Faraday rotation*). The proportionality factor depends on the strength of the magnetic field and is called *Rotation Measure* (RM): $RM = 0.81 \int_0^d dl\, n_e(l) B_\parallel(l)$, where $[n_e] = \mathrm{cm}^{-3}$ is the electron density along the *line-of-sight* and the field is given in $[B_\parallel] = \mu\mathrm{G}$ (Sun et al., 2008).

direction in the other half (Prouza and Šmída, 2003; Pshirkov et al., 2011; Sun et al., 2008):

$$B_\phi^{\rm H} = B_0^{\rm H}\left[1+\left(\frac{|z|-z_0^{\rm H}}{z_1^{\rm H}}\right)^2\right]^{-1}\cdot\frac{r}{R_0^{\rm H}}\exp\left(1-\frac{r}{R_0^{\rm H}}\right), \tag{2.10}$$

where $B_0^{\rm H}=4\,\mu$G, $R_0^{\rm H}=4\,$kpc, $z_0^{\rm H}=1.5\,$kpc and $z_1^{\rm H}=0.2\,$kpc $(0.4\,$kpc$)$ for $|z|<z_0^{\rm H}$ $(|z|\geq z_0^{\rm H})$.

The turbulent component is poorly constrained, but observations disfavor a correlation with the regular field (Beck, 2001), hence we implement the simplest possible azimuthally-symmetric configuration (Sun et al., 2008):

$$B_{\rm turb}(r,z) = B_{\rm turb,0}\exp\left(-\frac{r-R_\odot}{R_B}\right)\exp\left(-\frac{|z|}{z_B}\right), \tag{2.11}$$

where $B_{\rm turb,0}=7.5\,\mu$G, $R_B=6\,$kpc and $z_B=2\,$kpc.

The Interstellar Radiation Field. The Galactic environment is filled with electromagnetic radiation generated in processes of different nature. This goes under the name of *Interstellar Radiation Field* (ISRF) and has therefore different components, such as thermal emission from starlight and from the dust injected by galaxies, γ-rays emitted by traveling cosmic rays, and the background radiation composed by the *Cosmic Microwave Background* (CMB), *Infrared Radiation* (IR), *optical radiation* and *Ultra-Violet radiation* (UV). Accurate knowledge of the ISRF is important as these low-energy photons constitute the targets for high-energy CRs to scatter off via the *Inverse Compton* (IC) process. Here, we adopt the modelization described in Porter and Strong (2005), which is based on a realistic distribution of stars and dust in our Galaxy.

The source term. We assume that the bulk of cosmic rays in the Milky Way gets accelerated and injected by Supernova Remnants (Blasi, 2013). The phenomenological parametrization of the source term takes the following form:

$$S(r,z,\rho) = S_0\,\mathcal{R}_{\rm SN}(r,z)\Phi_{\rm inj}(\rho)e^{-\frac{\rho}{\rho_c}}, \tag{2.12}$$

where S_0 is a normalization factor, $[\mathcal{R}_{\rm SN}(r,z)]=L^{-3}\cdot T^{-1}$ is the rate per unit volume of SN explosions in the Milky Way, $\Phi_{\rm inj}(\rho)$ is the injection spectrum and ρ_c is the cutoff rigidity.

In our runs, we consider the rates of explosion of SNe of type I and II as parametrized in Ferriere

(2001) as a function of the Galactic latitude z:

$$\begin{aligned}
\mathcal{R}_{\rm I}(r,z) &= \left(7.3\,{\rm kpc}^{-3}\,{\rm Myr}^{-1}\right)\cdot e^{-\frac{r-R_\odot}{4.5\,{\rm kpc}}-\frac{|z|}{0.325\,{\rm kpc}}} \\
\mathcal{R}_{\rm II}^{\rm in}\Big|_{r\leq 3.7\,{\rm kpc}}(r,z) &= \left(177.5\,{\rm kpc}^{-3}\,{\rm Myr}^{-1}\right)\cdot\left\{0.79\,e^{-\left(\frac{|z|}{0.212\,{\rm kpc}}\right)^2}+0.21\,e^{-\left(\frac{|z|}{0.636\,{\rm kpc}}\right)^2}\right\}\cdot e^{\left(-\frac{r-3.7\,{\rm kpc}}{2.1\,{\rm kpc}}\right)^2} \\
\mathcal{R}_{\rm II}^{\rm out}\Big|_{r>3.7\,{\rm kpc}}(r,z) &= \left(50\,{\rm kpc}^{-3}\,{\rm Myr}^{-1}\right)\cdot\left\{0.79\,e^{-\left(\frac{|z|}{0.212\,{\rm kpc}}\right)^2}+0.21\,e^{-\left(\frac{|z|}{0.636\,{\rm kpc}}\right)^2}\right\}\cdot e^{\left(-\frac{r-R_\odot}{6.8\,{\rm kpc}}\right)^2}.
\end{aligned} \tag{2.13}$$

In this parametrization, type-II SNe are traced by the HII regions or by pulsars, while type-I SNe follow the distribution of old stars found in the Galactic disk.

The injection spectrum $\Phi_{\rm inj}(\rho)$ that we use is assumed to be the same for each source and follows a multiply broken power-law, where the position of the break and the slope in each rigidity-interval are chosen by the user.

Stochastic reacceleration of cosmic-rays. The process known as *reacceleration* or, alternatively, *distributed acceleration*, is the exchange of energy between particles and turbulent waves, and it is a process of order $\mathcal{O}(v_A/c)$, thus not present in pure QLT expressions, as discussed in Section 2.2.1. Observational evidence tells us that it cannot be the main mechanism responsible for particle acceleration in the Galaxy, at least in the energy range $1\,{\rm GeV}\lesssim E\lesssim 100\,{\rm GeV}$. In fact, if this was the case, then it would mean that higher-energy particles have reached such energy because they spent more time in the Galaxy, but this would imply that secondary-to-primary ratios would have an opposite trend with respect to the observation (Strong et al., 2007). On the other hand, reacceleration is likely more important at lower energies, where it could be responsible for the peak in the B/C ratio, for instance. From the technical point of view, it is taken into account in our runs by means of the following parametrization (Drury and Strong, 2016; Osborne and Ptuskin, 1988; Seo and Ptuskin, 1994):

$$D_{pp}=\frac{1}{\alpha(4-\alpha)(4-\alpha^2)}\frac{p^2v_A^2}{D_{\parallel}}, \tag{2.14}$$

where α is the slope of the turbulence spectrum $W(k)\sim k^{-\alpha}$ and $D_{\parallel}\propto(p/p_0)^{\delta}$ is the parallel diffusion coefficient seen in Equation (1.61), here isotropized to have $D_{\parallel}\approx D_{\perp}$.

Reacceleration is only marginal in our calculations. In fact the Alfvén velocity can be computed as follows — this is the same expression derived in Section 1.3.1, but in more convenient units:

$$v_A=\frac{B_0}{\sqrt{4\pi\rho_{\rm ISM}}}\,{\rm cm}\cdot{\rm s}^{-1}, \tag{2.15}$$

where $[B_0]={\rm G}={\rm cm}^{-1/2}\cdot{\rm g}^{1/2}\cdot{\rm s}^{-1}$ and $[\rho_{\rm ISM}]={\rm g}\cdot{\rm cm}^{-3}$ and, due to typical ISM conditions, we

obtain $v_A \sim \mathcal{O}(1-10)\,\mathrm{km}\cdot\mathrm{s}^{-1}$. Of course, due to large uncertainties in the values of both the magnetic field and the ISM, this parameter might in principle change a lot. However, we choose to to keep it low, $v_A = 13\,\mathrm{km}\cdot\mathrm{s}^{-1}$.

Adiabatic losses due to advection. As mentioned in Section 1.3.3, the vertical (along $\hat{z}$) motion of Galactic winds occurs at increasing velocity $\frac{d\boldsymbol{u}_w}{dz} > 0$ and it is always accompanied by the expansion of the wind cloud. Therefore, in order to preserve the total energy, cosmic rays trapped in the cloud loose energy adiabatically, according to the coupled advection equations:

$$\begin{cases} \dfrac{\partial N_i}{\partial t} = -\dfrac{\partial (u_w N_i)}{\partial z} \\ -D_{zz}\dfrac{\partial^2 N_i}{\partial z^2} - \dfrac{\partial (u_w N_i)}{\partial z} = S(r, z=0)\delta(z) \end{cases} \tag{2.16}$$

for the species i, that can be solved independently of the other equations, due to the *operator splitting* procedure. For the first equation, we assume Gaussian initial condition $N_i(z, t=0) = \sqrt{2\pi\sigma_z^2}\exp\left(-\frac{z^2}{2\sigma_z^2}\right)$, while for the second we impose $N_i(|z| = L_\mathrm{H}) = 0$, with L_H size of the Galactic halo. In our runs, we consider a linearly increasing wind velocity $|\boldsymbol{u}_w|(z) = u_{w,0} + \frac{du_w}{dz}z$ (Strong and Moskalenko, 1998), where the input parameters are chosen according to Zirakashvili et al. (1996).

2.2.2 Cosmic-ray non-adiabatic energy losses

In this paragraph we briefly describe all the mechanisms of energy-loss suffered by cosmic-ray particles. We have seen that the interstellar environment contains both radiation and matter, therefore we distinguish the energy-losses occurring to charges due to their passage through (i) a gas of photons, (ii) a gas of atoms or molecules, either ionized, partially ionized or neutral.

(i) When a charged particle traverses a photon gas, it scatters against photons via a process known as *Inverse Compton scattering* (IC or ICS), and accelerates them. At low energy, we can visualize the direct process (*Compton scattering*) as an electron that gets scattered by an electromagnetic wave and starts to oscillate due to the oscillating electric field transported by the wave — this is known as *Thomson scattering*. Accelerated particles of charge q traveling at relativistic speed emit electromagnetic radiation, according to the well-known *Larmor formula* (Barone, 2004):

$$\mathcal{P} \equiv -\frac{dE}{dt} = \frac{2q^2}{3c^3}\,\dot{\boldsymbol{v}}^2. \tag{2.17}$$

In our case, the particle accelerates due to the force $\boldsymbol{F} = q\boldsymbol{E}(\boldsymbol{x}, t)$ exerted by the electric field $\boldsymbol{E}(\boldsymbol{x}, t) = \hat{\boldsymbol{\epsilon}}E_0\,\sin(\omega_\mathrm{wave}t)$, with ω_wave frequency of the wave. Thus $\dot{\boldsymbol{v}} = \frac{q\hat{\boldsymbol{\epsilon}}E_0\,\sin(\omega_\mathrm{wave}t)}{m}$, and it is clear that the power emitted in form of dipole-radiation is at expenses of the oscillating field. This means that this

process involves exchange of energy between the charge and the field and, as a consequence, its complete treatment requires the use of quantum electrodynamics.

On the other hand, when the same charge encounters a *static* magnetic field, it only feels a Lorentz force perpendicular to its direction of motions. Therefore, no field-particle energy-exchange is involved, and the classical treatment is valid at all energies. The radiation emitted is called in this case *Synchrotron radiation*.

In both the synchrotron and IC cases, the emitted radiation comes from the acceleration of the charged particle (either in direction or momentum), which is of course much more efficient for light particles. This is why synchrotron and IC scattering can be neglected for protons and nuclei. This will be quantified below.

(ii) As for the passage of the CRs through matter, the nature of the interaction is mainly of Coulomb origin, and thus regulated by the famous *Rutherford formula* for the scattering cross-section, for which we remind to Rutherford (1911). In fact, charged particles scatter off the medium nuclei, causing their *excitation* — when the quantum state changes — or ionization — when an external electron is ripped off. The energy loss resulting from this mechanism changes based on the degree of ionization of the medium, whether it is neutral/weakly ionized (*i.e.* interstellar gas) or fully ionized (*i.e.* a plasma) and its rate depends on the different declinations of the general *Bethe-Bloch* formula, formalizing the *stopping-power* ($-\frac{dE}{dx} = -\frac{1}{v}\frac{dE}{dt}$) of a medium under different conditions (Ginzburg and Haar, 2013). For a satisfactory physical treatment, we remind to the classic book Ginzburg and Haar (2013) (pages $357 - 387$). In particular, when particles traverse neutral or weakly ionized gases, the process is technically referred to as *ionization*, otherwise in fully ionized plasmas the process is simply called *Coulomb scattering* (Mannheim and Schlickeiser, 1994). As expected, both processes involve the charge of the particles (not the mass) and are only affected by the properties of the media they are propagating into (their density and the mass of the ionizing electron). Therefore they are equally efficient for electrons and nucleons.

When the interaction does not involve the change of state of the target nucleus nor of the incident particle, the Coulomb interaction leads to an acceleration (or deceleration) of the projectile, emitting as expected an electromagnetic radiation that is commonly known as *Bremsstrahlung* (literally *braking radiation*) (see Ginzburg and Haar (2013), Chapter 16). Again, the change of the particle velocity is more efficient for light particles, and therefore will be here neglected for nucleons.

Finally, hadronic interactions between the CR nucleons and the nucleons of the interstellar gas lead to the production of pions and other composite particles, according to *quantum chromodynamics* (QCD), as pointed out in Mannheim and Schlickeiser (1994).

In what follows, we discuss the rates of energy losses for the above-described processes, as they are implemented in our DRAGON runs.

Synchrotron radiation. The power of the electromagnetic radiation emitted by accelerated charged particles can be computed in general via the relativistic extension of the *Larmor formula* (Barone, 2004):

$$\mathcal{P} \equiv -\frac{dE}{dt} = \frac{2q^2\gamma^2}{3m^2c^3} \cdot \left[\left(\frac{d\boldsymbol{p}}{dt}\bigg|_{\rm gyr} \right)^2 - \frac{1}{c^2} \left(\frac{dE}{dt}\bigg|_{\rm gyr} \right)^2 \right], \tag{2.18}$$

where $\gamma = E/(mc^2)$ is the Lorentz factor.

In the specific case where there is only a uniform and time-independent magnetic field $\boldsymbol{B}_0$, in each gyration the variation of the particle momentum is large in direction, as given by the Lorentz force $\frac{d\boldsymbol{p}}{dt} = \frac{q}{c} v B_0 \sin\chi = \frac{m\gamma c^2 \beta^2}{r_L} \sin\chi$ — χ is the angle between the particle velocity and the $\boldsymbol{B}_0$-field — while its energy variation can be neglected. Therefore, Equation (2.18) becomes:

$$-\frac{dE}{dt} = \frac{2q^2 c}{3r_L^2} \beta^4 \left(\frac{E}{mc^2} \right)^4 \sin\chi, \tag{2.19}$$

which is the power emitted in the form of *synchrotron radiation*. We immediately notice that, due to the proportionality $\propto m^{-4}$ of the equation above and to the mass ratio $m_e/m_p \approx 10^{-3}$, electrons are largely more affected by synchrotron losses than protons.

To obtain the loss-rate in a randomly-oriented magnetic field, we finally average over the angle χ (Blumenthal and Gould, 1970):

$$-\frac{dE}{dt}\bigg|_{\rm Syn} = \frac{4}{3} \sigma_T c \beta^2 \frac{E^2}{m^2c^4} \cdot \frac{B_0^2}{8\pi}, \tag{2.20}$$

where we defined the *Thomson* cross-section $\sigma_T = \frac{8\pi}{3} \left(\frac{q^2}{mc^2} \right)^2$, $r_L = \frac{pc}{qB_0}$ is, as usual, the Larmor radius and $\left[\frac{B_0^2}{8\pi} \right] = \mathrm{erg} \cdot \mathrm{cm}^{-3}$ is the energy density of the magnetic field.

Synchrotron radiation, in the reference frame of the observer, is peaked around a characteristic frequency $\nu_c \simeq \frac{\gamma^3}{2\pi} \frac{qB_0}{m\gamma c} = \frac{\gamma^3}{2\pi} \omega_L$, that depends on the gyration frequency of the particle (Jackson, 1975). This can be rearranged in a practical way as follows:

$$E_{\gamma,\rm Syn} = \gamma^3 \hbar \omega_L = \hbar \frac{E_e^2 q B_0}{m_e^3 c^6} \simeq 5 \cdot 10^{-6} \left(\frac{B_0}{\mu\mathrm{G}} \right) \left(\frac{E_e}{10\,\mathrm{GeV}} \right)^2 \mathrm{eV}, \tag{2.21}$$

from which we get that the synchrotron emission for typical ISM magnetic fields of the order $B_0 \sim 1\,\mu$G is expected in the range from high-frequency *radio waves* ($\sim \mathcal{O}(100)$ MHz) up to the *infrared* band ($\sim \mathcal{O}(100)$THz).

Inverse Compton scattering. We have seen above that CRs can scatter off photons of the ISRF accelerating them and that this process can be neglected for massive particles like protons. The energy loss rate is implemented in its most complete form, valid for any energy regime (Blumenthal and Gould,

1970):

$$-\left.\frac{dE}{dt}\right|_{\rm IC} = 3\sigma_T c \int_0^\infty d\epsilon_i\, \epsilon_i \int_{1/(4\gamma_e^2)}^1 dq\, \frac{(4\gamma_e^2-\Gamma)q-1}{(1+\Gamma q)^3}\frac{d\eta}{d\epsilon_i}\times \\ \times\left\{1+2q\left(\log q - q + \frac{1}{2}\right)+\frac{1-q}{2}\frac{(\Gamma q)^2}{1+\Gamma q}\right\}, \tag{2.22}$$

where $q \equiv \frac{\hat{\boldsymbol{\epsilon}}_f}{\Gamma(1-\hat{\boldsymbol{\epsilon}}_f)}$, $\hat{\boldsymbol{\epsilon}}_f \equiv \frac{\epsilon_f}{\gamma_e m c^2}$, (ϵ_i, ϵ_f) are the initial and final energies of the scattered photon, respectively, $\Gamma \equiv \frac{4\gamma_e \epsilon_i}{mc^2}$ and $\frac{d\eta_a}{d\epsilon_i}$ is the *black-body* Planck distribution of the a-component of the ISRF:

$$\frac{d\eta_a}{d\epsilon_i} = \mathcal{N}_a \frac{8\pi\epsilon_i^2}{(2\pi\hbar c)^3}\left(e^{\frac{\epsilon_i}{k_b T_a}}-1\right)^{-1}.$$

The normalization $\mathcal{N}_a$ and temperature T_a are taken according to Delahaye, T. et al. (2010), where the observational ISRF from Porter and Strong (2005) is fitted with the superposition of 6 different photon-fields Planck distributions.

The *Thomson* low-energy limit of the process reduces to (Blumenthal and Gould, 1970):

$$-\left.\frac{dE}{dt}\right|_{\rm IC}^{\rm Thomson} = \frac{4}{3}\sigma_T c\,\beta^2 \frac{E^2}{m^2c^4}\cdot U_{\rm rad}, \tag{2.23}$$

where $U_{\rm rad}$ is the energy density of the radiation field.

This expression is the same as Equation (2.20) giving the synchrotron loss-rate. This is not a coincidence: in fact, as synchrotron radiation is produced from particles gyrating about *static* magnetic-field lines, it can be considered as the radiation generated by a Compton process against a *virtual* photon — namely a photon that does not carry observable momentum. Furthermore, as for the synchrotron, the loss rate scales as $\propto m^{-4}$ with the mass of the charge, which is why IC losses can be ignored for protons and heavier nuclei.

As for the spectrum of the resulting radiation, a *rule of thumb* can be found considering the average rate of scattered photons:

$$\langle n_\gamma \sigma v_{CR}\rangle \simeq \sigma_T c \frac{U_{\rm rad}}{\hbar\omega_0}\,[T]^{-1},$$

where $[n_\gamma] = {\rm cm}^{-3}$ is the radiation-field number density and $\hbar\omega_0$ the energy of a single scattered photon.

Based on the energy-loss rate in the *Thomson*-limit, Equation (2.23), we have:

$$\left\langle\frac{dE}{dt}\right\rangle = \left\langle\frac{4}{3}\beta^2\left(\sigma_T c\frac{U_{\rm rad}}{\hbar\omega_0}\right)\hbar\omega_0\gamma^2\right\rangle \quad\Rightarrow\quad \langle dE\rangle \sim \frac{4}{3}\beta^2\gamma^2\hbar\omega_0, \tag{2.24}$$

from which it follows that $\hbar\omega \approx \frac{4}{3}\gamma^2\hbar\omega_0$ (Longair, 2011) for relativistic electrons ($\beta \approx 1$). From this relation, we immediately find that the emitted photons have energies going from the UV ($\sim 10^{15}$ Hz) up to the intermediate γ-rays ($\sim 10^{20}$ Hz) — for 10 GeV electrons scattering off the CMB photons.

Bremsstrahlung. As introduced above, this is the radiation emitted when a charged projectile interacts with the charges of the medium (ions) and changes its state of motion. In a classical way, we consider the *Larmor* formula in Equation (2.17), where the acceleration — consequence of the Coulomb's law — is written in natural units as $a = -\frac{Zq^2}{mr^2}$, where r is the distance between the CR charge and the medium charge. Therefore, the power emitted during this process is derived as follows:

$$-\frac{dE}{dt} = \frac{2Z^2q^6}{3c^3}\frac{1}{m^2r^4}. \tag{2.25}$$

As anticipated above, given the $\propto m^{-2}$ dependence of the mass of the CR particle, this form of radiation is only significant for electrons.

Fully quantum-mechanical and relativistic expressions are implemented in DRAGON, according to Blumenthal and Gould (1970); Ginzburg and Haar (2013), and change based on the degree of ionization of the crossed medium:

$$\begin{aligned} -\left(\frac{dE}{dt}\bigg|_{\rm Brem}\right)_{\rm WS} &= \frac{3\alpha c\sigma_T}{2\pi} m_e\gamma c^2 \left[\log(2\gamma) - \frac{1}{3}\right] \sum_{i=H,He} Z_i(Z_i+1)n_i \\ -\left(\frac{dE}{dt}\bigg|_{\rm Brem}\right)_{\rm SS} &= cE \sum_{i=H,He} \frac{n_i M_i}{\lambda_i}, \end{aligned} \tag{2.26}$$

where the labels WS and SS stand for *weakly-shielded* neutral gas (also ionized) and *strongly-shielded* neutral gas, M_i is the atomic mass and $(\lambda_H, \lambda_{He}) \approx (62.8,\, 93.1)\,\mathrm{g\cdot cm^{-2}}$ the radiation lengths of hydrogen and helium, respectively. The shielding refers to how the projectile CR feels the Coulomb potential of the medium charges: if it is weak or not present at all, a small Lorentz factor is sufficient to produce radiation — the first equation holds for $\gamma < 100$. On the other hand, if there is a strong shielding, the braked particle can produce radiation only if moving extremely fast, indeed the second equation is valid for $\gamma \geq 800$. In the intermediate Lorentz-factor values ($100 < \gamma < 800$), we use a linear interpolation of the two relations.

For what concerns the resulting radiation, it presents a continuous spectrum that can be understood as the conversion of the kinetic energy of the projectile electron. Thus, the spectrum is rather flat up to a frequency $\nu_{\rm max} = E_e/h$, h being the Planck constant. However, looking at Figure 2.4, we see that for typical ISM conditions *Bremsstrahlung* is dominating typically in a very small electron-energy window ($10^{-1}\,\mathrm{GeV} < E_e < 10\,\mathrm{GeV}$), which corresponds to a photon energy in the γ-ray range.

Ionization. When an electron is removed from an atom or excited to a higher energy-state, the CR projectile loose a part of its energy, according to the famous *Bethe-Bloch* formula, which contains several terms that depend on the status of the crossed medium. For hadrons, DRAGON contains the following

expression (Mannheim and Schlickeiser, 1994):

$$-\left(\left.\frac{dE}{dt}\right|_{\rm Ion}\right)_p = \frac{3\sigma_T m_e c^3}{4\beta} Z^2 \sum_{i=H,He} n_i \left[\log\left(\frac{2m_e c^2 \beta^2 \gamma^2 Q_{\rm max}}{\langle I_i\rangle^2}\right) - 2\beta^2\right], \tag{2.27}$$

where $(\langle I_H\rangle, \langle I_{He}\rangle) = (19,\, 44)\,\mathrm{eV}$ are the geometrical means of the ionization potentials of hydrogen and helium, respectively, in all their possible configurations regarding energy levels and angular momenta, and $Q_{\rm max} \sim \frac{2m_e c^2\beta^2\gamma^2}{1+2\gamma m_e/M}$ is the maximum energy transferred by the CR particle of mass M to the electron, valid under the condition $M \gg m_e$.

When we consider the case of CR electrons, its inertial mass is the same as that of the removed particle, therefore the simplifications in the general *Bethe-Bloch* formula have to change and we use the following expression (Longair, 2011):

$$\begin{aligned}-\left(\left.\frac{dE}{dt}\right|_{\rm Ion}\right)_e = \frac{3\sigma_T m_e c^3}{4\beta} \sum_{i=H,He} Z_i n_i \Bigg[&\log\left(\frac{\gamma^2 m_e c^2 Q_{\rm max}}{2I_i^2}\right) \\ &- \left(\frac{2}{\gamma} - \frac{1}{\gamma^2}\right)\log 2 + \frac{1}{\gamma^2} + \frac{1}{8}\left(1 - \frac{1}{\gamma}\right)^2\Bigg],\end{aligned} \tag{2.28}$$

where $(I_H, I_{He}) = (13.6,\, 24.59)\,\mathrm{eV}$ are the ionization potentials of the ground-state atoms and $Q_{\rm max} = \frac{\gamma^2 m_e c^2}{1+\gamma}$.

Coulomb scattering. Coulomb collisions in a completely ionized plasma are dominated by scattering off the thermal electrons. For hadrons, we use the following expression (Mannheim and Schlickeiser, 1994):

$$-\left(\left.\frac{dE}{dt}\right|_{\rm Coul}\right)_p = \frac{3}{2}\sigma_T m_e c^3 Z^2 n_e \log\Lambda \frac{1}{\beta} W_e\left(\frac{\beta}{\beta}\right), \tag{2.29}$$

where $\beta \equiv \sqrt{\frac{2k_b T_e}{m_e c^2}}$, (n_e, T_e) are the density and temperature of the ionized thermal plasma, respectively, the function $W_e(x)$ is defined as follows:

$$W_e(x) = \mathrm{erf}(x) - \frac{2}{\sqrt{\pi}}\left(1 + \frac{m_e}{A m_p}\right) x e^{-x^2},$$

with A atomic mass of the projectile CR, and $\log\Lambda = \frac{1}{2}\log\left(\frac{m_e^2 c^2}{\pi r_e \hbar^2 n_e}\frac{A m_p \gamma^2\beta^4}{A m_p + 2\gamma m_e c^2}\right)$ is called *Coulomb logarithm* and it is here defined in the cold-plasma limit (Dermer, 1985).

As for electrons and positrons, we implement the loss rate following Ginzburg and Haar (2013):

$$-\left(\left.\frac{dE}{dt}\right|_{\rm Coul}\right)_{e^\pm} = \frac{3}{4}\sigma_T m_e c^3 n_e \left[\log\left(\frac{E m_e c^2}{4\pi r_e \hbar^2 c^2 n_e}\right) - \frac{3}{4}\right]. \tag{2.30}$$

Pion production. Cosmic-ray nucleons impacting against photons or nucleons of the interstellar gas generate hadronic showers, mainly in the form of charged and neutral pions. Basically, the interesting processes are the following:

$$p + \gamma \longrightarrow \Delta^+ \longrightarrow \begin{cases} p\pi^0 \\ n\pi^+ \end{cases} \qquad p + p \longrightarrow \begin{cases} pp\pi^0 \\ pn\pi^+ \\ pp\pi^+\pi^- \\ \dots \end{cases}$$

depending on whether CRs scatter off diffuse photons or interstellar matter.

Then, in turn, pions decay nearly always ($\sim 99\%$) via the following channels:

$$\pi^0 \longrightarrow \gamma\gamma \qquad \pi^+ \longrightarrow \mu^+\nu_\mu \quad \mu^+ \longrightarrow e^+\bar{\nu}_\mu\nu_e \qquad \pi^- \longrightarrow \mu^-\bar{\nu}_\mu \quad \mu^- \longrightarrow e^-\nu_\mu\bar{\nu}_e.$$

From the kinematics of the $p\gamma$ and pp processes, it can be easily seen — by creating the secondary products at rest in the *center-of-mass* (CM) reference frame — that the threshold energies of the projectile protons are $E^{\rm th}_{pp} = m_p + \frac{m_\pi^2 + 4m_p m_\pi}{2m_p} \approx 1.2\,{\rm GeV}$ and $E^{\rm th}_{p\gamma} = \frac{m_p m_\pi + m_\pi^2/2}{E^{\rm t}_\gamma} \approx 10^{17}\left(\frac{1\,{\rm eV}}{E^{\rm t}_\gamma}\right)$ eV, where $E^{\rm t}_\gamma$ indicates the target photon energy. Due to the much higher threshold of the process, proton-γ interactions are mostly important for extra-galactic CRs, that are less abundant than lower-energy ones (see Figure 1.1). This is why it is commonly assumed that the highest contribution to the pion production comes from pp scattering.

The energy spectrum of the pions is found from the proton spectrum $S_p \propto E^{-\delta}$, considering the scattering targets and the dynamics of the process, namely the cross section σ_{pp}:

$$Q_{\pi^{0,\pm}}(E) = c \int dE_p\, S_p(E_p)\delta(E - K_{p\pi^0}E_p)\sigma_{pp}(E_p)n_{\rm gas}, \tag{2.31}$$

where $K_{p\pi^0}$ is the mean fraction of the proton-energy carried away by the secondary pion.

From experiments, it is found $K_{p\pi^0} \simeq 0.17$ for each collision — this parameter is called *inelasticity*. Besides, from the kinematics we have that, on average, $\langle E_\gamma \rangle \approx \frac{1}{2}E_{\pi^0}$ and $\langle E_{\nu,\bar{\nu}} \rangle \approx \frac{1}{4}E_{\pi^\pm}$ (Mannheim and Schlickeiser, 1994). From this, we derive that a *rule-of-thumb* estimation for the resulting photon

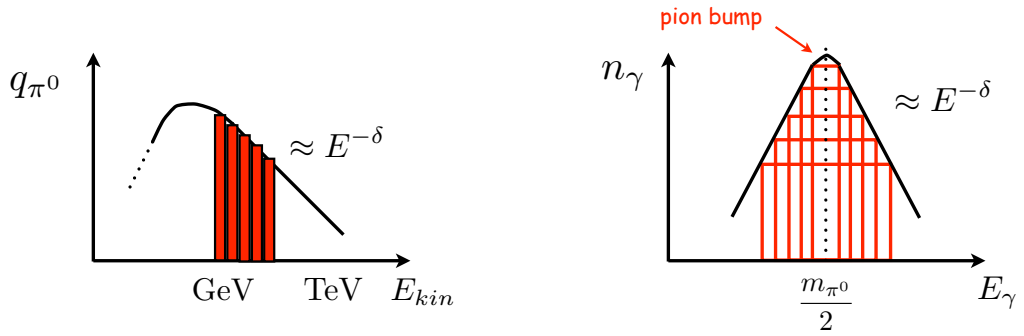

Figure 2.3: Spectrum of the photons coming from $\pi^0 \to \gamma\gamma$. Each energy-interval of the pion spectrum (red boxes on the left figure) results in a flat distribution — symmetric with respect to $\log(m_{\pi^0})/2$ — between $E_\gamma^{\min}$ and $E_\gamma^{\max}$ for the secondary photons (red empty boxes in the right figure). Its convolution is peaked around $\log(m_{\pi^0})/2$ and scales as the progenitor pion spectrum.

and neutrino energies from the above processes gives:

$$E_\gamma \simeq 0.1 E_p, \qquad\qquad E_{\nu,\bar{\nu}} \simeq 0.05 E_p.$$

Photons can be further characterized, as they only come from the two-body decay of the neutral pion. In fact, in the CM, their final energy is half of the pion mass $E_\gamma^* = \frac{m_{\pi^0}}{2}$, which has to be Lorentz-transported in the *laboratory* frame, where it has minimum and maximum values $E_\gamma = \gamma_{\pi^0} \frac{m_{\pi^0}}{2} (1 \pm \beta_{\pi^0})$. Therefore, in $\log_{10}$-scale, we have:

$$\frac{\log_{10}(E_\gamma^{\min}) + \log_{10}(E_\gamma^{\max})}{2} = \log_{10}\left(\frac{m_{\pi^0}}{2}\right). \tag{2.32}$$

Besides, coming in a two-body decay, photons present a flat distribution — $\frac{dn_\gamma}{dE_\gamma} = \text{const}$ — between $E_\gamma^{\min}$ and $E_\gamma^{\max}$, both depending on the Lorentz factor of the progenitor proton.

In conclusion, in $\log_{10}$-scale we expect a flat distribution for each dE-interval of the pion energy, each of them peaked around the half of the pion mass $E_\gamma \simeq 70\,\text{MeV}$ — this falls in the high-energy γ-ray band. This is sketched in Figure 2.3, where the characteristic *pion bump*, which serves as the identification feature for the pion-decay component of the γ-ray spectra, is shown. Furthermore, the secondary-photon spectra have the same slope as the pion's that, in turn, has the same spectrum as the progenitor proton — this can be immediately seen from Equation (2.31) due to a constant cross-section in this energy regime ($E_p > E_{pp}^{\text{th}} \approx 1.2\,\text{GeV}$) (Pancheri and Srivastava, 2017).

Regarding the produced neutrinos, we notice that Equations (2.31) and (2.32) still hold — the latter slightly modified to include the neutrino energy in the CM frame, E_ν^*. This implies that, as far as the two-body processes $\pi^\pm \to \mu_\pm \overset{(-)}{\nu}_\mu$ are concerned, the resulting neutrinos present an energy spectrum peaked around $E_\nu^* = \frac{m_\pi^2 - m_\mu^2}{2m_\pi} \simeq 29.8\,\text{MeV}$, with the same slope of the progenitor pion — and of the proton as well — due to the kinematics. On the other hand, the neutrinos generated in the three-body

decay of the muons have a broad spectrum typical of such processes, depending on the Lorentz factor of the progenitors.

In DRAGON, the processes above cause the CR-particles to loose energy at a rate (Krakau and Schlickeiser, 2015):

$$-\left.\frac{dE}{dt}\right|_{\text{Pion}} = 3.85 \cdot 10^{-16} \left(\frac{n_{HI} + 2n_{H_2}}{\text{cm}^{-3}}\right) \left(\frac{E}{\text{GeV}}\right)^{1.28} \cdot \left(\frac{E}{\text{GeV}} + 200\right)^{-0.2} \text{GeV s}^{-1}. \tag{2.33}$$

Analogously, to model the energy loss by heavier nuclei, Equation (2.33) is increased by a factor $A^{0.79}$ (Krakau and Schlickeiser, 2015), where A is the atomic mass of the nucleus.

The occurrence of the processes described above can be evaluated in terms of their characteristic time scales, defined by:

$$\tau_{\text{loss}} = E \Big/ \left|\frac{dE}{dt}\right|, \tag{2.34}$$

in each energy interval $[E, E + dE]$.

These time scales are shown in Figure 2.4 separately for leptons (left column) and nucleons (right column) and in different Galactic environments, around us (upper row) and in the Galactic center (bottom row) for reference densities and ISRF as reported in the caption. For comparison, the diffusion timescale $\tau_{\text{diff}} = \frac{L^2_{\text{Halo}}}{2D(E)}$ is shown. From this figure, it is clear that, for leptons, losses dominate over diffusion from $E > 10\,\text{GeV}$ ($E > 100\,\text{GeV}$) in the Galactic center (locally), while for hadrons diffusion is always the fastest process.

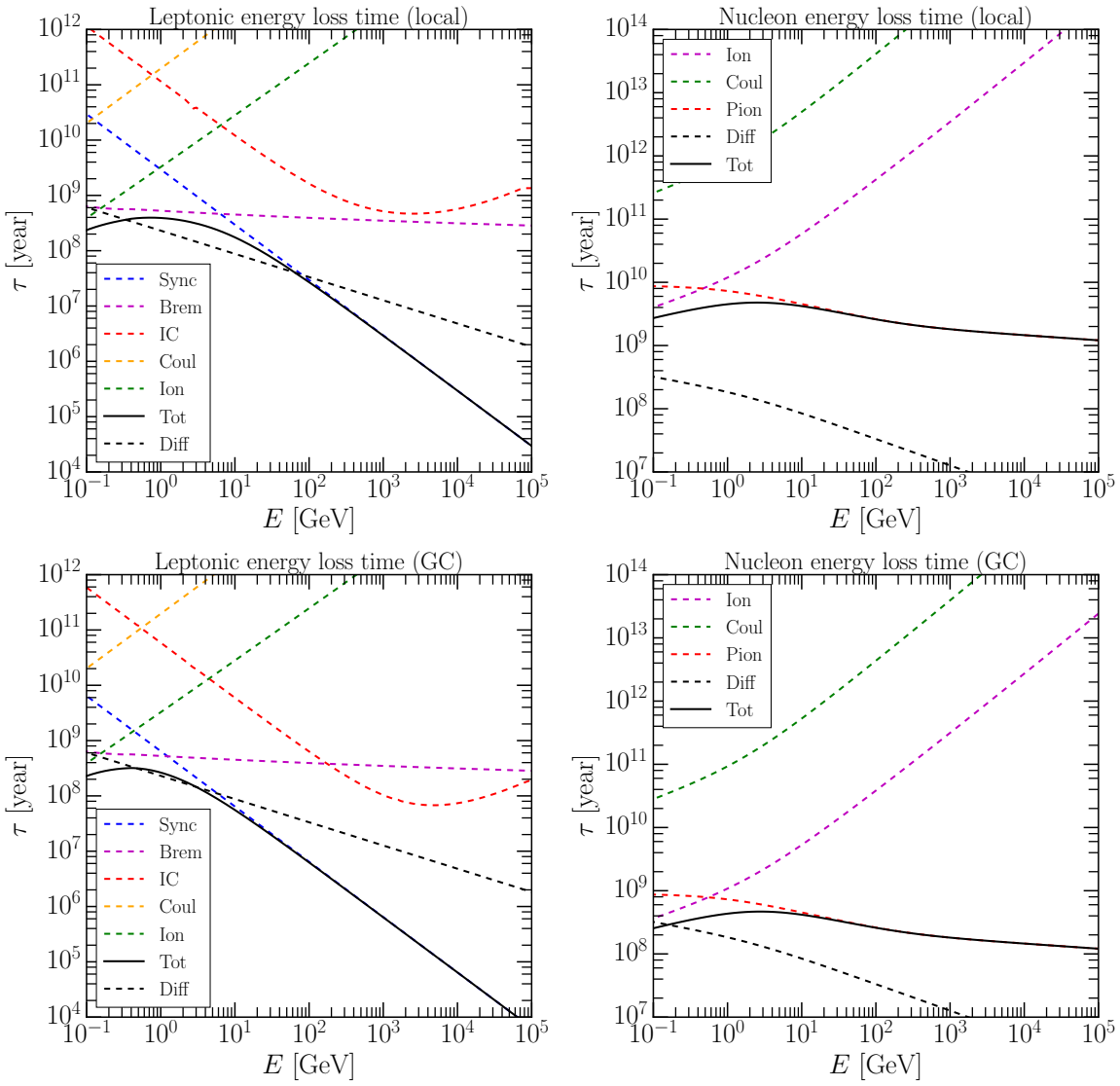

Figure 2.4: The timescales for energy losses are shown for leptons (left column) and hadrons (right column), around the solar system (upper row) and at the Galactic center (bottom row), for reference densities $n_{\rm H}^{\rm loc} = 0.9\,{\rm cm}^{-3}$ ($n_{\rm H}^{\rm GC} = 10\,{\rm cm}^{-3}$) and ISRF as reported in Delahaye, T. et al. (2010) The diffusion time scale is computed for $D_0 = 10^{28}\,{\rm cm}^2 \cdot {\rm s}^{-1}$, $\delta = 0.4$ and a halo size $L_{\rm Halo} = 4\,{\rm kpc}$. Figure from Evoli et al. (2017a).

2.3 Multi-messenger implications of CR transport in the Galaxy

In the previous section we discussed the physical processes leading each cosmic-ray particle to the loose part of its energy. In most cases, these losses occur along with the emission of secondary photons and neutrinos of energy defined by the specific loss mechanism. This is summarized in Table 2.1.

	CR involved	Target	Secondary ID	Secondary E
Synchrotron	$e^{\pm}$	$\boldsymbol{B}$-field	γ	*radio band*
Brems		ISM gas		X-rays
ICS		ISRF		high γ-rays
$\pi^0 \to \gamma\gamma$	p, He, nuclei	ISM gas+ decay		high γ-rays
$\pi^{\pm} \to \mu_{\pm}{}^{(\overline{)}}\nu_{\mu}$			ν	high-energy ν
$\mu^{\pm} \to e^{\pm}{}^{(\overline{)}}\nu_{\mu}{}^{(\overline{)}}\nu_{e}$	sec μ			broadband

Table 2.1: The table summarizes the interaction processes involving the emission of secondary γ's and ν's. Specified are the primary particle, the target, the type of the produced secondary and its emission energy-range.

These particles, measured by dedicated observatories, trace the passage of the cosmic rays and therefore are clear imprints to identify the nature and distribution of the CR sources. This broad-range overview of the problem is usually referred to as *multi-messenger approach* and it has become an extremely promising field of research in recent times. In what follows, we show some of the implications of the CR models described in the previous section.

The photon emission due to energy losses can be quantified in a quantity called *emissivity*, which is the result of an integration, over the progenitor energy, of (i) the CR spectrum, (ii) the target distribution (ISRF for IC and gas density for $\pi^0 \to \gamma\gamma$ and bremsstrahlung), (iii) the cross section of the interaction. For the exact formulas we remind to the classic book Longair (2011).

The emissivity integral, involving space/energy distributions of such ingredients, requires dedicated codes to be calculated numerically. Here — for illustrative purposes only — we use the results from the numerical tool `GammaSky`*. The following set of figures — Figures 2.5-2.6-2.7 — shows the photon emissivity due to IC, pion decay and bremsstrahlung processes calculated with `GammaSky` for three different photon energies — $E_\gamma = 1.5\,\mathrm{GeV},\ 100\,\mathrm{GeV},\ 1\,\mathrm{TeV}$. The CR model-setup is the one adopted in Fornieri et al. (2020b) — this will be described in detail in Section 3 — the ISRF is com-

*https://github.com/cosmicrays/hermes

puted in Vernetto and Lipari (2016) and the gas distribution is an improved version of Remy et al. (2017, 2018a,b). We notice that such parametrizations for the ISRF and the gas distribution are more recent than the ones currently implemented in DRAGON, but do not significantly differ from them.

From the figures, it is clear that the decay of the neutral pion — produced in pp interactions — dominates the photon production in the whole energy-range here probed, with contaminations from bremsstrahlung and leptonic IC scattering, both, however, at least one order of magnitude smaller. Besides, nearly all the emission is concentrated in the Galactic plane, strongly correlating the sources of cosmic rays with the distribution of the gas.

To support this conclusion, in Figure 2.8 we show the emissivity measured by the *Fermi* Collaboration*, integrated over the energy range covered by the *Fermi Large-Area Telescope* (*Fermi*-LAT), *i.e.* from $1\,\mathrm{GeV}$ up to the $\sim\,\mathrm{TeV}$ scale, calculated over 5 years of data taking†.

From the *Fermi* map, we can easily recognize more luminous spots, which identify high-luminosity isolated sources. However, the ability to isolate these spots gets reduced around the Galactic center. In this region, the three processes have comparable emissivities up to $\mathcal{O}(100)\,\mathrm{GeV}$, while from Figure 2.7 we see that, at $1\,\mathrm{TeV}$, π^0 decay is by far the only process contributing to the γ-ray sky. The possibility to study powerful sources and the diffuse γ-ray emission at the center of our Galaxy justifies the need for γ-ray detectors above the $\sim\,\mathrm{TeV}$ threshold. Above this energy, *Cherenkov telescopes* are necessary: among them, *H.E.S.S.*‡, *MAGIC*§, *VERITAS*¶ are already operating, while *CTA*‖ is expected to start taking data by the end of 2025.

For what concerns the neutrino sky, neutrino emissivity can be computed similarly to what explained for photons (Longair, 2011). On the other hand, the state of the current observations is considerably different. In fact, taking part only in the weak interaction, neutrinos are at the same time unambiguous witnesses of the astrophysical events where they are produced and the most elusive particles to detect. Dedicated observatories require large sizes due to the low number of events. For this reason they have to be built on Earth, thus detecting a huge amount of atmospheric background, *i.e.* the hadronic showers generated when CRs impact our surrounding atmosphere.

Roughly speaking, atmospheric neutrinos present a power-law spectrum that, with respect to the CR spectrum locally observed $\left(\frac{dN_{\mathrm{CR}}}{dE} \propto E^{-2.7}\right)$ gets softened due to the atmospheric processes: in particular, it is expected to be $\frac{dN_\nu^{\mathrm{atm}}}{dE} \propto E^{-3.7}$ (Aartsen et al., 2013). On the other hand, astrophysical (or, alternatively, cosmic) neutrinos are produced at the source and the travel unaltered to the Earth, hence their flux is expected to reflect the *diffusive-shock-acceleration* $\propto E^{-2}$ spectrum of the parent cosmic

*https://fermi.gsfc.nasa.gov/
†https://svs.gsfc.nasa.gov/11342
‡https://www.mpi-hd.mpg.de/hfm/HESS/
§https://magic.mpp.mpg.de/
¶https://veritas.sao.arizona.edu/
‖https://www.cta-observatory.org/

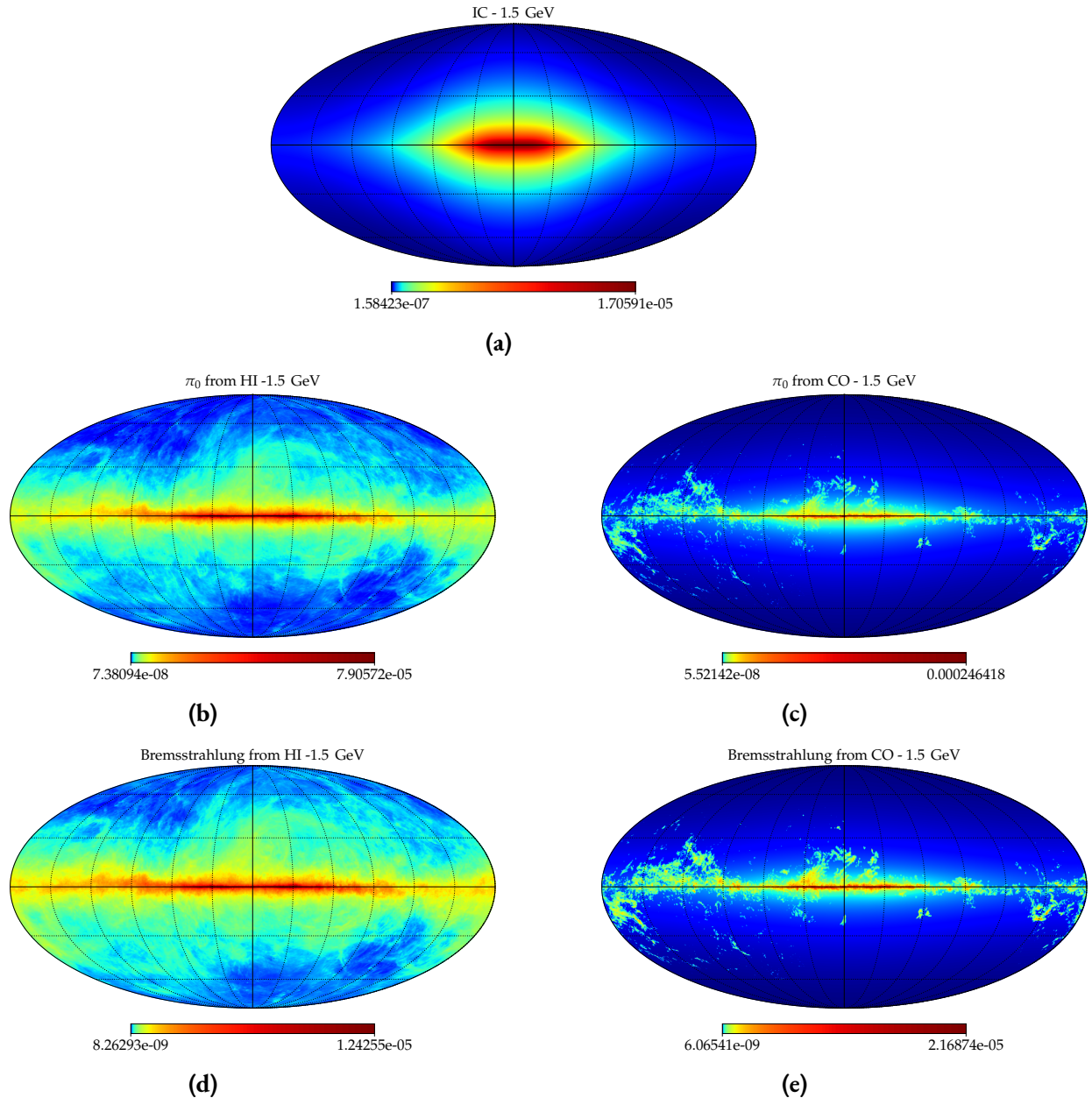

Figure 2.5: Photon emissivities due to **(a)** IC, **(b,c)** pion decay and **(d,e)** bremsstrahlung are shown, for a photon energy $E_\gamma = 1.5\,\mathrm{GeV}$.

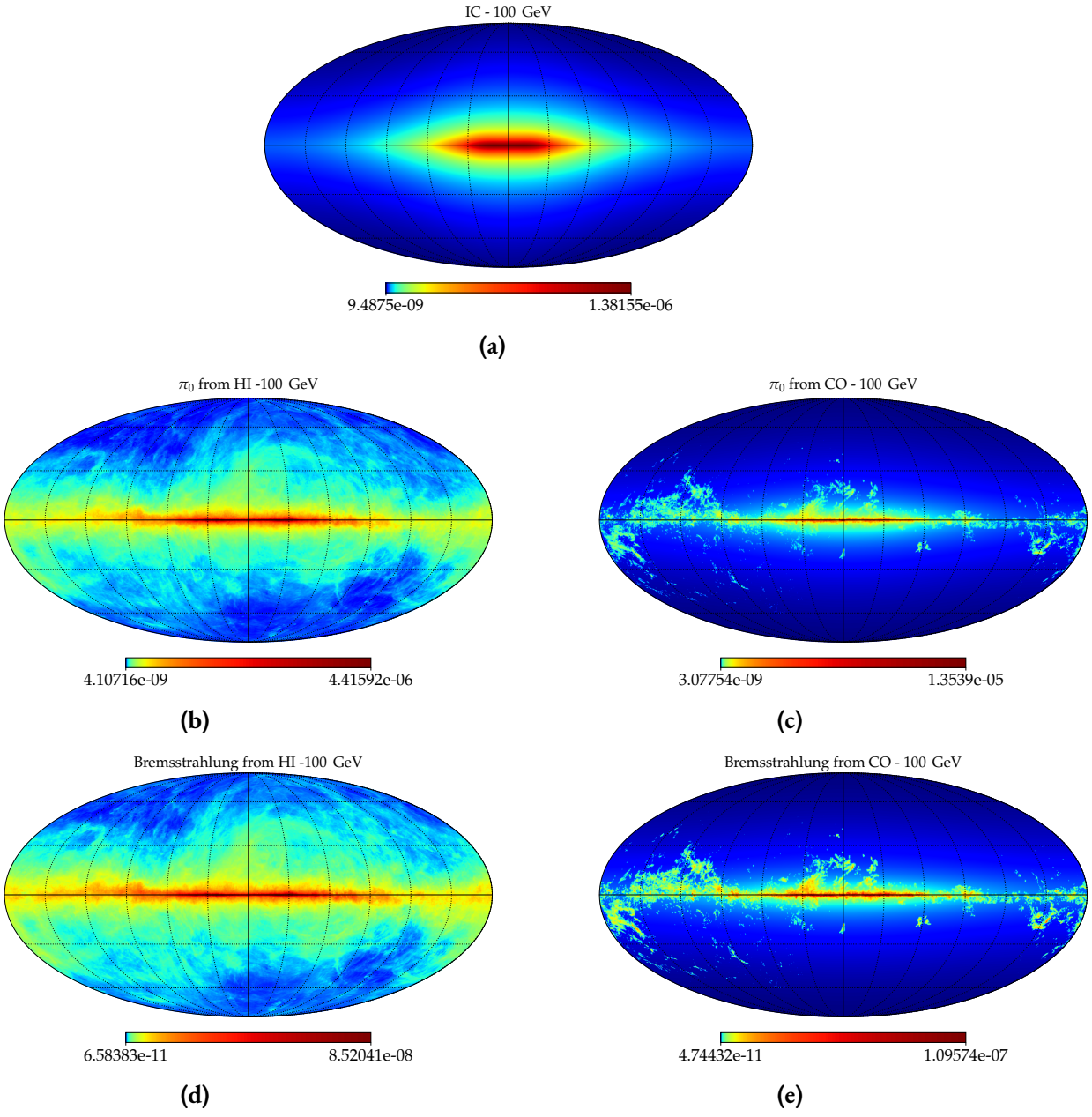

Figure 2.6: Photon emissivities due to **(a)** IC, **(b,c)** pion decay and **(d,e)** bremsstrahlung are shown, for a photon energy $E_\gamma = 100\,\mathrm{GeV}$.

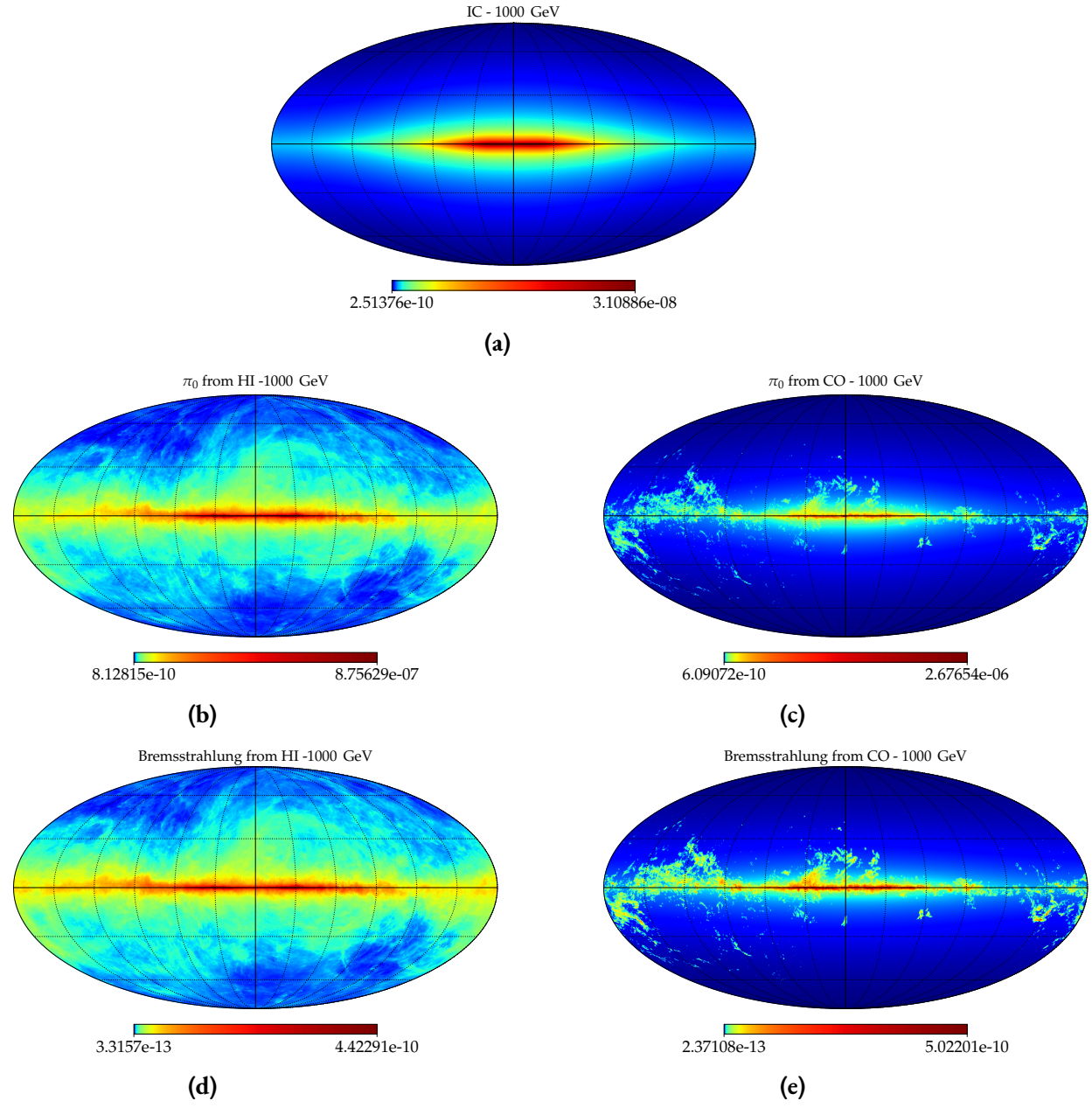

Figure 2.7: Photon emissivities due to **(a)** IC, **(b,c)** pion decay and **(d,e)** bremsstrahlung are shown, for a photon energy $E_\gamma = 1\,\mathrm{TeV}$.

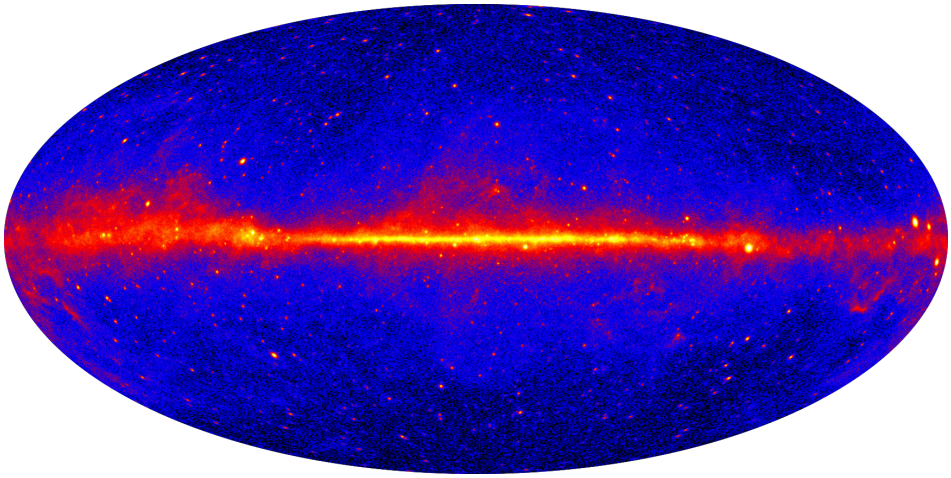

Figure 2.8: Galactic view of the γ-ray sky, after 5 years of data taking from *Fermi Gamma-ray Space Telescope*. The map shows photon emission above $E_\gamma = 1\,\mathrm{GeV}$, mainly due to $\pi^0 \to \gamma\gamma$ decay with IC contamination. Clearly visible is the intense emission from the Galactic plane. Credit: `NASA Goddard Media Studios`.

rays. Models on the cosmic-neutrino flux predict indeed $\frac{dN_\nu^{\mathrm{cosm}}}{dE} \propto E^{-2.15}$ (Loeb and Waxman, 2006). To discriminate the two components, neutrino telescopes are typically built where they can be shielded: this can be done with underground detectors such as *SuperKamiokande*[*] in Japan, or with detectors aiming at observing only one half of the Galactic hemisphere, the one shielded by the Earth. This is the case of *IceCube*[†] at the South Pole, in joint collaboration with the northern-hemisphere telescope *ANTARES*[‡].

So far, the overall signal-distribution on the sky is consistent with being isotropic, although a weak hint (2σ significance) has been found to correlate the diffuse neutrino background with the Galactic plane (Aartsen et al., 2019; Albert et al., 2018) at energies above $E_\nu \sim 100\,\mathrm{TeV}$, within a framework where a radial dependence of the diffusion coefficient is introduced, as in Gaggero et al. (2017). With this regard, we notice that the possibility to improve the accuracy of γ-ray and neutrino joint observations around the Galactic center has important implications on the cosmic-ray diffusion (Pothast et al., 2018). In fact, as seen in Section 2.1, a vertical component of the Galactic magnetic field could be significant in this region, leading to a different scaling of the diffusion coefficient with rigidity.

In conclusion, a joint effort of the *multi-messenger* community is now acknowledged to be of

[*] `http://www-sk.icrr.u-tokyo.ac.jp/sk/index-e.html`
[†] `https://icecube.wisc.edu/`
[‡] `https://antares.in2p3.fr/`

paramount importance for the understanding of the astrophysical environments so far unaccessible to the observatories, as well as of the physics of the cosmic-ray transport, still far from being completely understood.

2.4 Summary of the chapter

In this chapter, we described the overall structure of the DRAGON numerical code that will be used in the following parts of the thesis to solve the cosmic-ray transport equation for the CR diffuse component. First, we discussed the physical model-settings regarding the Galactic environment: in particular, a cylindrically symmetric Galaxy and an azimuthal magnetic field are adopted. Then, we presented in detail the physical ingredients implemented in the transport equation, paying particular attention to the physics of the energy losses that are suffered by both hadrons and leptons. In fact, energy losses are often accompanied by the production of secondary γ-rays and neutrinos, that can serve as informative tracer of the passage of the charged particles in both photon- and matter-gases. With this regard, we have shown that γ-ray emission is concentrated on the Galactic plane, correlating photon emission with the sources of cosmic rays and the gas distribution, while neutrino signal is so far compatible with an isotropic distribution. The necessity of further clarifying this secondary emission, especially in the region around the Galactic center, justifies the joint effort recently born with the name of *multi-messenger* astrophysics.

Part II
Impact of local sources on the hadronic and leptonic spectra

3

Features in the lepton spectra set the ground for a hidden nearby source

In this chapter, we interpret the most relevant cosmic-ray observables — namely B/C ratio, fluxes of protons and light-nuclei, leptonic spectra — in a numerical setup based on the physical ingredients discussed in the previous chapter. As seen above, even though the interstellar environment is modeled in light of independent experimental observations, particles are injected and propagate according to a transport framework that is driven by phenomenological considerations, namely is set on the data. With this regard, we solve the transport equation with the DRAGON numerical solver, identifying a small number of free parameters the allow to tune the model on the most recent data, both modulated and unmodulated. On top of this large-scale background, when considering the well-known *excess in the positron fraction* and observing a missing flux in the electron as well, we study the leptonic spectra as coming from discrete sources. In doing so, we treat the positron and electron fluxes independently, assuming that they are injected by two different classes of sources. In particular, we fit the e^+ flux assuming a pulsar origin, implementing an injection spectrum typical of the already-mentioned magnetic-reconnection mechanism; on the other hand, e^- are believed to be of SNR origin, with an injection typical of the DSA mechanism.

3.1 Motivations

As mentioned in some of the previous sections, several experiments have recently provided accurate measurements of the leptonic (e^-, e^+ and $e^+ + e^-$) cosmic-ray spectra up to $\sim \mathcal{O}(10)$ TeV and have revealed significant — as well as unexpected — features.

Regarding the e^-, we point out in particular that the AMS-02 spectrum exhibits a hardening at $\simeq 40$ GeV (Aguilar et al., 2019a). At even higher energies, H.E.S.S. (Aharonian et al., 2009; Kerszberg, 2017), DAMPE (Ambrosi et al., 2017) and CALET (Adriani et al., 2018) measured the $e^- + e^+$ spectrum up to $\simeq 20$ TeV and outlined a sharp softening at $\simeq 1$ TeV. Above that energy, the power-law spectrum extends, with no clear sign of cutoff, all the way up to the maximal detected energy.

On the e^+ side, we know that a guaranteed flux is expected due to the interaction of CR nuclei (mainly protons and Helium) with the ISM gas — this is the secondary-positron component. This contribution is expected to decrease with respect to the $e^- + e^+$ flux as energy increases (Blasi, 2013). However, the discovery of the opposite trend in the positron fraction above 10 GeV by PAMELA (Adriani et al., 2009), later confirmed and better characterized by AMS-02 (Aguilar et al., 2013), was then corroborated by the measurement of the absolute e^+ spectrum by both experiments (Adriani et al., 2013; Aguilar et al., 2014a). This result showed that the anomaly cannot be attributed to a steeper-than-expected e^- spectrum, but instead that a primary origin of Galactic high-energy positrons needs to be identified. As discussed in a long series of papers (see *e.g.* Blasi and Amato (2011); Grasso et al. (2009); Harding and Ramaty (1987); Hooper et al. (2009)), the electron+positron pairs accelerated at *Pulsar Wind Nebulae* (PWNe) provide a reasonable explanation for this flux, both in terms of energy budget and spectral shape. With this regard, we notice that a scenario invoking PWNe as the origin of the positron excess has recently been further debated after the detection of TeV γ-ray halos around the Geminga and Monogem nearby pulsars by HAWC (Abeysekara et al., 2017) and by *Fermi*-LAT (Di Mauro et al., 2019), interpreted in terms of IC emission from a fresh population of electrons and, plausibly, positrons (Hooper et al., 2017), confined in the vicinity of those pulsars. Also, recent studies conducted on bow-shock wind nebulae associated to a nearby (~ 150 pc) millisecond pulsar (BSWN) discuss the contribution to the positron excess coming from those compact objects, and to the all-lepton flux as well coming from the shocked medium (Bykov et al., 2019). Finally, several times in the literature, outflows of relativistic leptons have been reported in correspondence to fast neutron stars: see for instance the Guitar Nebula (Cordes et al., 1993) and the Lighthouse nebula (Pavan et al., 2014).

The accurate measurement the leptonic features described above may offer valuable clues on the ages/positions of the potential sources, as well as on the details of the CR transport. In fact, given the $\propto E^2$ scaling of the leptonic energy-loss rate, the effective *horizon* associated to the CR leptons progres-

sively shrinks as energy increases, hence the stochastic nature of the sources is expected to play a more and more important role with increasing energy. This trend implies even more pronounced features at high energies, as noticed already in Shen (1970) and further elaborated in more recent times (Aharonian et al., 1995; Kobayashi et al., 2004).

We point out however that, in light of these recent observations, a unified picture of the leptonic observables embedded in an up-to-date transport scenario is still lacking. Here, we propose a significant step forward towards such a picture and provide a comprehensive, state-of-the-art discussion about the origin of these spectral features and their connection with the physical properties of the nearby accelerators. The key elements of novelty are the following: (i) Regarding the interpretation of the positron flux, in the context of the PWN-origin scenario we account for the large and often unaccounted uncertainties due to the unknown details of the emission process (unknown acceleration spectrum; unknown duration of the emission). (ii) Regarding the interpretation of the all-lepton flux, we implement some realistic realizations of the scenario proposed in Recchia et al. (2019) in which the $e^{\pm}$ flux above the $\sim$ TeV is dominated by the emission of a hidden, middle-aged remnant with declining luminosity. After a careful assessment of the contribution of the known nearby supernova remnants, we show that the emission of such hidden SNR is required to reproduce the spectral feature reported by H.E.S.S. and characterize its properties.

The chapter is structured as follows. In Section 3.2, we first identify a transport scenario that provides a satisfactory description of light-nuclei CR-data released by AMS-02 mostly, solving the transport equation with the DRAGON code. Such step is required to fix the diffusion parameters that will enter in determining the shape and features of the propagated lepton spectra. Then, in Section 3.3, we turn our attention to the positron flux and model its observed spectrum in terms of (i) a conventional secondary component produced by hadronic spallation, (ii) a primary extra-component that dominates at intermediate energies and originates by a large number of distant, old pulsars, (iii) and one or few nearby pulsars as the main possible contributors at high-energies. Finally, in Section 3.4, we concentrate on the all-lepton data and analyze the contributions from nearby asymmetric accelerators within the same transport scenario.

3.2 Characterization of the large-scale CR transport scenario

In this section we settle the cosmic-ray transport setup that will be adopted throughout the chapter. This will allow to account for the diffuse component of each of the considered CR observables and is computed with DRAGON, according to the modelization described in detail in Section 2.2. As anticipated, our runs are performed in a 2D cylindrically symmetric approximation of our Galaxy.

3.2.1 Setting source and transport parameters against CR nuclei data

While gas density, magnetic- and *interstellar-radiation-field* distributions are fixed (though with some uncertainties) on the basis of astronomical data, CR injection spectra and diffusion parameters are largely unknown and have to be settled by comparing DRAGON predictions with CR data. We use here AMS-02 data for almost all species (Aguilar et al., 2015a; Aguilar et al., 2017) and for the B/C ratio (Aguilar et al., 2016), complemented with Voyager data (Cummings et al., 2016) for low-energy protons and other nuclei. Finally, HEAO-3 (Binns et al., 1989) data are considered to determine the normalization of nuclear species heavier than Nitrogen.

Voyager data (below $1\,\mathrm{GeV/n}$) are collected outside the Heliosphere, allowing us to tune the low-energy injection spectra without being affected by solar modulation. This is here taken into account within the *force-field* approximation (Gleeson and Axford, 1968), introducing a new parameter referred to as *modulation potential* $\phi_{\rm mod}$.

Once the injection spectra are fixed, we are able to constrain the value of $\phi_{\rm mod}$ by fitting the low-energy ($\lesssim 10$ GeV/n) AMS-02 modulated data. The values of $\phi_{\rm mod}$ that we obtain are consistent with the independent measurement performed at ground-based detectors (Usoskin et al., 2005, 2011).

With this cross-checked estimation of $\phi_{\rm mod}$ at hand, we can connect with the intermediate-energy ($E > 10\,\mathrm{GeV/n}$) AMS-02 points, and conclude that a first injection break at low energy ($E \lesssim 10\,\mathrm{GeV/n}$) is required to reproduce the proton/nuclei data. This procedure is very important because (i) it justifies the presence of a low-energy break also in the e^- spectrum (although we are agnostic here about its physical origin) if we consider a common origin for CR protons/nuclei and electrons (*e.g.* SNRs); (ii) it validates the values used for the modulation potential, which significantly affects the leptonic spectra all the way up to ~ 30 GeV.

A second break has to be implemented in the hadronic species at a few hundred of GeV, as reported by the AMS-02 observations cited above. The origin of this break is still under debate. However, the more pronounced hardening found in secondary nuclei seems to point towards a diffusive origin, and the physical interpretations proposed so far deal with a different nature (Evoli et al., 2018a) — or behaviour (Yan and Lazarian, 2002a, 2004, 2008) — of the turbulent cascade in the halo and in the disk. We will discuss this topic in details in the next chapters.

Given that the propagated spectrum of the primaries scales as $\sim E^{-\Gamma_{\rm inj}-\delta}$ above $\sim \mathcal{O}(10)$ GeV, we effectively mimic the diffusive break with a break in the injection. We notice that this choice leads to a slightly underestimated production of secondaries at energies of the order $\sim \mathcal{O}(100)\,\mathrm{GeV}$. However, for what concerns the B/C ratio, this affects the interpretation of the last data points only — where they are more uncertain. Therefore, for the purpose of this chapter, this approximation does not produce a

sizeable effect and is completely equivalent to implementing a break in the diffusion coefficient. Indeed, here we aim at building a background model to study the role of nearby sources. We will see instead that it will play a central role in the results presented in Chapter 4.

On the other hand, we emphasize that a completely different treatment is required for primary leptons: in fact, at $\sim \mathcal{O}(100)$ GeV, leptons are mostly coming from the local region, so they spend most of their time in the same galactic environment. For this reason, no spectral break is likely present in the primaries and we choose to model the smooth leptonic component as a single power-law in rigidity above ~ 10 GeV, as it will be seen in Section 3.2.2.

In order to implement what discussed above, we performed several two-dimensional runs with DRAGON in a grid with 41 linearly spaced points along the radial axis $R \in [0, 12]$ kpc and 81 linearly spaced points in the vertical axis $z \in [0, \pm 4]$ kpc, where we propagated particles of energy $E_{\rm k} \in [10\,{\rm MeV}, 30\,{\rm TeV}]$, logarithmically spaced according to $E_{\rm k}[i] = \exp(\ln(E_{\rm k,min}) + i\,\ln(E_{\rm k,factor}))$, where $E_{\rm k,factor} = 1.2$ GeV. Based on this setup, we identify a satisfactory scenario, characterized by the parameters listed in Table 3.1. As reported there, and also shown in Figures 3.1a and 3.1b, the observed spectra are reproduced introducing a low-energy break at 7 GeV/n, for all species, and a high-energy hardening at $335(165)$ GeV/n for protons (heavier nuclei). We note that this break is required also to match the Voyager unmodulated data, therefore is not related to the solar modulation.

	$v_{\rm A}$ [km/s]	D_0 [cm^2/s]	δ	$\Gamma_{\rm inj,l}$	$E_{\rm b,1}$ [GeV/n]	$\Gamma_{\rm inj,m}$	$E_{\rm b,2}$ [GeV/n]	$\Gamma_{\rm inj,h}$
p	13	$1.98 \cdot 10^{28}$	0.45	1.8	7	2.4	335	2.26
He				2.0		2.28	165	2.15
C				2.0		2.38	165	2.15
O				2.0		2.38	165	2.15

Table 3.1: The table reports the injection parameters of our reference transport model. The labels (l,m,h) refer to *low*, *medium* and *high* energy injection indices.

It should be noted that an approximate degeneracy holds between the diffusion coefficient normalization and the diffusive-halo height-scale H since the CR escape time, hence the secondary/primary ratio, only depends on the ratio D_0/H. In this chapter we use $H = 4$ kpc. We notice that a different choice of H within a wide range of allowed values has no significant effect on the electron spectrum and may affect the positron spectrum only below ~ 10 GeV (see Figure 4 in Di Bernardo et al. (2013)) with no impact on the results of this analysis.

Similarly to the results reported in Di Bernardo et al. (2010), and — more recently — in Génolini et al. (2019); Yuan et al. (2017), the B/C ratio is nicely matched for a value of δ close to 0.45. Performing

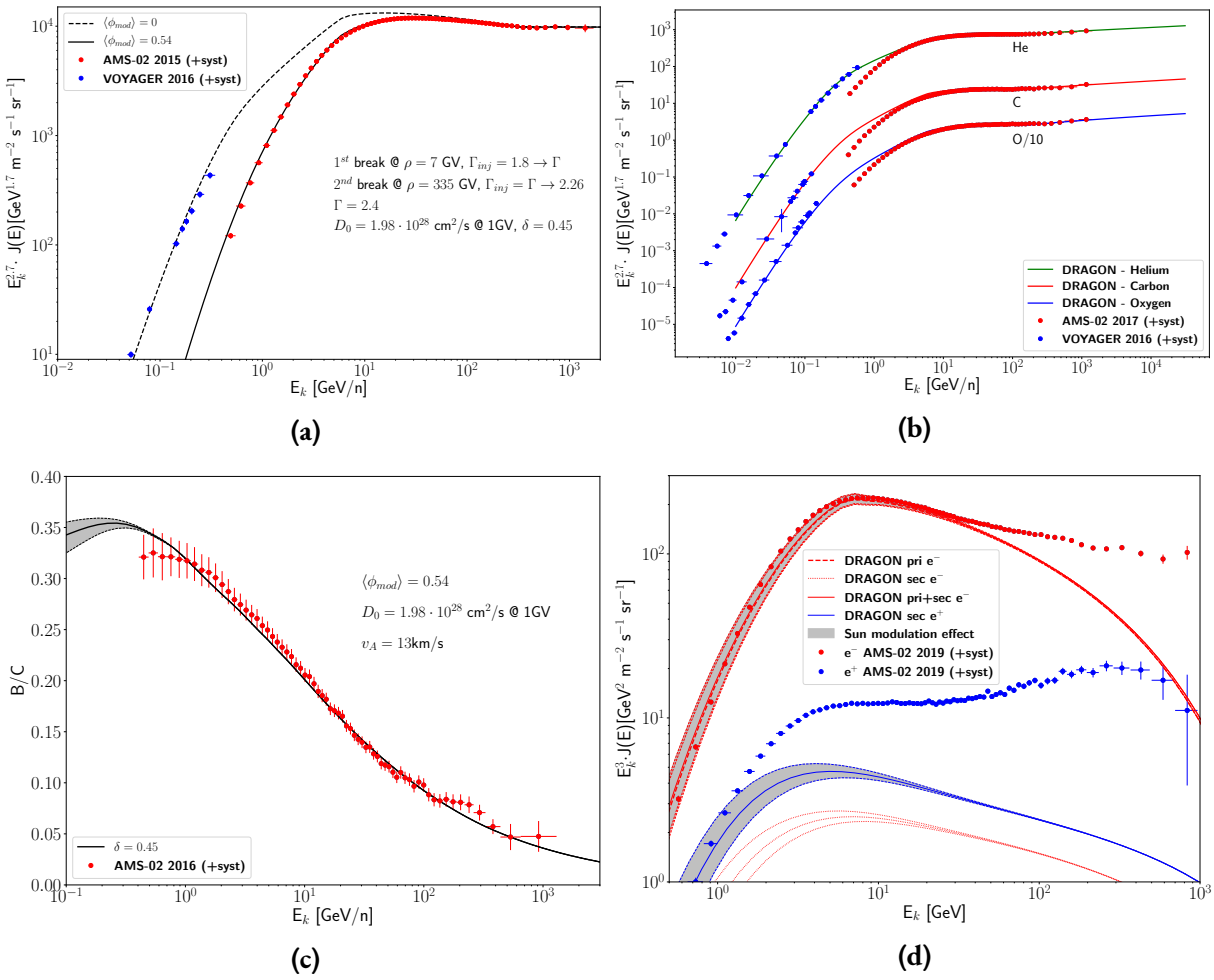

Figure 3.1: The propagated spectra computed with our reference model of **(a)** protons, **(b)** Helium, Carbon and Oxygen (Oxygen flux is divided by 10 for clarity) are compared with AMS-02 (Aguilar et al., 2015a; Aguilar et al., 2017) (accounting for solar modulation) and Voyager (Cummings et al., 2016) (interstellar) data. For Voyager C and O data, data points may overlap due to measurements coming from different telescopes and modes (denoted as TT in the reference). In **(c)** the B/C ratio is computed for the same model and is plotted against AMS-02 experimental data (Aguilar et al., 2016). **(d)** Primary and secondary e^- and e^+ spectra computed with DRAGON accounting only for the contribution of distant SNRs and secondary production in the ISM. The red and blue dots are AMS-02 experimental data (Aguilar et al., 2019a; Aguilar et al., 2019). The silver band accounts for the solar modulation $\langle\phi_{\rm mod}\rangle = 0.54 \pm 0.10$, estimated according to Usoskin et al. (2005, 2011) for the whole period of data taking.

a statistical analysis aimed at the determination of the uncertainties in the propagation parameters, involving the full set of secondary/primary ratios, is beyond the aims of what discussed in this thesis. We mention however that varying the main parameters in the small allowed ranges found in Génolini et al. (2019) would have no relevant impact on the electron and positron spectra and therefore on the conclusions derived in this chapter.

3.2.2 Primary electrons and secondary positrons

In the standard CR transport scenario, the Galactic SNRs are expected to generate the bulk of the observed CR electrons as well. Moreover, as seen in Section 2.2.2, a guaranteed source of secondary electrons and positrons is provided by the scattering of CR nuclei — mostly protons and ^{4}He — with the ISM gas.

For what concerns the primary electrons, we remark that, although the acceleration mechanism is expected to be the same as the one at work for the nuclear species, the injection spectrum into the ISM should be steeper (with $\Delta\Gamma$ as large as ~ 0.4) due to synchrotron losses in the SNR magnetic field, which is also amplified by CR-induced turbulence (Diesing and Caprioli, 2019). We notice that the DRAGON output is in good agreement with analytical computations (Bulanov and Dogel, 1974; Lipari, 2019a) predicting a propagated spectral index $\Gamma = \Gamma_{\rm inj} + \frac{\delta}{2} + \frac{1}{2}$ above few GeV. We compute the propagated spectra at Earth with DRAGON adopting the setup derived in the previous paragraph and implementing an electron injection spectrum $\Gamma^e_{\rm inj} = 2.7$ (1.6) above (below) 7 GeV. This allows to reproduce the measured spectrum up to ~ 50 GeV, above which it displays a pronounced hardening (see Figure 3.1d).

It is our opinion that such feature corresponds to the expected breakdown of the assumption of a continuous, steady-state source term that characterizes the large-scale models developed with DRAGON. Indeed, the mean distance of active SNRs from the Earth is expected to be of few kpc's. As a consequence, we expect that already above ~ 100 GeV the energy losses will limit the number of SNRs contributing to the observed CR electron flux to just a few. The contribution of individual CR electron sources will be discussed in detail in Section 3.4.

Regarding the secondary positrons, they are computed with DRAGON as well, within the same transport setup. The result is also reported in Figure 3.1d. The plot clearly shows evidence of the well known *positron excess* above ~ 40 GeV, pointed out since the first release of the PAMELA data (Adriani et al., 2009). However, differently from other previous works (see *e.g.* Moskalenko and Strong (1998); Strong and Moskalenko (1998)), we find an excess at all energies above ~ 1 GeV: this is consistent with other dedicated analyses, such as Boudaud et al. (2017).

Even though alternative CR propagation scenarios may be invoked to account for the unexpected production of positrons (Lipari, 2017), as well as interpretations based on dark matter annihilation (see

for instance the recent review Gaggero and Valli (2018) and references therein), lepton pair emission from pulsar wind nebulae seems to be a more natural candidate. We will assess their contribution in the next paragraph.

3.3 The positron excess

In this section we focus on positron data and present a detailed discussion on their possible interpretation. In particular we address from the phenomenological point of view the role of local and distant sources of relativistic electron+positron pairs, such as *pulsar wind nebulae*: we discuss whether a scenario in which the positron flux is dominated by this class of sources is viable (both from the point of view of the energy budget and of the spectral features) and assess whether the current data allow us to pinpoint which PWNe are most likely to contribute in the different energy ranges.

3.3.1 Basic aspects of injection pulsar wind nebulae and relevant caveats

Pulsar wind nebulae are structures born inside the shells of supernova remnants, which emit a broadband spectrum of non-thermal radiation powered by fast-spinning magnetized neutron stars with a typical radius $R \sim 10$ km and periods of $\mathcal{O}(0.1 - 10)$ s, typically detected in the radio and/or gamma-ray band as *pulsars*.

As mentioned in Section 3.1, the role of pulsars and PWNe as relevant and efficient antimatter factories in the form of $e^{\pm}$ pairs and their contribution to the detected all-lepton flux have been debated for a long time in the literature, since the pioneering works of the past century (Atoyan et al., 1995; Harding and Ramaty, 1987; Shen, 1970). We will recall in this section some important aspects of the physics that characterizes these objects, in order to motivate our phenomenological parameterization of the problem.

To characterize the emission from a PWN, it is important to assess: 1) the energy release as a function of time, and 2) the acceleration mechanisms of the electron+positron pairs, hence the energy spectrum of such leptons when they are eventually released in the *interstellar medium*.

1. Regarding the former, we recall that the pulsar spin-down is usually described by the following model-independent equation:

$$\dot{\Omega}(t) = -\kappa_0 \cdot \Omega(t)^n, \tag{3.1}$$

where $\Omega(t) = P^{-1}(t)$ is the rotation frequency, κ_0 and n are parameters that depend on the specific energy-loss process; in particular n is commonly called *braking index*.

This equation can be solved to get $\Omega(t)$ and the time evolution of the luminosity, which, in terms of the conversion efficiency ($\eta^{\pm}$) of the released energy into $e^{\pm}$ pairs, can be written as follows:

$$L(t) = I\Omega(t)\dot{\Omega}(t) = \frac{\eta^{\pm} L_{0,\gamma}}{\left(1 + \frac{t}{\tau_0}\right)^{\frac{n+1}{n-1}}} \tag{3.2}$$

where $\tau_0 \equiv \frac{1}{(n-1)\kappa_0 \Omega_0^{n-1}}$ and t is the age of the source.

Under the assumption that at present time the pulsar rotation period is $P(t) \gg P_0 \equiv P(t=0)$, we can approximate t with its *characteristic age*, $t_{\rm ch} \approx \frac{P}{(n-1)\dot{P}}$ (Roberts et al., 2005).

According to Equation (3.2), the release process is regulated by the ratio $t_{\rm ch}/\tau_0$. When $t_{\rm ch}/\tau_0 \ll 1$, we can Taylor-expand the function $L(t) \approx \eta^{\pm} L_{0,\gamma}\,(1 - \frac{n+1}{n-1} \cdot t_{\rm ch}/\tau_0^{\rm MD})$ and approximate the luminosity as a constant over time. In the opposite limit $t_{\rm ch}/\tau_0 \gg 1$, the luminosity drops very fast and we can see the injection as a burst.

If the energy-loss mechanism responsible for the spin-down were exclusively magnetic dipole (MD) emission, then the braking index would be $n = 3$ (Roberts et al., 2005) and the characteristic timescale of the frequency (and luminosity) drop would be given by $\tau_0^{\rm MD} = \frac{3Ic^3}{B^2 R^6 \Omega_0^2}$, where I is the moment of inertia of the spinning neutron star, B is the surface magnetic field, Ω_0 is the initial frequency.

For all the nearby pulsars tabulated in the ATNF catalogue* (Manchester et al., 2005), the ratio $t_{\rm ch}/\tau_0^{\rm MD}$ given above is typically one order of magnitude lower than 1 (~ 0.3), which would point towards a constant-luminosity injection.

However, n can be inferred only when observations are long enough to allow the derivation of all three quantities $\Omega, \dot{\Omega}, \ddot{\Omega}$. For this reason, they are available for a limited number of cases only (Hamil et al., 2015), and in each of them the results show values of $1.9 < n < 2.8$, significantly different from the ideal MD model. Moreover, a comparison between the energy budget released by the pulsars calculated via MD-emission with the same quantity derived by observations, independently of the emission model, reveals significant discrepancies, as discussed in detail in Appendix 3.A3. Finally, even if the constant-luminosity injection were a good approximation, it would become progressively more unreliable for increasing pulsar age.

For these reasons, we are led to conclude that other energy-loss mechanisms, rather than MD-emission only, might be at work. Thus, in the following we will consider only the model-independent equations (3.1)-(3.2) and study the two limiting cases of burst-like (discussed many times in the literature) and constant-luminosity injection of $e^{\pm}$, in order to bracket the above-mentioned uncertainty.

*http://www.atnf.csiro.au/people/pulsar/psrcat/

2. As far as the acceleration spectrum is concerned, we recall that the broad-band radiation emitted by PWNe can be typically modeled as synchrotron and IC emission from a population of relativistic electrons and positrons distributed in energy as a broken power-law. These leptonic pairs, initially extracted by the surface of the neutron star, are then most likely accelerated at, or close to, the termination shock (TS) by a variety of possible mechanisms.

   The current data probing the non-thermal radiation (in *Radio* and *X-ray* frequencies) emitted from several well-observed PWNe (Jankowski et al., 2018) require a lepton spectrum which has the shape of a broken power law, with a hard spectrum (with slope $1 \lesssim \Gamma_{\rm inj} \lesssim 2$) below a break at $\sim 200 - 400$ GeV, and a steeper one ($\Gamma_{\rm inj} > 2$) at larger energies (see Amato (2014); Blasi and Amato (2011); Bucciantini et al. (2011); Bykov et al. (2017)). The hard, low-energy spectrum has been object of debate over the years, and several acceleration mechanisms were proposed, including magnetic reconnection and resonant absorption of ion-cyclotron waves.

   Motivated by these considerations, in the following we will adopt both a broken power-law and a single power law with exponential cutoff and compare our result with those obtained in several previous analyses (see for instance the recent reviews Gabici et al. (2019); Gaggero and Valli (2018) and the references therein).

As a final remark, we point out that the particles are expected to be released from the PWN region with some delay. A minimal contribution to this delay is given by the time the pulsar — due to its proper motions — takes to leave the associate SNR shell, which we estimate to be $t_{\rm rel} = 6.4 \cdot 10^4$ yr for pulsars (see Appendix 3.A1). That estimate could be even larger if we were to take into account the results of recent analyses of the HAWC (Abeysekara et al., 2017) and *Fermi*-LAT (Di Mauro et al., 2019) data for the Geminga and Monogem regions, showing that $e^{\pm}$ diffusion may be even more delayed around those objects — this was mentioned in Section 1.1. However, the possible consequences of these pockets of slow diffusion (the TeV-*halos*) around PWNe still have to be determined. In fact, while Profumo et al. (2018), for instance, states that a two-zone model separating the TeV-*halo* from the rest of the ISM still allows positrons from Geminga and Monogem to reach the Earth, in another recent study (Johannesson et al., 2019) the authors argue that the same result depends on the size and other properties of the halo. We believe that the growing interest of the community in these TeV-*halos* will lead to dedicated observations of other similar high-confinement regions, in order to establish if they are present around each PWN, as already outlined in Linden et al. (2017). Collecting more statistics will eventually allow to infer their physical properties and to shed light on the puzzle of the positron origin.

3.3.2 Diffusive propagation of leptons in the Galaxy: study of the analytical solution

With the parametrization of the source term and the delay of the particle release properly settled, we now turn our attention to the propagation of the electron+positron pairs from individual sources in the ISM.

We describe the transport process by means of a simplified version of the transport equation (2.1), where low-energy effects such as advection and reacceleration are neglected. In fact, comparing the timescales for diffusion $\left(\tau_{\rm diff} = \frac{H^2}{2 \cdot D(E)}\right)$ and advection $\left(\tau_{\rm adv} = \frac{H}{v_{\rm A}}\right)$ for typical ISM conditions — we have $v_A \sim \mathcal{O}(1-10)\,{\rm km \cdot s^{-1}}$, see Section 2.2.1) —, a Halo size of $H = 4$ kpc and a diffusion coefficient here invoked as $D(E) = 1.98 \cdot 10^{24} \left(\frac{E}{1{\rm GeV}}\right)^{0.45}\,{\rm m^2/s}$, we see that advection contributes to the CR transport only below $\sim$ 100 MeV. As we are interested in a high-energy regime (above $\sim$ 1 GeV), we can neglect the advection term and write the transport equation in polar coordinates as follows:

$$\frac{\partial N(E,t,r)}{\partial t} = \frac{D(E)}{r^2}\frac{\partial}{\partial r} r^2 \frac{\partial N}{\partial r} + \frac{\partial}{\partial E}(b(E)N) + Q(E,t,r), \tag{3.3}$$

where $Q(E,t,r)$ is the source term, $b(E) \equiv \frac{dE}{dt}$ the rate of energy-loss, and $N(E,t,r)$ is the usual particle number density per unit energy.

The loss term, in general, takes into account a variety of processes: ionization, Coulomb scattering, bremsstrahlung, Inverse Compton, synchrotron. Whereas the DRAGON setup properly accounts for all of them (see Section 2.2.1), in this section we approximate $b(E)$ with the following expression:

$$\frac{dE}{dt} \simeq -b_0\, E^2 \tag{3.4}$$

with $b_0 = 1.4{\cdot}10^{-16}\,{\rm GeV^{-1}\,s^{-1}}$, corresponding to a typical local interstellar gas density of $n_{\rm ISM} = 1\,{\rm cm^{-3}}$ and a total magnetic field $B_{\rm tot} = 5\,\mu G$, compatible with a recent analysis (Sofue et al., 2019). This expression captures the dominant leptonic processes (Inverse Compton and Synchrotron) in the local environment, as far as the energy range of interest for the present work is concerned ($E > 1\,{\rm GeV}$). It is worth mentioning that, although a full numerical treatment of the energy losses for relativistic leptons would require a correction to the $\propto E^2$ scaling due to the Klein-Nishina calculation of the IC scattering (Blumenthal and Gould, 1970), the authors of Delahaye, T. et al. (2010) showed that the propagated spectra would change only up to a factor of $\sim$ 1.5 in normalization for the adopted value of $B_{\rm tot}$ (see their Figure 2). This uncertainty does not affect the results presented in this chapter, therefore we neglect the full treatment.

Equation (3.3) can be solved analytically following the general treatment in Atoyan et al. (1995), for different injection scenarios.

Under the assumption that the emitting source is point-like, the Green-function approach to solve the equation gives the general solution (Berezinsky et al., 1990):

$$N(r,t,E) = \frac{Q(E_{\rm t})b(E_{\rm t})}{\pi^{3/2}b(E)r_{\rm diff}^3}\cdot e^{-\frac{r^2}{r_{\rm diff}^2}}, \tag{3.5}$$

where we drop the dependence of the source term Q on t and r for simplicity. $E_{\rm t}$ refers to the energy at a time $(t-t_{\rm rel})$ ago, that, given the currently-measured energy E and the rate of energy-loss $b(E) = -b_0E^2$, is $E_{\rm t} = \frac{E}{1-b_0(t-t_{\rm rel})E}$. Therefore, the solution in Equation (3.5) becomes:

$$N(r,t,E) = \frac{Q(E_{\rm t})}{\pi^{3/2}r_{\rm diff}^3}\cdot\frac{1}{\left[1-b_0(t-t_{\rm rel})E\right]^2}\cdot e^{-\frac{r^2}{r_{\rm diff}^2}}, \tag{3.6}$$

where $r_{\rm diff}^2(E_{\rm t},E) \equiv +4\int_{E_{\rm t}}^{E}\frac{D(E')}{b(E')}dE'$ is the diffusive distance travelled by a particle loosing its energy from $E_{\rm t}$ to E. This solution is still general, in that it does not contain any information about the injection term, that in general can be written $Q(E,t,r) = S(E)L(t)\delta(r)$, where we assume a power-law spectrum with index $\Gamma_{\rm inj}$, $S(E) = S_0\left(\frac{E}{E_0}\right)^{\Gamma_{\rm inj}}$.

Decaying-luminosity injection. When no further information is provided on the luminosity timescale, the decaying-luminosity function is in the general form $L(t) = \frac{L_0}{\left(1+\frac{t}{\tau_{\rm d}}\right)^{\alpha_{\rm d}}}$ — the same form introduced in Equation (3.2) —, where now $(\alpha_{\rm d},\tau_{\rm d})$ are parameters characteristic of the emission mechanism. Integrating over time the expression (3.6), we obtain:

$$N(r,t_{\rm age},E) = \int_{t_{\rm rel}}^{t_{\rm age}}dt'\frac{S(E_{t'})L(t')}{\pi^{3/2}r_{\rm diff}^3(E,E_{t'})}\cdot\frac{1}{\left[1-b_0(t_{\rm age}-t')E\right]^2}\cdot e^{-\frac{r^2}{r_{\rm diff}^2}}, \tag{3.7}$$

where $t_{\rm rel}$ is the release time of the particles.

Equation (3.7) is the most general form of the solution and it can be noticed that, as the integration over time is not performed yet, any injection feature can still be easily implemented in the expression of $S(E)$. In particular, throughout this and the following chapters we use source features such as an exponential cutoff or a break in the power-law:

- $S(E) = S_0\left(\frac{E}{E_0}\right)^{\Gamma_{\rm inj}}\cdot e^{-\frac{E}{E_{\rm cut}}}$
- $S(E) = S_0\left(\frac{E}{E_0}\right)^{\Gamma_{\rm inj}}\cdot\left(1+\left(\frac{E}{E_{\rm break}}\right)^{|\Delta\Gamma_{\rm inj}|\cdot s}\right)^{{\rm sign}(\Delta\Gamma_{\rm inj})/s}$,

where $\Delta\Gamma_{\rm inj}$ is the change in the injection index and s a parameter that regulates the sharpness of the change in the slope. It can be easily seen that in the two limits $E \ll E_{\rm break}$ and $E \gg E_{\rm break}$ we find the two different power-laws.

Constant-luminosity injection. This is a physical scenario that corresponds to the limiting case of

(3.7) where the luminosity timescale τ_0 is much larger than the age of the source. Based on this, the luminosity function can be approximated by $L(t) \to L_0 dt$.

Beside, if the injection function $S(E)$ does not have any dependence on time, the integral is easily performed and the solution takes the form:

$$N(r, t_{\rm age}, E) = \frac{L_0 S(E)}{4\pi D(E) r} \cdot \mathrm{erfc}\left(\frac{r}{\sqrt{4D(E)(t_{\rm age} - t_{\rm rel})}}\right), \tag{3.8}$$

with $\mathrm{erfc}(x) = \frac{2}{\sqrt{\pi}} \int_x^\infty e^{-t^2} dt$ the complementary error-function.

Burst-like injection. This scenario corresponds to the opposite limit with respect to the previous one, namely the case where τ_0 is much smaller than the age of the source. The luminosity function is therefore $L(t) \to L_0 \delta(t - t_{\rm rel}) dt$, and the solution (3.7) basically takes the form of the integrand function:

$$N(r, t_{\rm age}, E) = \frac{S(E_{t_{\rm age}})}{\pi^{3/2} r_{\rm diff}^3(E, E_{t_{\rm age}})} \cdot \frac{1}{\left[1 - b_0(t_{\rm age} - t_{\rm rel})E\right]^2} \cdot e^{-\frac{r^2}{r_{\rm diff}^2}}. \tag{3.9}$$

It is worth mentioning that any injection features such as the ones discussed before (*i.e.* cutoff and break) can be implemented at this step without worrying about the time integration, due to the presence of the delta function.

The decaying-luminosity and burst-like solutions are valid as long as the condition $1 - b_0(t_{\rm age} - t_{\rm rel})E \neq 0$ holds, which can also be written as $E \neq \frac{1}{b_0(t_{\rm age} - t_{\rm rel})}$. However, this expression represents the maximum energy that a particle can have after a time $(t_{\rm age} - t_{\rm rel})$ spent in the Galaxy. Therefore, the condition becomes immediately $E < \frac{1}{b_0(t_{\rm age} - t_{\rm rel})}$. This condition translates into a sharp cutoff in the spectrum for the burst injection and a peak in the case of decaying luminosity. For energies above this peak, the release time $t_{\rm rel}$ grows and the maximum energy becomes larger, even though the normalization decreases, due to the smaller luminosity. This behaviour does not occur for the constant-luminosity scenario, where emission lasts constantly up the current time $t_{\rm age}$, represented indeed by the simpler mathematical condition $t_{\rm age} - t_{\rm rel} > 0$.

For the purpose of what is here described, we are interested in the behaviour of the solution as a function of the age and the distance. A time-decaying luminosity function as given in Equation (3.2), assuming a power-law injection spectrum, yields the solutions plotted in Figure 3.2.

The prominent peak in in each curve is due (at fixed distance) to the interplay between the diffusion dominating at low energy and the energy losses at high energy. While a burst-like injection gives rise to a sharp cutoff above the peak energy, a long-lasting source results in a plateau or even a growing-with-energy behaviour for large values of τ_0 or short distances.

Taking into account the possible presence of a UV cutoff in the source spectrum (see discussion in

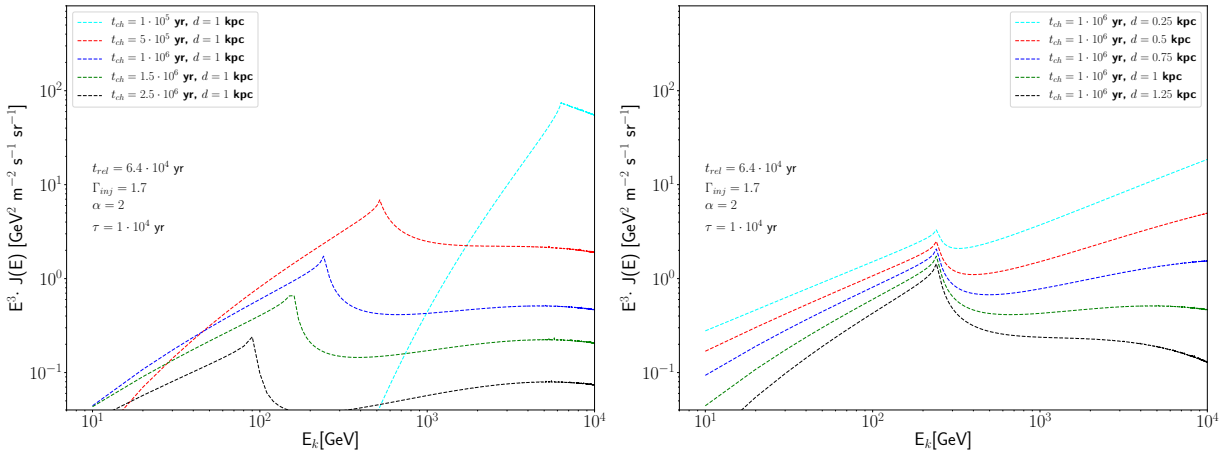

(a) **(b)**

Figure 3.2: Solution of the transport equation for a decaying-luminosity single source, plotted for pulsars of **(a)** different ages and fixed distance (1 kpc) and **(b)** different distances and fixed age ($1 \cdot 10^6$ yr). The order of magnitude of the energy-budget is compatible with the one expected from pulsar emission ($\mathcal{O}(10^{47} - 10^{49}\text{erg})$). The injection index is $\Gamma_{\text{inj}} = 1.7$, although we verified that the shifting is independent of it. As the source age increases, the emission peak shifts to the low-energy range.

the previous paragraph), the peak energy is determined by the condition

$$E_{\max}(t) = \min\left\{\frac{1}{b_0(t - t_{\text{rel}})}, E_{\text{cut}}\right\}, \tag{3.10}$$

where t is the age of the source and t_{rel} the time it takes for particles to leave the source region. Therefore, the peak progressively shifts towards lower energies for increasing PWN ages.

3.3.3 Contribution from old and young pulsars to the positron flux

We start by considering the low-energy part of the positron spectrum and assume that it is originated by a large number of PWNe with age older than $\sim 10^6$ years.

This assumption is motivated by the trend of the peak energy outlined above and by the fact that, below ~ 100 GeV, the diffusion horizon ($d_{\max} = \sqrt{4D(E)(t - t_{\text{rel}})}$) grows up to few kiloparsecs. Within that distance, a very large number of pulsars are observed, and — provided that the diffusive time of their injected particles is smaller than their ages — all of them are expected to contribute to the flux reaching the Earth, at energies that get lower with increasing age, as already outlined in Delahaye, T. et al. (2010). The cumulative spectrum of this "large scale" $e^{\pm}$ component is therefore the convolution of the contributions from many single sources, integrated over their age distribution.

A detailed Monte Carlo simulation of this integrated spectrum is beyond the scope of the present thesis and is postponed to a dedicated work. However, we tested the cumulative contribution from a sample of 10^4 pulsars with ages between 10^6 and 10^8 yr (the sample number is compatible with the

observed SN rate Cappellaro et al. (1999)), assuming that $e^{\pm}$ pairs are injected from these sources with a total energy budget in the $[10^{46} - 10^{49}]$ erg range, and with spectral indices between 1.3 and 1.9. We found that the simulated total spectrum from those sources displays a small scatter for different realizations of the pulsar distribution and — with good approximation — typically follows a smooth power-law.

Motivated by these considerations, we choose to consider an effective modeling of such large scale $e^{\pm}$ component within the DRAGON framework, similarly to what done in previous works (see *e.g.* Di Bernardo et al. (2013)). Therefore, we add to our setup a charge-symmetric smooth *extra-component* with the same spatial distribution of SNRs and tune its normalization and slope ($\Gamma_{\rm extra} = 2.28$) to reproduce the AMS-02 data. It is important to remark that, given the large number of sources involved, the resulting convoluted soft ($\Gamma_{\rm extra} > 2$) spectrum is not related to each single-source hard ($\Gamma_{\rm inj} < 2$) injection.

We now focus on the high-energy part $E > 100$ GeV of the $e^{\pm}$ spectrum which should receive a significant contribution either from relatively young pulsars ($t \lesssim 10^5$ years) or even by older pulsars if they are long lived.

The key aspect in this energy domain is the pronounced drop-off in the positron spectrum observed by AMS-02 above ~ 250 GeV. The considerations discussed so far may lead us to two distinct interpretations of this feature:

- Given the properties of the analytical solution, assuming that no relevant spectral steepening or cutoff is present at the source in this energy range, it is possible to ascribe the feature to the interplay between diffusion and energy loss. This would imply a dominant contribution in this range from a number of pulsar wind nebulae of approximate age of $\sim 10^6$ yr (see Figure 3.2a). Besides, in order to reproduce the above-mentioned drop-off in the data, such PWNe should be at a distance larger than or similar to $\sim \sqrt{4\,D(E = 230\text{GeV}) \cdot (t_{\rm age} = 10^6\text{yr})} \approx 1.5$ kpc (see Figure 3.2b).
- Alternatively, given our knowledge of the injection spectrum of PWNe, summarized in Section 3.3.1, a natural interpretation is that the positron flux around 200 GeV is dominated by few (or one) nearby, young pulsar wind nebulae, which provide a relevant contribution on top of the diffuse, large-scale component discussed above, and is characterized by either a spectral break or a cutoff at that energy, explained by the acceleration processes taking place near the termination shock.

In what follows we will explore the second option. We just mention that detailed Monte Carlo simulations have been recently performed in Cholis et al. (2018)* and in Manconi et al. (2020).

*Interestingly, their model E1 — which is characterized by diffusion and loss parameters very close to those

3.3.4 Characterization of the high-energy flux

We here investigate in further details the case where, on top of the secondary positron flux and a large-scale extra component associated to a large number of old PWNe — as discussed in Section 3.3.3 — the high-energy positron flux is dominated by the contribution from a prominent young object featuring a break or a cutoff in the injection spectrum of $e^{\pm}$ pairs.

In order to do so, we consider four different scenarios, deriving from the combination of two limit behaviours of the luminosity function (*i.e.* burst-like injection and constant-luminosity injection) with the two possibilities for the injection feature (*i.e.* exponential cutoff and break). These are parametrized in the single-source term $Q(E, r, t)$ of the transport equation (3.3).

In each case, the properties of the young, dominant object are assessed by means of a Bayesian fit. The fits are performed with the `PYTHON` module `emcee` (Foreman-Mackey et al., 2013), that is based on the *Markov chain Monte Carlo* (MCMC) approach to build the final *posterior distribution functions* (PDF) organized in form of *corner plots*, that evaluate the goodness of the results (for recent reviews on this topic, see *e.g.* Kruschke and Liddell (2017); Sharma (2017)). Given the corner plot associated to a fit procedure, the best-fit choice of each parameter can be represented by several possibilities:

- the *maximum-a-posteriori* (MAP), namely the peak-value of the posterior distribution function,
- the *mean* value,
- the *median* — also called 0.5-*quantile* —, namely the value dividing the sample in two equal parts.

The choice among these options may depend on the specific situation. For instance, it frequently happens that the PDFs are not well centered in a squared plot (see Appendix 3.A2 for clarity), which means that the choice of the *priors* may not be perfectly compatible with the data. In this case, choosing one between the *mean* and the *median* would not represent the most probable fit-parameter, but only an average over a sample that is not properly constructed. Therefore, for the sake of definitiveness, here we choose to consider the MAP value for each PDF. Note, additionally, that for well-resulting sets of PDFs, the three choices are consistent with each other, within the uncertainties.

We consider data from AMS-02 (Aguilar et al., 2019b) from 20 GeV on, to avoid problems deriving from solar modulation. We set priors on the injection index, that we expect to be $\Gamma_{\rm inj} \in [1, 2]$, and on the critical energy above which we expect the injection feature to come into play, $E_{\rm cut,break} > 150$ GeV. For the burst-like injection we consider the age and distance of the Monogem pulsar, while for the constant-luminosity we use the age and distance of Geminga. This is in accordance to what is shown

adopted in this chapter — predicts a positron fraction steadily growing with energy up to 100 GeV; above that energy, the fraction flattens reaching a maximum at about 300 GeV.

and discussed in Appendix 3.A3, where all the high-energy nearby (within $1.3\,\mathrm{kpc}$) sources are plotted in both injection scenarios, and the dominant contribution is assessed in both cases.

The resulting fluxes are shown in Figure 3.3, where the source terms entering each fit function are shown inside each canvas, and the MAP parameters of the fits are listed in Tables 3.2 and 3.3.

	N_0	$\Gamma_{\rm inj}$	$E_{\rm cut}$ [GeV]	$E_{\rm tot}$ [erg]	$\eta^{\pm}$
Burst	$2.4 \cdot 10^{48}\,[\mathrm{GeV}]^{-1}$	1.31	270.78	$2 \cdot 5.39 \cdot 10^{46}$	0.8
L_0	$1.17 \cdot 10^{35}\,[\mathrm{GeV \cdot s}]^{-1}$	1.07	200.43	$2 \cdot 2.02 \cdot 10^{45}$	$< 1.2 \cdot 10^{-2}$

Table 3.2: Our MAP values for the injection parameters from $e^{\pm}$ sources with an intrinsic cutoff, set to have a prior distribution with $E_{\rm cut} > 150$ GeV. The total energy injected in the ISM in the form of leptons is indirectly computed from the fit-parameters: the factor 2 is multiplied because of the $e^{\pm}$ symmetry. The conversion efficiency $\eta^{\pm}$ is calculated with respect to the nominal ATNF observed parameters: for what explained in the text, this is an upper bound.

	N_0	$\Gamma_{\rm inj}$	$\Delta\gamma$	$E_{\rm break}$ [GeV]	s	$E_{\rm tot}$ [erg]	$\eta^{\pm}$
Burst	$1.08 \cdot 10^{48}\,[\mathrm{GeV}]^{-1}$	1.02	-2.77	321.65	0.31	$2 \cdot 2.35 \cdot 10^{47}$	$\mathcal{O}(1)$
L_0	$1.11 \cdot 10^{35}\,[\mathrm{GeV \cdot s}]^{-1}$	1.10	-1.74	158.02	1.11	$2 \cdot 3.35 \cdot 10^{47}$	$\mathcal{O}(1)$

Table 3.3: Our MAP values for the injection-parameters from $e^{\pm}$ sources with an injection break, parametrized by the multiplying factor $\left(1 + \left(\frac{E}{E_{\rm break}}\right)^{|\Delta\gamma| \cdot s}\right)^{\mathrm{sign}(\Delta\gamma)/s}$, set to have a prior distribution with $E_{\rm break} > 150$ GeV. The total energy injected in the ISM in the form of leptons is indirectly computed from the fit-parameters: the factor 2 is multiplied because of the $e^{\pm}$ symmetry. The conversion efficiency $\eta^{\pm}$ is calculated with respect to the nominal ATNF observed parameters: for what explained in the text, this is an upper bound.

We notice that each of the four combinations is compatible with the positron data. The corner plots that we obtain outline a regular and well-behaved set of PDFs, that are shown in Appendix 3.A2. Nonetheless, when comparing the numerical values on the tables, relevant physical aspects have to be noticed:

- Even though we set a prior for the injection indices to be hard, data seem to favorite the very-hard end of the range: all the cases present $\Gamma_{\rm inj} \lesssim 1.3$, with the softest being the burst-like injection with intrinsic cutoff.
- For the burst-like solutions the injection features are found at energies higher ($E_{\rm cut,break} > 270\,\mathrm{GeV}$) with respect to the constant-luminosity case ($E_{\rm cut,break} \lesssim 200\,\mathrm{GeV}$): this effect is due to the peculiar shape of the burst-like solution, which features a sharp cutoff that is required to match the

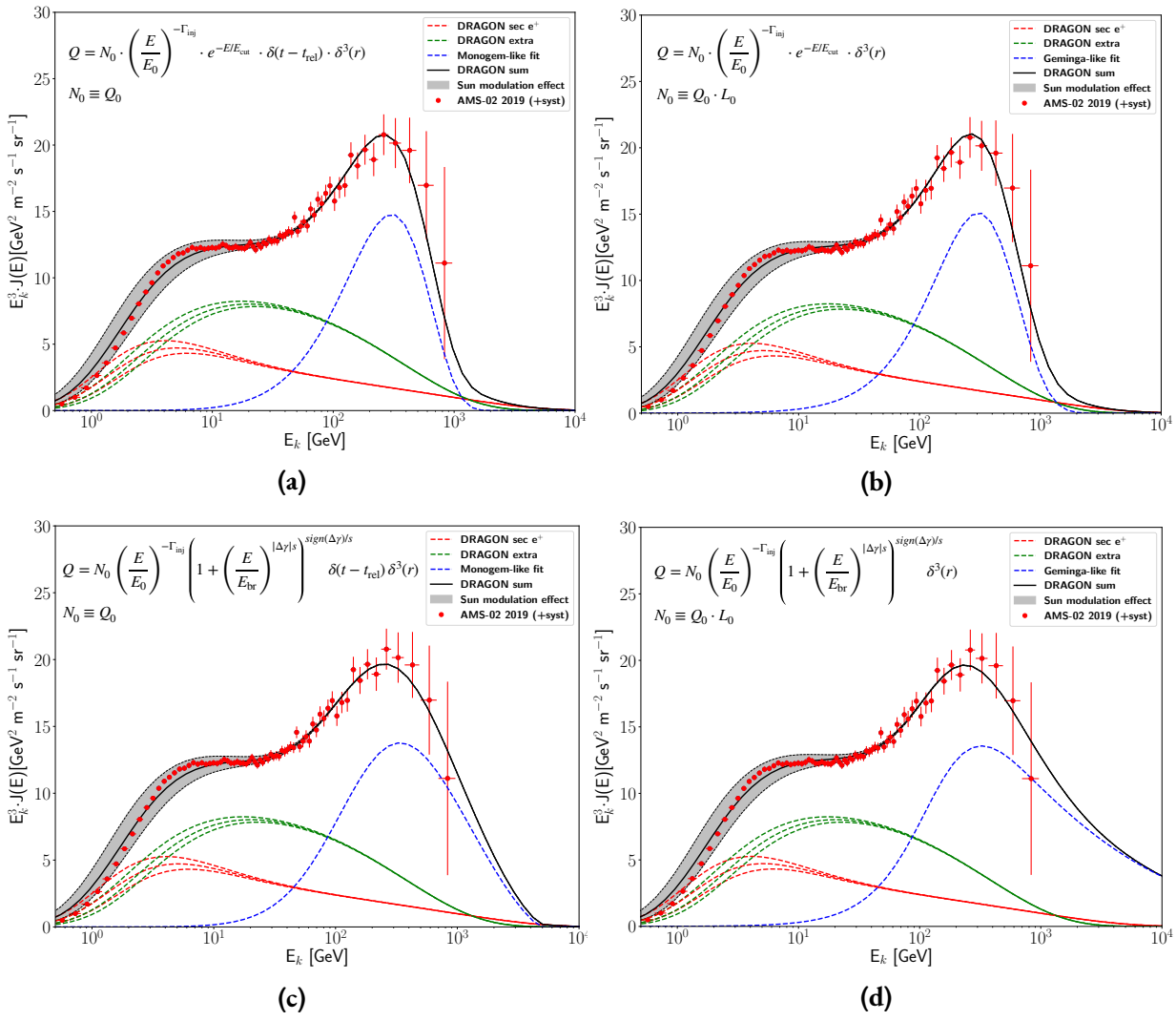

Figure 3.3: Fit to the AMS-02 positron flux for two classes of injection scenarios, where intrinsic features are added. **(a)** Burst-like injection with cutoff, **(b)** constant-luminosity injection with cutoff, **(c)** burst-like injection with broken power-law, **(d)** constant-luminosity injection with a broken power-law. The grey band represents the uncertainty in to the solar modulation potential $\langle \phi_{\rm mod} \rangle = 0.54 \pm 0.10$.

drop-off of the data.

- The total amount of energy converted into $e^{\pm}$ pairs is estimated by means of:

$$E_{\rm tot} = \int_{E_{\rm min}}^{E_{\rm max}} dE \int_{t_{\rm rel}}^{t_{\rm age}} dt \int dr\, E \cdot Q(E, t, r), \tag{3.11}$$

  where $E_{\rm min} = 1\,{\rm GeV}$ and $E_{\rm max} = +\infty$: only in the cases of logarithmic divergences a cut at very high-energies ($E_{\rm cut} = 100\,{\rm TeV}$) is set. Equation (3.11) gives values compatible with the order-of-magnitude energies that are thought to be injected by pulsars in the ISM (Amato, 2014). Besides, an efficiency is estimated with respect to the total energy injected by the source, that we compute multiplying the observed rate of rotational-energy loss $\dot{E}_{\rm rot} = \frac{d}{dt}\left(\frac{1}{2} I \Omega^2\right) = -I\Omega\dot{\Omega}$ by the characteristic age of the source. As discussed in detail in Appendix 3.A3, we observe that the quantity thus computed is actually a lower bound. Nevertheless, we notice that the values of $\eta^{\pm}$ estimated in the two injection scenarios are very different. This is not unexpected: in fact, at given age $t_{\rm ch}$ and loss rate $\dot{E}_{\rm rot}$, if a source is continuously emitting, then the total amount of energy injected in the ISM is much larger than in the burst-like case. Therefore, to match with the observed lepton spectrum, only a much smaller fraction of this energy needs to be converted into leptons (Blasi and Amato, 2011). These observations are visible only in the cases with a cutoff in the injection and are compatible with what is shown in Appendix 3.A3.

We point out that energetics (as listed in Table 3.3) cannot be taken as a strong argument against one scenario or the other, because we do not have a better model-independent estimation for $E_{\rm tot}$, and also because of the large statistical uncertainties on the high-energy positron flux. Future data with more statistics and higher energies may play a crucial role in this context: for instance, an additional data point in the TeV domain may allow to disentangle between the scenarios presented in the upper and lower panels of Figure 3.3.

As a final comment, we also remark that the grey band accounting for the solar modulation is within the intervals identified by the time structures discussed in Aguilar et al. (2018a).

In conclusion, in this section we found that scenarios characterized by a prominent young pulsar that dominates the high-energy positron flux, and a large number of middle-aged and old pulsars — modeled as a continuous contribution to the flux — are compatible with current data, under different hypotheses on both the injection spectrum and the timescale of the luminosity decline. The best-fit values for the injection spectra are compatible with the physical mechanisms outlined at the beginning of the section. However, different scenarios correspond to different estimates of the total energy budget and to a different hierarchy of the contributions from the nearby pulsars, as shown in Figure 3.9. Therefore, given the current data and the current knowledge on the physics of pulsar wind nebula emission, it is not possible to clearly identify which objects actually provide the most relevant contri-

bution to the positrons. Nevertheless, the measurement of the absolute positron flux has important implications. In fact, positrons are likely emitted in $e^{\pm}$ pairs, giving us the exact contribution of this class of sources to the electron flux as well. Therefore, since a significant part of the $e^+ + e^-$ spectrum is still missing after accounting for these contributions, we state that the high-energy lepton flux requires the presence of a different class of local electron-only sources. This allows us to focus on the next section, without worrying about the uncertainties on the positron origin.

3.4 Local electron accelerators explain the high-energy electron data

This section is dedicated to the interpretation of the all-lepton spectrum. We adopt the best-fit CR transport scenario evaluated in Section 3.2 and the best-fit $e^{\pm}$ flux (assumed charge symmetric) determined in the previous section for one of the four combinations discussed: the specific choice for the pulsar injection setup does not affect the results presented in this section. We will show that the closest observed SNRs are not sufficient to describe the observed spectrum and an additional source with specific characteristics has to be invoked to reproduce in particular the ~ 1 TeV break recently measured by the space-born and ground-based experiments H.E.S.S., VERITAS, CALET and DAMPE. Even though no information is given on the nature of the object, we model it as a SNR. This is because, mainly based on energetic arguments (see for instance Blasi (2013)), these objects are expected to provide the bulk of CRs observed at the Earth. Although not used here, we also notice that the combined study of the all-electron and radio emission of nearby SNR can also provide valuable complementary information (see *e.g.* the recent Manconi et al. (2019)).

3.4.1 Contribution from the known objects

Multi-wavelength observations show the presence of five Supernova Remnants (SNRs) in the local region (within ~ 1 kpc) surrounding the Earth* (Ferrand and Safi-Harb, 2012), identified with the names Vela Jr, Vela, Cygnus Loop, Simeis-147, IC-443.

We report in Table 3.4 the nominal ages and distances of these objects and the distances that particles with energy 1 TeV and 10 TeV can travel in the ISM via diffusive transport, as well as the ratios between the diffusive distance and the true distance of each source. We outline that, given the values reported in that table, the contribution of Vela Jr — the youngest remnant in the set under consideration — should peak around ~ 100 TeV, where we do not have reliable data. As far as the other SNRs are concerned, Vela is expected to provide the dominant contribution; the emissions of the other SNRs

*http://www.physics.umanitoba.ca/snr/SNRcat

are expected to be subdominant, though not negligible, since their diffusive distance is smaller than or comparable to the nominal one. Therefore, we choose to take into account all the remnants listed above with the only exception of Vela Jr.

	$t_{\rm age}$ [yr]	d [pc]	$r_{\rm diff,1TeV}$ [pc]	$r_{\rm diff,10TeV}$ [pc]	$\frac{r_{\rm diff,1TeV}}{d}$	$\frac{r_{\rm diff,10TeV}}{d}$
Vela Jr	$2.5 \cdot 10^3$	214.2	$1.08 \cdot 10^2$	$1.82 \cdot 10^2$	0.51	0.85
Vela	$1.23 \cdot 10^4$	250.92	$2.69 \cdot 10^2$	$4.52 \cdot 10^2$	1.07	1.80
Cygnus L	$8 \cdot 10^3$	449.82	$2.17 \cdot 10^2$	$3.64 \cdot 10^2$	0.48	0.80
Simeis-147	$4 \cdot 10^4$	918	$4.85 \cdot 10^2$	$8.14 \cdot 10^2$	0.52	0.89
IC-443	$3 \cdot 10^4$	918	$4.20 \cdot 10^2$	$7.05 \cdot 10^2$	0.46	0.77

Table 3.4: The nominal ages and distances of the five closest observed SNRs are listed. The diffusive distances are also shown for particles of 1 TeV and 10 TeV, in order to have a clear look on the sources that can contribute to the multi-TeV lepton flux. For a comparison with the loss-properties, $r_{\rm loss,1\,TeV} \simeq 1.15 \cdot 10^3$ pc and $r_{\rm loss,10\,TeV} \simeq 6.13 \cdot 10^2$ pc. From the numbers, Vela seems the one that can contribute the most to the $e^+ + e^-$ flux.

In order to estimate the contributions from the sources mentioned above, we perform a fit, based on the all-lepton data from AMS-02 (Aguilar et al., 2014) plus H.E.S.S. (Kerszberg, 2017), in which each SNR is modeled as a continuous source of e^-. The choice of the AMS-02 data is consistent with the previous part of the analysis, since we calibrated our model based on AMS-02 observations. Then, we choose to consider H.E.S.S. data, although in their preliminary release, because they provide the best combination of up-to-date and highest-energy observations, and are consistent within the error band with AMS-02 experiment.

It is possible to parametrize the problem with the same formalism we used for the pulsar decaying-luminosity injection, *i.e.* the luminosity function can be written as:

$$L(t) = \frac{L_0}{\left(1 + \frac{t}{\tau_{\rm d}}\right)^{\alpha_{\rm d}}}, \tag{3.12}$$

where now $\tau_{\rm d}$ and $\alpha_{\rm d}$ are specific for the release from a SNR and have nothing to do with pulsar injection mechanisms, and t is as usual the age of the source. The particle propagation is accounted for by solving the transport equation as described above.

The parameters we vary in the fitting procedure are the flux normalization N_0, the injection index $\Gamma_{\rm inj}$, and the luminosity-decline parameters $(\tau_{\rm d}, \alpha_{\rm d})$ of the sources. Based on the physical assumption that the acceleration mechanism is the *diffusive shock acceleration* (DSA) (Axford et al., 1977; Bell, 1978; Blandford and Ostriker, 1978; Krymskii, 1977), a prior is set for the injection indices to

be $\Gamma_{\rm inj} \in [2,3]$ (Caprioli et al., 2008; Malkov and Drury, 2001), as it was described in Section 1.2.2. The parameters $(\tau_{\rm d}, \alpha_{\rm d})$ are allowed to vary, but are set as identical for each source: we verified that this approximation has no significant impact on the final result, for values in the ranges $10^3 < \tau_{\rm d} < 10^6$yr and $1 < \alpha_{\rm d} < 3$, due to the relatively large distance of the sources of interest.

The results are shown in Figure 3.4, and the MAP parameters listed in Table 3.5.

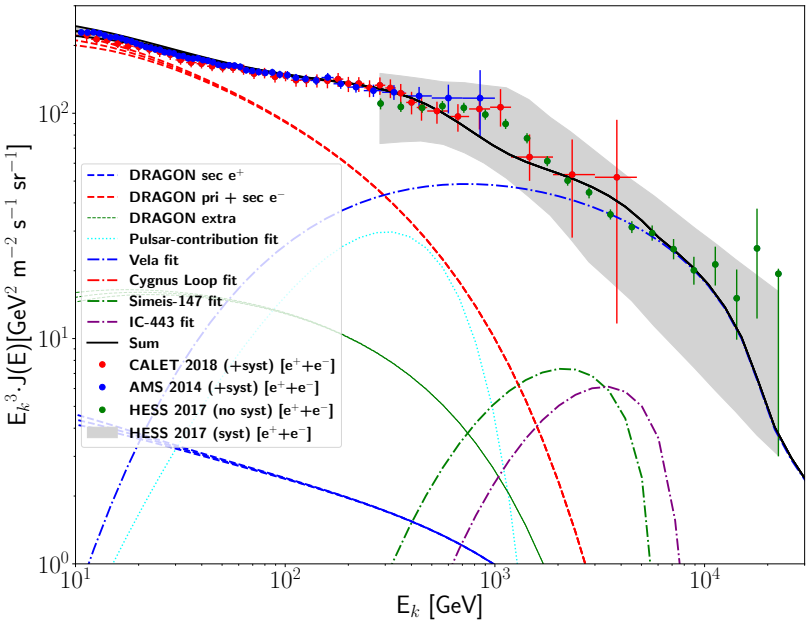

Figure 3.4: Fit of the $e^+ + e^-$ flux. The secondary and primary production and the extra-component, along with the fitted pulsar contribution, are considered as background, while the four SNRs have their parameters resulting from the fit. The blue dots are data from AMS-02 (Aguilar et al., 2014), the red dots from CALET (Adriani et al., 2018) and the green dots from H.E.S.S. (Kerszberg, 2017).

	N_0 [GeV · s]$^{-1}$	$\Gamma_{\rm inj}$	$\tau_{\rm d}$ [yr]	$\alpha_{\rm d}$	$E_{\rm tot}$ [erg]
Vela	$1.31 \cdot 10^{41}$	2.84	$1.87 \cdot 10^3$	2.47	$9.52 \cdot 10^{48}$
Cygnus L	$6.11 \cdot 10^{39}$	2.95			$3.78 \cdot 10^{47}$
Simeis-147	$3.98 \cdot 10^{42}$	2.98			$2.59 \cdot 10^{50}$
IC-443	$1.03 \cdot 10^{41}$	2.93			$7.04 \cdot 10^{48}$

Table 3.5: The table reports the MAP parameters resulting from the fit. Also, the total energy injected by each source in the form of $e^{\pm}$ is computed, based on the normalization.

As expected, the main contribution to the all-lepton flux above $\sim$ 100 GeV comes from the Vela SNR, due to the interplay among the diffusive distance, the distance of the source and the energy-loss characteristic distance. Simeis-147 and IC-443 cannot give contribution to the $\mathcal{O}(10\text{TeV})$ flux, since

their distance is larger than the loss distance at this energy, and indeed their peaks lie at energies smaller than $\sim 8\,\mathrm{TeV}$. The contribution from Cygnus Loop is extremely suppressed and even not visible in the plot, because the source is younger than the others and its peak would appear at an energy too-high to be compatible with the data. Finally, the energy budgets of those sources are compatible with those expected at SNR events ($\sim 10^{51}\,\mathrm{erg}$), taking into account the conversion efficiency into leptons within the range $\eta^{\pm} \sim 10^{-4} - 10^{-1}$ (Zirakashvili and Ptuskin, 2017), due to physical phenomena such as the particle escape at the shock front (Gabici, 2011; Schwartz and Skilling, 1978).

The most relevant implication of this result is that the $\sim 1\,\mathrm{TeV}$ spectral break cannot be reproduced with known sources. In fact, as noticed in Recchia et al. (2019), the propagated spectrum from a nearby SNR would peak at that energy only for a source as old as $\sim 2 \cdot 10^5$, a much larger age compared to that of the observed sources considered here.

Finally, we notice that those conclusions strictly hold as long as we consider only statistical errors for the H.E.S.S. data. However, the systematic uncertainty quoted by the H.E.S.S. experiment is actually much larger than the statistical one, therefore the claim relies on the assumption of a very high correlation among the systematic errors of the different energy bins. We hope that a future better estimation for the covariance matrix will help to better assess the compatibility between this scenario and the data.

3.4.2 Characterization of a source reproducing the $\sim 1\,\mathrm{TeV}$ break

A fit considering the emission of all the known sources in the current catalogs has shown that either a radical change in the propagation paradigm or an unknown source are needed. In particular, an old ($\sim 10^5\,\mathrm{yr}$) SNR seems to be necessary to reproduce correctly the $\sim 1\,\mathrm{TeV}$ break, as first pointed out in Recchia et al. (2019).

In order to better characterize this potential source in terms of its distance and energy budget, we perform a fit of the data in two different scenarios:

1) none of the listed known sources contribute to the flux,

2) all of them add their maximal contributions to the flux.

The free parameters of the fit in both cases are the normalization N_0, the injection index Γ_{inj}, the $(\tau_{\mathrm{d}}, \alpha_{\mathrm{d}})$ luminosity parameters, the age and distance of the source. We set a flat prior for the injection index in the range $\Gamma_{\mathrm{inj}} \in [2, 3]$, since we assume DSA to be the acceleration mechanism at work. In the second case, we also assume a flat prior for the distance in the range $d < 1.2 \cdot 10^3\,\mathrm{pc}$ because we do not expect $\sim 1\,\mathrm{TeV}$ leptons to come from more distant sources, due to energy-losses. For the fit, we use the same data set as before.

The outcome of this procedure is shown in 1) Figure 3.5a and 2) Figure 3.5b and the parameters summarized in Table 3.6.

	N_0 $[\mathrm{GeV}\cdot\mathrm{s}]^{-1}$	Γ_{inj}	τ_{d} [yr]	α_{d}	t_{age} [yr]	d [pc]	E_{tot} [erg]
1 hidden	$2.14\cdot10^{39}$	2.25	$1.13\cdot10^{5}$	2.40	$1.54\cdot10^{5}$	658.21	$2.45\cdot10^{49}$
4+1 hidden	$6.10\cdot10^{39}$	2.05	$4.97\cdot10^{3}$	2.45	$4.97\cdot10^{5}$	$1.19\cdot10^{3}$	$1.94\cdot10^{49}$

Table 3.6: The table reports the MAP parameters resulting from the fit to the all-lepton flux. The (1 hidden) scenario identifies the case where only an unknown object is considered, while (4+1 hidden) fits an unknown SNR on top of the observed SNRs. The total energy injected by each source in the form of $e^{\pm}$ is also computed, based on the normalization.

As a result of this analysis, we find that a hidden old remnant of $\sim 10^5\,\mathrm{yr}$ is actually needed to reproduce correctly the data, and the best-fit distance is expected to be in the range (600 – $1200\,\mathrm{pc}$). This range of distances is far from the one quoted in Recchia et al. (2019), where a very close source ($d = 100$ pc) is invoked to match the observed all-lepton data. The discrepancy is mainly due to the propagation model: we checked and found that, in accordance with Recchia et al. (2019), such a close source would correctly reproduce the data only if a diffusion coefficient with a Kolmogorov-like rigidity scaling ($\delta = 0.33$) and a smaller normalization were assumed. However, we exclude these parameters as they are not compatible with the observables we considered to calibrate our propagation setup (p, nuclei, B/C). Furthermore, we remark that our reference transport scenario with $\delta = 0.45$ is consistent with the MCMC analysis carried out in Yuan et al. (2017).

Given the required age, such a remnant would most likely be in its final *radiative* phase and may be not clearly detectable (while this would be unrealistic for the much smaller distance found in Recchia et al. (2019)). The SNR catalogue (Ferrand and Safi-Harb, 2012) reports a possible candidate that we find particularly interesting, the Monogem Ring, which is categorized as *uncertain Supernova Remnant*. However, this source is too close ($d < 300\,\mathrm{pc}$) to the Earth and its propagated spectrum does not seem to be compatible with the high-energy ($E > 10\,\mathrm{TeV}$) all-lepton data, according to our propagation scenario. We will see in Chapter 4 that a different parametrization of the diffusion coefficient could reveal a different behaviour of the propagated spectrum from such distance.

We point out that, as mentioned above, alternative explanations of the features we have analyzed so far have been recently put forward in the literature. In particular, in López-Coto et al. (2018) an undiscovered pulsar is invoked to account for the all-lepton data. Another physical picture that requires a change in the propagation paradigm is found in Lipari (2019a,b). In that scenario the positron flux is entirely of secondary origin and the spectral break in the all-lepton spectrum is generated by energy-loss effects, possibly motivated by a much smaller ($\simeq 0.7 - 1.3\,\mathrm{Myr}$) residence time of the charged cosmic

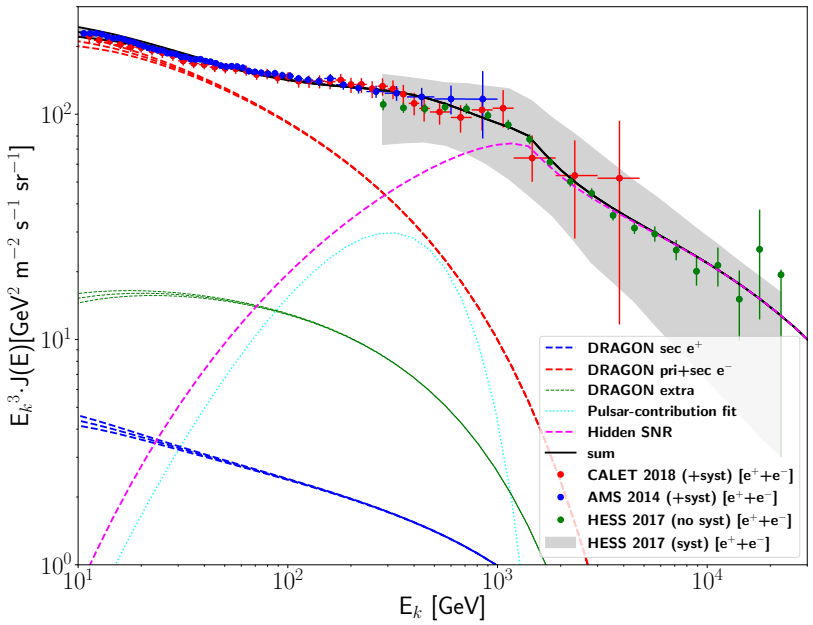

(a)

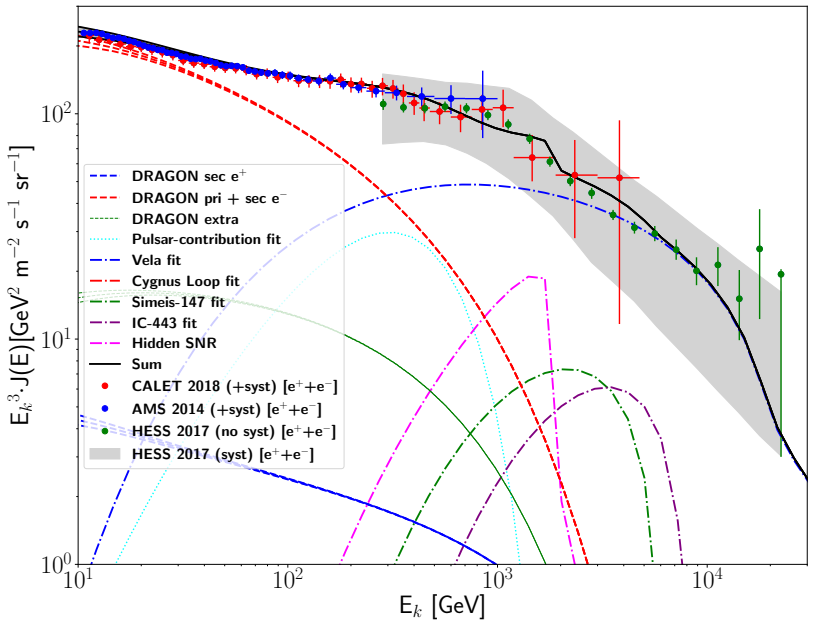

(b)

Figure 3.5: Fits of the $e^+ + e^-$ flux: the secondary and primary production, the extra-component and the fitted pulsar contribution, are considered as background. An additional hidden SNR with free parameters $(N_0, \Gamma_{\rm inj}, \alpha_{\rm d}, \tau_{\rm d}, t_{\rm age}, r_{\rm dist})$ is fitted when: **(a)** no known SNR is taken into account, **(b)** contributions from all the observed SNRs are also considered. The blue dots are data from AMS-02 (Aguilar et al., 2014), the red dots from CALET (Adriani et al., 2018) and the green dots from H.E.S.S. (Kerszberg, 2017).

rays in the Galaxy compared to conventional scenarios; moreover, the break at $1\,\mathrm{TeV}$ in the lepton spectrum would correspond to the energy at which the loss time becomes comparable with the diffusion timescale. We remark that a coherent picture that includes charged CR channels, together with γ-ray and radio data, based on this idea has not been provided yet. However, it is an intriguing possibility that can be further tested with future, more accurate data. Furthermore, we notice again that the presence of a spectral hardening at $\simeq 40\,\mathrm{GeV}$ in the electron spectrum can be interpreted, in our scenario, as the breakdown of the assumption of a continuous source term, and the signature of local sources that start to dominate the flux; on the other hand, this feature does not have a simple explanation in the alternative scenario based on purely secondary origin.

3.5 Summary of the chapter

In this chapter we provided a comprehensive discussion about the origin of the most relevant features observed in the positron, electron and all-lepton data recently released by the AMS-02, CALET, and H.E.S.S. Collaborations.

We first identified a CR transport scenario that very well reproduces B/C data published by AMS-02, and the proton, He, C and O data measured by AMS-02 and Voyager.

With this propagation setup at hand, we considered the positron data, that show a remarkable excess with respect to the secondary flux expected from the conventional proton-proton spallation process, and studied the expected contribution from individual pulsar wind nebulae. Starting from a careful study of the analytical solution of the diffusion-loss equation from individual sources, we characterized the contribution due to a large number of old PWNe as a large scale extra-component which is often neglected in the related literature. Then we focused on the prominent peak and drop-off in the positron spectrum recently found by AMS-02 around $300\,\mathrm{GeV}$. After pointing out that this feature is not compatible with alternative scenarios in which the largest part of the positron population is originated by CR nuclei scattering onto the ISM gas, we described it in terms of the emission from a young PWN under different conditions. We emphasize that, given the poor knowledge of the emission processes' details, we chose not to rely on a specific model but rather on purely observational information, and performed a fit of the injection parameters for the extremal assumptions of burst-like and continuous injections, and for different injected spectral features. We found that a hard acceleration spectrum and a spectral break or a cutoff at few hundred GeV are required to match the data, which is consistent with recent theoretical modeling of the typical acceleration mechanisms at the termination shock of PWNe.

Finally, we turned our attention to the all-lepton spectrum and tried to reproduce its shape accounting for the contribution of known and possibly hidden SNRs. We pointed out that the contribution of local SNRs takes over the softer large-scale component at $\simeq 40\,\mathrm{GeV}$. We found however that known nearby SNRs cannot reproduce the $\sim\,\mathrm{TeV}$ feature recently identified by the H.E.S.S. Collaboration. Then, building on previous results from Recchia et al. (2019), we found that, if a relatively near, old remnant is included in the calculation — with declining luminosity and with age $\sim 10^5\,\mathrm{yr}$ and distance in the range $600 - 1200\,\mathrm{pc}$ — then the data points are nicely reproduced within the propagation setup described in the first part, consistently with all the hadronic and leptonic channels under consideration.

3.A1 Estimation of the release time from PWNe

Since the release of the PAMELA data on the positron fraction, several phenomenological scenarios invoked a relevant delay between pulsar formation and the release of the electron+positron pairs in the ISM (see for instance Grasso et al. (2009)). The physical picture behind this time delay, extensively discussed for example in Blasi and Amato (2011), is the following. A typical pulsar forms in a core collapse supernova event with a natal kick velocity of $\simeq 400\,\mathrm{km/s}$ or larger; this relevant proper motion drives the compact object far from the place of its formation, across the supernova remnant and then across the shocked ejected material. After the escape from the remnant, as a consequence of the impact of the relativistic PWN wind onto the ISM, a bow shock forms. Such structure can hardly confine the electron+positron pairs accelerated within the PWN: the particles can hence escape from the PWN and contribute to the diffuse sea of cosmic radiation.

In this appendix, guided by this physical picture, we estimate the release time by computing the time needed by a pulsar with a typical kick velocity to escape a typical SN Ia remnant. The time evolution of the SNR shock radius is computed following the prescriptions summarized in Gaggero et al. (2018). In particular, the ejecta-dominated phase is described by the self-similar solutions provided by Chevalier (1982), and the subsequent Sedov phase is modeled adopting the thin-shell approximation (Ostriker and McKee, 1988), based on the assumption that the mass is mostly concentrated within a shell of negligible thickness at the forward shock. Given these assumptions on the SNRs, and within a wide range of pulsar kicks, spanning from 100 to $1000\,\mathrm{km/s}$, we obtain release times in the interval $[10^4 - 6.5 \cdot 10^5]\,\mathrm{yr}$. This is shown in Figure 3.6, where we see that the release time corresponds to the intersection value between the curve representing the time-evolution of the shock radius and the distance travelled by a pulsar with a given initial kick. For the result we aim at presenting, we consider an intermediate reference value $t_{\mathrm{rel}} = 6.4 \cdot 10^4\,\mathrm{yr}$, that corresponds to a pulsar with kick $v_{\mathrm{pulsar}} = 400\,\mathrm{km/s}$.

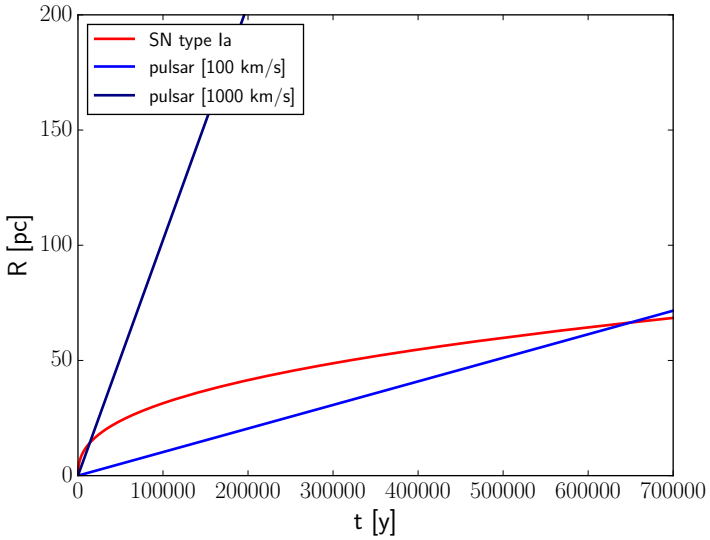

Figure 3.6: The time-evolution of the shock radius of a type-Ia SN (red line) and the distance travelled by two pulsars with initial kick $v_{\rm pulsar} = 100\,{\rm km/s}$ (blue line) and $v_{\rm pulsar} = 1000\,{\rm km/s}$ (purple line) are shown. These two values span the uncertainties in pulsars' initial velocity.

3.A2 Posterior distribution functions for the fit to the positron flux

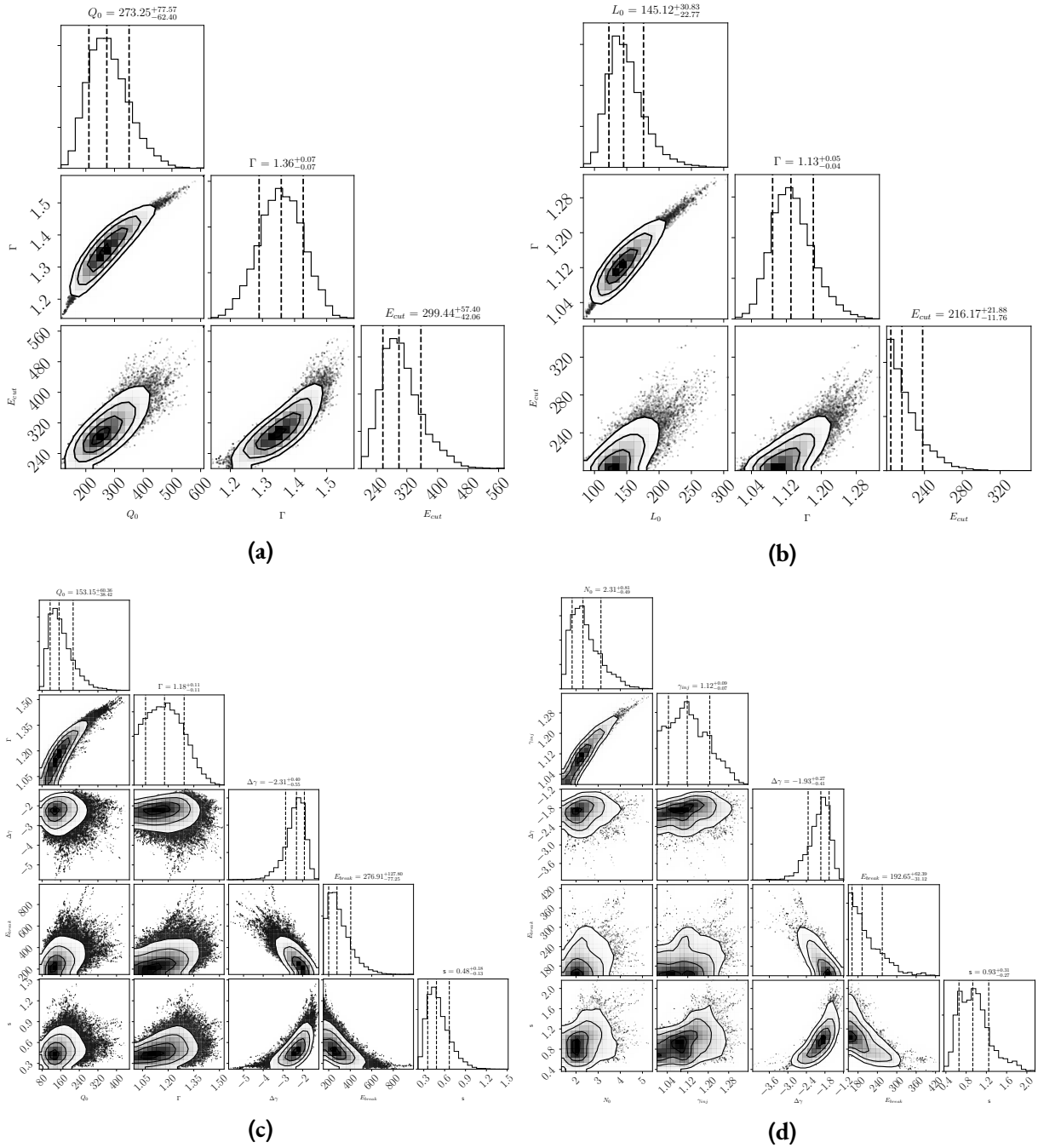

Figure 3.7: Posterior distribution functions of the bayesian fit to the positron flux, corresponding to the four different scenarios discussed in the text: **(a)** burst-like injection with exponential cut-off, **(b)** constant-luminosity injection with exponential cutoff, **(c)** burst-like injection with broken power-law, **(d)** constant-luminosity injection with broken power-law. The value of the *median*, the 0.16-*quantile* and 0.84-*quantile* are also shown.

3.A3 Notes on the pulsars from ATNF Catalogue

The position of the peak in the positron flux ($\sim 250\,\mathrm{GeV}$) requires sources that are as old as $\sim 10^6\,\mathrm{yr}$, based on $E_{\rm peak} = 1/(b_0 \cdot (t_{\rm ch} - t_{\rm rel}))$. A particle diffusing in the Galaxy for this time interval is coming from a distance $\sqrt{4 \cdot D(E_{\rm peak}) \cdot (t_{\rm ch} - t_{\rm rel})} \simeq 1.3\,\mathrm{kpc}$.

In Figure 3.8 we report all the pulsars listed in the ATNF Catalogue that are found within this distance and younger than $2 \cdot 10^8\,\mathrm{yr}$. We make them inject leptons with a hard spectrum ($\Gamma_{\rm inj} = 1.5$) up to an energy $E_{\rm cut} = 300\,\mathrm{GeV}$, where an exponential cutoff $e^{-\frac{E}{E_{\rm cut}}}$ is implemented. This is consistent with Amato (2014), where it is argued that pulsar emission requires an injection break due to a change in the accelerating site around the compact object: leptons up to $200 - 400\,\mathrm{GeV}$ are accelerated within the nebula by mechanisms that are not fully understood (*e.g.* magnetic reconnection — which was briefly mentioned in Section 1.2), with a hard injection $\Gamma_{\rm inj} < 2$, while more energetic leptons are accelerated at the termination shock, thus with a softer spectrum $\Gamma_{\rm inj} > 2$ characteristic of the DSA. It is not clear whether the second population can be considered subdominant, thus justifying a cutoff instead of a break. However, this does not affect much the energy budget injected by the source. After the injection, we make them propagate through the Galaxy via the transport-equation (3.3).

For the release time of the leptons, we consider the value $t_{\rm rel} = 6.4 \cdot 10^4\,\mathrm{yr}$, corresponding to a pulsar with birth speed $v_{\rm pulsar} = 400\,\mathrm{km/s}$, as described in Appendix 3.A1. We verified that the extreme values discussed there do not change qualitatively the results.We observe that a different release time from the PWN effectively mimics the effect of a surrounding confinement region, like the ones observed by HAWC (Abeysekara et al., 2017), although we are not taking into account the possible reshaping of the spectral index introduced by losses inside those regions.

With this emission paradigm, we plot all the sources that in Figure 3.8 are marked as *high-energy pulsars*. This denomination is due to the emission frequency, but we consider them because they uniformly span the scatter plot and thus constitute a good sample. The result is shown in Figure 3.9, where the constant-luminosity (3.9a) and the burst-like (3.9b) solutions to (3.3) are compared: only the constant luminosity injection can reproduce the positron data. This can be due to the total amount of injected energy, that we estimated trivially as $E_{\rm tot} = |\dot{E}_{\rm loss}| \cdot t_{\rm ch}$.

As it can be easily understood, this is a lower bound (LB), since it is based on the current measurements of Ω and $\dot{\Omega}$ in $\dot{E}_{\rm loss} = -I\Omega\dot{\Omega}$. In fact the rotational frequency Ω is currently smaller than at the beginning of its life, as well as its variation $\dot{\Omega}$. We can do an attempt to improve the estimation for $E_{\rm tot}$ by implementing the magnetic dipole (MD) radiation model, as follows:

$$E_{\rm tot,MD} = \int_{t_{\rm rel}}^{t_{\rm age}} |\dot{E}_{\rm MD}|\, dt, \tag{3.A3.1}$$

where $\dot{E}_{\rm MD} = -\frac{B^2 R^6 \Omega^4}{6c^3}$, $\Omega(t) = \frac{\Omega_0}{\sqrt{1+\frac{t}{\tau_{0,\rm MD}}}}$.

Carrying out the integral, we obtain:

$$E_{\rm tot,MD} = \tau_{0,\rm MD} \frac{B^2 R^6 \Omega_0^4}{6c^3} \cdot \left(\frac{1}{1+\frac{t_{\rm rel}}{\tau_{0,\rm MD}}} - \frac{1}{1+\frac{t_{\rm age}}{\tau_{0,\rm MD}}} \right). \tag{3.A3.2}$$

With the ATNF parameters, we find $E_{\rm tot,MD} < E_{\rm tot,LB}$, which is a hint that the emission mechanism requires some modification. Different values of $t_{\rm rel}$ do not affect this conclusion.

Regardless, there are two model-independent aspects that we observe:

1. There is a very different conversion efficiency for the two injection scenarios, compatibly with what is discussed in Section 3.3.4.
2. Among the dominant sources, the hierarchy is inverted between Monogem and Geminga: this is expected as well, if one considers the interplay among the nominal parameters of the two pulsars. In fact, when particles are injected instantaneously (burst-like), the younger source dominates over the older one, as particles had less time to loose energy. On the other hand, for the constant-luminosity case, the sources are still emitting, therefore the discriminating parameter here is $E_{\rm tot}$.

In both cases, one source dominates by a factor of ~ 2, which helps supporting our parametrization of the fits in Section 3.3.4 with one prominent source.

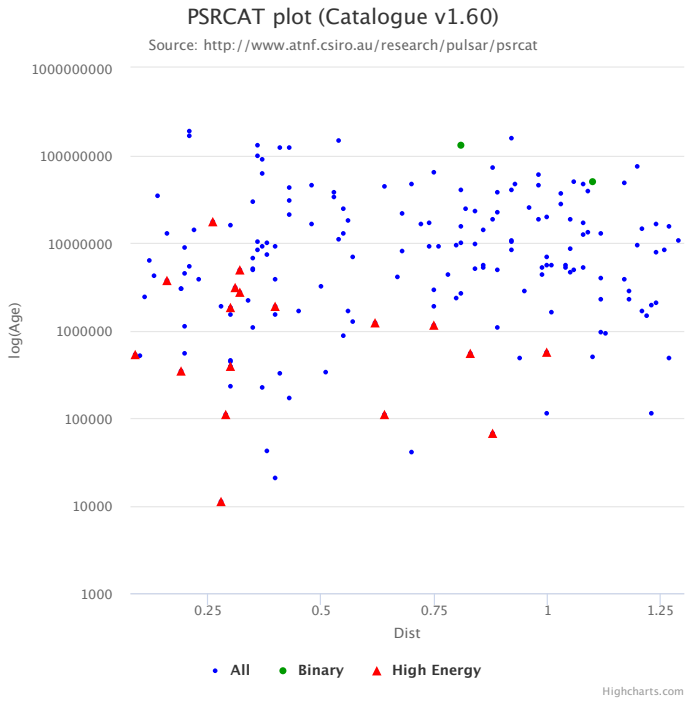

Figure 3.8: The figure is a (distance, age) scatter plot of all the pulsars in the ATNF Catalogue within 1.3 kpc and younger than $2 \cdot 10^8$ yr. Marked with red triangles there are high-energy pulsars, that have an emission at frequency higher than infrared. As they are distributed quite uniformly, we will consider them as a good sample of pulsar population.

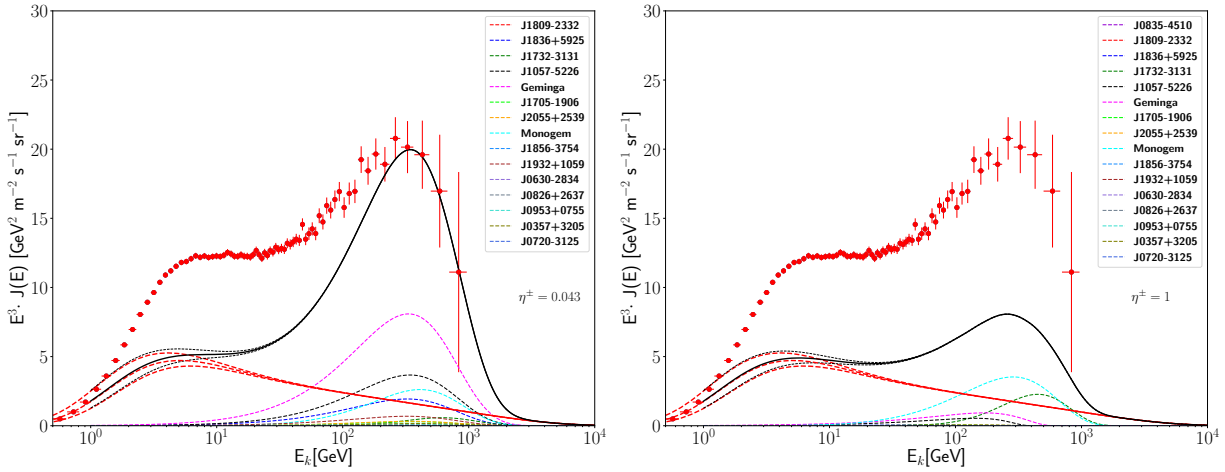

(a) **(b)**

Figure 3.9: We plot here all the high-energy pulsars within 1.3 kpc and younger than $2 \cdot 10^8$ yr found in Figure 3.8. **(a)** Sources are propagated from a constant-luminosity injection: the high-energy data are reproduced with a conversion efficiency of $\eta^{\pm} = 0.043$. **(b)** Sources are propagated from a burst-like injection: the high-energy data cannot be matched, due to the insufficient nominal injected energy. The black line is the sum of all the contributions. Notice the inverted hierarchy of the dominant sources.

4

A varying-slope diffusion coefficient connects the lepton and proton spectra

In this chapter, we want to build upon the hidden, nearby source scenario, hypothesized previously. As we have studied above, in the standard scenario where Supernova Remnants are the largely-dominant sources of cosmic-ray particles, the high-energy $e^+ + e^-$ spectrum observed is not reproduced by their large-scale distribution. Contributions from known, nearby objects seems to be not sufficient, due to the specific age of the source needed to reproduce the $\sim 1\,\mathrm{TeV}$ spectral break; moreover, γ-ray observations favor the picture where none of these objects significantly contribute to the all-lepton spectrum. Considering another observational channel, it is known that SNRs also inject protons, that therefore are expected to contribute somehow to the proton propagated flux. To challenge this picture, sources of protons at the considered relatively-small distance ($d \lesssim 600\,\mathrm{pc}$) are likely to be seen in the dipole anisotropy observed in the directional CR-flux: in particular, their anisotropy is well-above the data points in a framework where the diffusion coefficient scales with energy as a single power-law. On the other hand, we discussed about the CR hardening observed above $\sim 250\,\mathrm{GeV}$ in the primary and secondary hadronic species. Within the assumption of a diffusive origin for such spectral feature, we then expect that the same hardening would be experienced by particles injected by potential nearby sources as well. Therefore, in what follows, we consider a realistic picture where particles coming from the single source are injected into the ISM at an energy-dependent release time, and propagate within the same large-scale diffusion setup, that was tuned to reproduce the most relevant CR species.

4.1 Motivations

In the recent years, the AMS-02 Collaboration measured the fluxes of light nuclei and showed that the spectral index of several species progressively hardens at high rigidities ($\sim 250\,\mathrm{GeV}$), (Aguilar et al., 2015a, 2016). However, the observed hardening in secondary hadronic species is twice as large as the one observed in primaries (Aguilar et al., 2018b), suggesting a diffusive origin for this feature, as discussed for instance in Génolini et al. (2017); Vladimirov et al. (2012). More recently, the DAMPE Collaboration has confirmed this feature in the high-energy CR proton spectra and reported a softening at 13.6 TeV, with the spectral index changing from 2.60 to 2.85 (An et al., 2019). This spectral *bump* — independently measured by the ATIC and NUCLEON experiments — might be originated from a nearby Supernova Remnant (SNR). However, in order to reconcile this possibility with the current anisotropy data, an anomalously slow diffusion in the region between the remnant and the Earth has been invoked in a recent analysis (Fang et al., 2020). In absence of such a high-confinement region — and with a single-power-law diffusion coefficient — the predicted anisotropy would overshoot the observed data by more than one order of magnitude. Another attempt to simultaneously reproduce the nuclei spectra and the dipole anisotropy recently considered a two-zone (disk/halo) diffusion, though applied to the background particles only and with no connection with the leptonic spectrum (Liu et al., 2019; Yuan et al., 2020).

With this regard, in the lepton domain, the spectral break at $\sim 1\,\mathrm{TeV}$, consistently measured by the H.E.S.S. (Aharonian et al., 2009; Kerszberg, 2017), CALET (Adriani et al., 2018) and DAMPE (Ambrosi et al., 2017) collaborations, has been considered to point towards a nearby old remnant, as shown originally in Recchia et al. (2019) and later elaborated in a wider context in Fornieri et al. (2020b). Moreover, attempts to assign the high-energy ($E \geq 1\,\mathrm{TeV}$) observed leptons to known nearby sources — such as Vela and Cygnus Loop — using radio data have recently revealed their subdominant contributions (see for example Manconi et al. (2019)).

In this chapter, we propose a comprehensive scenario that correctly reproduces all these spectral features. Our model features two key-points of novelty. (i) First of all, we argue that a nearby, possibly hidden, old Supernova Remnant is responsible for both the hadronic *bump* measured by DAMPE/NUCLEON/ATIC and the leptonic break reported by H.E.S.S.
(ii) Moreover, we consider, in the background+source context, a transport scenario featuring a rigidity scaling that progressively hardens — deviating from the single power-law — as suggested by AMS-02 light nuclei data. We show that this is the crucial ingredient that allows to satisfy the anisotropy constraints.

The chapter is structured as follows. In Section 4.2, we describe the adopted transport model, with particular attention to the phenomenological treatment that allows to implement a variable slope

of the diffusion coefficient for the nearby-source solution as well. In Section 4.3, we characterize the contributions from a hidden nearby source, connecting for the first time the leptonic and hadronic features and showing that those interpretations are consistent with the CR dipole anisotropy. Finally, in Section 5.5, we discuss the results and derive some conclusions. The single-source solutions of the transport equation — for both protons and electrons — in the general setup discussed throughout the chapter are computed with the code in Fornieri (2020b)*.

4.2 Our transport setup

In this section, we describe the propagation setup that will be used throughout the whole chapter, which is based on the model settings presented in Chapter 3 (Fornieri et al., 2020b). In particular, we consider a large-scale diffuse background of hadronic and leptonic cosmic particles, plus a contribution from a nearby accelerator. While the latter component is computed in a semi-analytical way, the former (*i.e.* a smooth contribution) is characterized by solving the general diffusion-loss transport equation with the `DRAGON2` (Evoli et al., 2008; Evoli et al., 2017a) numerical code.

However, a key difference with respect to the aforementioned work resides in the assumption on the diffusion coefficient. As mentioned in the introduction, the more pronounced effect detected in the purely secondary species seems to point towards a feature in the transport. Specifically, the CR particle spectrum-density at the disk level, that is found by solving the transport equation, can be written as $N_0(E) \sim S(E)/D(E)$, where $S(E)$ is the particle injection-spectrum and $D(E) \sim E^{\delta}$ the diffusion coefficient. For primary species, $S(E) \sim E^{-\Gamma_{\rm inj}}$, from which we get $N_0^{\rm pri} \sim E^{-\Gamma_{\rm inj}-\delta}$, while for secondaries, the injection spectrum is the propagated spectrum of the primaries, resulting in $N_0^{\rm sec} \sim E^{-\Gamma_{\rm inj}-\delta}/D(E) = E^{-\Gamma_{\rm inj}-2\delta}$. This implies that any change in the slope of the diffusion coefficient will produce a change in the secondaries' spectrum that is twice as large as that in the primaries. This is what is observed by AMS-02 (Aguilar et al., 2018b) for the CR hardening at $\sim 200\,\mathrm{GeV}$.

As a consequence, assuming this hardening to be of diffusive origin, it appears quite natural that equal changes in the transport properties should affect the propagation of particles from nearby sources as well.

To consider this, we study the phenomenological setup considered in Tomassetti (2012), where the slope of the diffusion coefficient — typically parametrized as $D(E) = D_0 \left(\frac{E}{E_0}\right)^{\delta(E)}$, with D_0 normalization at reference energy E_0 and δ here changing with E — smoothly hardens as energy (or, equivalently,

*https://github.com/ottavio fornieri/Hidden_Remnant

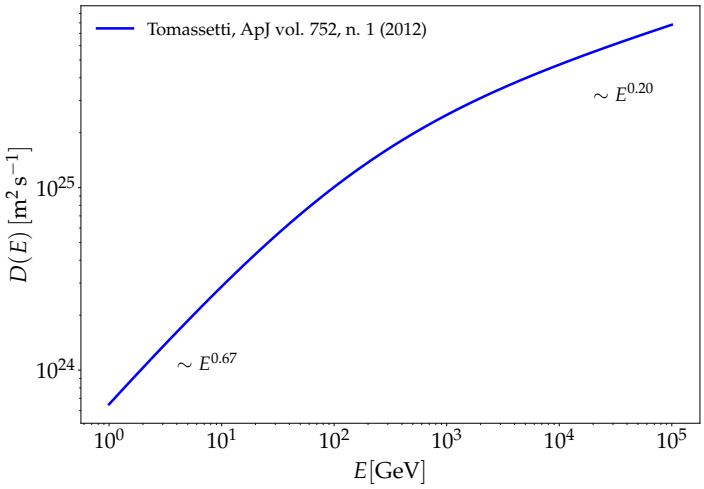

Figure 4.1: The diffusion coefficient obtained from the parametrization $D(E) = D_0 \left(\frac{E}{E_0}\right)^{\delta(E)}$, modifying the parameters $(\gamma_{\rm High}, \Delta)$ starting from the THMb model in Tomassetti (2012), as described in the text.

rigidity) increases, assuming the following expression:

$$\frac{dD(\rho)}{d\rho} \equiv \gamma(\rho) \approx \gamma_{\rm high} + \frac{\Delta}{1 + \frac{\xi}{1-\xi}\left(\frac{\rho}{\rho_0}\right)^{\Delta}}, \tag{4.2.1}$$

where ρ is the particle rigidity, ρ_0 is the reference rigidity and $(\gamma_{\rm high}, \Delta, \xi)$ are free parameters of the model.

In order to account for the nearby-source contribution to the proton flux, we slightly modify the parameters $(\gamma_{\rm High}, \Delta)$ starting from their THMb-model (*Two-Halo Model b*) values. In what follows, we set $\gamma_{\rm high} = 0.19$, $\Delta = 0.53$, while the others are left unchanged, as $\xi = 0.1$, with a normalized diffusion coefficient $D_0 = 1.21 \cdot 10^{28}\,{\rm cm^2\,s^{-1}}$ at reference rigidity $2\,{\rm GV}$. With these parameters, the diffusion coefficient presents a smooth transition, specifically as shown in Figure 4.1.

The key point shown in Tomassetti (2012) is that such a setup is formally equivalent to a two-zone transport model featuring a change in the properties of the *interstellar medium* between an inner-halo ($|z| < \xi L$) region and an extended-halo ($\xi L < |z| < L$) region, where $L \sim 4\,{\rm kpc}$ and $\xi \sim \mathcal{O}(0.1)$. Possible physical explanations for this change in the diffusive properties of the two zones have been proposed. (i) One assigns it to a transition between a diffusion regime, generated by self-generated turbulence, to another one for which an external cascade is responsible (Blasi et al., 2012). (ii) Alternatively, as suggested in Yan and Lazarian (2004, 2008, 2002b), this change is interpreted within a framework where different damping mechanisms, occurring in the two regions, produce a different behaviour in the turbulent waves, which are the scattering centers that cause CR diffusion. This, in turn, leads to a diffusion coefficient that may not be a single power-law (Fornieri et al., 2020a) (see Chapter 5).

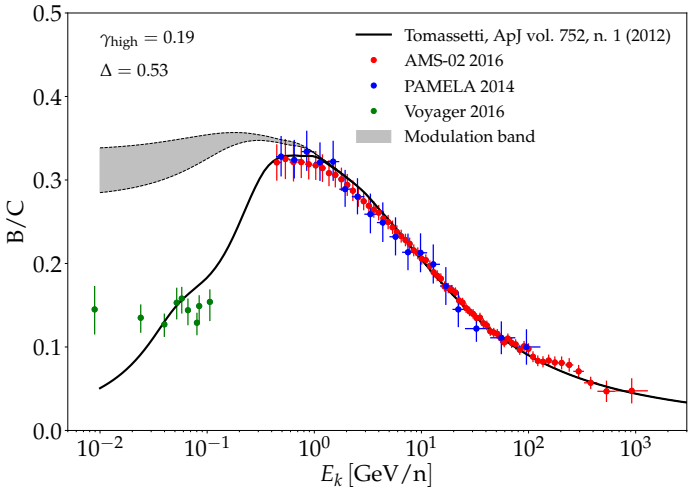

Figure 4.2: B/C ratio computed for the described model with the DRAGON2 numerical solver with and without adding the influence of the solar modulation, against AMS-02 (red) and PAMELA (blue) data points. Voyager unmodulated data points are also shown at low energy (green). References are in the text.

In Tomassetti (2012), the transport equation is analytically solved under simplifying conditions and the diffusion parameters of Equation 4.1 are adjusted to the B/C data available at that time. Later, the same author found a better agreement to the updated observations by incorporating a factor β^η (where $\beta = v/c$ and $\eta \sim -0.4$) into the definition of the diffusion coefficient, in Feng et al. (2016a). This change in the low energy trend of $D(E)$ has been interpreted in terms of dissipation of magneto-hydrodynamic waves in the interstellar plasma (Ptuskin et al., 2006) or, alternatively, considering non-resonant interactions between the cosmic rays and the same turbulent waves (Reichherzer et al., 2019). As it is clear, adding this factor has a negligible effect at particle energies for which $\beta \to 1$, therefore it can be safely ignored in the computation of the spectra from our isolated nearby source.

Here, as mentioned above, we solve the equation for the large-scale background with the DRAGON2 numerical solver, that takes into account all the processes approximated in the analytical solution. As shown in Figure 4.2, we find that the B/C flux-ratio observed by AMS-02 (Aguilar et al., 2016) and PAMELA (Adriani et al., 2014) can be nicely reproduced using $\eta = -0.5$ and adjusting the values of $\gamma_{\rm high}$ and Δ to 0.19 and 0.53, respectively, as mentioned above and indicated in the figure. The Voyager-1 (Cummings et al., 2016) data points, measured outside of the heliopause, are captured at low energy by our unmodulated black solid line. The solar modulation is taken into account using the *force-field* approximation, with an effective potential $\langle \phi_{\rm mod} \rangle = 0.54 \pm 0.10$, exactly as described in Chapter 3. In the plot, its effect is shown as a grey band. We highlight that this framework suitably reproduces the high-energy range of the B/C observations as well as the hardening found in the primary CR-species, for which the model was originally built.

In this chapter, the transport setup described in Equation (4.2.1) — and shown in Figure 4.1 —

is adopted consistently in both the large-scale propagation and in the propagation of particles from the nearby remnant. As it will be shown below, this ingredient plays a key role in reconciling the high-energy break in the all-lepton spectrum ($E_{e^\pm} \sim 1\,\mathrm{TeV}$) with the *bump* recently reported by DAMPE in the proton spectrum at $E_p \sim 10\,\mathrm{TeV}$. Besides, it is crucial to correctly reproduce the cosmic-ray dipole anisotropy data.

4.3 A consistent picture for the electron, proton and anisotropy data

It has been mentioned in the introduction that particles coming from observed nearby sources cannot account for most of the measured high-energy leptons. However, it is natural to wonder whether it is plausible to invoke only one additional hidden source or rather a plurality of them. An answer, with a detailed estimation, is given in Appendix 4.A2. In fact, based on the rate of Supernova events in the Galaxy (Ferriere, 2001) — the same implemented in `DRAGON2` — and on the massive losses that leptons undergo during the journey towards the Earth, we find that we expect $N_{\mathrm{SNR}} \sim 2$ Supernova explosions in the vicinity of the Solar system. The catalogues already list more than five (Ferrand and Safi-Harb, 2012), which however have been found not to contribute to the propagated leptons (Fornieri et al., 2020b; Manconi et al., 2019). Hence, we conclude that considering only one hidden source is a physically well-motivated choice.

Therefore, within the transport setup presented above, we discuss here a scenario based on the contribution from an old, hidden Supernova Remnant as a time-dependent source of cosmic electrons and protons.

The accelerator we are considering is characterized by distance $d = 300\,\mathrm{pc}$ and age $t_{\mathrm{age}} = 2 \cdot 10^5\,\mathrm{yr}$. We assume that particles remain confined inside the SN shock as long as their energy is lower than the maximum allowed value — we refer to this value as *escape energy*. This implies an energy-dependent release time that is regulated by the different stages of the SNR evolution and is different for protons and electrons. In this work, we assume that the CR escape energy is dominated by the limited current that particles can generate to trigger non-resonant streaming instability during the *free expansion* and *Sedov* phases; conversely, it is limited by geometrical losses during the later radiative phases. The time scale of each phase of the SNR evolution, as well as the details to compute the escape energy at each time instant, are discussed in Appendix 4.A1.

After the escape, particles are injected into the ISM according to a time-dependent luminosity function $L(t)$ and transported from the source to the Earth via the simplified diffusion-loss equation described in the previous section — Equation (3.3).

Finally, as a consistency check, the total energy budget associated to each CR population injected

by the source can be calculated as follows:

$$E_{\rm tot} = \int dr \int_{t_{\rm rel}(E)}^{t_{\rm age}} dt \int_0^{+\infty} dE\, E \cdot Q(E,t,r), \tag{4.3.1}$$

where $t_{\rm rel}$ is the instant of the release and $t_{\rm age}$ the current age of the source.

As it is clear, the general calculation setup is similar to that presented in Section 3.3.2 in the previous chapter. However, we find useful to recall the equations when necessary, since new dependences for the physical quantities (such as $t_{\rm rel} \equiv t_{\rm rel}(E)$ and $\delta \equiv \delta(E)$) lead to a few modifications.

4.3.1 All-lepton spectrum

In the case of leptonic cosmic rays above $\sim 1\,\mathrm{GeV}$, the energy-loss term accounts for Inverse Compton (IC) scattering and synchrotron losses. The IC cross-section above $\sim 50\,\mathrm{GeV}$ gets modified by relativistic effects, as shown in Hooper et al. (2017), and the loss rate can be written as follows:

$$b(E) = -\frac{4}{3}\, c\sigma_T \left[f^i_{\rm KN} U_i + U_B \right] \left(\frac{E}{m_e c^2} \right)^2 \tag{4.3.2}$$

where $\sigma_T \simeq 6.65 \cdot 10^{-25}\,\mathrm{cm}^2$ is the Thomson cross-section, $(U_i,\, U_B)$ are respectively the energy density of the Interstellar Radiation Field (ISRF) components and of the background magnetic field, and $f^i_{\rm KN}$ is the approximated correction factor:

$$f^i_{\rm KN}(E) \simeq \frac{\frac{45}{64\pi^2} \cdot (m_e c^2 / k_{\rm B} T_i)^2}{\frac{45}{64\pi^2} \cdot (m_e c^2 / k_{\rm B} T_i)^2 + (E^2 / m_e^2 c^4)}, \tag{4.3.3}$$

where T_i are the black-body spectrum temperatures corresponding to the U_i. For each contribution, we adopted the reference value reported in Evoli et al. (2020b).

The Green function of Equation (3.3) reads:

$$N(r,t,E) = \frac{Q(E_{\rm t}) b(E_{\rm t})}{\pi^{3/2} b(E) r^3_{\rm diff}} \cdot e^{-\frac{r^2}{r^2_{\rm diff}}}, \tag{4.3.4}$$

where $E_{\rm t}$ refers to the energy at a time $(t - t_{\rm rel})$ ago and $r^2_{\rm diff}(E_{\rm t}, E) \equiv +4 \int_{E_{\rm t}}^{E} \frac{D(E')}{b(E')} dE'$ is the square of the diffusive distance travelled by a particle loosing its energy from $E_{\rm t}$ to E. This solution is still general, in that it does not contain any information about the injection term.

The dependence of the diffusion slope on energy has to be included in the integral giving the dif-

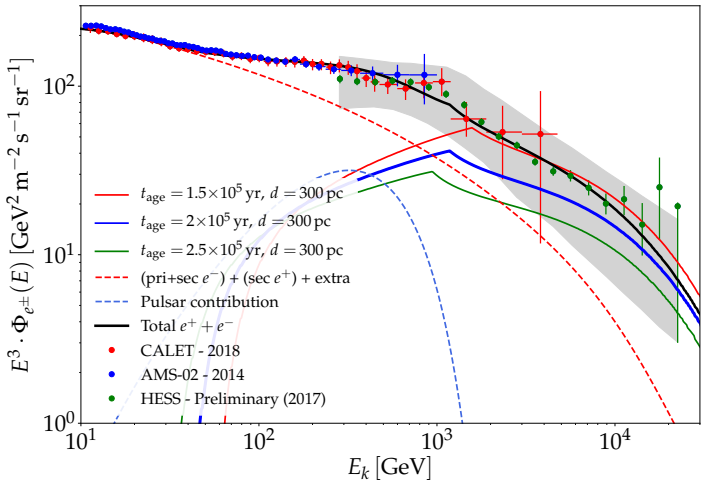

Figure 4.3: The all-lepton spectrum as the sum of a smooth background of primary e^- + secondary $e^\pm$ + extra $e^\pm$ (red dashed line), a fit of the positron flux (blue dashed line) and the single-source contribution calculated in this work for the corresponding age $t_{age} = 2\cdot10^5$ yr (blue solid line). Other ages (red and green solid lines) are added for comparison.

fusive distance $\sqrt{r^2_{diff}}$, as follows:

$$r^2_{diff}(E_t, E) = 4\int_{E_t}^{E} \frac{D_0 \left(\frac{E'}{E_0}\right)^{\delta(E')}}{b(E')} dE' = 4D_0E_0 \int_{\omega_t = E_t/E_0}^{E/E_0} \frac{\omega^{\delta(E_0\omega)}}{b(E_0\omega)} d\omega, \tag{4.3.5}$$

where the last step is justified by the simple change of variable $\omega = \frac{E'}{E_0}$. In lack of an analytic function $\delta(\omega)$, the integral can be solved numerically.

As a last step, to obtain the propagated spectra at Earth, we have to integrate Equation (4.3.4) over time, from the instant of the release from the source to the current time, featuring a model for the time evolution of the luminosity. This is discussed in details in Section 3.3.2.

In Figure 4.3 we show the $e^+ + e^-$ propagated spectrum resulting from the convolution of several components, plotted against data from AMS-02 (Aguilar et al., 2014b), CALET (Adriani et al., 2018) and H.E.S.S. (Kerszberg, 2017). Data from other experiments have not been added to avoid superposition, being consistent with the present ones. The smooth diffuse background (red dashed line) is the sum of: (i) primary e^-, injected with DRAGON2 with a power-law spectrum $\Gamma^{\texttt{DRA}\,e^-}_{inj} = 2.74$ and a cutoff $E^{\texttt{DRA}\,e^-}_{cut} = 20$ TeV that is estimated equating the acceleration and loss timescales (Vink, 2012); (ii) secondary $e^\pm$, fixed by the DRAGON2-propagated primary species; (iii) the smooth *extra-component* of primary $e^+ + e^-$ pairs coming from the convolution of $\sim \mathcal{O}(10^4)$ old ($t_{age} > 10^6$ yr) pulsars (see Section 3.3.2).

The solar modulation is ignored in the plot, as it nearly has no effect at energies $E \geq 10$ GeV (see, for instance, Figure 3.4).

The blue dashed curve represents a fit of the positron flux: here, we invoke pulsars and use the fit

to the AMS-02 data points performed in Section 3.3.4, for the simplest case of a *burst-like* injection and an intrinsic cutoff in the injection spectrum. Other parametrizations of the positron component do not change the final contribution, as they are fit over the positron flux, expected to originate from a separate class of sources, regardless of the physical nature.

The three solid curves correspond to the contribution from the hidden remnant discussed in this work. They are computed by solving Equation (3.3) for different ages, with the calculations described above in this section. The electron population is injected as a single power-law with a slope $\Gamma_{\rm inj}^{e^-} = 2.45$. This spectrum is softer than the one used for the proton flux, as we will see in the next section. However, such difference is physically motivated by the sychrotron losses that electrons undergo before being released (Diesing and Caprioli, 2019). The total energy budget associated to the leptonic population, computed by means of Equation (4.3.1), is $E_{\rm tot}^{e^-} \simeq 4.5 \cdot 10^{47}\,{\rm erg}$.

Finally, the black curve is the sum of all the contributions, where we have chosen the source of age $t_{\rm age} = 2 \cdot 10^5\,{\rm yr}$ as our best-fit choice (blue solid).

The plot shows how the energy-dependent release cuts off the low-energy particles ($E \lesssim 100\,{\rm GeV}$) — they are the last ones to reach the energy to escape from the shock — that did not have the time to reach the Earth. This effect is slightly amplified by the KN correction. Indeed, a corrected cross-section increases the propagated flux of a factor $\sim 1.5 - 2$, with respect to the non-relativistic treatment, above energies $E \sim 200\,{\rm GeV}$ (Delahaye, T. et al., 2010). Therefore, in order to reproduce the $\sim 1\,{\rm TeV}$ peak, a lower injected flux is needed.

As far as the luminosity function is concerned, we varied $\alpha_{\rm d} \in [1,\,3]$ and reported negligible variations in the spectrum. On the other hand, while varying $\tau_{\rm d}$ in the range $[10^4,\,2 \cdot 10^5]\,{\rm yr}$ does not qualitatively change the results, smaller values cannot reproduce the data points above the $\sim$ TeV break. Indeed, since $\tau_{\rm d}$ acts as a timescale for the luminosity function, a quickly decaying luminosity would approach the limit of a burst-like injection ($L(t) \to L_0\,\delta(t - t_{\rm rel})\,dt$), and accordingly the $\sim$ TeV peak energy allowed by the source age would be followed by an abrupt cutoff in the spectrum. This leads us to conclude that a declining luminosity from the source is necessary to match the observations.

4.3.2 Proton spectrum

The proton data are characterized by a hardening at $\sim$ 200 GeV and a softening at energies as high as $\sim$ 13 TeV. Here, we connect this feature to the same hidden remnant considered in the previous section.

To compute the contribution from the nearby source to the proton flux, we use again Equation (3.3), neglecting the loss processes considered for leptons, as they would would start to play a role at much higher energies (above $\sim 100\,{\rm TeV}$). Besides, spallation and nuclear decay only affect the propagation of low energy particles (below $\sim 1\,{\rm GeV}$).

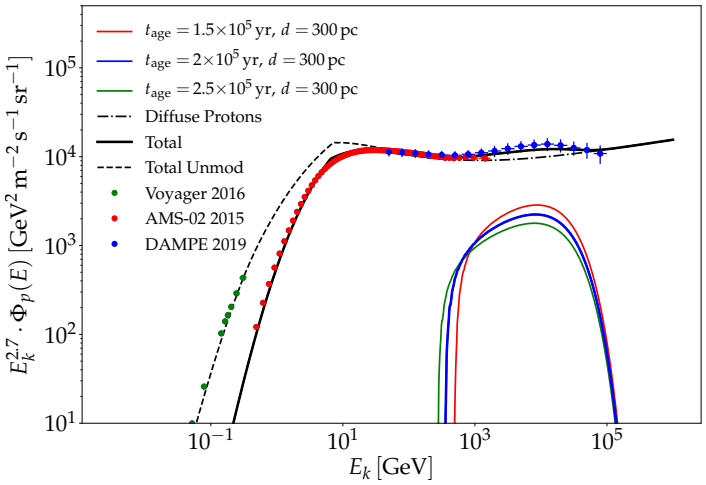

Figure 4.4: The total proton spectrum (black solid line), resulting from the sum of the DRAGON2 modulated spectrum (dashed-dotted line) and the solution of the single-source transport equation computed in this work, for the age $t_{age} = 2 \cdot 10^5$ yr (blue solid line). Other ages (red and green solid lines), as well as the unmodulated spectrum (black dashed line) are added for comparison.

Therefore, from the same Green function used for the leptons, Equation (4.3.4), we can reduce to the hadronic distribution function. Indeed, considering the losses as negligible, $b(E_t) \approx b(E)$. Besides, the diffusive distance $\sqrt{r^2_{diff}}$ is not dominated by the loss timescale and becomes $r^2_{diff}(E) = 4D(E)(t - t_{rel})$.

In conclusion, the Green function for protons can be written as follows:

$$N(r,t,E) = \frac{Q(E_t)}{\pi^{3/2} r^3_{diff}} \cdot e^{-\frac{r^2}{r^2_{diff}}} = \frac{Q(E_t)}{\left[4\pi D(E)(t - t_{rel})\right]^{3/2}} \cdot e^{-\frac{r^2}{4D(E)(t-t_{rel})}}. \tag{4.3.6}$$

In the above expression we can directly implement the effect of a variable diffusion slope as $D(E) = D_0 \left(\frac{E}{E_0}\right)^{\delta(E)}$.

Finally, as done for the leptons, we get the propagated spectra integrating the Green function (4.3.6) over time, from the release time to the current instant.

In Figure 4.4, we show our result. This is the sum of two different components: (i) the first is the diffuse CR background, *i.e.* a proton population injected with slope $\Gamma^{DRA\,p}_{inj} \simeq 2.4$ and propagated with DRAGON2 as described in Section 4.2. This component is shown unmodulated (dashed line) and modulated with the average effective potential discussed above $\langle \phi_{mod} \rangle = 0.54$ (dashed-dotted line); (ii) the single source, namely an injection spectrum $S(E)$ parametrized as a power-law with slope $\Gamma^p_{inj} = 2.1$, plus a data-driven high-energy exponential cutoff implemented at $E_{cut} = 20$ TeV. This contribution is computed by solving Equation (3.3), in the limit of negligible losses ($b(E_t) \approx b(E) \to 0$), and shown for three different ages.

The total energy budget of the proton population originating in the source is calculated again via

Equation (4.3.1) and found to be $E^p_{\rm tot} \simeq 2.5 \cdot 10^{49}\,{\rm erg}$ for the source of our choice, *i.e.* the one of age $t_{\rm age} = 2 \cdot 10^5\,{\rm yr}$. The model is plotted against data points from AMS-02 (Aguilar et al., 2015b) and DAMPE (An et al., 2019) in the whole energy range. Furthermore, Voyager data (Cummings et al., 2016) are also reported in the plot and appear consistent with the unmodulated propagated spectrum. Finally, the modulated sum of the two contributions is shown as the black solid line.

We notice that, as for the case of the all-lepton spectrum, the effect of the energy-dependent release time cuts off the low-energy ($E \lesssim 100\,{\rm GeV}$) part of the spectrum.

Even though the nearby-source contribution is small, we want remark its importance for two main reasons:

1. as we easily notice, without it the DAMPE points could not be reproduced,
2. it must be present, since, as mentioned before, a Supernova Remnant injects at the same time both electrons and protons.

In particular, the last statement is supported by what we find in terms of the two populations' energy budgets. In fact, the factor $E^{e^-}_{\rm tot}/E^p_{\rm tot} \simeq 1\%$, as well as the two quantities evaluated separately, are consistent with the theoretical predictions of a total energy budget for a SN explosion of $E_{\rm SNR} \sim 10^{51}\,{\rm erg}$, a conversion efficiency in protons of the order $\sim 10^{-1} - 10^{-2}$, and in electrons of the order $\sim 10^{-3} - 10^{-5}$ (Bell, 2013; Tatischeff, 2009; Zirakashvili and Ptuskin, 2017).

4.3.3 CR dipole anisotropy

The cosmic-ray dipole anisotropy (DA) provides a crucial complementary probe that allows to constrain the model proposed in this chapter. The high degree of isotropy (up to 1 part in $\sim 10^3$) detected by a variety of experiments in a wide energy range is especially constraining as far as the contribution from a local source is concerned. In particular, the interpretation of a single source as the origin of the spectral feature in the proton spectrum between 1 TeV and 10 TeV is heavily challenged in the context of a simple diffusion setup characterized by a single power-law. This consideration led the authors of several recent papers to consider more complex diffusion scenarios featuring an extended high-confinement zone surrounding the source of interest (see for instance Fang et al. (2020)).

In this section, we consider instead the transport scenario suggested by the hardening in the light nuclei, as described in Section 4.2, and compute the dipole anisotropy associated with the hidden remnant, with the formalism described below.

The CR dipole anisotropy is the first order of the expansion in spherical harmonics of the CR intensity as a function of the arrival direction, $I(\theta, \phi)$ (Ahlers and Mertsch, 2017). In the case of an isolated nearby source, the dipole term is dominant and can be written as follows (Ginzburg and Syrovatskii,

1964b):

$$I(\alpha) = \bar{I} + \delta_i \bar{I} \cos\alpha, \qquad \delta_i = \frac{I_{\max} - I_{\min}}{I_{\max} + I_{\min}}, \tag{4.3.7}$$

where α is the angle of the observation line, denoted as $\hat{\boldsymbol{n}}$, with respect to the source direction, labelled as $\hat{\boldsymbol{r}}$.

In the diffusive-regime approximation, we obtain:

$$\delta_i = \frac{3D(E)}{c} \left| \frac{\nabla N_i}{N_i} \right|, \tag{4.3.8}$$

where $N_i \equiv N_i(r, t, E)$ is the CR number-density per unit energy transported from the single source.

The total dipole anisotropy, assuming the presence of a set of sources, can be written as:

$$\Delta_{\rm tot} = \frac{\sum_i N_i \, \delta_i \, \hat{\boldsymbol{r}} \cdot \hat{\boldsymbol{n}}}{\sum_i N_i}. \tag{4.3.9}$$

If we directly observe in the direction of the anisotropy source, $\hat{\boldsymbol{r}} \cdot \hat{\boldsymbol{n}} = 1$, and the total anisotropy can be decomposed as the part coming from the dominant source plus an average term coming from the background:

$$\Delta_{\rm tot} \simeq \frac{N_i \, \delta_i}{\sum_i N_i} + \left\langle \frac{\sum_i N_i \, \delta_i}{\sum_i N_i} \right\rangle. \tag{4.3.10}$$

To support the interpretation of the total anisotropy as two separate terms, we notice that, at the energy where the anisotropy amplitude presents an evident break ($E \sim 100\,\mathrm{GeV}$), we also observe phase flip from R.A.$\simeq 4h$ to the direction of the Galactic Center (GC) (see Ahlers and Mertsch (2017), their Figure 7). In other words, the DA data above this energy can be associated to the large-scale diffuse background and are assumed to follow a simple power-law (Ahlers and Mertsch, 2017). It is worth mentioning that the anisotropy associated to the diffuse cosmic rays, in principle, should directly come from the propagated distribution function computed with `DRAGON2`. However, we propagated the protons with a homogeneous diffusion coefficient, neglecting the vertical component of the Galactic magnetic field in the GC region. In terms of the associated γ-rays, this simplification leads to what is referred to as the *gradient problem*. As discussed in Section 2.1, this is the discrepancy (for $E_\gamma \geq 100\,\mathrm{MeV}$) between the theoretical CR-flux profile obtained with a distribution of SNRs in the Galaxy and that inferred from the EGRET and *Fermi*-LAT γ-ray diffuse observations. Physically, ignoring the vertical escape of CRs around the GC causes a longer residence time (*i.e.* less-efficient diffusion) — with respect to the exact $D(E)$ parametrization — of the particles around the Galactic Center, resulting in a larger production of photons. Analogously, we would expect the same overproduction of CRs in the GC region to overestimate the real dipole anisotropy.

Motivated by these considerations, in Figure 4.5 we show that the hypothesis of one nearby old

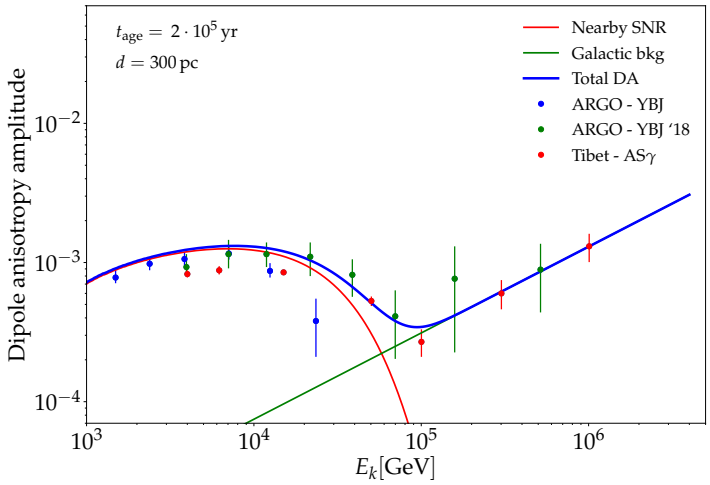

Figure 4.5: Cosmic-ray dipole anisotropy amplitude for protons calculated as the sum of a background anisotropy (green solid line) and the single source contribution (red solid line) for the source of age $t_{age} = 2 \cdot 10^5$ yr. Anisotropy data are consistent with each other, therefore here we plot a subset of them, to avoid confusion. The plotted points are from ARGO (Bartoli et al., 2015, 2018) and Tibet-ASγ (Amenomori, 2017).

remnant originating the CR populations, responsible for both the leptonic and the hadronic features, is compatible with the current anisotropy data.

To reproduce the diffuse contribution, we use the fit parameters recently suggested in Fang et al. (2020), according to which the background anisotropy can be written as $\Delta_{bkg} = c_1 \left(\frac{E}{1\,\mathrm{PeV}}\right)^{c_2}$, where $(c_1, c_2) = (1.32 \cdot 10^{-3}, 0.62)$. The result is the green solid line in the figure.

On the other hand, the single-source contribution is found under the assumption of diffusive behaviour for the released particles. This component corresponds to the red solid line in the figure, for the source of age $t_{age} = 2 \cdot 10^5$ yr, the same considered in the previous sections.

We want to remark again that a key role to reproduce the observations is here played by the slope of the diffusion coefficient, that, according to Equation (4.2.1), becomes harder in the high-energy region ($\delta \lesssim 0.2$ at $E > 10\,\mathrm{TeV}$).

4.4 Discussion

As a first discussion point, we want to comment on the nature of the source here invoked. Given its old age, it is reasonable to assume that the remnant is currently in the final stage of its evolution, deep into the radiative phase. Hence, we expect it to be quite extended and the detection of its faint multi-wavelength signature to be very challenging, especially from a distance as large as $\sim 300\,\mathrm{pc}$. In particular, if $\sim 100\,\mathrm{GeV}$ protons are still confined in the SNR at its age, then one should expect a γ-ray emission, resulting from pion decay, cutting off around $\sim 10\,\mathrm{GeV}$. Electrons at these energies emit

synchrotron radiation up to a frequency of $\sim 300\,\mathrm{GHz}$ and the source may be of interest for future *Square-Kilometer Array* (SKA) observations. Moreover, electrons contribute to IC γ-ray emission up to $\sim 100\,\mathrm{MeV}$, $\sim 1\,\mathrm{GeV}$ and $\sim 10\,\mathrm{GeV}$ for IR, optical, UV soft photons background.

From a wider prospective, regarding a SNR origin for the $e^+ + e^-$ spectrum, it is worth noticing that, due to the incompleteness of the catalogues, especially for old remnants, a proof of concept would be represented by a Monte Carlo simulation of all the possible configurations of source distributions in our Galaxy. A step in this direction is presented in Evoli et al. (2020a), suggesting that the SNR explanation is disfavored at more than 2σ, with respect to the average configuration. This result is model dependent, in particular is based on a source distribution that is set to follow the Galactic spiral arms. However, the Solar system is found in the so-called *Orion Spur*, a minor arm-structure in the Milky Way between two major arms. This is not included in that work, whereas we believe it to be of major importance, in particular for the leptonic observables above $1\,\mathrm{TeV}$. The amount of the uncertainty can be estimated in their Figure 6, where the lepton horizons — as caused by their energy-loss rate — for particles of $E = 100\,\mathrm{GeV},\ 1\,\mathrm{TeV}, 10\,\mathrm{TeV},$ are sketched. In particular, the $10\,\mathrm{TeV}$ horizon includes two arcs of two major arms at equal distance from the Solar system. Therefore, we estimate that ignoring the *Orion Spur* results in neglecting roughly $\sim 1/3$ of the leptons of this energy. Similarly, we estimate that $\sim 20/25\%$ of the particles are missing from the $1\,\mathrm{TeV}$ range of the $e^+ + e^-$ spectrum. This lack can abundantly account for the 2σ dispersion of the Monte Carlo average curve. It is therefore the reason why, on average, the high-energy ($E \sim 1\,\mathrm{TeV}$) range of the all-lepton spectrum cannot be captured by their calculations.

In this context, we want to comment on the number of nearby SNRs that we may expect to contribute to the high-energy part of the leptonic and hadronic spectra. We remark that a limited number of young sources exist in the vicinity of the Sun, and they may also provide a sizable contribution to the observed fluxes. In particular, we emphasize the possible role of the young type II Supernova Remnant in the southern constellation Vela. The young age of this accelerator ($\simeq 1.1 \cdot 10^4\,\mathrm{yr}$) restricts its potential signature in the lepton spectrum at energies as large as $\sim 10^4\,\mathrm{GeV}$, thus not limiting our proposed scenario. However, its presence could constrain the parameters involved in the luminosity function and in the energy-dependent release time. Indeed, a rough calculation of its emission based on our reference transport setup has revealed a predicted flux that is strongly dependent on the parameters of the model, and that can span between a negligible contribution — as small as more than 2 orders of magnitude below the level of the data points — and a dominant one. However, a detailed modeling of this object constrained by multi-wavelength data is beyond the scope of the present work.

Moreover, we are confident that more accurate data in this domain — $E \sim 1 - 50\,\mathrm{TeV}$, subject of interest for the *Cherenkov Telescope Array* (CTA) — expected in the near future will help to disentangle the question, possibly revealing the presence of a spectral feature.

A final important point that is worth to discuss regards the implications of using the same rigidity-dependent diffusion coefficient for both the diffuse CR component and the isolated nearby source. In particular, this means that hardening at $\sim 200\,\mathrm{GeV}$ is actually due to a superposition of two effects: (i) the diffusive origin coming from physical differences in the halo and in the disk; (ii) the nearby-source contribution. In this sense, an important role is played by the softening in the DAMPE spectrum, that is interpreted as an intrinsic cutoff of the hidden remnant. In fact, even though a more pronounced hardening with no additional sources could be considered to account for the mismatch between AMS-02 and DAMPE data, this would be still not sufficient to reproduce the complex structure observed by DAMPE — the *softening* at $E \sim 10\,\mathrm{TeV}$. In particular, no theoretical models predict so far a cutoff in the proton propagated spectra below the *knee* ($E_{\mathrm{knee}} \sim 5\,\mathrm{PeV}$). As a consequence, the scenario here proposed predicts that the CR spectrum above $E \sim 100\,\mathrm{TeV}$ would have a slope similar to that observed after the $\sim 200\,\mathrm{GeV}$ hardening. With this aim, higher energy data points in the future will certainly help to disentangle this puzzle.

4.5 Summary of the chapter

In this chapter, we proposed the idea that the spectral feature at $\sim 13\,\mathrm{TeV}$ in the cosmic-ray proton spectrum, recently reported by the DAMPE Collaboration, together with the spectral break at $\sim 1\,\mathrm{TeV}$ measured by H.E.S.S. in the lepton spectrum, have a common origin and can be associated to a nearby, fading Supernova Remnant. We believe this simultaneous interpretation to be of paramount importance, since SNRs are accelerators for both electrons and protons.

We injected the particles with a realistic — and physically motivated — energy-dependent release time, which considers the different stages of the SNR evolution as well as the surrounding medium, and with a luminosity function that declines over time. Then, we computed their propagation from such object in a spherically symmetric setup, and found that all the available observables can be simultaneously reproduced. The key ingredient in the calculation is a transport setup based on a diffusion coefficient that presents a smooth transition to a progressively harder rigidity-scaling at higher energies, as suggested by the light-nuclei spectra measured by the AMS-02 Collaboration. This feature allowed to reproduce the cosmic-ray anisotropy data without any further assumption. Moreover, the combined leptonic and hadronic data led us to characterize the properties of the particles accelerated by such object, that are in a very good agreement with the theoretical expectations.

4.A1 Energy-dependent release time from Supernova remnant shocks

In this appendix, we review the dominant mechanisms that confine particles inside the Supernova shocks. Once those processes are overcome, particles can be released from the source. As leptons suffer from severe energy losses and are $m_p/m_e \sim 10^3$ times less efficient than hadrons in generating streaming instabilities, the release processes for hadrons and leptons will be discussed separately.

Release time for hadrons

Hadrons can escape from SNRs because of two main reasons: (i) due to geometrical losses, when their mean free path gets larger than a fraction of the shock radius (Berezhko et al., 1994); (ii) due to the limited current they are able to trigger *upstream** of the shock (Schure and Bell, 2013). In the latter case, the CR current is necessary to trigger the non-resonant streaming instability and to produce magnetic field amplification at the shock precursor (Bell, 2004). As the non-resonant instability growth rate scales as $\sim u_{\rm sh}^3$, with $u_{\rm sh}$ velocity of the shock — for a $\propto E^{-2}$ particle distribution that we assume hereafter — it likely controls the maximum CR energy at the early stages of the evolution of the SNR shock, *i.e.* during free expansion and, possibly, Sedov-Taylor phases.

Maximum energies imposed by geometrical losses are set because the CR diffusive path in the precursor reaches a fraction $\xi < 1$ of the shock radius $R_{\rm sh}$, namely

$$\ell = \frac{D(E)}{u_{\rm sh}(t)} = \xi R_{\rm sh}(t), \tag{4.A1.1}$$

where the diffusion coefficient is here parametrized in terms of its Bohm value $D(E) = \eta_{\rm acc} r_{\rm L} c/3$, where $\eta_{\rm acc}$ is a numerical factor $\eta_{\rm acc} \geq 1$. We consider relativistic particles of charge Ze, with a Larmor radius $r_{\rm L} = E/ZeB(t)$ (hereafter we only consider protons, so $Z = 1$). Therefore the maximum energy fixed by geometrical losses is

$$E_{\rm max,Geo} = \frac{3\xi e}{\eta_{\rm acc} c} R_{\rm sh}(t) u_{\rm sh}(t) B(t). \tag{4.A1.2}$$

Hereafter we fix $\xi = 0.3$ and $\eta_{\rm acc} = 1$.

Limited-current loss process dominates in case of strong magnetic field amplification, hence during the SNR evolution stages where the shock strength is high. The maximum CR energy in that case depends on the type of ambient medium: either *Circum-Stellar gas* (CSM) — as for a core-collapse

*The region *upstream* — as opposed to the *downstream* — of the shock is the region where the shock front has already passed.

Supernova — or *Interstellar gas* (ISM) — as for a type Ia Supernova — (Schure and Bell, 2013):

$$\phi E_{\rm esc,Cur,CSM} = \frac{e\sqrt{\pi}}{\gamma\tau c}\chi u_{\rm sh}(t)^2 R_{\rm sh}(t)\sqrt{\rho(t)}\,, \tag{4.A1.3}$$

$$\phi E_{\rm esc,Cur,ISM} = \frac{e\sqrt{\pi}}{2\gamma\tau c}\chi u_{\rm sh}(t)^2 R_{\rm sh}(t)\sqrt{\rho}, \tag{4.A1.4}$$

where $\gamma\tau$ is the number of e-folding growth time necessary to amplify the magnetic field (we take $\gamma\tau = 5$ hereafter), $\chi = U_{\rm CR}/\rho u_{\rm sh}^2$, is the fraction of the shock kinetic energy imparted into CRs (we take $\chi = 0.1$ hereafter), ρ is the ambient gas mass density and $\phi = \ln(E_{p,\rm max}/m_p c^2)$.

We consider a shock radius scaling with time as $\sim t^b$, where b depends on the evolution stage: $b = 1$, $b = 2/5$, $b = 3/10$, $b = 1/4$ in the *free expansion* (Free), *Sedov-Taylor* (Sed), *pressure-driven snowplough* (PDS) and *momentum-conservation phases* (MCS), respectively. We use the scaling laws derived in Cioffi et al. (1988); Truelove and McKee (1999) to evaluate the shock radius and speed at the transition between two phases. The magnetic field strength is assumed to vary as a certain power of the shock speed, namely $B(t) \propto u_{\rm sh}^a$, where a may depend on the SNR evolution stage. Once the time dependence of $E_{p,\rm max}$ is explicit, we can inverse it to find the release time $t(E_{p,\rm max})$.

With this procedure, the timescales for the different stages of the SNR evolution, from the Sedov phase until the dissipation of the remnant (*merging stage*), can be calculated as follows:

$$\begin{aligned}
t_{\rm Sed,kyr} &= 0.3 E_{\rm SNR,51}^{-1/2} M_{\rm ej,\odot} n_{T,1}^{-1/3} \\
t_{\rm PDS,kyr} &= \frac{36.1 e^{-1} E_{\rm SNR,51}^{3/14}}{\xi_n^{5/14} n_{T,1}^{4/7}} \\
t_{\rm MCS,kyr} &= \min\left[\frac{61 v_{\rm ej,8}^3}{\xi_n^{9/14} n_{T,1}^{3/7} E_{\rm SNR,51}^{3/14}}, \frac{476}{(\xi_n \Phi_c)^{9/14}}\right] t_{\rm PDS,kyr} \\
t_{\rm merge,kyr} &= 153 \left(\frac{E_{\rm SNR,51}^{1/14} n_{T,1}^{1/7} \xi_n^{3/14}}{\beta C_{06}}\right)^{10/7} t_{\rm MCS,kyr},
\end{aligned} \tag{4.A1.5}$$

where $E_{\rm SNR,51}$ is the total energy of the SN explosion in units of 10^{51} erg, $M_{\rm ej,\odot}$ is the mass of the ejected material in units of 1 Solar masses, $n_{T,1}$ is the ambient medium density in units of $1\,{\rm cm}^{-3}$, ξ_n is the ambient medium metallicity, $v_{\rm ej,8}$ is the speed of the ejected material in units of 10^8 cm/s, $\Phi_c = 1$ is the thermal plasma conductivity, $\beta = 2$ and $C_{06} = 1$. In this work, we fix the energy budget to $E_{\rm tot,SNR} = 10^{51}$ erg, the ejecta mass $M_{\rm ej} = 1\,M_\odot$, the ejecta velocity to $v_{\rm ej} = 10^9\,{\rm cm/s}$ and the ambient density to $n_T = 10\,{\rm cm}^{-3}$. These timescales are expressed in kiloyears.

In this work we consider that the maximum CR energy is current-limited in the free expansion and Sedov phases, while it is limited by geometrical losses during the later radiative phases. Strong magnetic field amplification only occurs during the first two adiabatic phases. The magnetic field is

assumed to scale as $u_{\rm sh}^{3/2}$ in the adiabatic phases and as $u_{\rm sh}$ in the radiative phases (see discussion in Völk et al. (2005)). We further assume that the maximum magnetic field strength and the maximum CR energy are reached at the start of the Sedov phase. They are fixed to $100\,\mu$G and $1\,$PeV respectively.

To summarize, we used Equation (4.A1.3) to calculate the proton escape energy as a function of time as follows:

- $\ln\left(\frac{E_{\rm esc,Cur}(t)}{m_p c^2}\right) E_{\rm esc,Cur}(t) = \ln(E_M(t_{\rm Sed}))\left(\frac{t}{t_{\rm Sed}}\right)^{-6/5}$, such that $E_M \equiv E_{p,\rm max}(t_{\rm Sed}) = 1\,$PeV
- $E_{\rm esc,Geo,1}(t) = E_{\rm M}(t_{\rm PDS})\left(\frac{t}{t_{\rm PDS}}\right)^{-11/10} = E_{\rm esc,Cur}(t_{\rm PDS})\left(\frac{t}{t_{\rm PDS}}\right)^{-11/10}$
- $E_{\rm esc,Geo,2}(t) = E_{\rm M}(t_{\rm MCS})\left(\frac{t}{t_{\rm MCS}}\right)^{-5/4} = E_{\rm esc,Geo,1}(t_{\rm MCS})\left(\frac{t}{t_{\rm MCS}}\right)^{-5/4}$.

Release time for leptons

Besides the processes already discussed for hadrons, leptons are also sensitive to radiative losses. The maximum energy fixed by radiative losses is $E_{e,\rm max,loss}$. These losses can prevent them to escape the SNR until the condition $E_{e,\rm max,loss} \leq E_{p,\rm max}$ is fulfilled (Ohira et al., 2012). The energy $E_{e,\rm max}$ is set by the condition $t_{\rm acc} = t_{\rm loss}$ where $t_{\rm acc}$ and $t_{\rm loss}$ are the acceleration and loss timescales respectively. We assume here a simple form of the acceleration timescale, $t_{\rm acc} = \eta_{\rm acc} f(r) D_{\rm Bohm}/u_{\rm sh}^2$, where $f(r)$ is a function of the shock compression ratio. For a parallel shock $f(r) \sim 3r(r+1)/(r-1)$, while, if magnetic field amplification occurs upstream of the shock, the function assumes the form $f(r) \sim 6.6r/(r-1)$ (Parizot et al., 2006). A compression ratio $r = 4$ is adopted hereafter. The time dependence of radiative losses is imposed by the time variation of the magnetic field strength $B(t)$ in the synchrotron process. Synchrotron loss-timescale for an electron of energy E is $t_{\rm loss,syn} = 6\pi m_e^2 c^4/\sigma_T c B(t)^2 E$, where m_e is the electron mass and σ_T is the Thomson cross section.

In conclusion, assuming that geometrical losses are responsible for electron escape at each stage of the SN evolution from the Sedov phase on, to calculate the electron escape energy as a function of time we proceed with the following steps:

- $E_{\rm esc,Geo,0}(t) = E_{\rm M}(t_{\rm Sed})\left(\frac{t}{t_{\rm Sed}}\right)^{-11/10}$, such that $E_M \equiv E_{e,\rm max}(t_{\rm Sed}) = 100\,$TeV
- $E_{\rm esc,Geo,1}(t) = E_{\rm M}(t_{\rm PDS})\left(\frac{t}{t_{\rm PDS}}\right)^{-11/10} = E_{\rm esc,Geo,0}(t_{\rm PDS})\left(\frac{t}{t_{\rm PDS}}\right)^{-11/10}$
- $E_{\rm esc,Geo,2}(t) = E_{\rm M}(t_{\rm MCS})\left(\frac{t}{t_{\rm MCS}}\right)^{-5/4} = E_{\rm esc,Geo,1}(t_{\rm MCS})\left(\frac{t}{t_{\rm MCS}}\right)^{-5/4}$.

4.A2 On the expected number of nearby hidden remnants

In this appendix, we discuss the motivations to consider only one additional source to look for in the vicinity of the Earth. We consider the rate — per unit volume, at the solar circle, as a function of the

Galactic latitude z — of both type Ia and type II Supernova events that are implemented in DRAGON2 — these are the same rates as in Equation (2.13), for the case $r = R_\odot$ (Ferriere, 2001):

$$\begin{aligned}\mathcal{R}_{\rm I}(z) &= \left(7.3\,{\rm kpc}^{-3}\,{\rm Myr}^{-1}\right)\cdot e^{-\frac{|z|}{325\,{\rm pc}}}\\ \mathcal{R}_{\rm II}(z) &= \left(50\,{\rm kpc}^{-3}\,{\rm Myr}^{-1}\right)\cdot\left\{0.79\,e^{-\left(\frac{|z|}{212\,{\rm pc}}\right)^2}+0.21\,e^{-\left(\frac{|z|}{636\,{\rm pc}}\right)^2}\right\}.\end{aligned} \tag{4.A2.1}$$

Since we are testing the hypothesis of a Supernova as source of high-energy leptons ($E_{e^\pm} > 1\,{\rm TeV}$), we integrate those rates in a cylinder of half-height $h_{\rm cyl} = 1\,{\rm kpc}$, as this is roughly the distance that those leptons can travel, due to their massive energy-loss. Thus we need to compute:

$$n_{\rm SNR}[{\rm kpc}^{-2}\cdot{\rm Myr}^{-1}] = \int_{-1\,{\rm kpc}}^{+1\,{\rm kpc}} dz\ \left(\mathcal{R}_{\rm I}(z)+\mathcal{R}_{\rm II}(z)\right). \tag{4.A2.2}$$

The result of the integral has to be multiplied by the base area of the cylinder $A = \pi r_{\rm cyl}^2$, where $r_{\rm cyl} = 1\,{\rm kpc}$ for the same losses reasons, and by the lifetime of a typical Supernova Remnant, $\tau_{\rm age} \sim 5\cdot 10^5\,{\rm yr}$. Therefore, within one SNR lifetime and $1\,{\rm kpc}$ from the Earth, we expect $N_{\rm SNR} \simeq 2.2$ Supernova Remnants potentially contributing to the observed lepton flux.

Since we already observe five of them Fornieri et al. (2020b), we expect the lowest possible number of additional hidden sources to dominate the observed all-lepton spectrum on Earth. This assumption is corroborated by the observation of a directional bump in the dipole anisotropy amplitude (see Ahlers and Mertsch (2017) and references therein), as discussed in Section 4.3.3.

As a comment on the estimation of the event rate, it might be argued that the Solar system is embedded in what is referred to as the Local Bubble, a low-density ($n_{\rm HI} \lesssim 0.1\,{\rm cm}^{-3}$) region of the Galaxy of radius $r_{\rm LB} > 300\,{\rm pc}$ that likely originated by the explosion of several SNe (Pelgrims et al., 2020). This could imply a different rate of Supernova events inside it. However, since the age of the Bubble is estimated to be $\sim \mathcal{O}(10^7)$, which is much larger than the average lifetime of a SN, this can only affect the calculation in the sense of lowering the number of expected events.

Part III
Impact of the microphysics of the MHD modes on CR transport

5

The role of fast magnetosonic modes in cosmic-ray diffusion

In this chapter, we investigate in detail how the different magneto-hydro-dynamic (MHD) modes affect the efficiency of cosmic-ray confinement by a turbulent cascade. We have seen above that the phenomenological expression of the diffusion coefficient — $D(E) \propto E^{\delta}$, which is typically considered in the literature — is inspired by the results of the *quasi-linear theory* of scattering off alfvènic perturbations. On the other hand, the physics of the turbulence changes significantly based on the environment where the cascade generates. As a matter of fact, the study of the turbulent cascades in magnetized plasmas reveals that the turbulence power may not be isotropically distributed among the wavenumbers' components — $k_{\perp}$ and $k_{\parallel}$, with respect to the local magnetic-field direction — for certain orientations of the fluctuations' displacement. In particular, the alfvénic cascade has been found to evolve anisotropically, with little power left for large wavenumbers to efficiently scatter cosmic rays. Conversely, the fast magnetosonic modes cascade isotropically and, therefore, may constitute the dominant scattering centers for the cosmic-ray particles. As a consequence of the interplay among the different MHD modes, the resulting diffusion coefficient may not be a single power law and the transport properties of the particles might be revised with respect to typical physical picture.

5.1 Motivations

As we have extensively discussed, resonant interactions between cosmic particles and the Alfvénic part of the MHD turbulent cascade have been considered as the main origin of cosmic-ray confinement in the Galaxy. A perturbative theory able to predict the scattering rate as a function of the particle rigidity (in the limit of small *isotropic* perturbations on top of a regular background magnetic field), namely the QLT, has inspired most phenomenological characterizations of the cosmic-ray sea in terms of the diffusion equation solved by means of the numerical or semi-analytical codes discussed above. In most of these studies, however, both the normalization and slope of the diffusion coefficient are not determined by first principles, but rather fitted to secondary-to-primary flux ratios (*e.g.*, the Boron-to-Carbon ratio, B/C). Furthermore, as seen in Section 1.3.2, QLT formally predicts only the transport along the magnetic-field lines, whereas its applications to an isotropic diffusion model is typically justified in terms of large-amplitude turbulent fluctuations of the magnetic field at the scales of their injection (Strong et al., 2007). However, a rigorous proof that this allows to treat cosmic-ray transport as an effectively isotropic diffusion does not exist to date.

The DRAGON package, in particular, has provided some very significant steps forward in this context, *i.e.*, by moving away from the naive zero-order modeling of isotropic, homogeneous diffusion and implementing in some contexts position-dependent diffusion coefficients. Even so, such attempts do not contain a description of cosmic-ray transport that fully captures the microphysics of the interaction between CRs and the magnetized turbulent plasma. A proper implementation of these microphysical processes seems compelling in order to usher in a new era of cosmic-ray modeling, thus providing a proper link between theories and the plethora of increasingly accurate measurements.

From the theoretical point of view, our picture of MHD turbulence and our understanding of CR interactions with the turbulent plasma have dramatically improved during the latest decades with respect to the simple QLT mentioned above. These developments have now led to a more appropriate description of the turbulent cascade in the *interstellar medium* and its interactions with the diffuse CR *sea*. As seen in Section 1.3.1, MHD turbulence can be decomposed into a mixed cascade of (incompressible) Alfvénic fluctuations, as well as (compressible) slow and fast magnetosonic fluctuations, as theoretically demonstrated and numerically confirmed by simulations (Cho and Lazarian, 2002; Cho et al., 2002). Regarding the Alfvénic component, a reference scenario is the model put forward by Goldreich and Sridhar (hereafter, GS95 model (Goldreich and Sridhar, 1995; Sridhar and Goldreich, 1994); see also Cho et al. (2003) for a general review). The model stems from the observation that mixing field lines in directions perpendicular to the regular magnetic field on a hydrodinamical-like timescale is easier than bending the lines themselves, because of the magnetic tension. This perpendicular mixing is able to couple wave-like motions that travel along the regular field,

obeying a *critical balance* condition: $k_\parallel v_A \sim k_\perp u_k$. As the turbulent energy cascades down to smaller and smaller perpendicular scales (larger wavenumbers) with a Kolmogorov-like spectrum, it becomes progressively more difficult for the (weaker and smaller) eddies to bend the field lines and develop small-scale parallel structures. Therefore, most of the power is transferred to scales perpendicular to a mean-magnetic-field direction, and the model implies a high degree of anisotropy of the Alfvénic cascade. These considerations are captured by the scaling relations $E_A(k_\perp) \propto k_\perp^{-5/3}$ (Kolmogorov-like spectrum in the perpendicular direction), and $k_\parallel \propto k_\perp^{2/3}$. As shown in Cho and Lazarian (2002), the same anisotropic scaling relations hold for a cascade of slow magnetosonic (or, pseudo-Alfvén) perturbations, while fast magnetosonic fluctuations were shown to feature a *isotropic* cascade, with a different scaling of the energy spectrum: $E_M(k) \propto k^{-3/2}$. Moreover, as mentioned in Ptuskin et al. (2006), all the relevant phases of the *interstellar medium* can be approximated as a low-beta plasma (the plasma β parameter is the ratio between the plasma thermal pressure and the magnetic pressure). In this regime, fast-magnetosonic modes are less damped than Alfvénic fluctuations (see Barnes, 1966, and references therein); a result also confirmed by means of (collisionless) kinetic simulations of plasma turbulence showing that, when injecting random magnetic-field perturbations at the MHD scales, magnetosonic-like fluctuations may compete with (and possibly dominate over) the Alfvénic cascade as the plasma beta decreases below unity (Cerri et al., 2016, 2017).

As a consequence of this paradigm, the picture of the microphysics of cosmic-ray pitch-angle scattering may be deeply revised. As shown in Chandran (2000), the cosmic-ray scattering rates, evaluated for the GS95 highly anisotropic Alfvénic spectrum, significantly decrease with respect to the simple assumption of isotropic cascade. On the other hand, the isotropy of the fast-magnetosonic cascade may allow these modes to dominate CR scattering for most of the pitch angle range (Yan and Lazarian, 2002a).

A non-linear theory of scattering on magnetosonic modes (NLT) has been developed *e.g.* in Völk (1973); Yan and Lazarian (2002a, 2004, 2008); a seminal attempt to implement these phenomena in a numerical code, and compare the predictions with a wide set of data, has been recently presented in Evoli and Yan (2014). This theory naturally leads to a set of well-defined predictions for the diffusion tensor, depending on the local ISM properties.

In fact, the properties of fluctuations' damping associated to different regions of the ISM play a crucial role in the possible suppression of magentosonic turbulence. For instance, in an environment such as the magnetized, diffuse halo of our Galaxy, *i.e.*, characterized by very low density ($n_H \sim 10^{-3}\,\mathrm{cm}^{-3}$) and high temperatures ($T \sim 10^6\,\mathrm{K}$), the mean-free-path associated to Coulomb scattering can be as large as $\sim 10^7$ astronomical units (Yan and Lazarian, 2008). As a result, collisionless (Landau-type) damping is expected to be the dominant process affecting turbulent fluctuations. On the other hand, in regions where a significant amount of warm ionized hydrogen is present (*i.e.*, the extended Galac-

tic disk, $|z| \lesssim 1\,\mathrm{kpc}$), the Coulomb collisional mean free path can be as low as an astronomical unit. Hence, viscous damping has to be taken into account, to the point that it may dominate over collisionless damping. This in turn affects the relative effectiveness of the pitch-angle scattering rate associated to different MHD modes. Given this picture, NLT allows to consistently compute the diffusion coefficients for a wide rigidity range in both environments, and depending on several parameters, including the plasma β and the amplitude of the injected turbulent fluctuations.

In this chapter, we aim at providing a first phenomenological analysis based on the NLT of cosmic-ray scattering simultaneously including magnetosonic and Alfvénic modes. By identifying a set of parameters that characterize the ISM properties in the two Galactic regions mentioned above (and thus the relevant damping mechanisms of turbulent fluctuations therein), we compute the associated diffusion coefficients from first principles, following the formalism outlined in Yan and Lazarian (2004, 2008). We then implement these coefficients in the DRAGON2 numerical package and test the predictions of the theory against the most recent data provided by the AMS-02 Collaboration. In particular, we focus on the fluxes of protons and light nuclei, as well as on the boron-to-carbon flux ratio.

The chapter is organized as follows: in Section 5.2, we describe the general physical setup, leaving the detailed calculations to Appendix 5.A1; in Section 5.3, we show how the relevant physical quantities characterizing the diffuse Galactic halo and the extended Galactic disk shape differently the diffusion coefficients within these two environments; in Section 5.4, we show that the computed diffusion coefficients — implemented in a two-zone model in DRAGON2 — can reproduce the primaries' flux spectra, as well as the boron-over-carbon ratio, above $\sim 200\,\mathrm{GeV}$, for reasonable choices of the physical parameters. Finally, in Section 5.5, we derive the conclusions and discuss some physical implications of the presented results.

5.2 Scattering rate and diffusion coefficient in MHD turbulence

Here we present a summary of the calculation leading to the diffusion coefficient experienced by a cosmic particle with charge q and mass m in a turbulent plasma. To address the contributions to the scattering efficiency arising from the different MHD cascades (namely, Alfvénic and fast/slow magnetosonic), we follow the approach based on the non-linear extension — developed in Völk (1973) — of the original *quasi-linear theory* of pitch-angle scattering on Alfvénic and magnetosonic turbulence (Jokipii, 1966b; Kulsrud and Pearce, 1969). We refer to Appendix 5.A1 for the detailed calculations leading to the expressions reported in this Section.

In this formalism, a particle with velocity $\boldsymbol{v}$ forming an angle θ with the background magnetic field $\boldsymbol{B}_0$ (*i.e.*, having a pitch angle $\mu \equiv v_\parallel/|\boldsymbol{v}| = \cos\theta$) propagating in a turbulent environment whose

fluctuations' power spectrum is described by I, exhibits a scattering rate in pitch-angle space that can be expressed by the following expression, already introduced in Section 1.3.2 (Kulsrud and Pearce, 1969; Voelk, 1975):

$$D_{\mu\mu} = \Omega^2(1-\mu^2)\int d^3\boldsymbol{k} \sum_{n=-\infty}^{+\infty} R_n(k_\parallel v_\parallel - \omega + n\Omega)\left[\frac{n^2 J_n^2(z)}{z^2} I^{\rm A}(\boldsymbol{k}) + \frac{k_\parallel^2}{k^2} J_n'^2(z) I^{\rm M}(\boldsymbol{k})\right], \qquad (5.2.1)$$

where: $\Omega = qB_0/m\gamma c$ is the particle's Larmor frequency; $\boldsymbol{k}$ is the wave-vector of the turbulent fluctuations; $k_\parallel \equiv |\boldsymbol{k}|\cos\alpha_{\rm wave}$ is its field-aligned component ($\alpha_{\rm wave}$ being the angle between the wave vector and the direction of the background magnetic field); $\omega = \omega(\boldsymbol{k})$ the associated fluctuations' frequency.

In Equation (5.2.1), the power spectrum of the fluctuations has been explicitly split into its Alfvénic ($I^{\rm A}$) and magnetosonic ($I^{\rm M}$) contribution, since sub-gyro-scale fluctuations belonging to these two components are "filtered" differently by particles' gyro-motion: this effect is described by the different coefficients involving the n-th order Bessel functions $J_n(z)$ (with $z \equiv k_\perp r_L$, where $r_L = v_\perp/\Omega$ is the particle's Larmor radius*) which (typically) gyro-average out the fluctuations at scales much smaller than the particle gyro-radius (*viz.*, $z \gg 1$). This, in turn, means also that different fluctuations' components, Alfvénic and magnetosonic, differently feed back into particles' motion itself (through the resulting $D_{\mu\mu}$).

Finally, R_n represents a function that "resonantly" selects fluctuations whose frequency, in a reference frame that streams along $\boldsymbol{B}_0$ with the particle ($\omega' \equiv \omega - k_\parallel v_\parallel$), is either zero ($n = 0$; Landau-like wave-particle interaction†) or matching a multiple (*i.e.*, harmonic) of the particle gyro-frequency ($n = 1, 2, 3, \ldots$; gyro-resonant wave-particle interaction). In the standard QLT treatment of purely Alfvénic turbulence, this function is a Dirac δ-function. In the present treatment, instead, we include the effect of turbulent fluctuations on the local magnetic-field strength, *i.e.* the fact that the modulus $|\boldsymbol{B}|$ may not be spatially homogeneous. This is clearly dependent on the level of the fluctuations at the injection scale, and is particularly relevant in the presence of magnetosonic (*i.e.*, *compressible*) turbulence, whose finite-$\delta B_\parallel$ fluctuations provide first-order corrections to the magnetic-field strength (Völk, 1973).

Before proceeding further, we find physically instructive to recall the steps that lead to the resonance function that we will adopt in this chapter. To do this, we follow the treatment from Yan and

*In the literature, one typically finds z rewritten in terms of the pitch angle μ and dimensionless rigidity $R = L^{-1}|\boldsymbol{v}|/\Omega$ (L being the injection scale of the turbulence), as $z = k_\perp L\, R\sqrt{1-\mu^2}$.

†In the case of Alfvénic fluctuations, this is the standard Landau damping of Aflvén waves, which, however, within this framework does not contribute to the pitch-angle scattering rate to the first order in fluctuations' amplitude, $\delta B_\perp/B_0$. On the other hand, in the case of magnetosonic turbulence, there is a first-order correction to the magnetic-field strength, due to $\delta B_\parallel$ fluctuations. As a result, there is a non-zero gradient of $|\boldsymbol{B}|$ along the field lines, which provides a "mirroring force", $\boldsymbol{F}_{\rm mirr} \propto \boldsymbol{\nabla}_\parallel |\boldsymbol{B}|$, that determines a Landau-like damping, typically referred to as *transit-time damping* (TTD). This TTD provides a non-zero contribution to the pitch-angle scattering rate.

Lazarian (2008). The physical problem aims at understanding how it is possible to make efficient the mirroring scattering between a cosmic-ray particle and a turbulent wave (Barnes, 1966). In fact, this interaction occurs when particles experience a non-null gradient in the magnetic-field strength along their propagation direction, and this has a sizeable effect only when the particle velocity matches the phase velocity of the propagating wave, $v\mu \simeq \omega/k_{\parallel}$, in order to have a large number of collisions.

As extensively discussed in Section 1.3.2, the main assumption in QLT is that of the unperturbed orbits of particle, whose motion can be decomposed as the motion of the *guiding center* and that about the *guiding center*. Therefore, within QLT, this *transit-time damping* is effective for a limited range of pitch-angles μ. However, it can be shown that, if the total magnetic-field strength changes slowly along the particle motion, the quantity $v_{\perp}/|\boldsymbol{B}|$ becomes an *adiabatic invariant*, namely its variations are negligible along the particle Larmor radius (Landau and Lifshitz, 2003). This implies that, if B is not spatially homogeneous, the perpendicular component of the particle velocity, $v_{\perp}$, has to change accordingly, and so has to do $v_{\parallel}$. This increases the range of allowed pitch angles for the particle and the wave to scatter efficiently via TTD.

This has an important consequence on the motion of the *guiding center*, that we now assume to perturb with a Gaussian spread in the particle-motion direction, $\hat{\boldsymbol{z}}$. In fact, the oscillating component of the magnetic perturbation seen by the particle (corresponding to the function $\cos(k_{\parallel}z - \omega t \pm n\Omega t) = \mathrm{Re}\left[e^{i\left(k_{\parallel}z-\omega t\pm n\Omega t\right)}\right]$ in Equation (1.55)) gets its z function changed, according to the following variation in the averaged coordinate of the *guiding center*:

$$e^{ik_{\parallel}z}\Big|_{\mathrm{pert}} = \int_{-\infty}^{+\infty} dz\, e^{ik_{\parallel}z}\left(\frac{1}{\sqrt{2\pi}\sigma_z}e^{-\frac{(z-\langle z\rangle)^2}{2\sigma_z^2}}\right) = e^{ik_{\parallel}\langle z\rangle}\cdot e^{-k_{\parallel}^2\frac{\sigma_z^2}{2}} \tag{5.2.2}$$

where $\langle z\rangle = v_{\parallel}t$ is the mean position of the *guiding center* and $\sigma_z^2 = \left\langle \Delta v_{\parallel}^2\right\rangle t^2$ the half-width of the Gaussian distribution.

It can be shown (Voelk, 1975) that the first-order contribution to the parallel velocity displacement is given by the turbulence component parallel to the regular field $\boldsymbol{B}_0$. In particular, neglecting higher orders in $\left\langle \delta B_{\perp}^2\right\rangle^2$:

$$\frac{\Delta v_{\parallel}}{v_{\perp}} \simeq \left[\frac{\left\langle \delta B_{\parallel}^2\right\rangle}{B_0^2}\right]^{1/4},$$

from which, using Equation (5.2.2), we obtain $\sigma_z^2 = v_{\perp}^2\left(\frac{\left\langle \delta B_{\parallel}^2\right\rangle}{B_0^2}\right)^{1/2}t^2$.

Based on the above consideration, the resonance function (corresponding to the *delta* function in

Equation (1.49)) becomes:

$$R_n\left(k_\parallel v_\parallel - \omega + n\Omega\right) \equiv \mathrm{Re}\left[\int_0^\infty dt\, e^{i\left(k_\parallel z_{\mathrm{pert}} - \omega t + n\Omega t\right)}\right]$$
$$= \mathrm{Re}\left[\int_0^\infty dt\, e^{i\left(k_\parallel v_\parallel - \omega + n\Omega\right)t - \frac{1}{2}k_\parallel^2 v_\perp^2 t^2 \left(\frac{\left\langle \delta B_\parallel^2 \right\rangle}{B_0^2}\right)^{1/2}}\right]. \tag{5.2.3}$$

With little further algebra, the expression above can be written as follows:

$$R_n(k_\parallel v_\parallel - \omega + n\Omega) = \frac{\sqrt{\pi}}{|k_\parallel| v_\perp M_{\mathrm{A}}^{1/2}} e^{-\frac{(k_\parallel v\mu - \omega + n\Omega)^2}{k_\parallel^2 v^2 (1-\mu^2) M_{\mathrm{A}}}}, \tag{5.2.4}$$

where the broadening is determined by the level of the fluctuations through the Alfvénic Mach number at the injection scale L, $M_{\mathrm{A}} \sim (\delta B/B_0)_L$. The resonance function in (5.2.4) indeed becomes narrower and narrower as M_{A} decreases (to the point that reduces to a Dirac δ-function, $R_n \to \pi\,\delta(k_\parallel v_\parallel - \omega + n\Omega)$, in the limit $M_{\mathrm{A}} \to 0$).

From Equations (5.2.3) and (5.2.4), we see that the resonance function R_n is now broadened, and it is the reason why TTD interaction will be extremely important in the following study. Indeed, Equation (5.2.4) allows the non-linear effect to play here an important role.

If we now searched for the resonant peak, we would have:

$$\frac{dR_n(k_\parallel v_\parallel - \omega + n\Omega)}{dk_\parallel} = 0 \quad \Rightarrow \quad k_\parallel^{(1,2)} = \frac{v_\parallel n\Omega \pm \sqrt{\left(v_\parallel n\Omega\right)^2 + 2n^2\Omega^2\Delta v_\parallel^2}}{\Delta v_\parallel^2}, \tag{5.2.5}$$

which, for $\mu \to 0\,(\theta \to 90°)$, tends to $k_\parallel \sim \frac{\Omega}{\Delta v_\parallel}$. This, in contrast with the QLT result that $k_\parallel^{\mathrm{QLT}} \sim \frac{\Omega}{v_\parallel}$, implies that the $90°$ scattering does not require any particular treatment.

We can now go back to the main purpose. For the turbulent power spectra $I^{\mathrm{A,M}}$, we follow the prescription given in Schlickeiser (2002); Yan and Lazarian (2002a) and consider the two-point correlation tensors between the fluctuation components (see Appendix 5.A1):

$$\langle \delta B_i(\boldsymbol{k})\, \delta B_j^*(\boldsymbol{k'})\rangle / B_0^2 = \delta^3(\boldsymbol{k} - \boldsymbol{k'})\, \mathcal{M}_{ij}\,, \tag{5.2.6}$$

where $I^{\mathrm{A,M}} = \sum_{i=1}^3 \mathcal{M}_{ii}$ and the spectral scalings are resulting from simulations (Cho and Lazarian, 2002; Cho et al., 2002). In particular, we use

$$I^{\mathrm{A,S}}(k_\parallel, k_\perp) = C_a^{\mathrm{A,S}}\, k_\perp^{-10/3} \exp(-L^{1/3} k_\parallel / k_\perp^{2/3}) \tag{5.2.7}$$

for the Alfvén and slow modes, consistent with the usual Goldreich-Sridhar (GS95) spectrum (Goldreich and Sridhar, 1995), while for fast modes we use the isotropic spectrum

$$I^{\mathrm{F}}(k) = C_a^{\mathrm{F}}\, k^{-3/2}. \tag{5.2.8}$$

As a final comment on the calculation of $D_{\mu\mu}$, the integral has to be performed up to the *truncation scale* $k_{\max}$ of the turbulence, namely up to the wave-number at which the cascading timescale equals the dissipation scale, as discussed in Yan and Lazarian (2004). In general, the truncation scale for each damping process is a function of the angle α_{wave}, hence the damping mechanism is in general *anisotropic*. We refer to the next section and to the Appendix for more details on this quantity.

Once all the contributions from the three modes are computed, we can obtain the spatial diffusion coefficient D as a function of the (dimensionless) particle rigidity $R = L^{-1}|\boldsymbol{v}|/\Omega$. The expression of $D(R)$ obtained will be then implemented in `DRAGON` to calculate the propagated particle spectra measured at Earth (Schlickeiser, 2002):

$$D(R) = \frac{1}{4}\int_0^{\mu^*} d\mu\, \frac{v^2\,(1-\mu^2)^2}{D_{\mu\mu}^{\mathrm{M,T}}(R) + D_{\mu\mu}^{\mathrm{M,G}}(R) + D_{\mu\mu}^{\mathrm{A,G}}(R)}, \tag{5.2.9}$$

where μ^* is the the largest $\mu \in [0,1]$ for which a particle can be considered as confined by turbulence (*i.e.*, to be in the diffusion regime). In particular, this means that a CR with rigidity R and pitch angle μ should undergo a number of scattering $\mathcal{N} \gg 1$ while traveling a distance of the order of a fraction of the Galactic region where it propagates. In this work, we choose $L_{\mathrm{H,D}}/5 \equiv L'_{\mathrm{H,D}}$, that roughly corresponds to the typical coherence scales of the magnetic field in those regions (L_{H} and L_{D} are the typical length scale of the diffuse Galactic halo and of the extended Galactic disk, respectively). In other words, if $\tau_{\mathrm{stream}} \sim L'_{\mathrm{H,D}}/v$ is the streaming timescale of a CR across a distance $L'_{\mathrm{H,D}}$, the pitch-angle scattering time of such cosmic particle, $\tau_{\mu\mu} \sim (1-\mu^2)/D_{\mu\mu}$, (*i.e.*, the typical timescale between two consecutive pitch-angle scattering events) must be much shorter than τ_{stream}:

$$\frac{\tau_{\mu\mu}}{\tau_{\mathrm{stream}}} \sim \frac{v}{L'_{\mathrm{H,D}}}\frac{(1-\mu^2)}{D_{\mu\mu}} \ll 1\,. \tag{5.2.10}$$

Based on this criterion, we observe that μ^* strongly depends on the strength of the turbulence and on the damping parameters, but for $M_{\mathrm{A}} \geq 0.3$ it closely approaches 1 for all the energies of interest for the present work ($10^{-1}\,\mathrm{GeV} \leq E \leq 10^5\,\mathrm{GeV}$) in the disk and in the halo, while particles in the disk exit the diffusive regime for $M_{\mathrm{A}} = 0.1$ even at low energy ($E \lesssim 1\,\mathrm{GeV}$).

5.3 Diffusion coefficients in Galactic disk and halo and ISM properties

In this section, we want to analyze how the diffusion coefficient is shaped by the parameters involved in the calculations. We take into account two different environments, as sketched in the Introduction: the *"extended disk"*, characterized by the presence of warm ionized hydrogen and a low value of the Coulomb collisional mean free path, and the *"diffuse halo"*, where a low-density plasma characterized by a negligible Coulomb scattering rate is present. Calculations are carried out using the code in Fornieri (2020a)*.

Figures 5.1a - 5.1b and Figures 5.1c - 5.1d visualize the diffusion coefficient as a function of the rigidity in the halo and in the disk, respectively, plotted for several values of the Alfvénic Mach number $M_{\rm A}$, given a fixed injection scale $L_{\rm inj}$ and plasma β. We also show a reference diffusion coefficient resulting from what presented in Chapter 3 (Fornieri et al., 2020b), designed to correctly reproduce the AMS-02 data on both primary and secondary species.

First of all, we notice that (i) the high-rigidity slope *predicted* by the theory (and fixed by the scaling of the fast magnetosonic cascade) is perfectly compatible with the high-rigidity slope of the reference diffusion coefficient fitted on CR data, and (ii) the theory predicts a clear departure from a simple power law for all values of the relevant parameters; however, this departure does not describe the low-energy downturn of the reference coefficient, that reflects the behaviour of AMS-02 data. Hence, we may argue that the theory may provide a correct description of CR confinement above $\simeq 200$ GV, while an accurate low-energy treatment may require additional theoretical arguments. This argument will be further developed in the next Section. The normalization spans several orders of magnitude; it is important to notice that it is mainly governed by the value of $M_{\rm A}$, and that reasonable values of this parameter are associated to the correct normalization.

We will now elaborate more on this aspect and discuss the following key points: (i) the behaviour with respect to the Alfvénic Mach number, that reflects the strength of the injected turbulence, (ii) the features associated to the different damping mechanisms involved in the process, and (iii) the role of the Alfvén modes. The effect of variations on the plasma β parameter and the injection scale, $L_{\rm inj}$ will be also briefly addressed.

$D(E)$ variation with $M_{\rm A}$. Both figures clearly show that $D(E)$ is a decreasing function of the Alfvénic Mach number. This is due to the fact that an increased level of turbulence results in a more effective scattering rate of cosmic particles. In fact, by definition $M_{\rm A} \equiv \delta u / v_{\rm A}$: therefore, larger values of $M_{\rm A}$ characterize larger-amplitude turbulent fluctuations that enhance the pitch-angle scattering rate,

*https://github.com/ottaviofornieri/Diffusion_MHD_modes

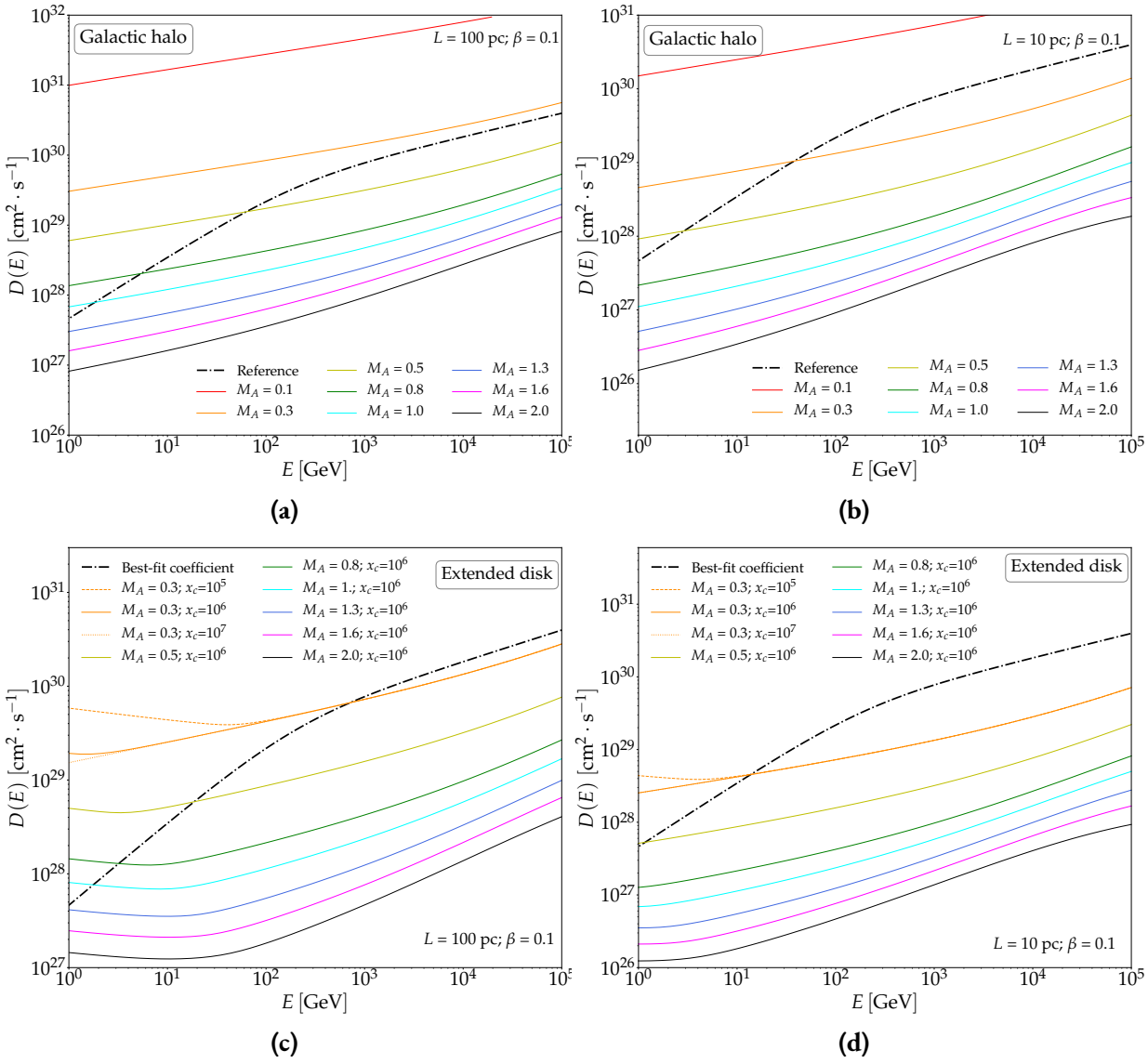

Figure 5.1: We show the diffusion coefficients associated to the pitch-angle scattering onto MHD (magnetosonic and Alfvénic) fluctuations as a function of the rigidity in the halo, **(a)** and **(b)**, and in the "extended disk", **(c)** and **(d)**, given a fixed injection scale $L_{\rm inj}$ and plasma β, for several values of $M_{\rm A}$. Black dashed line: reference diffusion coefficient taken from Fornieri et al. (2020b), designed to correctly reproduce the AMS-02 data on both primary and secondary species.

$D_{\mu\mu}$. As a result, CRs are more efficiently confined at high-$M_{\rm A}$, which results in a lower spatial diffusion coefficient, $D(E)$.

Effect of damping. The most relevant difference between the behaviour of $D(E)$ in the halo (Figures 5.1a - 5.1b) and in the extended disk (Figures 5.1c - 5.1d) is the minimum in the low-energy domain ($\rho_{\rm min} \sim 50 - 100\,{\rm GV}$) in the latter case.

This feature can be explained following this train of thoughts.

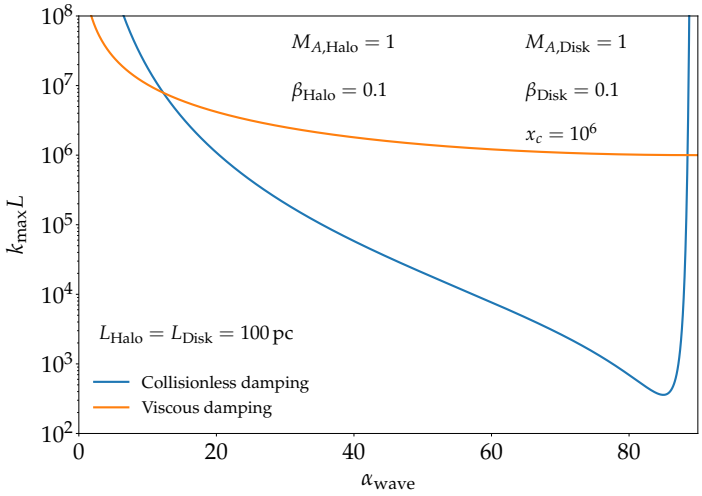

Figure 5.2: We show the truncation scale $k_{\max}$ of the scattering-rate integral as a function of the pitch angle of the turbulent wave with respect to $\boldsymbol{B}_0$ for the different damping processes considered in this work. Viscous damping is effective in the extended disk only. The values of the corresponding physical quantities are shown in the plot.

- As mentioned in the previous Section, the expression for $D_{\mu\mu}$ involves an integral in the wave vector space $d^3\boldsymbol{k}$ up to a truncation scale $k_{\max}$. This integral is dominated by the contributions associated to waves with small angle α_{wave} with respect to the direction of the regular magnetic field (see Yan and Lazarian, 2004).

- The truncation scale as a function of α_{wave} associated to the collisionless damping (present in both the extended disk and in the halo), and to the viscous damping (present in the extended disk only) is shown in Figure 5.2. In the critical region associated to small angles, the truncation scale associated to collisionless damping is much larger than the one associated to viscous damping.

- As a consequence, *in the extended disk* environment, the truncation of the scattering-rate integral over $d^3\boldsymbol{k}$ at relatively small wavenumbers ($k_{\max}L \sim 10^7$) implies a lower value of $D_{\mu\mu}$ for CRs at the low energies, the ones that would resonate with comparable (or larger) wavenumbers. This is reflected in the low-rigidity upturn of the *spatial* diffusion coefficient shown in Figures 5.1c - 5.1d. It can also be easily understood that the position of this upturn shifts in energy depending on the intersection point of the two truncation-scale curves in Figure 5.2.

Role of the Alfvén modes in the confinement process. Here, we want to comment on the importance of the fast magnetosonic modes in confining charged CRs. In Figure 5.3 we show the diffusion coefficient when fast modes are included (lower panel) compared to the case where only Alfvén modes enter the calculation (upper panel).

Studying the case with no fast modes, two features are immediately visible:

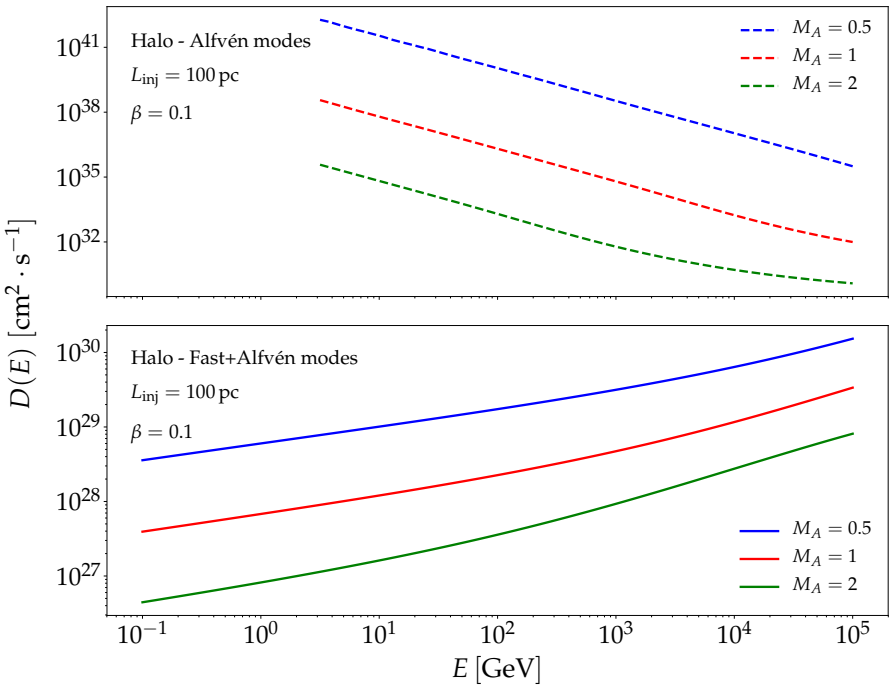

Figure 5.3: We show the total diffusion coefficient with fast magnetosonic modes included in the calculation (lower panel) compared to the case in which only Alfvén fluctuations are taken into account (upper panel). Alfvénic turbulence is not efficient in confining Galactic CRs, due to the anisotropy of the cascade (see also Chandran (2000); Yan and Lazarian (2004)).

- The normalization of $D(E)$ spans from just a few up to ~ 15 orders of magnitude more than the case where fast modes are included. Based on the abundances and average lifetimes of unstable elements, the average residence time of CRs in the Galaxy is found to be $\tau_{\rm esc} \simeq 15\,{\rm Myr}$ in the GeV domain (Yanasak et al., 2001). This implies that, in order to be confined in a halo of a few kpc, CRs should experience a diffusion coefficient that can be at most $\langle D \rangle = \frac{L_{\rm H}^2}{2\tau_{\rm esc}} \sim 10^{30}\,{\rm cm}^2/{\rm s}$. Therefore, if only Alfvén modes were responsible for confinement, the current data on secondary and unstable species would not be reproduced. Moreover, the scattering rate would be so low that the diffusion approximation would not be valid anymore, and the CR "sea" would be highly suppressed due to ballistic escape from the Galaxy.

- The behaviour of the diffusion coefficient with rigidity shows a declining trend in the pure alfvénic case, while the total coefficient *increases* with rigidity.

Both features derive from the anisotropic behaviour of the alfvénic cascade. Indeed, as shown in Equation (5.2.7), Alfvén modes cascade anisotropically, evolving on the isosurfaces identified by $k_\parallel \propto k_\perp^{2/3}$ (Goldreich and Sridhar, 1995). This relation implies that turbulent eddies are spatially elongated along $\boldsymbol{B}$, or, equivalently, that in the momentum space they are elongated in the perpendicular direction. So the majority of the power goes into a $k_\perp$ cascade. This leaves very little power (*i.e.* scat-

tering efficiency) to the cascade in parallel wave numbers $k_\parallel$ that, according to the resonance function (5.2.4), is the component involved in the wave-particle interaction. Since $k_\parallel \sim \ell_\parallel^{-1}$, particles with small rigidity and small Larmor radius — interacting with large $k_\parallel$ — get weakly confined, while high-energy CRs scatter more efficiently. As a result, the spatial diffusion coefficient $D(E)$ is shaped as a *decreasing* function of the energy, if only the alfvénic component is taken into account.

Therefore, an efficient wave-particle scattering with Alfvén modes can occur only at high energies, that resonate with scales that are not too far from the injection scale, where the anisotropic nature of the cascade has not become significant yet. We can have an estimate of this scale, by computing for instance how many $k_\perp$-orders the cascade has to evolve in order to change $k_\parallel$ of one order of magnitude. Indeed, as already said $k_\parallel \propto k_\perp^{2/3}$, which means that the spectral anisotropy of the fluctuations increases as follows:

$$\frac{k_\parallel}{k_\perp} \sim \left(\frac{k_\perp}{k_{\rm inj}}\right)^{-1/3} ,$$

where we denoted with $k_{\rm inj}$ the (isotropic) wavenumber associated to the injection scale, $L_{\rm inj}$.

As a safe estimate, we can consider the cascade anisotropy to be really important when there is roughly an order of magnitude between the parallel and perpendicular wave numbers corresponding to the same level of turbulent energy, *i.e.*, $k_\parallel/k_\perp \sim 1/10$. According to the above relation, this level of cascade anisotropy is reached at $k_\perp/k_{\rm inj} \sim 10^3$. If we now consider an injection scale $L_{\rm inj} \sim 100\,{\rm pc}$, this will happen at $\ell_{\rm an} \sim 10^{-3} L_{\rm inj} \simeq 0.1\,{\rm pc}$. The Larmor radius of a charged CR is $r_L = 3.37 \cdot 10^{12}\,{\rm cm}\,(p/{\rm GeV}) \simeq 1.08 \cdot 10^{-6}\,{\rm pc}\,(p/{\rm GeV})$. Therefore, a $\ell_{\rm an} \sim 0.1\,{\rm pc}$ scale roughly corresponds to the Larmor radius of particles belonging to energies $\sim 10^5\,{\rm GeV} \sim 100\,{\rm TeV}$. (Note, however, that considering the anisotropy to be important at $k_\parallel/k_\perp \sim 1/10$ is quite arbitrary, and one may push the above constraint to even larger energies by considering, *e.g.*, $k_\parallel/k_\perp \sim 1/3$ to be already relevant – this would correspond to CR energies of $\sim 3\,{\rm PeV}$.) As a consequence, we would not observe any contribution to $D(E)$ at energy scales that are currently of interest. If, on the other hand, turbulence is injected at smaller scales — say $L_{\rm inj} = 10\,{\rm pc}$ for instance — the same effect comes into play at smaller scales, which therefore contains non-negligible scattering power even at CR energies that are low enough to be experimentally explored ($E \sim 10^4 - 10^5\,{\rm GeV}$). This is indeed visible in the change of slope in $D(E)$ for the larger Mach numbers of Figures 5.1a - 5.1b and 5.1c - 5.1d (in the right panels, corresponding to $L = 10\,{\rm pc}$).

This is of course only a rough estimation, since it depends on the strength of the injection — related to the value of $M_{\rm A}$ — and holds as soon as the critical balance is reached and the cascade follows the GS95 spectrum. This would happen at the scale $\ell_{\rm tr} \sim L_{\rm inj} M_{\rm A}^2$ or at $\ell_{\rm A} \sim L_{\rm inj}/M_{\rm A}^3$ for sub-Aflvénic ($M_{\rm A} < 1$) or super-Alfvénic ($M_{\rm A} > 1$) injection, respectively (Lazarian et al., 2020), *i.e.*, at scales smaller than $L_{\rm inj}$ if $M_{\rm A} \neq 1$. So it is a reasonable estimation for $M_{\rm A} \approx 1$ and this is why there is no imprint of a change of slope in the blue and red dashed lines in the upper panel of Figure 5.3. By increasing

the strength of the injection (*i.e.*, increasing $M_{\rm A}$), anisotropy starts to play a role at lower and lower energies, as exhibited in the green dashed line of the figure. However, there are indications that typical values of the Alfvénic Mach number in the ISM do not significantly exceed $M_{\rm A} \approx 2$ (Tofflemire et al., 2011).

In conclusion, for the injection scale $L_{\rm inj}$ and Alfvénic Mach number we are considering throughout this work, anisotropy of the Alfvén cascade always plays a key role and therefore cannot efficiently confine cosmic rays, while the fast magnetosonic cascade is able to induce a very efficient pitch-angle scattering rate.

Another important parameter to be monitored is the size of the extended disk and Galactic halo. The Galactic halo size determines the volume where cosmic rays propagate, thus influencing the normalization of the diffusion coefficient. Variations on these parameters are important when computing the total diffusion coefficient at a given position in the Galaxy. In general, what is expected to matter is the relation between their sizes. While the halo half-size could be constrained to be between $3-12\,{\rm kpc}$ (Di Bernardo et al., 2013; Evoli et al., 2020; Zaharijas et al., 2013), the extended disk half-size could vary from 0.5 to $2\,{\rm kpc}$ (Feng et al., 2016b). Along this chapter, we will refer to the size of these extended zones as their half-size, *i.e.* a halo size of $L_{\rm H}$ means that it extends from $-L_{\rm H}$ to $+L_{\rm H}$ in the vertical (perpendicular to the Galactic plane) coordinate.

Finally, variations of the plasma beta parameter lead to more efficient confinement of charged particles (*i.e.*, a smaller diffusion coefficient) as β decreases — this is due to the fact that the fast-magnetosonic mode becomes progressively more important in the confinement process*. This will be shown in the next Section.

To summarize, these calculations allow us to examine how plausible plasma properties characterizing the different Galactic zones can lead to different values of the diffusion coefficient and, therefore, to different spectra of Galactic cosmic-ray fluxes. Different combinations of the plasma parameters in the extended disk and Galactic halo will be explored in the next Section in comparison to experimental data.

5.4 Phenomenological implications of the theory

In this Section we compare the propagated CR spectrum, obtained adopting the diffusion coefficients discussed above, with the most relevant CR observables.

We implement the coefficients in `DRAGON`, and solve the usual diffusion-loss equation previously

*This is because fast-magnetosonic modes become less and less damped at lower beta (cf., *e.g.*, Barnes, 1966; Cerri et al., 2016). This feature can be appreciated through the behaviour of their *collisionless* truncation scale with β (see Appendix 5.A1).

described, Equation (2.1). We adopt the setup described in detail in Chapter 2, with the cross-section network presented in Evoli et al. (2017b) and implemented in the DRAGON2 version available online*. This version allows to implement the chosen expressions for the diffusion coefficient in the two-zone model here presented.

A key observable in the context of CR phenomenology is the B/C flux ratio. In fact, Boron is entirely secondary and is mostly produced in spallation reactions involving heavier, and mostly primary, species (including Carbon): therefore, the ratio between those two nuclei fluxes has been widely used over the latest years to constrain the *grammage* accumulated by CRs while residing in the Galactic disk, and ultimately the features of the diffusion coefficient.

Given these considerations, we start our analysis by focusing on this observable, recently measured with high accuracy all the way up to the TeV scale by the AMS-02 Collaboration (Aguilar et al., 2016). In particular, we pay attention to the dependence of the computed B/C flux ratio on the Alfvénic Mach number parameter of pre-existing MHD turbulence, $M_{\rm A}$, which was shown to play a key role in the overall normalization of the transport coefficients. We scan over this parameter, and find that larger values of $M_{\rm A}$ are likely to be associated with a significant over-production of Boron, especially at high energies. This is due to the high efficiency of the confinement mechanism that characterize scenarios featuring turbulence with large Alfvénic Mach numbers.

- In a *simple setup* characterized by the same value of $M_{\rm A}$ in both the extended disk and the halo, we find that values of order $M_{\rm A} \sim 0.4$ for the effective Alfvénic Mach number are compatible with current data in the high-energy range (above $\sim 100\,\mathrm{GeV}$) (see Figure 5.4, *top panel*). We emphasize that this result is achieved with no *ad hoc* retuning on the data, and naturally stems from the theoretical expression of the diffusion coefficient computed in detail in this work.

- In a *more general setup* where extended disk and halo exhibit different values of this parameter, a diverse range of combinations is allowed by the data (see Figure 5.4, *bottom panel*).

  We also show for illustrative purposes in Fig. 5.5 the impact of the extended disk size on the same observable, keeping the alfvénic Mach number in the extended disk and halo fixed to one of the combinations allowed by data.

  We remark again that in all cases the high-energy slope is correctly reproduced, while the low-energy domain suggests an extra grammage possibly associated to a different confinement mechanism (not captured by the theory presented here) that starts to dominate below $\sim 200\,\mathrm{GeV}$. This point will be further discussed below.

We now widen our perspective and consider a variety of secondary and primary species.

*https://github.com/cosmicrays

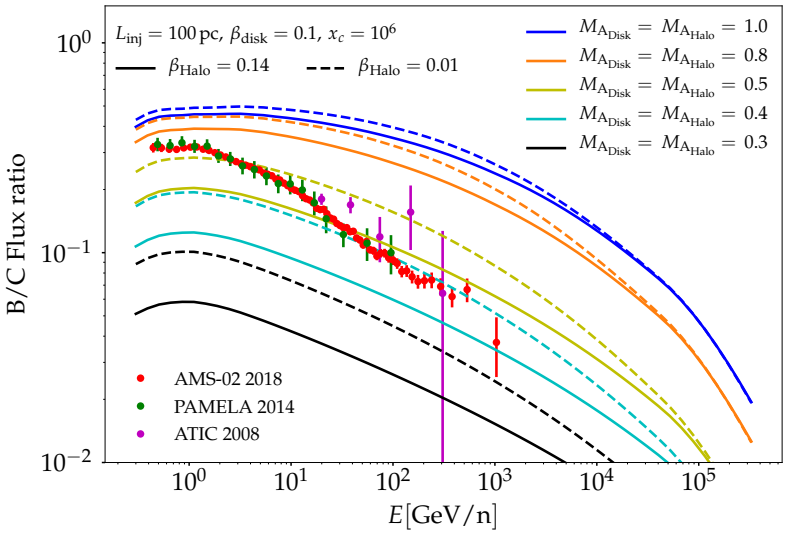

(a)

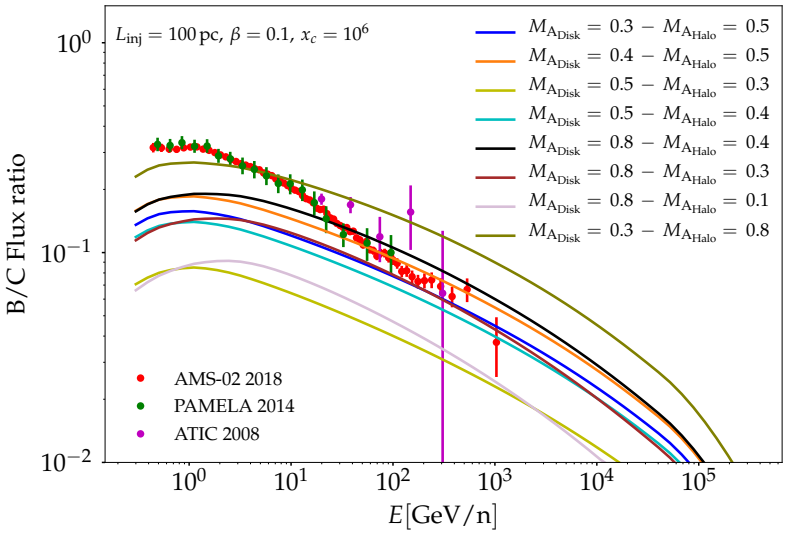

(b)

Figure 5.4: We plot the theoretical prediction (obtained with an updated version of the DRAGON code) for the B/C within *simple setup* characterized by the same value of $M_{\rm A}$ in both the extended disk and the halo up to TeV energy (top panel), and a more general setup where extended disk and halo exhibit different values of this parameter (bottom panel). We show the most recent data in the energy range of interest from AMS-02, PAMELA and ATIC experiments.

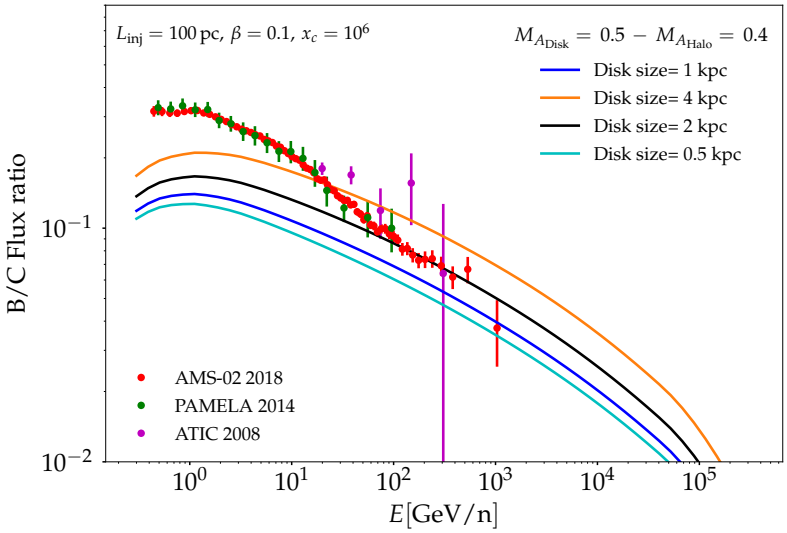

Figure 5.5: We plot the theoretical prediction for the B/C for different values of the extended disk vertical size.

The AMS-02 Collaboration has recently measured the spectra of several CR light nuclei fluxes and ratios (Aguilar et al., 2015a, 2016, 2018c). These data provided major improvement in the precision and dynamical range, and have revealed relevant features. The most relevant is a progressive hardening in primary species, with the spectral index varying from $\simeq 2.8$ in the 50 - 100 GV rigidity range to a significantly harder value around $\simeq 2.7$ above 200 GV. Regarding the primary species, we emphasize that the slopes of the primary species depend on both the rigidity scaling of the diffusion coefficients, and on the slope that is injected in the *interstellar medium* as a consequence of the acceleration mechanism taking place at the sources and subsequent escape from the sources themselves. Hence, they do not offer a direct constraint on the scaling of the diffusion coefficient with rigidity, which is one of the key predictions of the theory: only the purely secondary species can be exploited to this purpose. Regarding secondaries, an indication of an even more pronounced hardening in secondary species is also present, suggesting a transport origin for the feature (Génolini et al., 2017). Such spectral feature may be attributed, for instance, as discussed in Aloisio et al. (2015); Blasi et al. (2012) (see also Farmer and Goldreich (2004) for a pioneering prediction) to a transition between two different regimes: (i) the low-energy range where CR transport is expected to be dominated by self-confinement due to the generation of Alfvén waves via *streaming instability*; (ii) the high-energy range where CR confinement is expected to be dominated by scattering off pre-existing turbulent fluctuations (*i.e.*, for which self-generation effects are not expected to play a relevant role).

Motivated by these considerations, and given the aspects highlighted in the study of B/C, we aim at providing a comprehensive picture of the *high-energy portion of the spectrum*, above the afore-

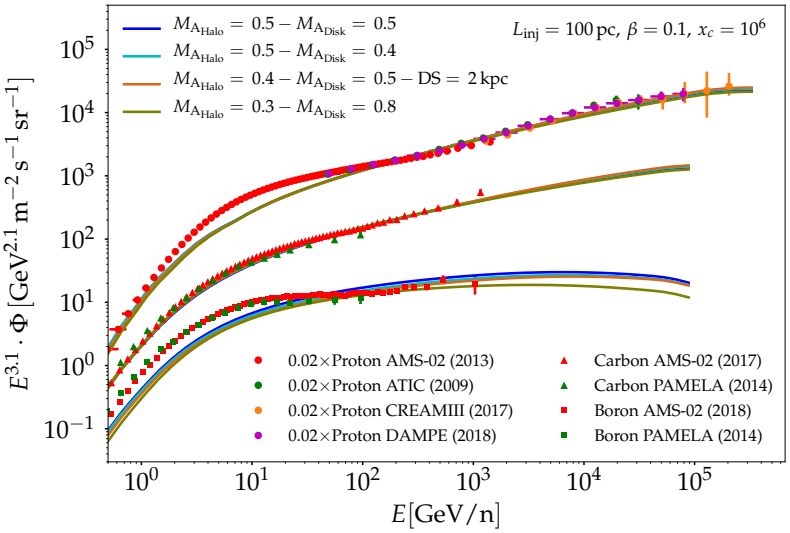

Figure 5.6: We plot the theoretical prediction for the Hydrogen, Carbon and Boron fluxes (obtained with an updated version of the DRAGON code) for a few selected combinations of the parameters of interest. The primary injection spectrum is tuned to fit the data above 200 GeV. All high-energy data can be consistently reproduced within our theoretical framework. An extra confinement mechanism may be required to explain the low-energy excess.

mentioned break, where the confinement due to scattering onto *isotropic fast magnetosonic turbulence* should be the dominant physical mechanism (*i.e.*, given on the one hand the lower impact of self-confinement and, on the other hand, the negligible role played by scattering on the pre-existing anisotropic Alfvénic cascade). In the case of primary species, we aim at identifying a reasonable choice of the injection spectrum that correctly reproduce the data, given the degeneracy mentioned above.

In Figure 5.6 we show a particular realization that satisfies all the experimental constraints in the high-energy regime. We show that we can consistently reproduce all the observed data above the 200 GV spectral feature, by assuming a reasonable injection slope ($\gamma = 2.3$) and propagating the particles within our model. The "excess" at low energy cannot be reproduced within the framework discussed in the present work, and it strongly suggests the presence of another confinement mechanism, possibly associated to the self-generation of Alfvénic turbulence via streaming instability.

5.5 Discussion

The work discussed in this chapter is aimed at presenting the first comprehensive study on the phenomenological implications of the theory describing cosmic-ray scattering onto magnetosonic fluctuations. In this section we discuss potential caveats and future developments of the current work.

As a first discussion point, we want to argue on the potential impact of the anisotropic nature of

cosmic-ray transport. In this chapter, following the line of thought outlined for instance in Strong et al. (2007) and adopted in most papers featuring a numerical description of cosmic-ray transport, we worked under the hypothesis of isotropic diffusion, assuming that the same scaling relations apply to parallel and perpendicular transport (see also Evoli and Yan (2014)). Within the current theoretical framework, this is formally correct only for values of $M_A \simeq 1$. In fact, in Yan and Lazarian (2008) the authors demonstrated that the perpendicular coefficients in the NLT of scattering onto fast magnetosonic modes depend very strongly on the alfvénic Mach number of the turbulence, exhibiting a $\propto M_{\rm A}^4$ scaling. However, many different mechanisms may lead to an effective isotropization of the diffusion tensor* and a commonly adopted assumption that has allowed to successfully reproduce all local observables is that CR transport is well described by an effective scalar coefficient. A careful assessment of this aspect is clearly well beyond the scope of the present work. In fact, it would require a full three-dimensional anisotropic treatment of CR diffusion and a careful modeling of the topology of the Galactic regular magnetic field. However, in future studies, we will address in more detail the intrinsic anisotropic nature of CR transport within the theory presented here. We expect that the impact of a different scaling for the perpendicular transport may potentially be of some relevance as far as non-local observables — γ-rays and radio waves for instance — are concerned, especially in regions that feature values of $M_{\rm A}$ significantly smaller than 1 (see Cerri et al. (2017b) for a pioneering study on the impact of anisotropic transport on non-local CR observables).

Another important aspect that potentially requires a dedicated study is the interplay with self-confinement due to alfvénic turbulence originated by *CR-streaming instability*. It has been pointed out in Blasi et al. (2012); Farmer and Goldreich (2004) that this effect may dominate the low-energy confinement. As a consequence, the transition between a confinement regime dominated by scattering off self-generated turbulence and a regime dominated by scattering onto pre-exisiting MHD turbulence may be the origin of the spectral feature at $\simeq 200\,{\rm GV}$ outlined in detail by the AMS-02 Collaboration in all the CR species. On the other hand, we have shown that the relative importance of alfvénic confinement progressively increases at high energy (Figure 5.3 upper panel). This is due to the lower degree of anisotropy of the alfvénic cascade at scales closer to the injection scale. Consequently, a spectral feature may be present in the high-energy spectrum, close to the PeV domain. A careful assessment of such a feature, its dependence on the environmental properties, and the potential of future experiments (such as LHAASO) to detect it, may constitute another very interesting future avenue in this research field.

As a final discussion point, we mention the necessity to perform complementary observations

*For instance, the role of *compound diffusion*, resulting from the convolution of diffusion in the parallel and perpendicular directions with respect to the magnetic field line, has been studied in a series of papers, where, in particular, the role of *field line random walk* (FLRW) is found to be very important, especially for small turbulence perturbations (Jokipii, 1966b; Jokipii and Parker, 1969a,b; Kóta and Jokipii, 2000; Shalchi and Schlickeiser, 2004; Webb et al., 2006).

and analyses aimed at highlighting the actual presence of magnetosonic fluctuations in the interstellar plasma. In this context, the statistical study of the Stokes parameters of the synchrotron-radiation polarization is a very promising technique. As recently demonstrated in Zhang et al. (2020b), polarization analyses provide a unique opportunity to shed light on the plasma modes composition of the Galactic turbulence, and have led to a discovery of magnetosonic modes in the Cygnus X superbubble.

As a take-home message for this discussion, we want to emphasize the complementarity between different approaches. On the one hand, the arguments above outline the need of a dedicated effort from the experimental side, regarding direct measurements of local CR fluxes, aimed at detecting and characterizing spectral features over a wide energy range and with particular focus on the TeV - PeV domain. On the modeling side, we have emphasized the potential for a significant advance, aimed at analyzing the prediction of the theories in a realistic framework that takes into account the three-dimensional structure of the Galaxy, the topology of its magnetic field, and the properties of the *interstellar medium*. Both efforts are complemented by a research program directed towards analyzing the properties of interstellar turbulence. Thanks to the interplay among these developments, we may finally shed light on the long-standing puzzle of cosmic-ray confinement in the Galaxy.

5.6 Summary of the chapter

In this chapter, we presented a comprehensive phenomenological study of the theory of non-linear scattering of cosmic rays onto *magneto-hydro-dynamic* fluctuations.

We considered a state-of-the-art description of pitch-angle scattering for various MHD cascades, *i.e.*, decomposed into a (anisotropic) cascade of Alfvénic fluctuations, and slow and fast (isotropic) magnetosonic turbulence. We studied the interaction of a charged, relativistic particle with such modes and, adopting the formalism developed in Yan and Lazarian (2004, 2008), we computed the associated transport coefficients from first principles.

We identified a set of parameters that characterize the *interstellar medium* and have significant impact on our result (*i.e.* the Alfvénic Mach number, the plasma β, and some parameters that describe the damping processes in different environments), and presented a complete study of the dependence of the diffusion coefficients with respect to those parameters.

Then, we implemented the coefficients in the numerical framework of the `DRAGON2` code, and tested the theory against current experimental data, with particular focus on the extremely accurate AMS-02 dataset. We found that the high-energy behaviour of the transport coefficients nicely matches the secondary-over-primary slope in that regime, and a reasonable range of the aforementioned parameters allowed us to reproduce the correct normalization as well, without invoking any *ad hoc* tuning. Overall, we found a natural and reasonable agreement with all CR channels within a reasonable choice of both the ISM parameters governing the transport process, and other parameters (*e.g.* injection slope) that characterize our setup.

The theory is therefore adequate to describe the microphysics of Galactic CR confinement in the high-energy domain, in particular above the $\sim 200\,\mathrm{GeV}$ feature highlighted in all primary and secondary hadronic species by the AMS-02 Collaboration. On the other hand, we confirm that the pitch-angle scattering on pre-existing Alfvénic turbulence cannot provide a satisfactory description of CR confinement: in fact, the highly anisotropic Alfvénic cascade turns out to be extremely inefficient in scattering CRs of energies $\lesssim 100\,\mathrm{TeV}$. Our work strongly suggests that the interpretation of AMS-02 data in terms of pitch-angle scattering onto turbulent fluctuations naively described in terms of a Kolmogorov-like isotropic spectrum cannot be considered satisfactory, and a more accurate description of interstellar turbulence has to be considered.

The behaviour of CR observables below $\sim 200\,\mathrm{GV}$ cannot be reproduced within our framework. The steeper spectrum observed by AMS-02 below that energy seems to require additional physical effects. The self-confinement due to self-generated Alfvénic fluctuations via *CR-streaming instability* seems to be a good candidate in this context.

5.A1 Pitch-angle coefficient for MHD turbulence

In this appendix we briefly review the calculations carried out in Yan and Lazarian (2008) to compute the relative contributions from each MHD mode to the spatial diffusion coefficient. In particular, in Yan and Lazarian (2008) the authors mostly implement the case of trans-alfvénic turbulence ($M_{\rm A} \simeq 1$), whereas here we consider a broader range of Alfvénic Mach number, pertaining also to sub- and super-Alfvénic regimes (*i.e.*, roughly within the range $0.1 \lesssim M_{\rm A} \lesssim 2$). As shown in Yan and Lazarian (2004), slow magnetosonic modes follow very closely the behaviour of the shear Alfvén modes.

The starting point is Equation (5.2.1) for the pitch-angle scattering rate of a charged particle in turbulent fluctuations, that we report here for convenience:

$$D_{\mu\mu} = \Omega^2 (1-\mu^2) \int d^3\boldsymbol{k} \sum_{n=-\infty}^{+\infty} R_n(k_\parallel v_\parallel - \omega + n\Omega) \left[\frac{n^2 J_n^2(z)}{z^2} I^{\rm A}(\boldsymbol{k}) + \frac{k_\parallel^2}{k^2} J_n'^2(z) I^{\rm M}(\boldsymbol{k}) \right], \qquad (5.A1.1)$$

where we remind the reader that $\Omega = qB_0/m\gamma c$ is the particle's gyro-frequency, $\mu = v_\parallel/|\boldsymbol{v}| = \cos\theta$ its pitch angle (θ being the angle between the particle's velocity $\boldsymbol{v}$ and the background magnetic field $\boldsymbol{B}_0$), $\boldsymbol{k}$ and ω are the fluctuations' wave-vector and frequency, respectively, and $I(\boldsymbol{k})$ their turbulent power spectrum at scales $\sim k^{-1}$ (which is modified by a combination of the Bessel's functions $J_n(k_\perp r_{\rm L})$, as effectively seen through a particle's gyro-motion whose Larmor radius is $r_{\rm L}$, and that scatters via a resonance-like function R_n).

To model the turbulent fluctuations of the magnetic field and of the fluid velocity at MHD scales, δB and δu, respectively, we follow the prescription given in Yan and Lazarian (2002a) for their correlation functions:

$$\langle \delta B_i(\boldsymbol{k}) \cdot \delta B_j^*(\boldsymbol{k'}) \rangle / B_0^2 = \delta^3(\boldsymbol{k}-\boldsymbol{k'})\, \mathcal{M}_{ij}(\boldsymbol{k}) \qquad (5.A1.2a)$$

$$\langle \delta u_i(\boldsymbol{k}) \cdot \delta B_j^*(\boldsymbol{k'}) \rangle / v_A B_0 = \delta^3(\boldsymbol{k}-\boldsymbol{k'})\, \mathcal{C}_{ij}(\boldsymbol{k}) \qquad (5.A1.2b)$$

$$\langle \delta u_i(\boldsymbol{k}) \cdot \delta u_j^*(\boldsymbol{k'}) \rangle / v_A^2 = \delta^3(\boldsymbol{k}-\boldsymbol{k'})\, \mathcal{K}_{ij}(\boldsymbol{k}), \qquad (5.A1.2c)$$

where the indices $i, j = 1, 2, 3$ represent the different components of the fluctuation vector, and the $\langle\,\rangle$ operator indicates the average over a phase-space ensemble (Kubo, 1957). These correlation functions are related to the energy density of the fluctuations, *e.g.*, $\langle \delta B(\boldsymbol{x}) \delta B^*(\boldsymbol{x}) \rangle$ for magnetic-field fluctuations. In terms of their Fourier components, $\delta B(\boldsymbol{x}) = \int d^3\boldsymbol{k}\, e^{-i\boldsymbol{k}\cdot\boldsymbol{x}}\, \delta B(\boldsymbol{k})$ and $\delta B^*(\boldsymbol{x}) = \int d^3\boldsymbol{k}\, e^{i\boldsymbol{k}\cdot\boldsymbol{x}}\, \delta B^*(\boldsymbol{k})$, the

fluctuations' energy density can be written as

$$\langle \delta B(\boldsymbol{x})^2 \rangle = \sum_{i,j} \int d^3\boldsymbol{k} \int d^3\boldsymbol{k'}\, e^{-i(\boldsymbol{k}-\boldsymbol{k'})\cdot\boldsymbol{x}} \, \langle \delta B_i(\boldsymbol{k}) \cdot \delta B_j^*(\boldsymbol{k'}) \rangle \tag{5.A1.3}$$

$$= B_0^2 \cdot \sum_{i,j} \int d^3\boldsymbol{k}\, \mathcal{M}_{ij}(\boldsymbol{k}), \tag{5.A1.4}$$

such that the integral of the normalized fluctuation spectrum over wave-numbers gives the spatial energy density. This is in agreement with Voelk (1975) (their Equation (32)). The spectrum of a given turbulent field is then obtained as the trace of the correlation tensor of its fluctuations. For instance, the trace of $\mathcal{M}_{ij}$ provides the magnetic-field turbulent spectrum: $\sum_{i=j} \mathcal{M}_{ij} = I^{\mathrm{A,S,F}}$, where A labels the Alfvén mode, and S, F the slow and fast magnetosonic modes, respectively. In what follows, only the magnetic-field fluctuations and their correlation tensor in (5.A1.2a) will enter the calculations.

For what concerns the explicit form of the magnetic-field fluctuations' correlation tensor $\mathcal{M}_{ij}$, we will make use of the expressions outlined in Cho et al. (2002), which were obtained via numerical simulations in the trans-Alfvénic regime $M_{\mathrm{A}} \simeq 1$. However, as mentioned above, in this work we consider turbulent regimes that span from the sub-Alfvénic ($M_{\mathrm{A}} < 1$) to the super-Alfvénic ($M_{\mathrm{A}} > 1$) case. Therefore, the general correlation tensor (and the corresponding turbulent spectrum) of the Alfvénic cascade that will be considered here must include an extra scaling with the Alfvénic Mach number M_{A} (a scaling that also depends whether we are in the sub-Alfvénic or in the super-Alfvénic case, as outlined in Lazarian et al. (2020), and from which the usual GS95 scaling (Goldreich and Sridhar, 1995) is anyway recovered in the trans-Alfvénic limit, $M_{\mathrm{A}} \sim 1$). By taking into account these generalizations, the correlation tensors pertaining to the Alfvén and fast modes scale as follows:

$$\mathcal{M}_{ij}^{\mathrm{A(S),sub}} = C_a^{\mathrm{A(S),sub}} I_{ij} k_\perp^{-10/3} \cdot \exp\left(-\frac{L^{1/3}|k_\parallel|}{M_{\mathrm{A}}^{4/3}\, k_\perp^{2/3}}\right) \qquad (M_{\mathrm{A}} \leq 1) \tag{5.A1.5}$$

$$\mathcal{M}_{ij}^{\mathrm{A(S),super}} = C_a^{\mathrm{A(S),super}} I_{ij} k_\perp^{-10/3} \cdot \exp\left(-\frac{L^{1/3}|k_\parallel|}{M_{\mathrm{A}}\, k_\perp^{2/3}}\right) \qquad (M_{\mathrm{A}} > 1) \tag{5.A1.6}$$

$$\mathcal{M}_{ij}^{\mathrm{F}} = C_a^{\mathrm{F}} J_{ij} k^{-7/2}, \tag{5.A1.7}$$

where C_a are normalization constants, and parallel ($\parallel$) and perpendicular ($\perp$) here are defined with respect to the background magnetic field, $\boldsymbol{B}_0$. The tensors $I_{ij} = \delta_{ij} - k_i k_j / k_\perp^2$ and $J_{ij} = k_i k_j / k_\perp^2$ are 2D tensors defined in the sub-space perpendicular to the background magnetic field* (*e.g.*, if $\boldsymbol{B}_0$ is along z, then I_{ij} and J_{ij} above are defined in the xy-plane, and are zero if $i, j = z$). Within the

*If $\mathcal{I}_{ij} = \delta_{ij} - k_i k_j / k_\perp^2$ and $\mathcal{J}_{ij} = k_i k_j / k_\perp^2$ are the 3D version of I_{ij} and J_{ij} defined for any $i, j = 1, 2, 3$ index, then the 2D version can be generally written as $I_{ij} = \mathcal{T}_{ik}\mathcal{I}_{kl}\mathcal{T}_{lj}$ and $J_{ij} = \mathcal{T}_{ik}\mathcal{J}_{kl}\mathcal{T}_{lj}$, with $\mathcal{T}_{ij} = \delta_{ij} - B_{0,i}B_{0,j}/B_0^2$ being the projecting operator onto the plane perpendicular to $\boldsymbol{B}_0$.

plane perpendicular to $\boldsymbol{B}_0$, I_{ij} and J_{ij} are indeed projecting operators working as expected for the polarization of the Alfvén and fast modes: I_{ij} projects onto the direction perpendicular to $\boldsymbol{k}_\perp$, whereas J_{ij} projects onto the direction parallel to it. As an additional remark, we point out that the above scalings are the 3D extensions of the 1D spectra found in Cho and Lazarian (2002).

Finally, in order to determine the normalization constants C_a, we require that the energy of the turbulent fluctuations obtained by their correlation tensor (*i.e.*, $\langle \delta B(\boldsymbol{x})^2 \rangle$ from Equation (5.A1.3)) matches the root-mean-square value of the fluctuations at the injection scale L (*i.e.*, $\delta B^2_{\rm rms} \equiv \langle \delta B^2 \rangle_L$):

$$\langle \delta B(\boldsymbol{x})^2 \rangle \equiv B_0^2 \sum_{i,j} \int d^3\boldsymbol{k}\, \mathcal{M}_{ij}(\boldsymbol{k}) \stackrel{!}{=} \delta B^2_{\rm rms} \equiv \langle \delta B^2 \rangle_L \,, \tag{5.A1.8}$$

where $\langle \delta B^2 \rangle_L$ is related to the (outer-scale) Alfvénic Mach number $M_{\rm A}$ by $\langle \delta B^2 \rangle_L / B_0^2 \approx M_{\rm A}^2$.

5.A1.1 $D_{\mu\mu}$ from Alfvén modes

In this Section, we specialize to the case of a cascade of Alfvénic fluctuations, explicitly providing the steps of the calculation leading to the associated pitch-angle scattering rate, $D^{\rm A}_{\mu\mu}$, in the relevant regimes.

Normalization coefficient

To get the normalization coefficient $C_a^{\rm A}$ for the alfvénic cases, we make use of Equation (5.A1.8) with the spectrum (5.A1.5) or (5.A1.6) for the sub- or super-Alfvénic regime, respectively, where $\sum_{i=j} I_{ij} = 1$. Moreover, since Alfvénic fluctuations are anisotropic, it is convenient to write the integral decomposing it as $\int d^3\boldsymbol{k} = \int_{L^{-1}}^{+\infty} k_\perp dk_\perp \int_{-\infty}^{+\infty} dk_\parallel \int_0^{2\pi} d\phi$.

Sub- and trans-Alfvénic regime ***($M_{\rm A} \leq 1$).*** When dealing with sub-Alfvénic turbulence, the cascade of fluctuations at scales immediately below the injection scale belongs to the weak-turbulence regime. This means that, initially, fluctuations develop a $E(k_\perp) \sim k_\perp^{-2}$ spectrum in the direction perpendicular to B_0, while there is no turbulent cascade along the magnetic-field lines, $E(k_\parallel) = E(k_L) = {\rm cst}$. However, this weak-turbulence regime can be sustained only for a limited range of (perpendicular) scales, $[L^{-1}, \ell_{\rm tr}^{-1}]$, as the critical-balance condition will be anyway achieved at a scale $\ell_{\rm tr} \sim L M_{\rm A}^2$ that determines the transition to the strong-turbulence regime (Goldreich and Sridhar, 1995). At perpendicular scales $\lambda_\perp \leq \ell_{\rm tr}$, the cascade follows the modified GS95 spectrum in (5.A1.5). Therefore, to obtain the normalization constant $C_a^{\rm A,sub}$, we now use the fact that the integral of the magnetic-field fluctuations' correlation tensor should match the energy of the fluctuations at the transition scale $\ell_{\rm tr}$, *i.e.*, $\int d^3\boldsymbol{k}\, \mathcal{M}_{ij}^{\rm A,sub}(\boldsymbol{k}) = \langle \delta B^2 \rangle_{\ell_{\rm tr}} / B_0^2$. Also, since the parallel scale does not evolve in the weak-turbulence regime, we remind the reader that the parallel wavelength $\lambda_{\parallel,{\rm tr}}$ corresponding to a turbulent eddy of

perpendicular size $\lambda_\perp = \ell_{\rm tr}$ is still the injection scale, *i.e.* $\lambda_{\parallel,\rm tr} = L$. As a result, the exponential function that describes surfaces of constant energy in $(k_\perp, k_\parallel)$ space still contains the outer-scale factor, $L^{1/3}$, as for the trans-Alfvénic limit, $M_{\rm A} = 1$. The equation that determines $C_a^{\rm A,sub}$ is therefore:

$$C_a^{\rm A,sub}\cdot 2\pi\int_{\ell_{\rm tr}^{-1}}^{k_{\perp,\rm max}} k_\perp dk_\perp \int_{\left[-k_{\parallel,\rm max},-L^{-1}\right]\cup\left[L^{-1},k_{\parallel,\rm max}\right]} dk_\parallel\, k_\perp^{-10/3}\cdot\exp\left(-\frac{L^{1/3}|k_\parallel|}{M_{\rm A}^{4/3}\,k_\perp^{2/3}}\right)\approx$$
$$\approx C_a^{\rm A,sub}\cdot 2\pi\int_{\ell_{\rm tr}^{-1}}^{+\infty} k_\perp dk_\perp \int_{-\infty}^{+\infty} dk_\parallel\, k_\perp^{-10/3}\cdot\exp\left(-\frac{L^{1/3}|k_\parallel|}{M_{\rm A}^{4/3}\,k_\perp^{2/3}}\right) \stackrel{!}{=} \frac{\langle\delta B^2\rangle_{\ell_{\rm tr}}}{B_0^2}.$$

The above approximations in the limits of integration involve both the cutoff and the injection wave-number scales: (i) the former corresponds to the cascade cutoff scales $(k_{\perp,\rm max}, k_{\parallel,\rm max})$, and letting them approach infinity does not lead to any appreciable modification. Indeed, the perpendicular spectrum is soft enough $(E(k_\perp)\sim k_\perp^{-10/3})$ that the large wave-numbers carry very little turbulent power. In particular, this is true for the parallel spectrum, since the GS95 critical-balance relation implies an even softer spectrum versus $k_\parallel$. (ii) As far as the low-$k_\parallel$ limit of integration is concerned, considering the proper injection scale $(k_{\parallel,\rm min}\sim L^{-1})$ introduces a correction factor $1/e$ in the normalization constant. This correction only affects Alfvèn and slow modes, that will be found to be anyway strongly subdominant in shaping the cosmic-ray diffusion coefficient, therefore, for the sake of simplicity, we neglect it. Notice, however, that we will use this approximation only for the normalization constant, while the correct wave-number range is considered when calculating $D_{\mu\mu}$, thus not affecting the resulting slopes of the diffusion coefficient.

Solving the integrals, the left-hand side of the above equation yields $C_a^{\rm A,sub}\,4\pi\cdot\frac{3M_{\rm A}^{4/3}\,\ell_{\rm tr}^{2/3}}{2L^{1/3}}$. Then, taking into account the scaling $\ell_{\rm tr}\sim LM_{\rm A}^2$ for the transition scale, we can obtain the normalization in terms of the injection scale L:

$$C_a^{\rm A,sub}\,4\pi\cdot\frac{3}{2}\,L^{1/3}\,M_{\rm A}^{8/3} \stackrel{!}{=} \frac{\langle\delta B^2\rangle_{\ell_{\rm tr}}}{\langle\delta B^2\rangle_L}\cdot\frac{\langle\delta B^2\rangle_L}{B_0^2}\approx M_{\rm A}^2\cdot M_{\rm A}^2 = M_{\rm A}^4,$$

where we have used the scaling of weak turbulence for the fluctuations, $\delta B_\lambda\sim\lambda_\perp^{1/2}$, to substitute $\langle\delta B^2\rangle_{\ell_{\rm tr}}/\langle\delta B^2\rangle_L = \ell_{\rm tr}/L\approx M_{\rm A}^2$, and $\langle\delta B^2\rangle_L/B_0\equiv M_{\rm A}^2$.

In conclusion, $C_a^{\rm A,sub} = M_{\rm A}^{4/3}\,L^{-1/3}/6\pi$ and the correlation tensor of the magnetic-field fluctuations for the Alfvén mode in the sub-Alfvénic (or trans-Alfvénic) regime is:

$$\mathcal{M}_{ij}^{\rm A,sub} = \frac{M_{\rm A}^{4/3}\,L^{-1/3}}{6\pi}\,I_{ij}\,k_\perp^{-10/3}\cdot\exp\left(-\frac{L^{1/3}k_\parallel}{M_{\rm A}^{4/3}\,k_\perp^{2/3}}\right). \tag{5.A1.9}$$

Super-alfvénic case: $M_{\rm A} > 1$. Conversely to what happens in the sub-Alfvénic case, when the

injected fluctuations are super-Alfvénic, the corresponding turbulent cascade at scales immediately below the injection scale L is "hydro-dynamical" in nature, *i.e.*, isotropic with a spectrum $E(k) \sim k^{-5/3}$. This hydrodynamic-like behaviour is, again, sustained only within a limited range of scales, $[L^{-1}, \ell_{\rm A}^{-1}]$, as the critical-balance condition will be eventually met at the Alfvén scale $\ell_{\rm A} \sim L M_{\rm A}^{-3}$ (Lazarian et al., 2020). At scales $\lambda \leq \ell_{\rm A}$ the turbulent cascade thus becomes anisotropic with respect to the magnetic-field direction, and follows the modified GS95 spectrum in (5.A1.6). Following the same reasoning of the sub-Alfvénic case, the equation for $C_a^{\rm A,super}$ reads as

$$C_a^{\rm A,super} \cdot 2\pi \int_{\ell_{\rm A}^{-1}}^{+\infty} k_\perp dk_\perp \int_{-\infty}^{+\infty} dk_\parallel \, k_\perp^{-10/3} \cdot \exp\left(-\frac{L^{1/3}|k_\parallel|}{M_{\rm A}\, k_\perp^{2/3}}\right) \stackrel{!}{=} \frac{\langle \delta B^2 \rangle_{\ell_{\rm A}}}{B_0^2}.$$

By explicitly solving the integral and taking into account the scaling $\ell_{\rm A} \sim L M_{\rm A}^{-3}$, one obtains:

$$4\pi C_a^{\rm A,super} \cdot \frac{3}{2} L^{1/3} M_{\rm A}^{-1} \stackrel{!}{=} \frac{\langle \delta B^2 \rangle_{\ell_{\rm A}}}{\langle \delta B^2 \rangle_L} \cdot \frac{\langle \delta B^2 \rangle_L}{B_0^2} \approx M_{\rm A}^{-2} \cdot M_{\rm A}^2,$$

where we have used the Kolmogorov-like scaling for the turbulent fluctuations, $\delta B_\lambda \sim \lambda^{1/3}$, to substitute $\langle \delta B^2 \rangle_{\ell_{\rm A}} / \langle \delta B^2 \rangle_L = (\ell_{\rm A}/L)^{2/3} \approx M_{\rm A}^{-2}$, and, again, $\langle \delta B^2 \rangle_L / B_0^2 = M_{\rm A}^2$ by definition.

In conclusion, $C_a^A = M_{\rm A}\, L^{-1/3}/6\pi$, and the correlation tensor of the magnetic-field fluctuations for the Alfvén mode in the super-Alfvénic regime is:

$$\mathcal{M}_{ij}^{\rm A,super} = \frac{M_{\rm A}\, L^{-1/3}}{6\pi} I_{ij}\, k_\perp^{-10/3} \cdot \exp\left(-\frac{L^{1/3} k_\parallel}{M_{\rm A}\, k_\perp^{2/3}}\right). \tag{5.A1.10}$$

Resonance function

In this work, we are adopting the resonance function, R_n, described in Yan and Lazarian (2008). Such function includes the broadening of the resonant scattering wave-number due finite-amplitude corrections in the magnetic-field strength*:

$$R_n(k_\parallel v_\parallel - \omega + n\Omega) = \frac{\sqrt{\pi}}{|k_\parallel| v_\perp M_{\rm A}^{1/2}} \cdot \exp\left(-\frac{(k_\parallel v\mu - \omega + n\Omega)^2}{k_\parallel^2 v^2 (1-\mu^2) M_{\rm A}}\right),$$

where we recall the reader that the above expression reduces to the usual Dirac δ-function in the limit of vanishing fluctuations amplitude, $M_{\rm A} \to 0$.

Within the present approximations, Alfvén modes can scatter CRs only via $n \neq 0$ gyro-resonance interactions, while the $n = 0$ Landau-damping interaction is neglected. Also, we consider low-frequency, non-relativistic MHD turbulence, *i.e.*, turbulent fluctuations within a range of frequencies ω and wave-

*An effect that is consistent with the inclusion in this scattering theory of the Landau-type wave-particle interaction usually referred to as *transit-time damping* (TTD).

numbers $\boldsymbol{k}$ such that their frequency is much smaller than the particles' gyro-frequency, $\omega \ll \Omega$, and their phase velocity is much smaller than the speed of light, $v_{\rm ph} \sim \omega/k \ll c$. In this limit, since cosmic particles' are relativistic (*i.e.*, their velocity is typically $v \approx c$), one can neglect the fluctuation frequency ω in the argument of the resonance function: $k_\parallel v\mu - \omega + n\Omega \simeq k_\parallel v\mu + n\Omega$.

Taking these considerations into account and rearranging the argument of the exponential, the resonance function that will be adopted for scattering on Alfvénic fluctuations reads

$$\begin{aligned} R_n(k_\parallel v_\parallel - \omega + n\Omega) &= \frac{\sqrt{\pi}}{|k_\parallel| v_\perp M_{\rm A}^{1/2}} \cdot \exp\left(- \frac{\left(\mu + \frac{n}{x_\parallel R}\right)^2}{(1-\mu^2) M_{\rm A}} \right) \equiv \frac{\sqrt{\pi}}{|k_\parallel| v_\perp M_{\rm A}^{1/2}} \cdot E_n \\ &= \frac{\sqrt{\pi}\,\Omega^{-1}}{|x_\parallel| R\, M_{\rm A}^{1/2}} \cdot E_n \,, \end{aligned} \tag{5.A1.11}$$

where we have defined $R \equiv v/(\Omega L) = (1-\mu^2)^{-1/2} r_{\rm L}/L$, with $r_{\rm L} = v_\perp/\Omega$ the cosmic particle's Larmor radius, and $x_{\parallel,\perp} \equiv k_{\parallel,\perp} L$.

Pitch-angle coefficient

To finally calculate the contribution from the Alfvén modes to the pitch-angle diffusion coefficient, we now make use of the spectra in Equations (5.A1.9) and (5.A1.10) in the following expression:

$$D_{\mu\mu}^{\rm A} = \Omega^2 (1-\mu^2) \int d^3\boldsymbol{k} \sum_{n=-\infty}^{+\infty} \frac{\sqrt{\pi}}{|k_\parallel| v_\perp M_{\rm A}^{1/2}} \cdot E_n \left[I^A(\boldsymbol{k}) \frac{n^2 J_n^2(z)}{z^2} \right]. \tag{5.A1.12}$$

$\boldsymbol{M_{\rm A} \leq 1}$. Using the dimensionless quantities described above, the expression for the pitch-angle scattering rate on Alfvénic fluctuations in the $M_{\rm A} \leq 1$ regime reads:

$$\begin{aligned} D_{\mu\mu}^{\rm A} &= \frac{\sqrt{\pi} v \sqrt{1-\mu^2}\, M_{\rm A}^{5/6}}{3R^2 L} \int dx_\perp \int dx_\parallel \sum_{n=-\infty}^{+\infty} \frac{n^2 J_n^2(z)}{z^2} \cdot \frac{x_\perp^{-7/3}}{|x_\parallel|} \cdot \exp\left(- \frac{x_\parallel}{M_{\rm A}^{4/3}\, x_\perp^{2/3}} \right) E_n \\ &= \frac{\sqrt{\pi}\,\Omega\, M_{\rm A}^{5/6}}{3R} \int dx_\perp \int dx_\parallel \sum_{n=-\infty}^{+\infty} \frac{n^2 J_n^2(z)}{z^2} \cdot \frac{x_\perp^{-7/3}}{|x_\parallel|} \cdot \exp\left(- \frac{x_\parallel}{M_{\rm A}^{4/3}\, x_\perp^{2/3}} \right) E_n, \end{aligned} \tag{5.A1.13}$$

where now $z \equiv x_\perp R (1-\mu^2)^{1/2}$. For Alfvén modes, $n \neq 0$, and we verified that the $n = \pm 1$ functions give the dominant contribution, so that $D_{\mu\mu}^{\rm A} \approx D_{\mu\mu}^{{\rm A},n=1} + D_{\mu\mu}^{{\rm A},n=-1}$. Using the property $J_{-n}(z) = (-1)^n J_n(z)$, from which it follows $J_{-n}^2(z) = J_n^2(z)$, we finally get:

$$D_{\mu\mu}^{\rm A,sub} = \frac{2\sqrt{\pi}\,\Omega\, M_{\rm A}^{5/6}}{3R} \int dx_\perp \int dx_\parallel \frac{J_1^2(z)}{z^2} \cdot \frac{x_\perp^{-7/3}}{x_\parallel} \cdot \exp\left(- \frac{x_\parallel}{M_{\rm A}^{4/3}\, x_\perp^{2/3}} \right) (E^+ + E^-) \tag{5.A1.14}$$

where $E^+ \equiv E^+_{n=1} = \exp\left(-\frac{\left(\mu+\frac{1}{x_\parallel R}\right)^2}{(1-\mu^2)M_\mathrm{A}}\right)$, $E^- \equiv E^-_{n=-1} = \exp\left(-\frac{\left(\mu-\frac{1}{x_\parallel R}\right)^2}{(1-\mu^2)M_\mathrm{A}}\right)$ and the factor 2 comes from taking the integral only on $x_\parallel > 0$.

The lower boundary of integration can be found reminding that we integrate the GS95 spectrum from the scale where the critical balance is reached. For this $M_\mathrm{A} \leq 1$ case, we have seen that, up to the transition scale, the cascade evolves only in the direction perpendicular to the magnetic field. Therefore, we can write:

$$k_{\perp,\min}\ell_\mathrm{tr} = k_{\perp,\min}\cdot\left(\frac{\ell_\mathrm{tr}}{L}\right)L \stackrel{!}{=} 1 \quad \Rightarrow \quad x_{\perp,\min} = \frac{1}{\left(\frac{\ell_\mathrm{tr}}{L}\right)} \approx M_\mathrm{A}^{-2}$$

$$x_{\parallel,\min} = 1,$$

where we denoted with ℓ_tr the scale where the turbulence becomes of GS95 type.

$\boldsymbol{M_\mathrm{A} > 1}$. Following the same steps as for the $M_\mathrm{A} \leq 1$ case, we eventually obtain the following expression:

$$D^{\mathrm{A,super}}_{\mu\mu} = \frac{2\sqrt{\pi}\,\Omega\,M_\mathrm{A}^{1/2}}{3R}\int dx_\perp \int dx_\parallel \frac{J_1^2(z)}{z^2}\cdot\frac{x_\perp^{-7/3}}{x_\parallel}\cdot\exp\left(-\frac{x_\parallel}{M_\mathrm{A}\,x_\perp^{2/3}}\right)(E^+ + E^-)\,. \tag{5.A1.15}$$

In this case, the lower boundary for the integration can be obtained considering that the cascade evolves isotropically until the transition scale ℓ_A is reached. Hence, we obtain:

$$k_{\perp,\min}\ell_\mathrm{A} = k_{\perp,\min}\cdot\left(\frac{\ell_\mathrm{A}}{L}\right)L \stackrel{!}{=} 1 \quad \Rightarrow \quad x_{\perp,\min} = \frac{1}{\left(\frac{\ell_\mathrm{A}}{L}\right)} \approx M_\mathrm{A}^3$$

$$x_{\parallel,\min} \approx M_\mathrm{A}^3.$$

To evaluate the upper boundary of the integrals, we do not treat the two regimes separately and assume that Alfvén modes do not undergo significant damping and therefore the cascade proceeds up to the dissipation scale. Equivalently, we will truncate the integrals at a wave-number much larger than the inverse of the Larmor radius of the less energetic particle, $k_\perp \gg r_L^{-1}\big|_{E_\mathrm{min}}$. In practice, we will consider two order of magnitudes larger than that quantity. Since we are considering particles with energy as low as $10^{-2}\,\mathrm{GeV}$, with a Larmor radius of $r_L \simeq 3.37\cdot10^{12}\,\mathrm{cm}\left(\frac{p=10^{-2}\mathrm{GeV}}{\mathrm{GeV}}\right)\left(\frac{10^{-6}\,\mathrm{G}}{B}\right) = 3.37\cdot10^{10}\,\mathrm{cm}$, this corresponds to $k_{\perp,\max} = 10^2\cdot(3.37\cdot10^{10}\,\mathrm{cm})^{-1} = 3\cdot10^{-9}\,\mathrm{cm}^{-1}$. Also, according to the findings of the GS95 theory, $k_\parallel \propto k_\perp^{2/3}$.

In conclusion, the upper bounds for the integrals are:

$$x_{\perp,\max} = 3\cdot10^{-9}\cdot L[\mathrm{cm}], \qquad x_{\parallel,\max} = x_{\perp,\max}^{2/3}. \tag{5.A1.16}$$

5.A1.2 $D_{\mu\mu}$ FROM FAST MODES

In this Section, we instead consider the case of a cascade of fast-magnetosonic fluctuations. Analogously to the Alfvénic case, the details of the calculation leading to the associated pitch-angle scattering rate, $D^{\rm F}_{\mu\mu}$, are outlined.

Normalization coefficient

Again, to normalize the spectrum resulting from the simulations, we use Equation (5.A1.8) for the corresponding spectrum of fast-magnetosonic turbulence obtained from the trace of the correlation tensor in (5.A1.7) (we remind the reader that $\sum_{i=j} J_{ij} = \frac{k_i k_i + k_j k_j}{k_\perp^2} = 1$). Since fast modes are found to be isotropic, we can rearrange the integral over the intertial range as $\int d^3\boldsymbol{k} = \int_{L^{-1}}^{+\infty} k^2\, dk \int_0^\pi \sin\alpha\, d\alpha \int_0^{2\pi} d\phi$.

The equation to solve to get the normalization is therefore:

$$C_a^{\rm F} \cdot 2\pi \int_{L^{-1}}^{+\infty} k^2\, dk \int_0^\pi \sin\alpha\, d\alpha\, k^{-7/2} = \frac{\langle \delta B^2 \rangle_{{\rm rms},L}}{B_0^2} = M_{\rm A}^2$$

From this, we get that $C_a^{\rm F} = \frac{M_{\rm A}^2\, L^{-1/2}}{8\pi}$ and finally:

$$\mathcal{M}_{ij}^{\rm F} = \frac{M_{\rm A}^2\, L^{1/2}}{8\pi} J_{ij} k^{-7/2}. \tag{5.A1.17}$$

Resonance function

The resonance function is the same presented in Equation (5.A1.1), but split in two forms, as for scattering on fast modes contributions from both transit-time damping (TTD) and gyro-resonant interaction have to be taken into account.

Gyroresonance corresponds to the case $n \neq 0$, and the resulting function is the same described for the Alfvén modes:

$$R_n(k_\parallel v_\parallel - \omega + n\Omega) = \frac{\sqrt{\pi}}{|k\xi| v_\perp M_{\rm A}^{1/2}} \cdot \exp\left(-\frac{(\mu + \frac{n}{x\xi R})^2}{(1-\mu^2) M_{\rm A}} \right) \equiv \frac{\sqrt{\pi}}{|k\xi| v_\perp M_{\rm A}^{1/2}} \cdot E_n^{\rm G} \qquad (n \neq 0)$$

where $\xi \equiv \cos\alpha$ is the "pitch-angle" of the wave vector associated to the turbulent fluctuations (*i.e.*, α is the angle between $\boldsymbol{k}$ and $\boldsymbol{B}_0$).

Transit-time damping corresponds to $n = 0$, in which case we can rearrange the argument of the exponential as $\frac{\cancel{k_\parallel^2 v^2}\left(\mu - \frac{\omega}{k_\parallel v}\right)^2}{\cancel{k_\parallel^2 v^2}(1-\mu^2) M_{\rm A}} = \frac{\left(\mu - \frac{v_A}{\xi v}\right)^2}{(1-\mu^2) M_{\rm A}}$, where the last step holds because the phase velocity of the fast waves is the same order of magnitude as the Alfvén speed, $\omega \approx k v_{\rm A}$, in the low-$\beta$ limit.

In this case, the resulting function is:

$$R_n(k_\parallel v_\parallel - \omega + n\Omega) = \frac{\sqrt{\pi}}{|k\xi|v_\perp M_{\rm A}^{1/2}} \cdot \exp\left(-\frac{(\mu - \frac{v_{\rm A}}{\xi v})^2}{(1-\mu^2)M_{\rm A}}\right) \equiv \frac{\sqrt{\pi}}{|k\xi|v_\perp M_{\rm A}^{1/2}} \cdot E_n^{\rm T} \qquad (n=0).$$

Truncation scale

The integral over the inertial range is truncated as soon as the fastest damping mechanism for the turbulent spectra comes into play. This eventually depends on the environment that we are considering.

As discussed in Yan and Lazarian (2008), in the warm ionized medium (WIM) ($|d| \lesssim 1\,\mathrm{kpc}$) the gas is denser and colder with respect to the extended halo region ($d > 1\,\mathrm{kpc}$). Therefore, in the WIM, besides the standard *collisionless* damping, the *collisional* damping is also present. Since viscous forces involve small-size eddies, only particles with small Larmor radii can experience them. This will eventually affect the low-energy range of the resulting spatial diffusion coefficient in the WIM. In the extended halo region, on the other hand, only the collisionless damping is present, and this is why we expect $D(R)$ to be a monotonic function of R in such environment.

To estimate the truncation scale in the two different environments, we look for the wave number at which the energy cascading rate of the turbulence equals the dissipation rate associated to that wavenumber (Lazarian et al., 2020).

Following Yan and Lazarian (2008), the collisionless truncation scale results:

$$k_{\rm max} L = \frac{4\, M_{\rm A}^4\, \gamma\, \xi^2}{\pi\, \beta\, (1-\xi^2)^2} \cdot \exp\left(\frac{2}{\beta\, \gamma\, \xi^2}\right), \tag{5.A1.18}$$

where $\gamma = \frac{m_p}{m_e}$ and $\beta = \frac{P_g}{P_B}$ is the ratio between the gas pressure and the magnetic pressure.

On the other hand, the collisional truncation scale is:

$$k_{\rm max} L = \begin{cases} x_c\,(1-\xi^2)^{-2/3} & \beta \ll 1 \\ x_c\,(1-3\,\xi^2)^{-4/3} & \beta \gg 1, \end{cases} \tag{5.A1.19}$$

where $x_c = \left(\frac{6\,\rho\,\delta V^2\, L}{\eta_0\, v_A}\right)^{2/3} \sim 10^6$ contains the ambient variables, with η_0 being a longitudinal viscosity (Yan and Lazarian, 2008).

Pitch-angle coefficient

To calculate the contribution of the fast-magnetosonic modes to the pitch-angle diffusion coefficient, we plug in the spectrum (5.A1.17) in the following equation:

$$D^{\rm F}_{\mu\mu} = \Omega^2(1-\mu^2)\int d^3\boldsymbol{k} \sum_{n=-\infty}^{+\infty} \frac{\sqrt{\pi}}{|k_\parallel| v_\perp M_{\rm A}^{1/2}} \cdot E_n^{G,T}\left[\frac{k_\parallel^2}{k^2} J_n'^2(z)\, I^{\rm F}(\boldsymbol{k})\right], \tag{5.A1.20}$$

where now $z = k_\perp LR(1-\mu^2)^{1/2} = k(1-\xi^2)^{1/2}LR(1-\mu^2)^{1/2} \equiv xR(1-\xi^2)^{1/2}(1-\mu^2)^{1/2}$.

With the usual notation $R \equiv v/(\Omega L) = (1-\mu^2)^{-1/2} r_{\rm L}/L$ and $kL \equiv x$, and using that $\xi^2/|\xi|$ is an even function, so that $\int_{-1}^{+1} d\xi\, \xi^2/|\xi| = 2\int_0^{+1} d\xi\, \xi$, the general expression that computes the contributions from the fast modes to $D_{\mu\mu}$ is:

$$D^{\rm F}_{\mu\mu} = \frac{M_{\rm A}^{3/2} v\sqrt{\pi}}{2R^2 L}(1-\mu^2)^{1/2} \int_1^{k_{\max}L(\xi)} dx \int_0^{+1} d\xi\, \xi \sum_{n=-\infty}^{+\infty} x^{-5/2} J_n'^2(z) \cdot E_n^{\rm G,T} \tag{5.A1.21}$$

where:

$$E_n^{\rm G,T} = \begin{cases} E_n^{\rm T} = \exp\left(-\frac{(\mu - \frac{v_{\rm A}}{\xi v})^2}{(1-\mu^2)M_{\rm A}}\right) & (n=0) \\ E_n^{\rm G} = \exp\left(-\frac{(\mu + \frac{n}{x\xi R})^2}{(1-\mu^2)M_{\rm A}}\right) & (n \neq 0). \end{cases}$$

So, in the case of TTD interaction ($n=0$), we have:

$$D^{{\rm F},n=0}_{\mu\mu} = \frac{M_{\rm A}^{3/2} v\sqrt{\pi}}{2R^2 L}(1-\mu^2)^{1/2} \int_1^{k_{\max}L(\xi)} dx \int_0^{+1} d\xi\, \xi\, x^{-5/2} J_1^2(z) \cdot \exp\left(-\frac{(\mu - \frac{v_{\rm A}}{\xi v})^2}{(1-\mu^2)M_{\rm A}}\right) \tag{5.A1.22}$$

where we used the property $J_n'(z) = \frac{1}{2}\left(J_{n-1}(z) - J_{n+1}(z)\right)$ to get $J_0'(z) = -J_1(z)$.

In the case of gyroresonant interaction ($n \neq 0$), we have:

$$D^{{\rm F},n=1}_{\mu\mu} + D^{{\rm F},n=-1}_{\mu\mu} = \frac{M_{\rm A}^{3/2} v\sqrt{\pi}}{2R^2 L}(1-\mu^2)^{1/2} \int_1^{k_{\max}L(\xi)} dx \int_0^{+1} d\xi\, \xi\, x^{-5/2} \left(\frac{J_0(z) - J_2(z)}{2}\right)^2 (E^{\rm G,+} + E^{\rm G,-}), \tag{5.A1.23}$$

where $E^{\rm G,+} \equiv E^{\rm G,+}_{n=1} = \exp\left(-\frac{(\mu + \frac{n}{x\xi R})^2}{(1-\mu^2)M_{\rm A}}\right)$, $E^{G,-} \equiv E^{G,-}_{n=-1} = \exp\left(-\frac{(\mu - \frac{n}{x\xi R})^2}{(1-\mu^2)M_{\rm A}}\right)$ and we used that $J_n'^2(z) = J_{-n}'^2(z)$.

5.A1.3 $D_{\mu\mu}$ FROM SLOW MODES

For completeness, we also report the calculations of the pitch-angle coefficient of the magnetosonic slow modes, namely the following expression:

$$D^{\rm S}_{\mu\mu} = \Omega^2(1-\mu^2)\int d^3\boldsymbol{k}\sum_{n=-\infty}^{+\infty}\frac{\sqrt{\pi}}{|k_\parallel|v_\perp M_{\rm A}^{1/2}}\cdot E_n^{G,T}\left[\frac{k_\parallel^2}{k^2}\,J_n'^2(z)\,I^{\rm S}(\boldsymbol{k})\right], \tag{5.A1.24}$$

where we want to adopt the same notation used for the Alfvén modes, separating the parallel and perpendicular wave-number components, as with respect to the regular magnetic field, $z = k_\perp LR(1-\mu^2)^{1/2} \equiv x_\perp R(1-\mu^2)^{1/2}$.

The statistics of the slow modes is similar to that of the Alfvén modes, as indicated in Equations (5.A1.5)-(5.A1.6), while, on the other hand, they can interact with cosmic-ray particles by means of both TTD and gyro-resonance. Therefore their treatment involves parts of the calculations already detailed for the other two MHD modes. In particular:

- the normalized correlation tensors $\mathcal{M}^{\rm S}_{ij}$ for both the sub-alfvénic and super-alfvénic cases are the same calculated for the Alfvèn modes, reported in Equations (5.A1.9) and (5.A1.10), respectively;
- the resonance function is the same as for the fast modes, discussed in Section 5.A1.2, conveniently rewritten as follows to account for the present notation:

$$R_n^{\rm G,T} = \begin{cases} R_n^{\rm T} \equiv \frac{\sqrt{\pi}}{|k_\parallel|v_\perp M_A^{1/2}}\cdot E_n^T = \frac{\sqrt{\pi}}{|k_\parallel|v_\perp M_A^{1/2}}\cdot\exp\left(-\frac{(\mu-\frac{\omega}{k_\parallel v})^2}{(1-\mu^2)M_{\rm A}}\right) & (n=0) \\ R_n^{\rm G} \equiv \frac{\sqrt{\pi}}{|k_\parallel|v_\perp M_A^{1/2}}\cdot E_n^G = \frac{\sqrt{\pi}}{|k_\parallel|v_\perp M_A^{1/2}}\cdot\exp\left(-\frac{(\mu+\frac{n}{k_\parallel RL})^2}{(1-\mu^2)M_{\rm A}}\right) & (n\neq 0); \end{cases}$$

- the truncation scale is also the same as that discussed for the fast modes, in Section 5.A1.2.

Pitch-angle coefficient

To calculate the $D_{\mu\mu}$ caused by the slow modes, we account for the sub- and super-alfvénic nature of the injected cascade, separately.

Sub-alfvénic case: $M_{\rm A} \leq 1$. The general expression that calculates the contribution from the slow modes to the pitch-angle coefficient is then written as follows:

$$D^{\rm S}_{\mu\mu} = \frac{2\sqrt{\pi}v\sqrt{1-\mu^2}\,M_{\rm A}^{5/6}}{3R^2L}\int_{\mathbb{R}^+}dx_\perp\int dx_\parallel\sum_{n=-\infty}^{+\infty}\frac{x_\perp^{-7/3}}{\left(x_\parallel^2+x_\perp^2\right)}\cdot\exp\left(-\frac{x_\parallel}{M_{\rm A}^{4/3}\,x_\perp^{2/3}}\right)E_n^{G,T}, \tag{5.A1.25}$$

where we used the even parity of the integrating function to restrict only to the positive axis and the integral boundaries are the ones discussed in Section 5.A1.1.

In the case of TTD interaction ($n = 0$), the expression above reads:

$$D_{\mu\mu}^{\mathrm{S,sub},n=0} = \frac{2\sqrt{\pi}v\sqrt{1-\mu^2}\,M_{\mathrm{A}}^{5/6}}{3R^2L}\int_{\mathbb{R}^+} dx_\perp \int dx_\parallel \frac{x_\perp^{-7/3}}{\left(x_\parallel^2+x_\perp^2\right)} J_1^2(z)\cdot\exp\left(-\frac{x_\parallel}{M_{\mathrm{A}}^{4/3}\,x_\perp^{2/3}} - \frac{(\mu-\frac{\omega}{x_\parallel R\Omega})^2}{(1-\mu^2)M_{\mathrm{A}}}\right). \tag{5.A1.26}$$

In the case of gyro-resonant scattering ($n \neq 0$), on the other hand, Equation (5.A1.25) is written as follows:

$$D_{\mu\mu}^{\mathrm{S,sub},n=1} + D_{\mu\mu}^{\mathrm{S,sub},n=-1} = \frac{2\sqrt{\pi}v\sqrt{1-\mu^2}\,M_{\mathrm{A}}^{5/6}}{3R^2L}\int_{\mathbb{R}^+} dx_\perp \int dx_\parallel \frac{x_\perp^{-7/3}}{\left(x_\parallel^2+x_\perp^2\right)}\left(\frac{J_0(z)-J_2(z)}{2}\right)^2 \cdot\exp\left(-\frac{x_\parallel}{M_{\mathrm{A}}^{4/3}\,x_\perp^{2/3}}\right)\cdot\left(E^{G,+}+E^{G,-}\right) \tag{5.A1.27}$$

with obvious meaning of the terms $E^{G,+}$ and $E^{G,-}$.

Super-alfvénic case: $M_{\mathrm{A}} > 1$. In the case of super-alfvénic turbulence injected, the general expression for the pitch-angle coefficient is the following:

$$D_{\mu\mu}^{\mathrm{S}} = \frac{2\sqrt{\pi}v\sqrt{1-\mu^2}\,M_{\mathrm{A}}^{1/2}}{3R^2L}\int_{\mathbb{R}^+} dx_\perp \int dx_\parallel \sum_{n=-\infty}^{+\infty} \frac{x_\perp^{-7/3}}{\left(x_\parallel^2+x_\perp^2\right)}\cdot\exp\left(-\frac{x_\parallel}{M_{\mathrm{A}}\,x_\perp^{2/3}}\right) E_n^{G,T}. \tag{5.A1.28}$$

In the case of TTD particle-wave interaction ($n = 0$), this becomes:

$$D_{\mu\mu}^{\mathrm{S,sub},n=0} = \frac{2\sqrt{\pi}v\sqrt{1-\mu^2}\,M_{\mathrm{A}}^{1/2}}{3R^2L}\int_{\mathbb{R}^+} dx_\perp \int dx_\parallel \frac{x_\perp^{-7/3}}{\left(x_\parallel^2+x_\perp^2\right)} J_1^2(z)\cdot\exp\left(-\frac{x_\parallel}{M_{\mathrm{A}}\,x_\perp^{2/3}} - \frac{(\mu-\frac{\omega}{x_\parallel R\Omega})^2}{(1-\mu^2)M_{\mathrm{A}}}\right). \tag{5.A1.29}$$

In the case of gyro-resonant interaction ($n \neq 0$), instead, Equation (5.A1.28) becomes:

$$D_{\mu\mu}^{\mathrm{S,sub},n=1} + D_{\mu\mu}^{\mathrm{S,sub},n=-1} = \frac{2\sqrt{\pi}v\sqrt{1-\mu^2}\,M_{\mathrm{A}}^{1/2}}{3R^2L}\int_{\mathbb{R}^+} dx_\perp \int dx_\parallel \frac{x_\perp^{-7/3}}{\left(x_\parallel^2+x_\perp^2\right)}\left(\frac{J_0(z)-J_2(z)}{2}\right)^2 \cdot\exp\left(-\frac{x_\parallel}{M_{\mathrm{A}}\,x_\perp^{2/3}}\right)\cdot\left(E^{G,+}+E^{G,-}\right). \tag{5.A1.30}$$

Conclusions

In this thesis, we studied some of the open questions associated to the origin of the *Cosmic Rays* (CRs), as well as to their transport properties.

Following the increasing accuracy of the experimental observations, especially at energies of the order $\sim \mathcal{O}(100\,\mathrm{GeV} - 1\,\mathrm{TeV})$, recently achieved, the standard picture of a *Supernova Remnant* (SNR) origin and a diffusive random walk derived within the *Quasi-Linear Theory* (QLT) of scattering against Alfvén modes gets significantly challenged.

As far as their origin is concerned, we used the most relevant cosmic-ray observables to choose a set of free parameters, implemented in the `DRAGON` numerical solver, to tune our propagation setup. On top of this background, we studied the leptonic high-energy features. In particular, the rising of the positron fraction at $\sim 10\,\mathrm{GeV}$ was assigned to a population of primary positrons injected by nearby pulsars. Since pulsar injection models are still not clearly understood, we fitted four different scenarios, which allowed us to bracket such uncertainties. Then we turned our attention to the all-lepton spectrum, and observed that the high-energy range — and, in particular, the $\sim$ TeV break observed consistently by ground-based as well as space-born experiments — cannot be reproduced by a smoothly distributed SNR component plus nearby pulsars. Due to the massive energy losses that leptons suffer at this energy scale, their diffusive horizon is rather limited and we concluded that an old ($t_{\mathrm{age}} \sim 10^5\,\mathrm{yr}$) source located between $\sim 600\,\mathrm{pc}$ and $\sim 1\,\mathrm{kpc}$ is probably missing from the Catalogues.

Interpreting the hardening at $\sim 200\,\mathrm{GeV}$ — observed in the proton and nuclear species, both in the primary and in the secondary species — as a diffusive-origin feature, we studied the possibility of connecting the hypothetical nearby source of electrons with a signature in the proton spectrum as well. Indeed, Supernova Remnants release both electrons and protons, and a recent observation — a softening observed by DAMPE at $13\,\mathrm{TeV}$ — could be a signature of an intrinsic source-cutoff. Within a transport setup characterized by a smoothly hardening diffusion coefficient, $D(E) \propto E^{\delta(E)}$, we were able to match both hadronic and leptonic observables invoking an old ($t_{\mathrm{age}} = 2 \cdot 10^5\,\mathrm{yr}$), nearby ($d = 300\,\mathrm{pc}$) remnant, that correctly reproduced the cosmic-ray dipole anisotropy. We remark that, without such variable diffusion coefficient, the anisotropy data would be overshot by, at least, one order of magnitude.

Finally, we focused on the microphysics of cosmic-ray diffusion. Indeed, as extensively shown in the review section, Part I, the typical picture invokes the QLT scattering of cosmic-ray particles against isotropic Alfvén fluctuations, namely transverse modes, which gives rise to the typical parametrization of the diffusion coefficient with a single power law. On the other hand, *magneto-hydro-dynamic* turbulence includes two other propagating modes, *magnetosonic fast* and *slow*, that are typically ignored, as they suffer severe damping in the *Interstellar Medium* environments, as opposed to the Alfvén modes, that propagate essentially free of damping. However, when including the anisotropic nature

of the alfvénic cascade and a non-linear extension of the QLT, that enhances the scattering efficiency of the fast modes, that paradigm is found to change significantly. In particular, we found that the alfvénic cascade is extremely inefficient in confining cosmic rays, up to an energy $\sim 100\,\mathrm{TeV}$, where the anisotropy of the cascade is not developed yet and it is able to give a contribution comparable to that of the fast modes. Interestingly, when this occurs, the contribution of the Alfvén modes to the scattering efficiency manifest itself as a change of slope in the spatial diffusion coefficient. Within such setup, we implemented the resulting diffusion coefficients in `DRAGON2`, where two independent zones were considered: the Halo ($L_{\mathrm{Halo}} \sim 5 - 6\,\mathrm{kpc}$) and the Extended Disk, corresponding to the *Warm Ionized Medium* ($L_{\mathrm{WIM}} \sim 1\,\mathrm{kpc}$). Thus, we explored the parameter space of selected physical quantities, connected to the physics of the environments, and reproduced the hadronic fluxes, as well as the boron-over-carbon ratio, from $\sim 200\,\mathrm{GeV}$ above. Below this energy, we assumed that CR scattering against self-generated turbulence dominates the diffusion process. Remarkably, a good compatibility with experimental data was found with a reasonable choice of those physics parameters and did not require any *ad hoc* tuning or re-normalization.

In conclusion, the scientific contribution of the present thesis aimed at a comprehensive treatment of the open questions regarding the origin of the cosmic rays and their propagation properties. In particular, we explored a change in the standard paradigm of cosmic-ray diffusion generated by wave-particle scattering with *slab* turbulence, namely the transverse modes that inspired the QLT-based diffusion coefficient parametrized as a single power law. Within this framework, however, only parallel transport was treated, and large magnetic fluctuations that tend to isotropize diffusion on large scales were invoked, allowing to write $D_{\parallel} \approx D_{\perp}$. Therefore, a lot of work is still necessary to understand up to what extent this is a valid assumption and where perpendicular transport eventually contributes. From the phenomenological point of view, we highlight that the change of slope at high energy ($\sim 100\,\mathrm{TeV}$) in the $D(E)$, corresponding to the entrance of the Alfvèn modes in the scattering rate, represents a promising ground to test the validity of the presented theory. Indeed, such energy is expected to be explored in the next few years by the operating telescopes.

References

Aartsen, M. et al. (2013). The IceCube Neutrino Observatory Part II: Atmospheric and Diffuse UHE Neutrino Searches of All Flavors. In *33rd International Cosmic Ray Conference*.

Aartsen, M. et al. (2019). Search for Sources of Astrophysical Neutrinos Using Seven Years of IceCube Cascade Events. *Astrophys. J.*, 886:12.

Abdo, A. A. et al. (2010). Fermi Observations of Cassiopeia and Cepheus: Diffuse Gamma-ray Emission in the Outer Galaxy. *ApJ*, 710(1):133–149.

Abeysekara, A. U., Albert, A., Alfaro, R., Alvarez, C., Álvarez, J. D., Arceo, R., Arteaga-Velázquez, J. C., Avila Rojas, D., Ayala Solares, H. A., and Barber, A. S. (2017). Extended gamma-ray sources around pulsars constrain the origin of the positron flux at Earth. *Science*, 358(6365):911–914.

Ackermann, M. et al. (2011). Constraints on the Cosmic-ray Density Gradient Beyond the Solar Circle from Fermi γ-ray Observations of the Third Galactic Quadrant. *ApJ*, 726(2):81.

Ackermann, M. et al. (2013). Detection of the Characteristic Pion-Decay Signature in Supernova Remnants. *Science*, 339:807.

Adriani, O., Barbarino, G. C., Bazilevskaya, G. A., Bellotti, R., Boezio, M., Bogomolov, E. A., Bonechi, L., Bongi, M., Bonvicini, V., and Bottai, S. (2009). An anomalous positron abundance in cosmic rays with energies 1.5-100GeV. *Nature*, 458(7238):607–609.

Adriani, O. et al. (2009). An anomalous positron abundance in cosmic rays with energies 1.5-100 gev. *Nature*, 458:607–609.

Adriani, O. et al. (2011a). PAMELA Measurements of Cosmic-ray Proton and Helium Spectra. *Science*, 332:69–72.

Adriani, O. et al. (2011b). The cosmic-ray electron flux measured by the PAMELA experiment between 1 and 625 GeV. *Phys. Rev. Lett.*, 106:201101.

Adriani, O. et al. (2013). Cosmic-Ray Positron Energy Spectrum Measured by PAMELA. *Physical Review Letters*, 111(8):081102.

Adriani, O. et al. (2014). Measurement of boron and carbon fluxes in cosmic rays with the PAMELA experiment. *Astrophys. J.*, 791(2):93.

Adriani, O. et al. (2018). Extended Measurement of the Cosmic-Ray Electron and Positron Spectrum from 11 GeV to 4.8 TeV with the Calorimetric Electron Telescope on the International Space Station. *Phys. Rev. Lett.*, 120(26):261102.

Aguilar, M. et al. (2013). First Result from the Alpha Magnetic Spectrometer on the International Space Station: Precision Measurement of the Positron Fraction in Primary Cosmic Rays of 0.5–350 GeV. *Phys. Rev. Lett.*, 110:141102.

Aguilar, M. et al. (2014a). Electron and Positron Fluxes in Primary Cosmic Rays Measured with the Alpha Magnetic Spectrometer on the International Space Station. *Phys. Rev. Lett.*, 113:121102.

Aguilar, M. et al. (2014b). Precision Measurement of the $(e^+ + e)$ Flux in Primary Cosmic Rays from 0.5 GeV to 1 TeV with the Alpha Magnetic Spectrometer on the International Space Station. *Phys. Rev. Lett.*, 113:221102.

Aguilar, M. et al. (2014). Precision Measurement of the (e^++e^-) Flux in Primary Cosmic Rays from 0.5 GeV to 1 TeV with the Alpha Magnetic Spectrometer on the International Space Station. *Physical Review Letters*, 113(22):221102.

Aguilar, M. et al. (2015a). Precision measurement of the proton flux in primary cosmic rays from rigidity 1 gv to 1.8 tv with the alpha magnetic spectrometer on the international space station. *Phys. Rev. Lett.*, 114:171103.

Aguilar, M. et al. (2015b). Precision Measurement of the Proton Flux in Primary Cosmic Rays from Rigidity 1 GV to 1.8 TV with the Alpha Magnetic Spectrometer on the International Space Station. *Phys. Rev. Lett.*, 114:171103.

Aguilar, M. et al. (2016). Precision measurement of the boron to carbon flux ratio in cosmic rays from 1.9 gv to 2.6 tv with the alpha magnetic spectrometer on the international space station. *Phys. Rev. Lett.*, 117:231102.

Aguilar, M. et al. (2017). Observation of the identical rigidity dependence of he, c, and o cosmic rays at high rigidities by the alpha magnetic spectrometer on the international space station. *Phys. Rev. Lett.*, 119:251101.

Aguilar, M. et al. (2018a). Observation of Complex Time Structures in the Cosmic-Ray Electron and Positron Fluxes with the Alpha Magnetic Spectrometer on the International Space Station. *Phys. Rev. Lett.*, 121(5):051102.

Aguilar, M. et al. (2018b). Observation of New Properties of Secondary Cosmic Rays Lithium, Beryllium, and Boron by the Alpha Magnetic Spectrometer on the International Space Station. *Phys. Rev. Lett.*, 120(2):021101.

Aguilar, M. et al. (2018c). Precision measurement of cosmic-ray nitrogen and its primary and secondary components with the alpha magnetic spectrometer on the international space station. *Phys. Rev. Lett.*, 121:051103.

Aguilar, M. et al. (2019a). Towards Understanding the Origin of Cosmic-Ray Electrons. *Physical Review Letters*, 122(10):101101.

Aguilar, M. et al. (2019b). Towards Understanding the Origin of Cosmic-Ray Positrons. *Physical Review Letters*, 122(4):041102.

Aguilar, M. et al. (2019). Towards Understanding the Origin of Cosmic-Ray Positrons. *Phys. Rev. Lett.*, 122(4):041102.

Aharonian, F., Akhperjanian, A. G., Anton, G., Barres de Almeida, U., Bazer-Bachi, A. R., Becherini, Y., Behera, B., Bernlöhr, K., Bochow, A., and Boisson, C. (2009). Probing the ATIC peak in the cosmic-ray electron spectrum with H.E.S.S. *A&A*, 508(2):561–564.

Aharonian, F. A. (2013). Gamma rays from supernova remnants. *Astropart. Phys.*, 43:71–80.

Aharonian, F. A., Atoyan, A. M., and Völk, H. J. (1995). High energy electrons and positrons in cosmic rays as an indicator of the existence of a nearby cosmic tevatron. *A&A*, 294:L41–L44.

Ahlers, M. and Mertsch, P. (2017). Origin of Small-Scale Anisotropies in Galactic Cosmic Rays. *Prog. Part. Nucl. Phys.*, 94:184–216.

Albert, A. et al. (2018). Joint Constraints on Galactic Diffuse Neutrino Emission from the ANTARES and IceCube Neutrino Telescopes. *Astrophys. J. Lett.*, 868(2):L20.

Aloisio, R., Blasi, P., and Serpico, P. (2015). Nonlinear cosmic ray Galactic transport in the light of AMS-02 and Voyager data. *Astron. Astrophys.*, 583:A95.

Amato, E. (2014). The theory of pulsar wind nebulae. *Int. J. Mod. Phys. Conf. Ser.*, 28:1460160.

Ambrosi, G. et al. (2017). Direct detection of a break in the teraelectronvolt cosmic-ray spectrum of electrons and positrons. *Nature*, 552:63–66.

Amenomori, M. (2017). Northern sky Galactic Cosmic Ray anisotropy between 10-1000 TeV with the Tibet Air Shower Array. *Astrophys. J.*, 836(2):153.

An, Q. et al. (2019). Measurement of the cosmic-ray proton spectrum from 40 GeV to 100 TeV with the DAMPE satellite. *Sci. Adv.*, 5(9):eaax3793.

Atoyan, A. M., Aharonian, F. A., and Völk, H. J. (1995). Electrons and positrons in the galactic cosmic rays. *Phys. Rev. D*, 52:3265–3275.

Axford, W. I., Leer, E., and Skadron, G. (1977). The acceleration of cosmic rays by shock waves. *International Cosmic Ray Conference*, 11:132–137.

Barnes, A. (1966). Collisionless Damping of Hydromagnetic Waves. *Physics of Fluids*, 9(8):1483–1495.

Barone, V. (2004). *Relatività. Principi e applicazioni*. Programma di mat. fisica elettronica. Bollati Boringhieri.

Bartoli, B. et al. (2015). Argo-ybj Observation of the Large-scale Cosmic ray Anisotropy During the Solar Minimum Between Cycles 23 and 24. *Astrophys. J.*, 809(1):90.

Bartoli, B. et al. (2018). Galactic Cosmic-Ray Anisotropy in the Northern Hemisphere from the ARGO-YBJ Experiment during 2008–2012. *Astrophys. J.*, 861(2):93.

Beck, R. (2001). Galactic and Extragalactic Magnetic Fields. *Space Science Reviews*, 99:243–260.

Beck, R., Brandenburg, A., Moss, D., Shukurov, A., and Sokoloff, D. (1996). Galactic Magnetism: Recent developments and perspectives. *Ann. Rev. Astron. Astrophys.*, 34:155–206.

Bell, A. (2013). Cosmic ray acceleration. *Astropart. Phys.*, 43:56–70.

Bell, A. R. (1978). The acceleration of cosmic rays in shock fronts. I. *MNRAS*, 182:147–156.

Bell, A. R. (2004). Turbulent amplification of magnetic field and diffusive shock acceleration of cosmic rays. *MNRAS*, 353(2):550–558.

Berezhko, E. G. and Krymskii, G. F. (1988). Acceleration of cosmic rays by shock waves. *Phys. Usp.*, 31(1):27–51.

Berezhko, E. G., Yelshin, V. K., and Ksenofontov, L. T. (1994). Numerical investigation of cosmic ray acceleration in supernova remnants. *Astroparticle Physics*, 2(2):215–227.

Berezinsky, V. S., Bulanov, S. V., Dogiel, V. A., and Ptuskin, V. S. (1990). *Astrophysics of cosmic rays*. Amsterdam, Netherlands: North-Holland.

Binns, W. R., Garrard, T. L., Gibner, P. S., Israel, M. H., Kertzman, M. P., Klarmann, J., Newport, B. J., Stone, E. C., and Waddington, C. J. (1989). Abundances of ultraheavy elements in the cosmic radiation - Results from HEAO 3. *ApJ*, 346:997–1009.

Blandford, R. D. and Ostriker, J. P. (1978). Particle acceleration by astrophysical shocks. *ApJL*, 221:L29–L32.

Blasi, P. (2013). The Origin of Galactic Cosmic Rays. *Astron. Astrophys. Rev.*, 21:70.

Blasi, P. (2018). *Lecture Notes of the course on Cosmic-ray Physics*. Ph.D. course held at GSSI - L'Aquila.

Blasi, P. and Amato, E. (2011). Positrons from pulsar winds. *Astrophysics and Space Science Proceedings*, 21:624.

Blasi, P., Amato, E., and Serpico, P. D. (2012). Spectral breaks as a signature of cosmic ray induced turbulence in the Galaxy. *Phys. Rev. Lett.*, 109:061101.

Blumenthal, G. R. and Gould, R. J. (1970). Bremsstrahlung, synchrotron radiation, and compton scattering of high-energy electrons traversing dilute gases. *Rev. Mod. Phys.*, 42:237–270.

Bolatto, A. D., Wolfire, M., and Leroy, A. K. (2013). The CO-to-H_2 Conversion Factor. *ARA&A*, 51(1):207–268.

Boudaud, M., Bueno, E. F., Caroff, S., Genolini, Y., Poulin, V., Poireau, V., Putze, A., Rosier, S., Salati, P., and Vecchi, M. (2017). The pinching method for Galactic cosmic ray positrons: implications in the light of precision measurements. *Astron. Astrophys.*, 605:A17.

Boyd, T. J. M. and Sanderson, J. J. (2003). *The Physics of Plasmas*. Cambridge University Press.

Bronfman, L., Cohen, R. S., Alvarez, H., May, J., and Thaddeus, P. (1988). A CO survey of the southern Milky Way - The mean radial distribution of molecular clouds within the solar circle. *ApJ*, 324:248–266.

Bucciantini, N., Arons, J., and Amato, E. (2011). Modeling the spectral evolution of PWNe inside SNRs. *Mon. Not. Roy. Astron. Soc.*, 410:381.

Bulanov, S. V. and Dogel, V. A. (1974). The Influence of the Energy Dependence of the Diffusion Coefficient on the Spectrum of the Electron Component of Cosmic Rays and the Radio Background Radiation of the Galaxy. *Ap&SS*, 29(2):305–318.

Bykov, A., Ellison, D., Marcowith, A., and Osipov, S. (2018). Cosmic ray production in supernovae. *Space Sci. Rev.*, 214(1):41.

Bykov, A. M., Amato, E., Petrov, A. E., Krassilchtchikov, A. M., and Levenfish, K. P. (2017). Pulsar wind nebulae with bow shocks: non-thermal radiation and cosmic ray leptons. *Space Sci. Rev.*, 207(1-4):235–290.

Bykov, A. M., Petrov, A. E., Krassilchtchikov, A. M., Levenfish, K. P., Osipov, S. M., and Pavlov, G. G. (2019). GeV–TeV cosmic-ray leptons in the solar system from the bow shock wind nebula of the nearest millisecond pulsar j0437–4715. *The Astrophysical Journal*, 876(1):L8.

Cappellaro, E., Evans, R., and Turatto, M. (1999). A new determination of supernova rates and a comparison with indicators for galactic star formation. *A&A*, 351:459–466.

Caprioli, D. (2012). Cosmic-ray acceleration in supernova remnants: non-linear theory revised. *JCAP*, 07:038.

Caprioli, D., Blasi, P., Amato, E., and Vietri, M. (2008). Dynamical effects of self-generated magnetic fields in cosmic-ray-modified shocks. *The Astrophysical Journal*, 679(2):L139–L142.

Cerri, S. S., Califano, F., Jenko, F., Told, D., and Rincon, F. (2016). Subproton-scale Cascades in Solar Wind Turbulence: Driven Hybrid-kinetic Simulations. *Astrophys. J. Lett.*, 822(1):L12.

Cerri, S. S., Gaggero, D., Vittino, A., Evoli, C., and Grasso, D. (2017a). A signature of anisotropic cosmic-ray transport in the gamma-ray sky. *JCAP*, 10:019.

Cerri, S. S., Gaggero, D., Vittino, A., Evoli, C., and Grasso, D. (2017b). A signature of anisotropic cosmic-ray transport in the gamma-ray sky. *JCAP*, 1710(10):019.

Cerri, S. S., Servidio, S., and Califano, F. (2017). Kinetic Cascade in Solar-wind Turbulence: 3D3V Hybrid-kinetic Simulations with Electron Inertia. *Astrophys. J. Lett.*, 846(2):L18.

Chandran, B. D. G. (2000). Scattering of Energetic Particles by Anisotropic Magnetohydrodynamic Turbulence with a Goldreich-Sridhar Power Spectrum. *Phys. Rev. Lett.*, 85(22):4656–4659.

Chandrasekhar, S. (1943). Stochastic problems in physics and astronomy. *Rev. Mod. Phys.*, 15:1–89.

Chevalier, R. A. (1982). Self-similar solutions for the interaction of stellar ejecta with an external medium. *ApJ*, 258:790–797.

Cho, J. and Lazarian, A. (2002). Compressible sub-alfvénic mhd turbulence in low- β plasmas. *Phys. Rev. Lett.*, 88:245001.

Cho, J., Lazarian, A., and Vishniac, E. (2002). Simulations of magnetohydrodynamic turbulence turbulence in a strongly magnetized medium. *Astrophys. J.*, 564:291–301.

Cho, J., Lazarian, A., and Vishniac, E. T. (2003). *MHD Turbulence: Scaling Laws and Astrophysical Implications*, volume 614, pages 56–98.

Cholis, I., Karwal, T., and Kamionkowski, M. (2018). Studying the Milky Way pulsar population with cosmic-ray leptons. *Phys. Rev. D*, 98(6):063008.

Cioffi, D. F., McKee, C. F., and Bertschinger, E. (1988). Dynamics of Radiative Supernova Remnants. *ApJ*, 334:252.

Cordes, J. M., Romani, R. W., and Lundgren, S. C. (1993). The guitar nebula: a bow shock from a slow-spin, high-velocity neutron star. *Nature*, 362(6416):133–135.

Cordes, J. M., Weisberg, J. M., Frail, D. A., Spangler, S. R., and Ryan, M. (1991). The galactic distribution of free electrons. *Nature*, 354(6349):121–124.

Cox, P., Kruegel, E., and Mezger, P. G. (1986). Principal heating sources of dust in the galactic disk. *A&A*, 155:380–396.

Cummings, A. C., Stone, E. C., Heikkila, B. C., Lal, N., Webber, W. R., Jóhannesson, G., Moskalenko, I. V., Orlando, E., and Porter, T. A. (2016). Galactic cosmic rays in the local interstellar medium: Voyager-1 observations and model results. *The Astrophysical Journal*, 831(1):18.

De Marco, D., Blasi, P., and Stanev, T. (2007). Numerical propagation of high energy cosmic rays in the Galaxy. I. Technical issues. *JCAP*, 06:027.

Delahaye, T., Lavalle, J., Lineros, R., Donato, F., and Fornengo, N. (2010). Galactic electrons and positrons at the earth: new estimate of the primary and secondary fluxes. *A&A*, 524:A51.

Dermer, C. D. (1985). Binary collision rates of relativistic thermal plasmas. I Theoretical framework. *ApJ*, 295:28–37.

Di Bernardo, G., Evoli, C., Gaggero, D., Grasso, D., and Maccione, L. (2010). Unified interpretation of cosmic-ray nuclei and antiproton recent measurements. *Astropart. Phys.*, 34:274–283.

Di Bernardo, G., Evoli, C., Gaggero, D., Grasso, D., and Maccione, L. (2013). Cosmic ray electrons, positrons and the synchrotron emission of the Galaxy: consistent analysis and implications. *Journal of Cosmology and Astro-Particle Physics*, 2013(3):036.

Di Bernardo, G., Evoli, C., Gaggero, D., Grasso, D., and Maccione, L. (2013). Cosmic ray electrons, positrons and the synchrotron emission of the galaxy: consistent analysis and implications. *Journal of Cosmology and Astroparticle Physics*, 2013(03):036.

Di Mauro, M., Manconi, S., and Donato, F. (2019). Detection of a γ-ray halo around Geminga with the Fermi -LAT data and implications for the positron flux. *Phys. Rev. D*, 100(12):123015.

Diesing, R. and Caprioli, D. (2019). Spectrum of Electrons Accelerated in Supernova Remnants. *Phys. Rev. Lett.*, 123(7):071101.

Drury, L. O. (1983). REVIEW ARTICLE: An introduction to the theory of diffusive shock acceleration of energetic particles in tenuous plasmas. *Reports on Progress in Physics*, 46(8):973–1027.

Drury, L. O. and Strong, A. W. (2016). Cosmic-ray diffusive reacceleration: a critical look. *PoS*, ICRC2015:483.

Earl, J. A. (1973). Diffusion of Charged Particles in a Random Magnetic Field. *ApJ*, 180:227–238.

Earl, J. A. (1974). The diffusive idealization of charged-particle transport in random magnetic fields. *ApJ*, 193:231–242.

Evoli, C. (2018). The cosmic-ray energy spectrum.

Evoli, C., Amato, E., Blasi, P., and Aloisio, R. (2020a). Galactic factories of cosmic-ray electrons and positrons. *arXiv e-prints*, page arXiv:2010.11955.

Evoli, C., Blasi, P., Amato, E., and Aloisio, R. (2020b). The signature of energy losses on the cosmic ray electron spectrum. *arXiv e-prints*, page arXiv:2007.01302.

Evoli, C., Blasi, P., Morlino, G., and Aloisio, R. (2018a). Origin of the Cosmic Ray Galactic Halo Driven by Advected Turbulence and Self-Generated Waves. *Phys. Rev. Lett.*, 121(2):021102.

Evoli, C., Gaggero, D., Grasso, D., and Maccione, L. (2008). Cosmic-Ray Nuclei, Antiprotons and Gamma-rays in the Galaxy: a New Diffusion Model. *JCAP*, 10:018. [Erratum: JCAP 04, E01 (2016)].

Evoli, C., Gaggero, D., Vittino, A., Di Bernardo, G., Di Mauro, M., Ligorini, A., Ullio, P., and Grasso, D. (2017a). Cosmic-ray propagation with DRAGON2: I. numerical solver and astrophysical ingredients. *JCAP*, 2:015.

Evoli, C., Gaggero, D., Vittino, A., Di Mauro, M., Grasso, D., and Mazziotta, M. N. (2017b). Cosmic-ray propagation with DRAGON2: II. Nuclear interactions with the interstellar gas. *ArXiv e-prints*.

Evoli, C., Gaggero, D., Vittino, A., Di Mauro, M., Grasso, D., and Mazziotta, M. N. (2018b). Cosmic-ray propagation with DRAGON2: II. Nuclear interactions with the interstellar gas. *JCAP*, 1807(07):006.

Evoli, C., Morlino, G., Blasi, P., and Aloisio, R. (2020). AMS-02 beryllium data and its implication for cosmic ray transport. *Phys. Rev. D*, 101(2):023013.

Evoli, C. and Yan, H. (2014). Cosmic ray propagation in galactic turbulence. *Astrophys. J.*, 782(1):36.

Fang, K., Bi, X.-J., and Yin (2020). DAMPE proton spectrum indicates a slow-diffusion zone in the nearby ISM.

Farmer, A. J. and Goldreich, P. (2004). Wave Damping by Magnetohydrodynamic Turbulence and Its Effect on Cosmic-Ray Propagation in the Interstellar Medium. *ApJ*, 604(2):671–674.

Felice, G. M. and Kulsrud, R. M. (2001). Cosmic-Ray Pitch-Angle Scattering through 90°. *ApJ*, 553(1):198–210.

Feng, J., Tomassetti, N., and Oliva, A. (2016a). Bayesian analysis of spatial-dependent cosmic-ray propagation: astrophysical background of antiprotons and positrons. *Phys. Rev. D*, 94(12):123007.

Feng, J., Tomassetti, N., and Oliva, A. (2016b). Bayesian analysis of spatial-dependent cosmic-ray propagation: Astrophysical background of antiprotons and positrons. *Phys. Rev. D*, 94:123007.

Fermi, E. (1949). On the origin of the cosmic radiation. *Phys. Rev.*, 75:1169–1174.

Fermi, E. (1954). Galactic Magnetic Fields and the Origin of Cosmic Radiation. *ApJ*, 119:1.

Ferrand, G. and Safi-Harb, S. (2012). A census of high-energy observations of Galactic supernova remnants. *Advances in Space Research*, 49:1313–1319.

Ferrand, G. and Safi-Harb, S. (2012). A Census of High-Energy Observations of Galactic Supernova Remnants. *Adv. Space Res.*, 49:1313–1319.

Ferriere, K. M. (2001). The interstellar environment of our galaxy. *Rev. Mod. Phys.*, 73:1031–1066.

Feynman, R., Leighton, R., and Sands, M. (2011). *The Feynman Lectures on Physics, Vol. I: The New Millennium Edition: Mainly Mechanics, Radiation, and Heat*. The Feynman Lectures on Physics. Basic Books.

Foreman-Mackey, D., Hogg, D. W., Lang, D., and Goodman, J. (2013). emcee: The MCMC Hammer. *Publ. Astr. Soc. Pac.*, 125(925):306.

Fornieri, O. (2020a). ottaviofornieri/Diffusion_MHD_modes: Diffusion coefficient from MHD modes. DOI:10.5281/zenodo.4250807.

Fornieri, O. (2020b). ottaviofornieri/Hidden_Remnant: Protons and leptons from the remnant. DOI:10.5281/zenodo.4155415.

Fornieri, O., Gaggero, D., Cerri, S. S., Luque, P. D. l. T., and Gabici, S. (2020a). The theory of cosmic-ray scattering on pre-existing MHD modes meets data. arXiv:2011.09197.

Fornieri, O., Gaggero, D., and Grasso, D. (2020b). Features in cosmic-ray lepton data unveil the properties of nearby cosmic accelerators. *JCAP*, 02:009.

Fornieri, O., Gaggero, D., Guberman, D., Brahimi, L., and Marcowith, A. (2020c). Changes in cosmic-ray transport properties connect the high-energy features in the electron and proton data. arXiv:2007.15321.

Funk, S. (2015). Ground- and Space-Based Gamma-Ray Astronomy. *Ann. Rev. Nucl. Part. Sci.*, 65:245–277.

Gabici, S. (2011). Cosmic ray escape from supernova remnants. *Mem. Soc. Ast. It.*, 82:760.

Gabici, S., Evoli, C., Gaggero, D., Lipari, P., Mertsch, P., Orlando, E., Strong, A., and Vittino, A. (2019). The origin of Galactic cosmic rays: challenges to the standard paradigm. *Int. J. Mod. Phys. D*, 28(15):1930022.

Gabici, S., Gaggero, D., and Zandanel, F. (2016). Can supernova remnants accelerate protons up to PeV energies? In *28th Rencontres de Blois on Particle Physics and Cosmology*.

Gaggero, D., Grasso, D., Marinelli, A., Taoso, M., and Urbano, A. (2017). Diffuse cosmic rays shining in the galactic center: A novel interpretation of h.e.s.s. and fermi-lat γ-ray data. *Phys. Rev. Lett.*, 119:031101.

Gaggero, D. and Valli, M. (2018). Impact of cosmic-ray physics on dark matter indirect searches. *Adv. High Energy Phys.*, 2018:3010514.

Gaggero, D., Zandanel, F., Cristofari, P., and Gabici, S. (2018). Time evolution of gamma rays from supernova remnants. *Mon. Not. Roy. Astron. Soc.*, 475(4):5237–5245.

Génolini, Y. et al. (2017). Indications for a high-rigidity break in the cosmic-ray diffusion coefficient. *Phys. Rev. Lett.*, 119(24):241101.

Génolini, Y., Serpico, P. D., Boudaud, M., Caroff, S., Poulin, V., Derome, L., Lavalle, J., Maurin, D., Poireau, V., Rosier, S., Salati, P., and Vecchi, M. (2017). Indications for a High-Rigidity Break in the Cosmic-Ray Diffusion Coefficient. *Phys. Rev. Lett.*, 119(24):241101.

Ginzburg, V., Ginzburg, V., Sadowski, W., and Gallik, D. (1962). *Propagation of Electromagnetic Waves in Plasma*. Russian Monographs and Texts on the Physical Sciences. Gordon and Breach.

Ginzburg, V. and Haar, D. (2013). *Theoretical Physics and Astrophysics*. International Series on Nuclear Energy. Elsevier Science.

Ginzburg, V. L. and Syrovatskii, S. I. (1964a). *The Origin of Cosmic Rays*.

Ginzburg, V. L. and Syrovatskii, S. I. (1964b). *The Origin of Cosmic Rays*. Pergamon Press.

Gleeson, L. J. and Axford, W. I. (1968). Solar Modulation of Galactic Cosmic Rays. *ApJ*, 154:1011.

Goldreich, P. and Sridhar, S. (1995). Toward a Theory of Interstellar Turbulence. II. Strong Alfvenic Turbulence. *ApJ*, 438:763.

Gordon, M. A. and Burton, W. B. (1976). Carbon monoxide in the Galaxy. I - The radial distribution of CO, H2, and nucleons. *ApJ*, 208:346–353.

Grasso, D., Profumo, S., Strong, A. W., Baldini, L., Bellazzini, R., Bloom, E. D., Bregeon, J., Di Bernardo, G., Gaggero, D., and Giglietto, N. (2009). On possible interpretations of the high energy electron-positron spectrum measured by the Fermi Large Area Telescope. *Astroparticle Physics*, 32(2):140–151.

Greisen, K. (1966). End to the cosmic-ray spectrum? *Phys. Rev. Lett.*, 16:748–750.

Grevesse, N., Noels, A., and Sauval, A. J. (1996). Standard Abundances. In Holt, S. S. and Sonneborn, G., editors, *Cosmic Abundances*, volume 99 of *Astronomical Society of the Pacific Conference Series*, page 117.

Génolini, Y. et al. (2019). Cosmic-ray transport from AMS-02 boron to carbon ratio data: Benchmark models and interpretation. *Phys. Rev. D*, 99(12):123028.

Hall, D. E. and Sturrock, P. A. (1967). Diffusion, Scattering, and Acceleration of Particles by Stochastic Electromagnetic Fields. *Physics of Fluids*, 10(12):2620–2628.

Hamil, O., Stone, J. R., Urbanec, M., and Urbancová, G. (2015). Braking index of isolated pulsars. *Phys. Rev. D*, 91(6):063007.

Harding, A. K. and Ramaty, R. (1987). The Pulsar Contribution to Galactic Cosmic Ray Positrons. *International Cosmic Ray Conference*, 2:92.

Hasselmann, K. and Wibberenz, G. (1970). A Note on the Parallel Diffusion Coefficient. *ApJ*, 162:1049.

Hess, V. F. (1912). Über Beobachtungen der durchdringenden Strahlung bei sieben Freiballonfahrten. *Phys. Z.*, 13:1084–1091.

Hooper, D., Blasi, P., and Serpico, P. D. (2009). Pulsars as the Sources of High Energy Cosmic Ray Positrons. *JCAP*, 0901:025.

Hooper, D., Cholis, I., Linden, T., and Fang, K. (2017). HAWC observations strongly favor pulsar interpretations of the cosmic-ray positron excess. *Phys. Rev. D*, 96(10):103013.

Hugoniot, H. (1885). *Sur la propagation du mouvement dans les corps, et spécialement dans les gaz parfaits.-Comptes rendus... de l'Acad*. PhD thesis, d. sc. d. Paris, 101.

Hunter, S. D., Bertsch, D. L., Catelli, J. R., Dame, T. M., Digel, S. W., Dingus, B. L., Esposito, J. A., Fichtel, C. E., Hartman, R. C., Kanbach, G., Kniffen, D. A., Lin, Y. C., Mayer-Hasselwand er, H. A., Michelson, P. F., von Montigny, C., Mukherjee, R., Nolan, P. L., Schneid, E., Sreekumar, P., Thaddeus, P., and Thompson, D. J. (1997). EGRET Observations of the Diffuse Gamma-Ray Emission from the Galactic Plane. *ApJ*, 481(1):205–240.

Jackson, J. D. (1975). *Classical electrodynamics; 2nd ed.* Wiley, New York, NY.

Jankowski, F., van Straten, W., Keane, E. F., Bailes, M., Barr, E., Johnston, S., and Kerr, M. (2018). Spectral properties of 441 radio pulsars. *Mon. Not. Roy. Astron. Soc.*, 473(4):4436–4458.

Jansson, R. and Farrar, G. R. (2012). A New Model of the Galactic Magnetic Field. *ApJ*, 757(1):14.

Johannesson, G., Porter, T. A., and Moskalenko, I. V. (2019). Cosmic-Ray Propagation in Light of the Recent Observation of Geminga. *Astrophys. J.*, 879(2):91.

Jokipii, J. R. (1966a). Cosmic-Ray Propagation. I. Charged Particles in a Random Magnetic Field. *ApJ*, 146:480.

Jokipii, J. R. (1966b). Cosmic-Ray Propagation. I. Charged Particles in a Random Magnetic Field. *Astrophys. J.*, 146:480.

Jokipii, J. R. (1968). Addendum and Erratum to Cosmic-Ray Propagation. I. *ApJ*, 152:671.

Jokipii, J. R. and Lerche, I. (1973). On the transport of charged particles in turbulent fields: comparison of an exact solution with the quasilinear approximation. *Plasma Physics*, 15(7):619–625.

Jokipii, J. R. and Parker, E. N. (1969a). Cosmic-Ray Life and the Stochastic Nature of the Galactic Magnetic Field. *ApJ*, 155:799.

Jokipii, J. R. and Parker, E. N. (1969b). Stochastic Aspects of Magnetic Lines of Force with Application to Cosmic-Ray Propagation. *ApJ*, 155:777.

Kamae, T., Karlsson, N., Mizuno, T., Abe, T., and Koi, T. (2006). Parameterization of γ, $e^{+/-}$, and Neutrino Spectra Produced by p-p Interaction in Astronomical Environments. *ApJ*, 647(1):692–708.

Kennel, C. F. and Engelmann, F. (1966). Velocity Space Diffusion from Weak Plasma Turbulence in a Magnetic Field. *Physics of Fluids*, 9(12):2377–2388.

Kerszberg, D. (2017). The cosmic-ray electron spectrum measured with H.E.S.S. *International Cosmic Ray Conference, [CRI215] (2017)*.

Kirk, J. G., Lyubarsky, Y., and Petri, J. (2009). *The Theory of Pulsar Winds and Nebulae*, volume 357, page 421. Springer.

Kirk, J. G., Schlickeiser, R., and Schneider, P. (1988). Cosmic-Ray Transport in Accelerating Flows. *ApJ*, 328:269.

Kissmann, R. (2014). PICARD: A novel code for the Galactic Cosmic Ray propagation problem. *Astropart. Phys.*, 55:37–50.

Kobayashi, T., Komori, Y., Yoshida, K., and Nishimura, J. (2004). The Most Likely Sources of High-Energy Cosmic-Ray Electrons in Supernova Remnants. *ApJ*, 601:340–351.

Kóta, J. and Jokipii, J. R. (2000). Velocity Correlation and the Spatial Diffusion Coefficients of Cosmic Rays: Compound Diffusion. *ApJ*, 531(2):1067–1070.

Krakau, S. and Schlickeiser, R. (2015). Pion Production Momentum Loss of Cosmic Ray Hadrons. *ApJ*, 802(2):114.

Kruschke, J. K. and Liddell, T. M. (2017). The bayesian new statistics: Hypothesis testing, estimation, meta-analysis, and power analysis from a bayesian perspective. *Psychonomic Bulletin & Review*, pages 1–29.

Krymskii, G. F. (1977). A regular mechanism for the acceleration of charged particles on the front of a shock wave. *Soviet Physics Doklady*, 22:327.

Kubo, R. (1957). Statistical-mechanical theory of irreversible processes. I. General theory and simple applications to magnetic and conduction problems. *Journal of the Physical Society of Japan*, 12(6):570–586.

Kulsrud, R. and Pearce, W. P. (1969). The Effect of Wave-Particle Interactions on the Propagation of Cosmic Rays. *ApJ*, 156:445.

Lagage, P. O. and Cesarsky, C. J. (1983). The maximum energy of cosmic rays accelerated by supernova shocks. *A&A*, 125:249–257.

Landau, L. (1946). On the vibrations of the electronic plasma. *J. Phys. (USSR)*, 10:25–34.

Landau, L. and Lifshitz, E. (2003). *The Classical Theory of Fields*. Textbook Publishers.

Lazarian, A., Eyink, G. L., Jafari, A., Kowal, G., Li, H., Xu, S., and Vishniac, E. T. (2020). 3D Turbulent Reconnection: Theory, Tests and Astrophysical Implications. *Phys. Plasmas*, 27(1):012305.

Lemaitre, G. and Vallarta, M. (1933). On Compton's Latitude Effect of Cosmic Radiation. *Phys. Rev.*, 43(2):87–91.

Lerche, I. (1967). Unstable Magnetosonic Waves in a Relativistic Plasma. *ApJ*, 147:689.

Lerche, I. (1968). Quasilinear Theory of Resonant Diffusion in a Magneto-Active, Relativistic Plasma. *Physics of Fluids*, 11(8):1720–1727.

Linden, T., Auchettl, K., Bramante, J., Cholis, I., Fang, K., Hooper, D., Karwal, T., and Li, S. W. (2017). Using HAWC to discover invisible pulsars. *Phys. Rev.*, D96(10):103016.

Lipari, P. (2017). Interpretation of the cosmic ray positron and antiproton fluxes. *Phys. Rev. D*, 95(6):063009.

Lipari, P. (2019a). Spectral shapes of the fluxes of electrons and positrons and the average residence time of cosmic rays in the Galaxy. *Phys. Rev. D*, 99(4):043005.

Lipari, P. (2019b). Understanding the cosmic ray positron flux.

Liu, W., Guo, Y.-Q., and Yuan, Q. (2019). Indication of nearby source signatures of cosmic rays from energy spectra and anisotropies. *JCAP*, 10:010.

Loeb, A. and Waxman, E. (2006). The Cumulative background of high energy neutrinos from starburst galaxies. *JCAP*, 05:003.

Longair, M. S. (2011). *High Energy Astrophysics*.

López-Coto, R., Parsons, R. D., Hinton, J. A., and Giacinti, G. (2018). Undiscovered pulsar in the local bubble as an explanation of the local high energy cosmic ray all-electron spectrum. *Phys. Rev. Lett.*, 121:251106.

Lyubarsky, Y. and Kirk, J. G. (2001). Reconnection in a Striped Pulsar Wind. *ApJ*, 547(1):437–448.

Maccione, L., Evoli, C., Gaggero, D., and Grasso, D. (2011). DRAGON: Galactic Cosmic Ray Diffusion Code. Astrophysics Source Code Library.

Malkov, M. A. and Drury, L. O. (2001). Nonlinear theory of diffusive acceleration of particles by shock waves. *Reports on Progress in Physics*, 64:429–481.

Manchester, R. N., Hobbs, G. B., Teoh, A., and Hobbs, M. (2005). The Australia Telescope National Facility Pulsar Catalogue. *AJ*, 129:1993–2006.

Manconi, S., Di Mauro, M., and Donato, F. (2019). Multi-messenger constraints to the local emission of cosmic-ray electrons. *JCAP*, 2019(4):024.

Manconi, S., Di Mauro, M., and Donato, F. (2019). Multi-messenger constraints to the local emission of cosmic-ray electrons. *JCAP*, 04:024.

Manconi, S., Di Mauro, M., and Donato, F. (2020). Contribution of pulsars to cosmic-ray positrons in light of recent observation of inverse-Compton halos. *Phys. Rev. D*, 102(2):023015.

Mannheim, K. and Schlickeiser, R. (1994). Interactions of cosmic ray nuclei. *A&A*, 286:983–996.

Marcowith, A., Bret, A., Bykov, A., Dieckman, M. E., O'C Drury, L., Lembège, B., Lemoine, M., Morlino, G., Murphy, G., Pelletier, G., Plotnikov, I., Reville, B., Riquelme, M., Sironi, L., and Stockem Novo, A. (2016). The microphysics of collisionless shock waves. *Reports on Progress in Physics*, 79(4):046901.

Mertsch, P. (2018). Stochastic cosmic ray sources and the TeV break in the all-electron spectrum. *JCAP*, 11:045.

Mertsch, P. (2020). Test particle simulations of cosmic rays. *Ap&SS*, 365(8):135.

Millikan, R. A. and Cameron, G. H. (1928). The origin of the cosmic rays. *Phys. Rev.*, 32:533–557.

Moskalenko, I. V. and Strong, A. W. (1998). Production and propagation of cosmic ray positrons and electrons. *Astrophys. J.*, 493:694–707.

Niu, J.-S. (2020). Origin of the hardening in AMS-02 nuclei spectra at a few hundred GV.

Ohira, Y., Yamazaki, R., Kawanaka, N., and Ioka, K. (2012). Escape of cosmic-ray electrons from supernova remnants. *MNRAS*, 427(1):91–102.

Osborne, J. L. and Ptuskin, V. S. (1988). Cosmic-Ray Reacceleration in the Interstellar Medium. *Soviet Astronomy Letters*, 14:132.

Ostriker, J. P. and McKee, C. F. (1988). Astrophysical blastwaves. *Reviews of Modern Physics*, 60(1):1–68.

Pancheri, G. and Srivastava, Y. (2017). Introduction to the physics of the total cross-section at LHC: A Review of Data and Models. *Eur. Phys. J. C*, 77(3):150.

Parizot, E., Marcowith, A., Ballet, J., and Gallant, Y. A. (2006). Observational constraints on energetic particle diffusion in young supernovae remnants: amplified magnetic field and maximum energy. *A&A*, 453(2):387–395.

Parker, E. N. (1965). The passage of energetic charged particles through interplanetary space. *P&SS*, 13(1):9–49.

Pavan, L. et al. (2014). The long helical jet of the Lighthouse nebula, IGR J11014-6103. *Astron. Astrophys.*, 562:A122.

Pelgrims, V., Ferrière, K., Boulanger, F., Lallement, R., and Montier, L. (2020). Modeling the magnetized Local Bubble from dust data. *A&A*, 636:A17.

Porter, T. A. and Strong, A. (2005). A New estimate of the Galactic interstellar radiation field between 0.1 microns and 1000 microns. In *29th International Cosmic Ray Conference*, volume 4, pages 77–80.

Pothast, M., Gaggero, D., Storm, E., and Weniger, C. (2018). On the progressive hardening of the cosmic-ray proton spectrum in the inner Galaxy. *JCAP*, 10:045.

Press, W., Press, W., Teukolsky, S., Vetterling, W., Vetterling, W., Flannery, B., and Flannery, B. (2002). *Numerical Recipes in C++: The Art of Scientific Computing*. Cambridge University Press.

Profumo, S., Reynoso-Cordova, J., Kaaz, N., and Silverman, M. (2018). Lessons from HAWC pulsar wind nebulae observations: The diffusion constant is not a constant; pulsars remain the likeliest sources of the anomalous positron fraction; cosmic rays are trapped for long periods of time in pockets of inefficient diffusion. *Phys. Rev. D*, 97(12):123008.

Prouza, M. and Šmída, R. (2003). The Galactic magnetic field and propagation of ultra-high energy cosmic rays. *A&A*, 410:1–10.

Pshirkov, M. S., Tinyakov, P. G., Kronberg, P. P., and Newton-McGee, K. J. (2011). Deriving global structure of the Galactic Magnetic Field from Faraday Rotation Measures of extragalactic sources. *Astrophys. J.*, 738:192.

Ptuskin, V., Moskalenko, I. V., Jones, F., Strong, A., and Zirakashvili, V. (2006). Dissipation of magnetohydrodynamic waves on energetic particles: impact on interstellar turbulence and cosmic ray transport. *Astrophys. J.*, 642:902–916.

Ptuskin, V. S., Moskalenko, I. V., Jones, F. C., Strong, A. W., and Zirakashvili, V. N. (2006). Dissipation of Magnetohydrodynamic Waves on Energetic Particles: Impact on Interstellar Turbulence and Cosmic-Ray Transport. *ApJ*, 642:902–916.

Rankine, W. J. M. (1870). Xv. on the thermodynamic theory of waves of finite longitudinal disturbance. *Philosophical Transactions of the Royal Society of London*, 160:277–288.

Recchia, S., Gabici, S., Aharonian, F. A., and Vink, J. (2019). Local fading accelerator and the origin of TeV cosmic ray electrons. *Phys. Rev.*, D99(10):103022.

Reichherzer, P., Becker Tjus, J., Zweibel, E., Merten, L., and Pueschel, M. (2019). Turbulence-Level Dependence of Cosmic-Ray Parallel Diffusion.

Remy, Q., Grenier, I., Marshall, D., and Casandjian, J. (2017). Cosmic rays, gas and dust in nearby anticentre clouds - I. CO-to-H_2 conversion factors and dust opacities. *Astron. Astrophys.*, 601:A78.

Remy, Q., Grenier, I., Marshall, D., and Casandjian, J. (2018a). Cosmic-rays, gas, and dust in nearby anti-centre clouds : III – Dust extinction, emission, and grain properties. *Astron. Astrophys.*, 616:A71.

Remy, Q., Grenier, I., Marshall, D., and Casandjian, J. (2018b). Cosmic-rays, gas, and dust in nearby anticentre clouds : II. Interstellar phase transitions and the dark neutral medium. *Astron. Astrophys.*, 611:A51.

Roberts, N., Lorimer, D., Kramer, M., Ellis, R., Huchra, J., Kahn, S., Rieke, G., and Stetson, P. (2005). *Handbook of Pulsar Astronomy*. Cambridge Observing Handbooks for Research Astronomers. Cambridge University Press.

Rutherford, E. (1911). The scattering of alpha and beta particles by matter and the structure of the atom. *Phil. Mag. Ser. 6*, 21:669–688.

Schlickeiser, R. (1989). Cosmic-Ray Transport and Acceleration. I. Derivation of the Kinetic Equation and Application to Cosmic Rays in Static Cold Media. *ApJ*, 336:243.

Schlickeiser, R. (2002). *Cosmic Ray Astrophysics*.

Schure, K. M. and Bell, A. R. (2013). Cosmic ray acceleration in young supernova remnants. *MNRAS*, 435(2):1174–1185.

Schwartz, S. J. and Skilling, J. (1978). The Escape of Cosmic Rays from Supernova Remnants. *A&A*, 70:607.

Seo, E. S. and Ptuskin, V. S. (1994). Stochastic Reacceleration of Cosmic Rays in the Interstellar Medium. *ApJ*, 431:705.

Shalchi, A. (2005). Second-order quasilinear theory of cosmic ray transport. *Physics of Plasmas*, 12(5):052905–052905.

Shalchi, A. (2006). Analytical investigation of the two-dimensional cosmic ray Fokker-Planck equation. *A&A*, 448(3):809–816.

Shalchi, A. (2009). *Nonlinear Cosmic Ray Diffusion Theories*, volume 362.

Shalchi, A., Bieber, J. W., Matthaeus, W. H., and Qin, G. (2004). Nonlinear Parallel and Perpendicular Diffusion of Charged Cosmic Rays in Weak Turbulence. *ApJ*, 616(1):617–629.

Shalchi, A. and Schlickeiser, R. (2004). Quasilinear perpendicular diffusion of cosmic rays in weak dynamical turbulence. *A&A*, 420:821–832.

Sharma, S. (2017). Markov Chain Monte Carlo Methods for Bayesian Data Analysis in Astronomy. *Ann. Rev. Astron. Astrophys.*, 55:213–259.

Shen, C. S. (1970). Pulsars and Very High-Energy Cosmic-Ray Electrons. *ApJL*, 162:L181.

Skilling, J. (1971). Cosmic Rays in the Galaxy: Convection or Diffusion? *ApJ*, 170:265.

Sofue, Y., Nakanishi, H., and Ichiki, K. (2019). Magnetic field and ism in the local galactic disc. *Monthly Notices of the Royal Astronomical Society*, 485(1):924–933.

Sridhar, S. and Goldreich, P. (1994). Toward a Theory of Interstellar Turbulence. I. Weak Alfvenic Turbulence. *ApJ*, 432:612.

Strong, A. W. and Mattox, J. R. (1996). Gradient model analysis of EGRET diffuse Galactic γ-ray emission. *A&A*, 308:L21–L24.

Strong, A. W. and Moskalenko, I. V. (1998). Propagation of cosmic-ray nucleons in the galaxy. *Astrophys. J.*, 509:212–228.

Strong, A. W., Moskalenko, I. V., and Ptuskin, V. S. (2007). Cosmic-ray propagation and interactions in the Galaxy. *Ann. Rev. Nucl. Part. Sci.*, 57:285–327.

Sudoh, T., Linden, T., and Beacom, J. F. (2019). TeV Halos are Everywhere: Prospects for New Discoveries. *Phys. Rev.*, D100(4):043016.

Sun, X., Reich, W., Waelkens, A., and Enslin, T. (2008). Radio observational constraints on Galactic 3D-emission models. *Astron. Astrophys.*, 477:573.

Swann, W. (1933). Application of Liouville's Theorem to Electron Orbits in the Earth's Magnetic Field. *Phys. Rev.*, 44:224–227.

Tademaru, E. (1969). Plasma Instabilities of Streaming Cosmic Rays. *ApJ*, 158:959.

Tatischeff, V. (2009). Radio emission and nonlinear diffusive shock acceleration of cosmic rays in the supernova SN 1993J. *Astron. Astrophys.*, 499:191.

Tofflemire, B. M., Burkhart, B., and Lazarian, A. (2011). Interstellar Sonic and Alfvénic Mach Numbers and the Tsallis Distribution. *ApJ*, 736(1):60.

Tomassetti, N. (2012). Origin of the Cosmic-Ray Spectral Hardening. *Astrophys. J. Lett.*, 752:L13.

Truelove, J. K. and McKee, C. F. (1999). Evolution of Nonradiative Supernova Remnants. *ApJS*, 120(2):299–326.

Usoskin, I. G., Alanko-Huotari, K., Kovaltsov, G. A., and Mursula, K. (2005). Heliospheric modulation of cosmic rays: Monthly reconstruction for 1951-2004. *Journal of Geophysical Research (Space Physics)*, 110:A12108.

Usoskin, I. G., Bazilevskaya, G. A., and Kovaltsov, G. A. (2011). Solar modulation parameter for cosmic rays since 1936 reconstructed from ground-based neutron monitors and ionization chambers. *Journal of Geophysical Research (Space Physics)*, 116:A02104.

Vernetto, S. and Lipari, P. (2016). Absorption of very high energy gamma rays in the Milky Way. *Phys. Rev. D*, 94(6):063009.

Vietri, M. (2008). *Foundations of High-Energy Astrophysics*. Theoretical Astrophysics. Chicago Univ. Press, Chicago, IL.

Vink, J. (2012). Supernova remnants: the X-ray perspective. *Astron. Astrophys. Rev.*, 20:1.

Vladimirov, A. E., Jóhannesson, G., Moskalenko, I. V., and Porter, T. A. (2012). Testing the Origin of High-energy Cosmic Rays. *ApJ*, 752(1):68.

Vlasov, A. A. (1968). Reviews of Topical Problems: the Vibrational Properties of AN Electron Gas. *Soviet Physics Uspekhi*, 10(6):721–733.

Voelk, H. J. (1975). Cosmic ray propagation in interplanetary space. *Reviews of Geophysics and Space Physics*, 13:547–566.

Völk, H. J. (1973). Nonlinear Perturbation Theory for Cosmic Ray Propagation in Random Magnetic Fields. *Ap&SS*, 25(2):471–490.

Völk, H. J., Berezhko, E. G., and Ksenofontov, L. T. (2005). Magnetic field amplification in Tycho and other shell-type supernova remnants. *A&A*, 433(1):229–240.

Webb, G. M. and Gleeson, L. J. (1979). On the Equation of Transport for Cosmic-Ray Particles in the Interplanetary Region. *Ap&SS*, 60(2):335–351.

Webb, G. M., Zank, G. P., Kaghashvili, E. K., and le Roux, J. A. (2006). Compound and Perpendicular Diffusion of Cosmic Rays and Random Walk of the Field Lines. I. Parallel Particle Transport Models. *ApJ*, 651(1):211–236.

Wentzel, D. G. (1968). Hydromagnetic Waves Excited by Slowly Streaming Cosmic Rays. *ApJ*, 152:987.

Yaglom, A. and Silverman, R. (2004). *An Introduction to the Theory of Stationary Random Functions*. Dover books on intermediate and advanced mathematics. Dover Publications.

Yaglom, A. M. (1962). Some mathematical models generalizing the model of homogeneous and isotropic turbulence. *Journal of Geophysical Research (1896-1977)*, 67(8):3081–3087.

Yan, H. and Lazarian, A. (2002a). Scattering of cosmic rays by magnetohydrodynamic interstellar turbulence. *Phys. Rev. Lett.*, 89:281102.

Yan, H. and Lazarian, A. (2004). Cosmic ray scattering and streaming in compressible magnetohydrodynamic turbulence. *Astrophys. J.*, 614:757–769.

Yan, H. and Lazarian, A. (2008). Cosmic Ray Propagation: Nonlinear Diffusion Parallel and Perpendicular to Mean Magnetic Field. *Astrophys. J.*, 673:942.

Yan, H.-r. and Lazarian, A. (2002b). Scattering of cosmic rays by magnetohydrodynamic interstellar turbulence. *Phys. Rev. Lett.*, 89:281102.

Yanasak, N., Wiedenbeck, M., Binns, W., Christian, E., Cummings, A., Davis, A., George, J., Hink, P., Israel, M., Leske, R., Lijowski, M., Mewaldt, R., Stone, E., and von Rosenvinge., T. (2001). Cosmic-ray time scales using radioactive clocks. *Advances in Space Research*, 27(4):727 – 736.

Yuan, Q., Lin, S.-J., Fang, K., and Bi, X.-J. (2017). Propagation of cosmic rays in the AMS-02 era. *Phys. Rev.*, D95(8):083007.

Yuan, Q., Qiao, B.-Q., Guo, Y.-Q., Fan, Y.-Z., and Bi, X.-J. (2020). Nearby source interpretation of differences among light and medium composition spectra in cosmic rays.

Zaharijas, G., Conrad, J., Cuoco, A., and Yang, Z. (2013). Fermi-LAT measurement of the diffuse gamma-ray emission and constraints on the Galactic Dark Matter signal. *Nucl. Phys. B Proc. Suppl.*, 239-240:88–93.

Zatsepin, G. T. and Kuz'min, V. A. (1966). Upper Limit of the Spectrum of Cosmic Rays. *Soviet Journal of Experimental and Theoretical Physics Letters*, 4:78.

Zhang, H., Chepurnov, A., Yan, H., Makwana, K., Santos-Lima, R., and Appleby, S. (2020a). Identification of plasma modes in Galactic turbulence with synchrotron polarization. *Nature Astronomy*.

Zhang, H., Chepurnov, A., Yan, H., Makwana, K., Santos-Lima, R., and Appleby, S. (2020b). Identification of plasma modes in Galactic turbulence with synchrotron polarization. *Nature Astronomy*, 4:1001–1008.

Zirakashvili, V. N., Breitschwerdt, D., Ptuskin, V. S., and Voelk, H. J. (1996). Magnetohydrodynamic wind driven by cosmic rays in a rotating galaxy. *A&A*, 311:113–126.

Zirakashvili, V. N. and Ptuskin, V. S. (2017). Acceleration of particles and generation of nonthermal emission in old supernova remnants. *Bulletin of the Russian Academy of Sciences: Physics*, 81(4):434–436.